Author:
Rycerz, Jakub

Title:
Realising the Potential of Carbon Fibre Composites in Compression

Realising the Potential of Carbon Fibre Composites in Compression

Jakub Rycerz

A dissertation submitted to the University of Bristol in accordance with the requirements of the degree of Doctor of Philosophy in the Faculty of Engineering.

University of Bristol
Faculty of Engineering
Department of Aerospace Engineering
September 2020

Word Count: Thirty four thousand, seven hundred and sixty

Abstract

Compressive behaviour of carbon fibre composites is often simplified as linear elastic until brittle failure at a strain lower than tensile failure strain. Despite the apparent simplicity of the response under compression, the associated kink-band failure mode and its formation is not fully understood. Numerous models and theories predicting compressive failure of varying degrees of complexity exist, but test results are mostly limited to low strains and brittle failure.

Recent research suggests that high-strength carbon fibre can achieve very high strains in excess of 20% under compression while exhibiting ductile-like behaviour. This study aims to address the prevalence of low strains being reported in the literature and used for design of composite structures by providing relatively simple modelling tools and a new testing approach.

It is postulated that compressive strain to failure is not a fibre property, but a result of shear instability of the composite which is a function of the shear response of the material, its stiffness and the misalignment of the fibres. An equilibrium-based model is introduced for prediction of the onset of shear instability in unidirectional composite. The model is extended to allow for instability prediction in a hybrid composite consisting of two different unidirectional materials. A mechanical basis for hybrid effect in compression is explained.

A novel test method is developed for carbon fibre composites that achieves compressive strains to failure that are higher in magnitude than strains to failure in tension. A number of different materials is tested, and results are explained using the previously formulated model. The test method also allows for obtaining the Young's modulus of the material during the loading. The non-linear behaviour of carbon fibre at high compressive strains is investigated. Recommendations are given regarding the compressive testing of carbon fibre composites.

Acknowledgements

I would like to thank Professor Michael Wisnom for his support, wealth of ideas he shared with me, the knowledge he was able to offer, common sense and – most of all – his patience that allowed all this to be done.

Thanks to the lab support, colleagues and technical staff at the University of Bristol that made most of the experimental work contained within this thesis possible. In no particular order: Putu Suwarta, Ian Chorley, Julie Etches, Steve Rae, Ollie Nixon-Pearson, Yusuf Mahadik, Anastasia Koutsomitopoulou, Guy Pearn.

Thank you to my colleague and friend Dr Bradley Cox for his best efforts to keep my laziness in check. Don't ever change.

And most importantly, thank you to my family for your endless trust and support. I hope one day I will live up to be the person you believe I am.

Author's Declaration

I declare that the work in this dissertation was carried out in accordance with the requirements of the University's Regulations and Code of Practice for Research Degree Programmes and that it has not been submitted for any other academic award. Except where indicated by specific reference in the text, the work is the candidate's own work. Work done in collaboration with, or with the assistance of, others, is indicated as such. Any views expressed in the dissertation are those of the author.

SIGNED: ..... DATE:.....

Contents

List of Figures

List of Tables

1 Introduction

Fibrous composites are not easily characterized. Their behaviour can vary depending on their orientation, temperature and state of production. When thinking of carbon fibre, one rarely imagines a spool of dry material, thin and not sturdy at all. Why? It is the same material that is considered state-of-the-art when embedded in a resin.

Table 1-1: Qualitative prediction of strain to failure of a typical high-strength carbon fibre in a variety of tests.

Test Case	Tension		Compression	
	Strain at Failure	Behaviour	Strain at Failure	Behaviour
Long Single Fibre	Fibre Strain	Elastic Loading Followed by Fibre Breaking	N/A	Folding of Fibre
Long Single Tow	≈ Fibre Strain	Elastic Loading, Stochastic Breaking of Individual Fibres	N/A	Folding of Tow
Flat, Long Coupon with Tabs	≈ Fibre Strain	Elastic Loading Followed by Breaking	<< Fibre Strain	Elastic Loading, Elastic Buckling
Short Dogbone Coupon	≈ Fibre Strain	Elastic Loading Followed by Breaking	< Fibre Strain	Elastic Loading, Breaking
Flat, Long Carbon Specimen in Four-Point Bending	≈ Fibre Strain	Elastic Loading, Breaking of Tensile Side	> Fibre Strain	Elastic Loading, Breaking of Tensile Side (No Compressive Failure)

Table 1-1 shows a qualitative comparison between tension and compression failure for a variety of tests. It can be seen that in some cases the failure is impossible to reach in compression, for example when testing a single, long fibre. Application of displacement aimed to compress the fibre in such case would result in folding of the fibre with no damage. This could be considered a failure (similar to Euler buckling in the case of a long, flat coupon) and would therefore set the strain to failure of both the fibre and tow as zero (as they have no resistance to folding).

What if we embedded the dry fibres in clay? Would we still be able to push them apart with virtually no force? What about ice? Cement?

It is postulated here that the compressive response of a composite is not highly dependent on its fibres. Other factors such as shear stiffness, fibre alignment and longitudinal stiffness are the determining factors of the strain the composite can achieve before breaking.

1.1 Objectives

This work will attempt to address the following questions:

1. Can compressive failure of carbon fibre be predicted simply and by using other material properties?
2. What can be done to achieve high strain compressive behaviour using existing test methods?
3. Can new test methods be implemented to achieve high strains in compression?
4. How can the non-linear behaviour of carbon fibre be measured?

1.2 Thesis Outline

Chapter 2 will provide a brief overview of the literature relevant to this work. Known publications exploiting high-strain, non-linear behaviour of carbon fibre will be summarised. Methods of predicting the compressive behaviour will be assessed. A topic of hybrid composites will be investigated as potentially useful. Relevant test methods will be identified.

Chapter 3 will introduce an equilibrium-based model for predicting the shear instability of fibrous composites that is believed to lead to compressive failure in most cases. A hybrid effect in compression will be described and its usefulness for achieving higher strains

discussed in more detail. A parametric study will be performed using the model to establish what behaviour can be expected in the following sections.

Following the findings from Chapter 3, a hybrid lay-up will be utilised in Chapter 4 to achieve high strains using an existing direct compression (DC) test standard (modified ASTM D695 [1]). The results will be compared with the model predictions.

Chapter 5 will introduce a four-point bending (4PB) test aimed at obtaining high compressive strains in carbon indirectly through flexure of a hybrid beam. Numerous aspects of the test will be discussed. A correction for the non-linear geometric effects using the 4PB test will be derived. A broader testing methodology for utilization in parametric studies will be recommended.

The proposed test method will be used to test a number of different materials to high strain in Chapter 6. Two studies on materials with the same fibre type but different matrix response will be presented. Qualitative explanation of the results will be performed using the model introduced in Chapter 3. A 4PB test using the materials tested previously in Chapter 4 will be performed to compare the attainable strains.

Chapter 7 will briefly investigate the non-linear behaviour of carbon fibre and how it is obtained from the 4PB test introduced in Chapter 5.

Lastly, Chapter 8 will summarise the findings and make recommendations for future work.

2 Literature Review

This chapter provides a brief introduction to key concepts and the relevant literature.

2.1 Failure of Carbon Fibre in Compression

The idea for this work was inspired by a now widely cited publication by Ueda [2] in which a single carbon fibre is embedded into a resin block and compression tested inside a SEM as seen in Figure 2-1, using the microscope as a video gauge.

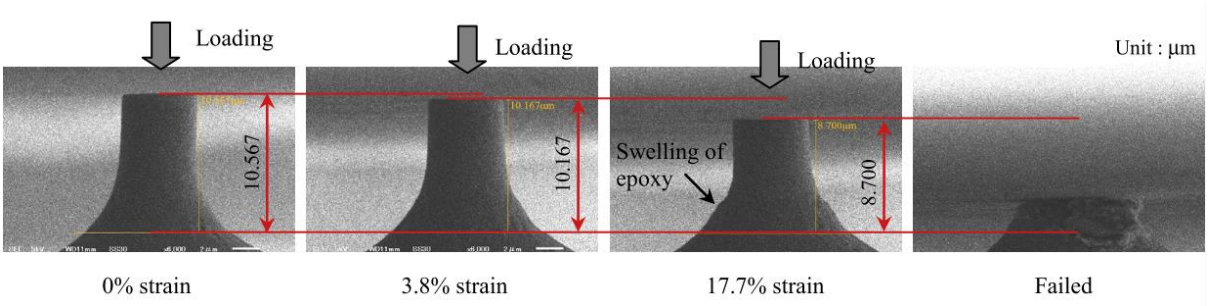

Figure 2-1: The progression of a single fibre compressive test. Adopted from [2].

While similar tests were performed in the past [3]–[5], they did not provide visual tracking of the test or the stress-strain curve results of such good quality. The novelty of the setup is undeniable, however the most relevant portion of the publication is the reported results, reproduced in Figure 2-2.

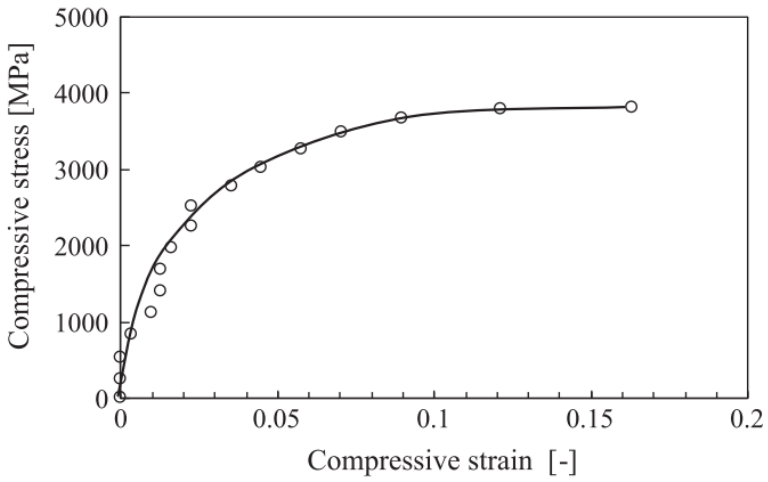

Figure 2-2: Stress-strain response of a single carbon fibre reported by Ueda. Adopted from [2].

The extremely high strain that is reported can raise questions about the test methodology and whether the authors were indeed measuring the strain in the fibre (Toray T800S, a PAN-based high-strength fibre), rather than indenting the supporting resin pillar with the fibre.

Another, more recent publication [6] confirmed the initial results and provided more insight into the damage formation in the single carbon fibre under compression. It was revealed that carbon fibre can achieve 90% of its fracture strain in compression repeatedly, seemingly without damage.

If the response of a single carbon fibre under the right conditions can be that high, why are the compressive strains to failure in composite materials reported to be low? A good representation of typical results from testing carbon fibre samples in compression is shown in Figure 2-3.

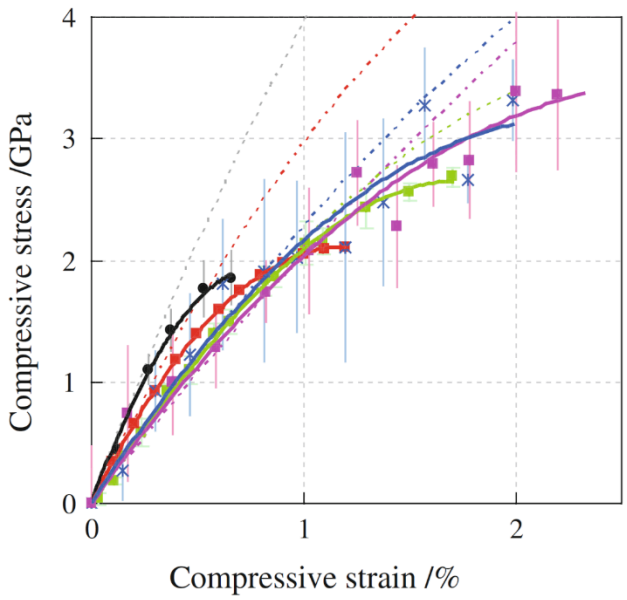

Figure 2-3: Collated results of testing various carbon fibre samples in compression. Strain values in excess of 2% are rare, even for high strength fibres. Adapted from [7].

It can be seen that results in excess of $\varepsilon_{c,max} = 2\%$ are rarely obtained for carbon fibre composites, while the same composites under tension will typically achieve both higher tensile stress and tensile strain at failure. This relationship holds true for most fibrous composites and is depicted in Figure 2-4.

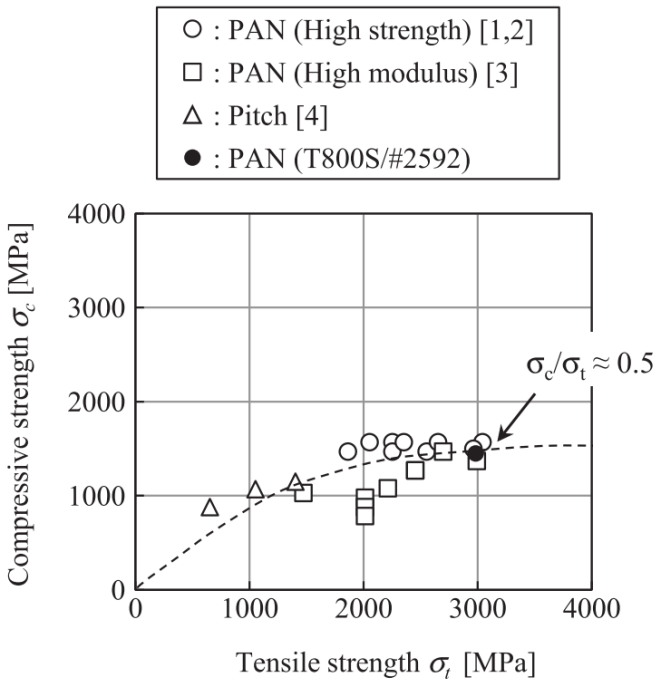

Figure 2-4: The relationship between tensile and compressive strength for a variety of carbon fibre composites. Adopted from [2].

Since carbon fibre seems to be capable of achieving high strain as per Figure 2-2, it could be argued that it is the surrounding matrix that limits the compressive performance of the composite. However, looking at the compressive strain capability of a modern epoxy resin (Epon E862) shown in Figure 2-5 suggests that the resin has a high strain capability under compressive loading.

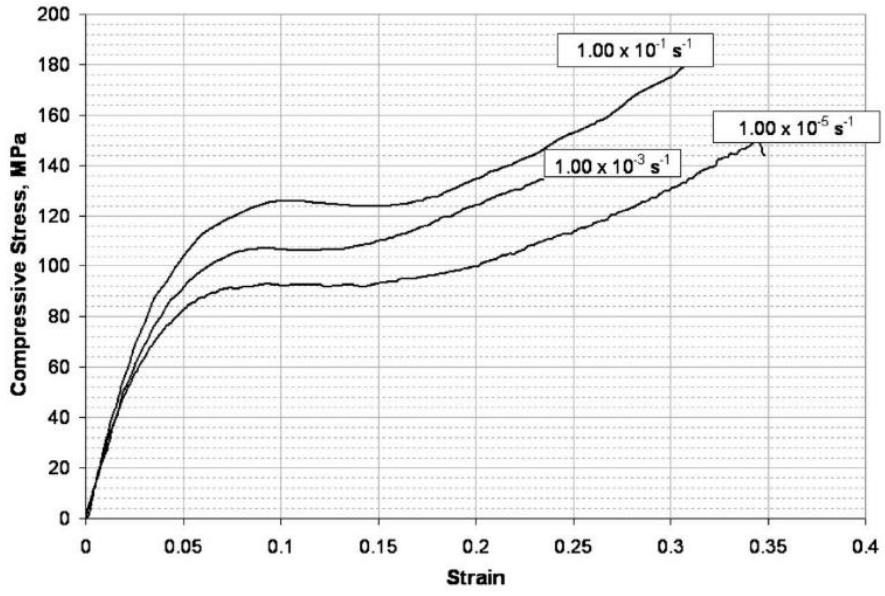

Figure 2-5: Compressive stress versus compressive strain of a Epon E862 epoxy resin a different strain ratios (shown for each curve). Adopted from [8].

In order to better understand compressive failure, let us take a look at the micrographs of the failure surface of the specimen. A typical slice of a failed compression sample in the damage area can be seen in Figure 2-6.

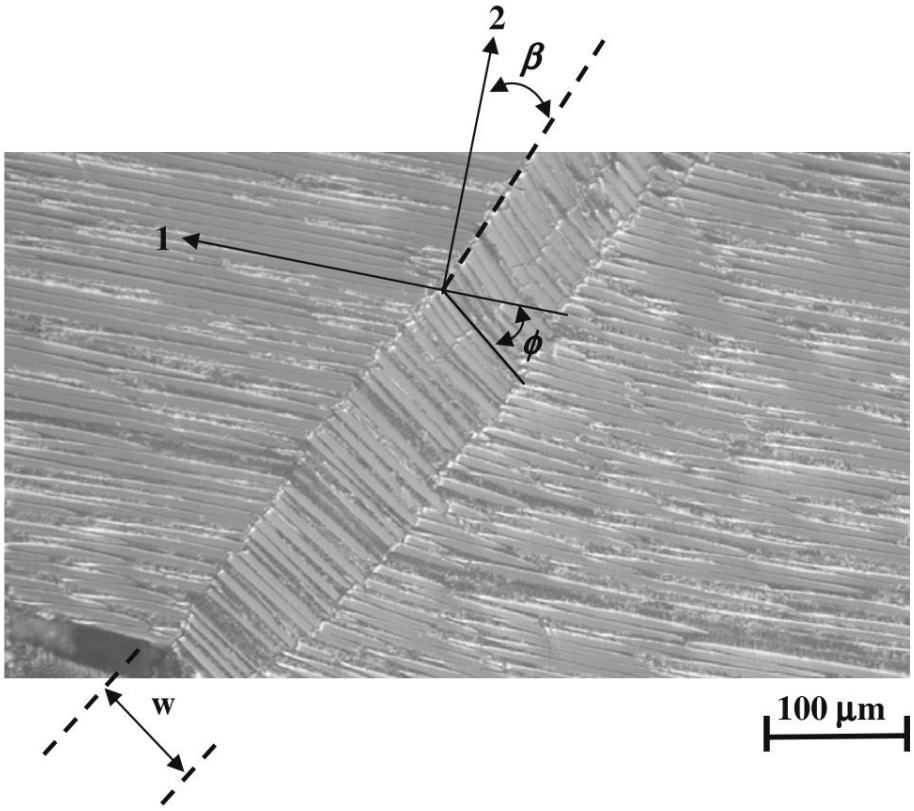

Figure 2-6: Close-up of damage to a carbon fibre specimen failed in compression. The band of sheared fibres is a typical feature of a compression failure called a kink-band. Adopted from [9].

The structure visible in the micrograph is a kink-band. It is widely seen in carbon fibre composites where failure occurs in compression. The failure progression is as follows [9]–[11]:

- As compression is applied to the specimen, the fibers are compressed axially.
- The long, slender fibres want to buckle into a lower energy state, but are constrained by the surrounding matrix, inducing matrix shear.
- When the compressive load becomes critical, the matrix is no longer able to support the fibres and buckling occurs. The location is likely correlated to the largest defect (resin rich area or fibre waviness).
- The load is moved from the failed region to the adjacent fibres, increasing the load and causing the kink-band to propagate until failure.

The kink-band terminology was originally used for metals [12] and geological faults [13], but early composites research [14] adopted the naming due to visual similarities between the failure modes. The kinking failure is common to fibrous composites loaded in compression, regardless of their size [15]. Introduction of holes and notches also results in kink-band failure, albeit at lower bulk section stress due to stress concentration induced by these features [11], [16].

Failure of carbon fibre composites in compression is not governed by the constituent material compressive properties, unlike the tensile failure which can be predicted by the rule of mixtures [17]. The compressive failure instead originates from instability. Let us look at the historical perspective next.

2.2 Brief History of Composite Compression Failure Theories

One of the earliest (published in 1965) pieces of literature on the mechanics of carbon fibre materials is by Rosen [18]. The author likens the compression of carbon fibres embedded in resin to a column resting on elastic (Winkler) foundation [19] and attributes the ultimate failure to elastic instability. The limit of the compressive strength of composite is given as:

$$\sigma_C = \frac{G}{1 - v_f} \tag{2.1}$$

Where σ_C is the ultimate compressive strength of the composite, G is the matrix shear modulus and v_f is the fibre volume fraction. It is postulated that using a stiffer matrix would increase the compressive strength of the composite.

Another take on the limits of compression dates back to 1972, formulated by Argon [20]. The author's formula for the compressive strength of the composite is:

$$\sigma_C = \frac{\tau_Y}{\theta} \tag{2.2}$$

Where σ_C is again the ultimate compressive strength of the composite, τ_Y is the yield strength of the matrix in shear and θ is the maximum fibre misalignment. This model is different from that of Rosen, as it assumes that shear strength, not shear stiffness governs the compressive response. In addition, there is a recognition that fibre misalignment directly affects the ultimate strength in compression. While Rosen's formula assumes elastic buckling, Argon proposes plastic kinking to occur.

Budiansky [21] later expanded Rosen's formula to:

$$\sigma_C = G + E_T \tan^2 \beta \tag{2.3}$$

Where G is the matrix shear modulus, E_T is the tensile transverse modulus of the composite and β is the kink band angle, as shown in Figure 2-7.

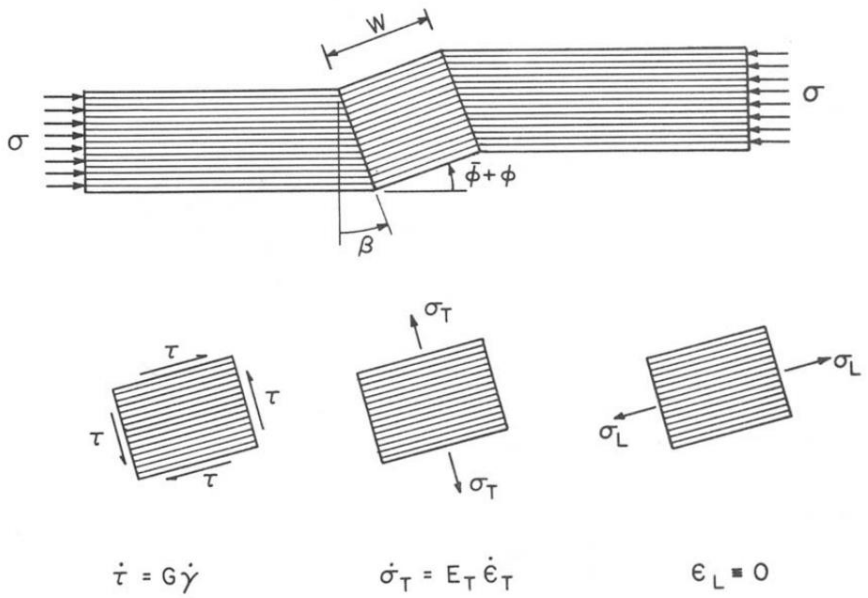

Figure 2-7: Geometry of the kink band as defined in [21]. Ibid.

However, it was Budiansky's view that elastic consideration of compressive failure was irrelevant and plasticity approach was required. He therefore expanded Argon's formula as well:

$$\sigma_C = \frac{\tau_Y}{\gamma_Y + \theta} \tag{2.4}$$

Where σ_C is the ultimate compressive strength of the composite, τ_Y is the yield strength of the matrix in shear, γ_Y is the yield strain of the matrix in shear and θ is the maximum fibre misalignment. This can also be written as:

$$\sigma_C = \frac{G}{1 + \frac{\theta}{\gamma_Y}} \tag{2.5}$$

Where G is the matrix shear stiffness. This model was later vastly expanded and generalised in a 1991 work by Budiansky and Fleck [22], which analyses many theoretical cases, but the most relevant finding seems to be the graph of non-dimensional kinking stress versus imperfection, shown in Figure 2-8.

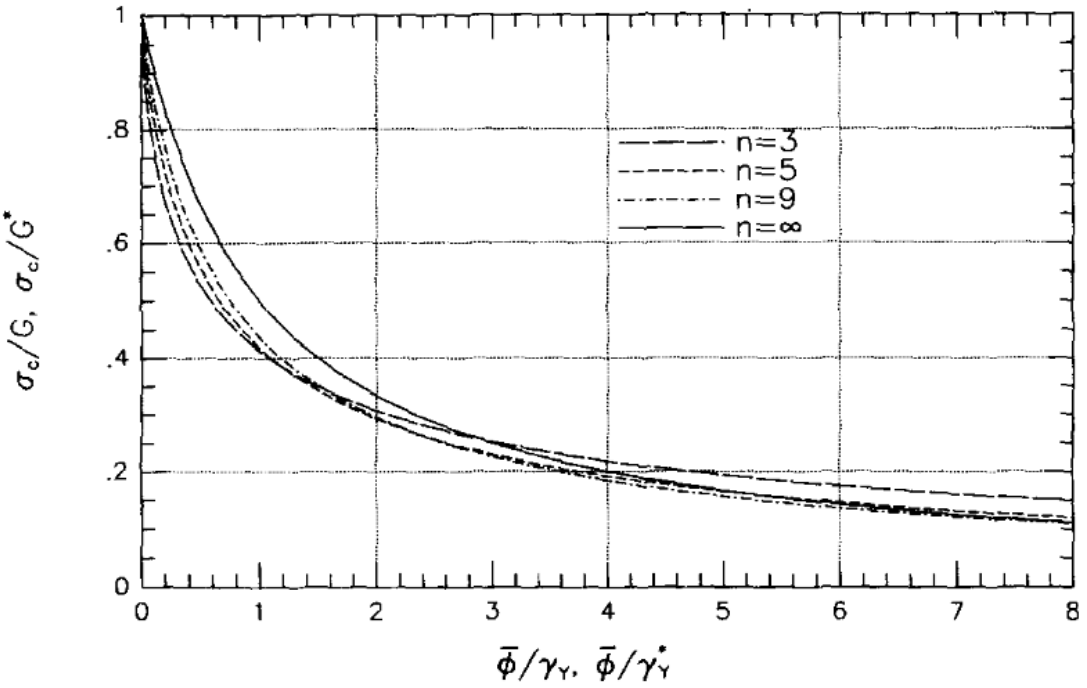

Figure 2-8: Kinking stress variation with imperfection. The stress in normalised against the matrix shear modulus and the fibre misalignment is normalised against the shear strain of the material. Adopted from [22].

The graph is interesting, as it establishes the main variables defining compressive strength of the composite as:

- The matrix shear stiffness G
- The fibre misalignment angle θ
- The matrix yield strain is shear γ_Y

The first two of these will later be shown to be the defining variables in the model presented in this work.

Wisnom [23] derived an instability-based model for predicting the failure of carbon fibre composites under compressive loading. The model assumes an infinitesimal element of material with initially misaligned fibres, as shown in Figure 2-9.

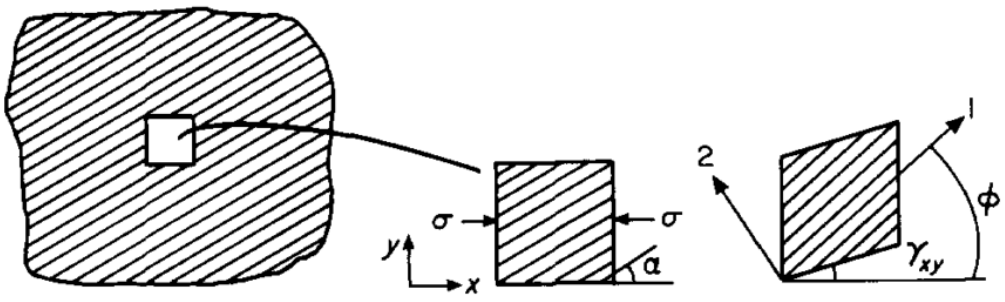

Figure 2-9: Shear instability model definition. Slice of material with initial fibre misalignment α is subject to compressive stress, generating shear deformation. Adopted from [23].

The model assumes an iterative approach. Applying compressive stress σ to a slice of material with initial fibre misalignment α results in generation of shear stress that in turn produces shear deformation γ_{xy}. This increases the induced shear stress and further drives the shear deformation. Iterative procedure is implemented to calculate stable equilibrium at a given compressive stress. However, when stress level is critical, the equilibrium becomes unstable, leading to the onset of microbuckling and subsequent failure. Calculation of the critical stress can be performed iteratively for different values of initial misalignment α. The results produced by the author are shown in Figure 2-10.

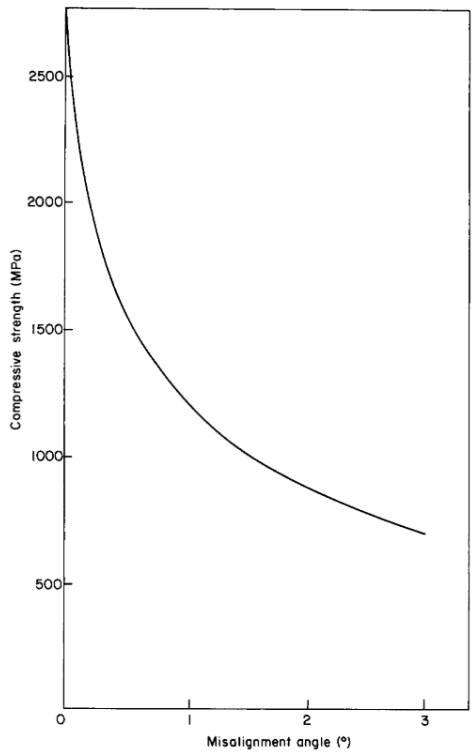

Figure 2-10: The relationship between misalignment angle and compressive strength (instability onset) of XAS/914 samples. Adopted from [23].

The predictions of the model were qualitatively proven in testing [24]. As the model is the basis of the work presented in section 3 of this thesis, it will be further elaborated upon there.

There is a similarity between the compressive strength curves seen in Figure 2-8 and Figure 2-10. Both start with a high compressive strength at low misalignment and decay in an exponential-like fashion as the misalignment increases. This indicates that regardless of the type of modelling and associated assumptions, the change of compressive behaviour with misalignment will follow a similar trend. Initial fibre misalignment can be deemed one of the factors affecting the maximum compressive strength of the composite.

2.3 Compression Testing of Composite Materials

As the misalignment is critical to the compressive strength that can be obtained, careful testing must be implemented to fully realise the potential of the material. Should the test setup introduce a misalignment in the sample, eccentricity in the loading or secondary bending for a direct compression test, the resulting ultimate strength value may be impacted significantly.

Some good reviews on the subject exist [25]–[27], and most direct test methods employ a jig to ensure good alignment of the top and bottom loading fixtures, as well as limiting structural buckling of the specimen. This is the case with ASTM D695 [28] which uses anti-buckling guides. Similarly, both ASTM D6641 [29] and ASTM D3410 [30] utilise a test fixture with bearings that ensures good sample alignment and linear movement only.

Similarly, the modified ASTM D695 [1] uses a large and solid jig to align the sample. A drawing of the jig is shown in Figure 2-11.

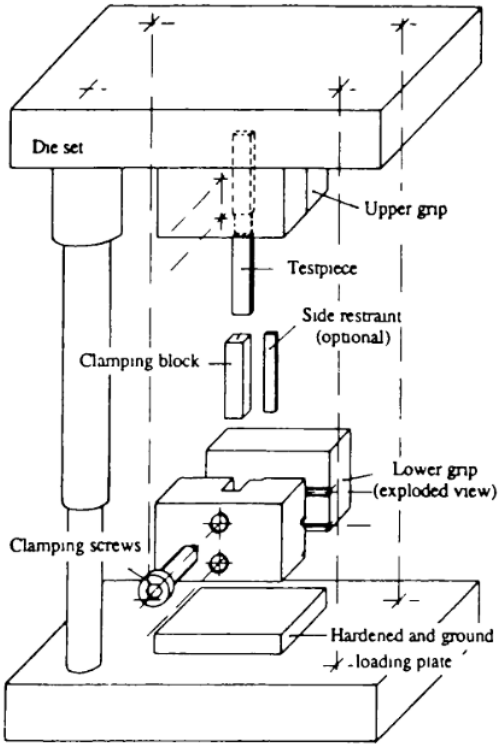

Figure 2-11: Modified ASTM D695 test rig. The solid steel plates at top and bottom and guides on bearings are designed to minimise unwanted eccentricity and bending. Adopted from [1].

It is one of the heaviest jigs available, and provides good results against other popular test methods, as shown in Figure 2-12.

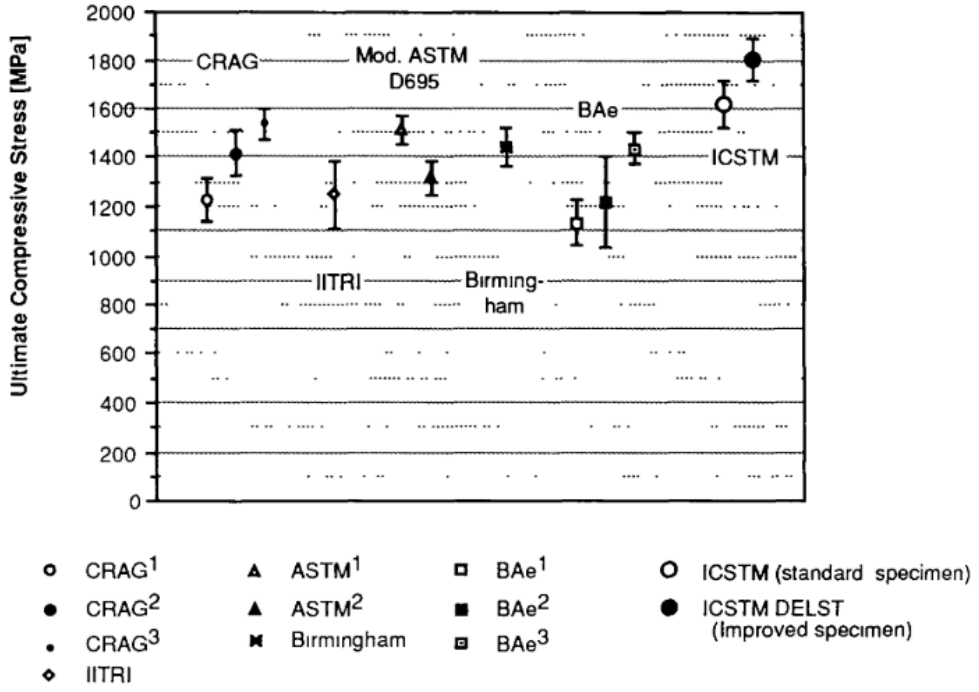

Figure 2-12: Comparison of the compressive stress attainable using the modified ASTM D695 test jig. Adopted from [1].

Non-direct test methods utilise bending or a combination of bending and compression. They typically yield higher ultimate stress results due to a strain gradient effect [31], [32] which provides support to the compressed fibres.

Bending tests can utilise a three-point bending arrangement for a localised bending moment peak, however they also introduce a shear loading into the specimen. One existing test standard is ASTM D790 [33]. Four-point bending tests have an advantage of constant bending moment over a distance between the internal supports and no shear in that region. ASTM D6272 [34] is easily adapted to various purposes as a basic test.

Wisnom [35] describes an interesting test arrangement, where the elongated sample is held at both ends that are allowed to rotate, as seen in Figure 2-13. The resulting loading is a superimposed compression and bending, decreasing the tension on the sagging side which tends to be the leading failure mode for all-carbon specimens in bending. An additional benefit of maximum compressive stress occurring in the middle of the specimen – far away from load introduction points – means that stress channelling [36] is less of a problem.

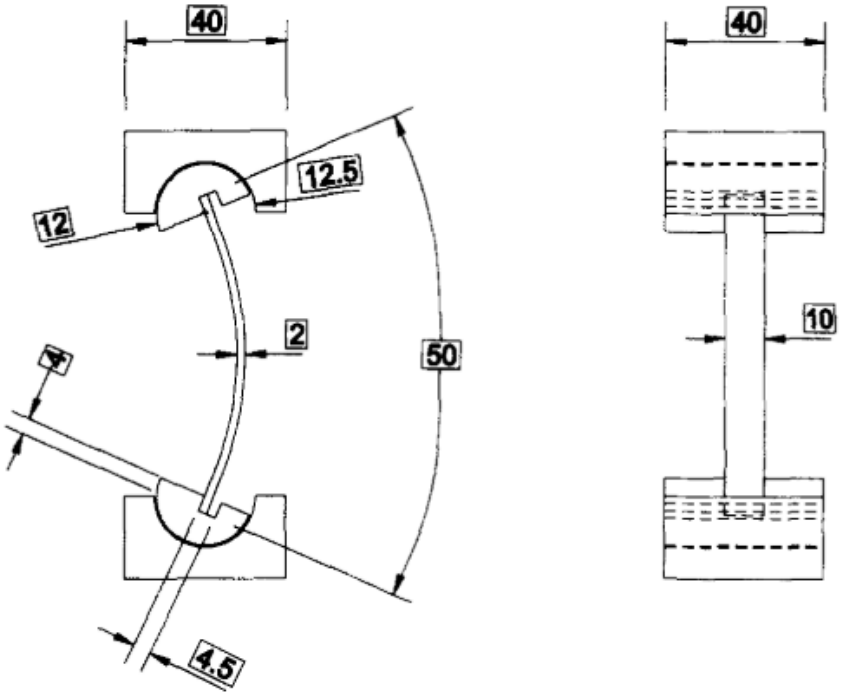

Figure 2-13: Schematic of a medium pin-ended buckling rig. Multiple sizes are described in the original study. Adopted from [35].

2.4 Hybrid Composites for Improved Failure Strain

Hybridisation of different fibres in a single composite has been attempted at least since the 1970's [37]–[39]. A comprehensive review of the subject has been performed by Swolfs et al. [40]. Under the right conditions, a hybrid laminate will exhibit improved properties as compared to a simple rule of mixtures. This is due to better utilising variability in material properties. An example of hybrid effect is shown in Figure 2-14.

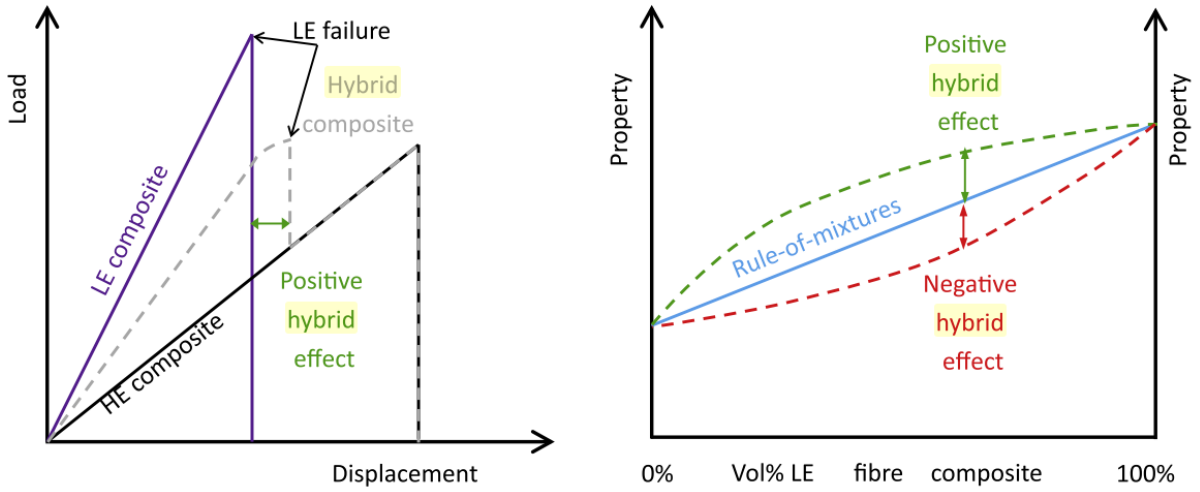

Figure 2-14: Left - hybrid effect resulting from hybridisation of stiffer low elongation (LE) composite with a high elongation (HE) composite. It can be seen that both load and displacement are improved through hybridisation as compared to the HE baseline. Right – deviation from the rule of mixtures possible with a hybrid composite. Please note that negative hybrid effect is possible, where the resulting properties are deteriorated compared to the baseline. Adopted from [40].

A notable development was presented by Czél and Wisnom [41], where thin-ply carbon was hybridised with E-glass to obtain a pseudo-ductile behaviour shown in Figure 2-15.

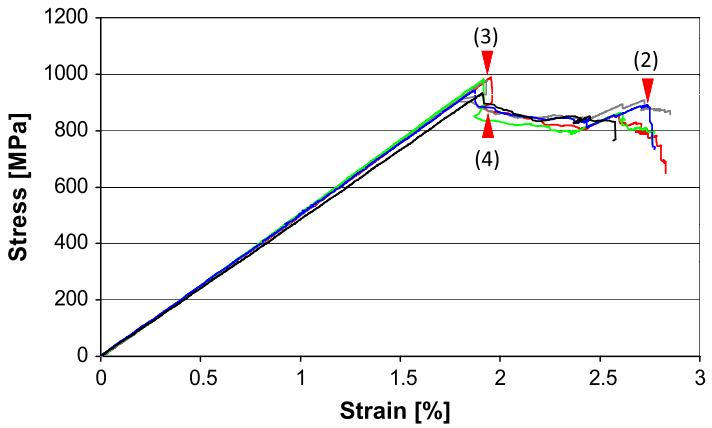

Figure 2-15: Pseudo-ductile behaviour of the composite samples due to hybridisation. Once the carbon fragments at point (3), the glass picks up the load (4) and continues to deform until the critical sample failure (2). Adopted from [41].

More interesting developments [42]–[44] from the group at the University of Bristol came about as part of the HiPerDuCT program [45] which this work was also part of. Use of hybridisation will be utilised and discussed in section 4.

2.5 Non-linear Behaviour of Carbon Fibre

It can be seen from Figure 2-1 that the modulus of carbon fibre drops as the compressive strain increases. Even for the limited strain range shown in Figure 2-3, the softening of the carbon composite is clearly visible. This non-linear (or non-hookean) behaviour of carbon fibre has been known since at least half a century at this point [46].

Most authors [7], [47], [48] attribute the non-linearity to the internal nanostructure of the fibres, which themselves consist of crystallites (crystalline clusters of carbon) embedded in an amorphous carbon matrix. The crystallites are orthotropic and directional. As the fibre is stretched or compressed, the crystallites rotate – thus changing the stiffness of the fibre. The mechanism is shown in Figure 2-16.

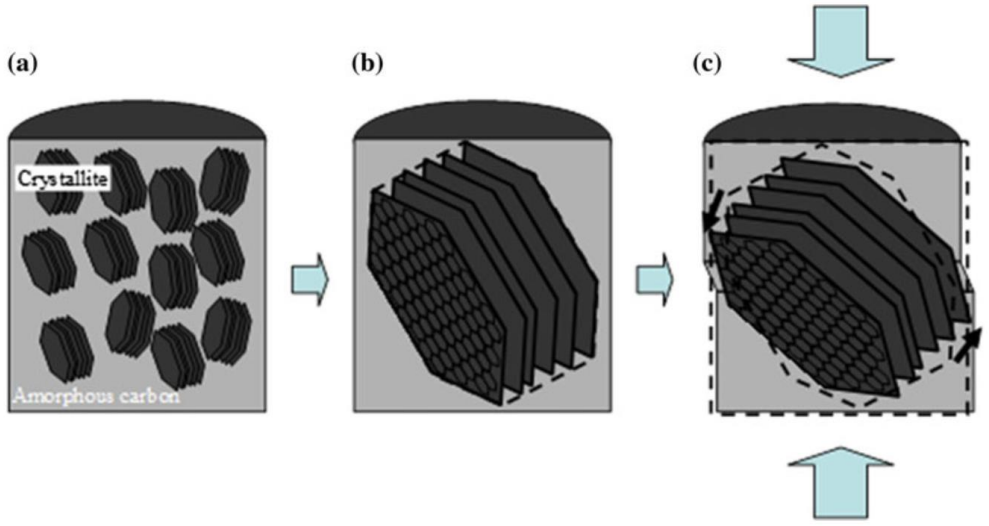

Figure 2-16: Microstructure of carbon simplified as crystallites in amorphous matrix (a). Single unit before (b) and after compression (c). The rotation of crystallites causes a modulus change. Adopted from [7].

Conversely, placing the carbon fibre under tension causes the crystallites to align their rigid direction with the axis of the fibre, increasing the stiffness as the tensile strain goes up. A paper by Kant and Penumadu [49] presents results of dynamic testing of a range of fibres and the change of modulus with strain, shown in Figure 2-17.

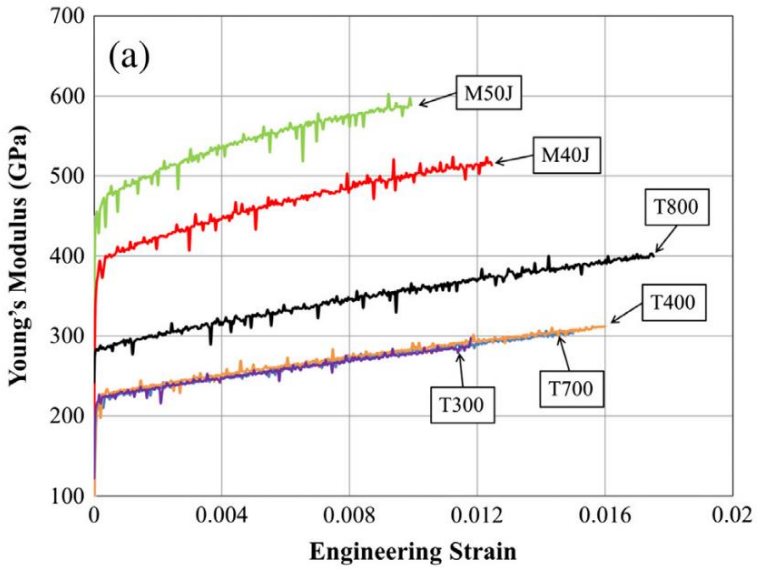

Figure 2-17: Variation of Young's modulus with tensile strain in the fibre for a range of carbon fibres. Adopted from [49].

The authors relate the linear coefficient of change of Young's modulus to the initial value, revealing that the gradient at which the modulus increases with tensile strain is proportional to the initial modulus, as shown in Figure 2-18.

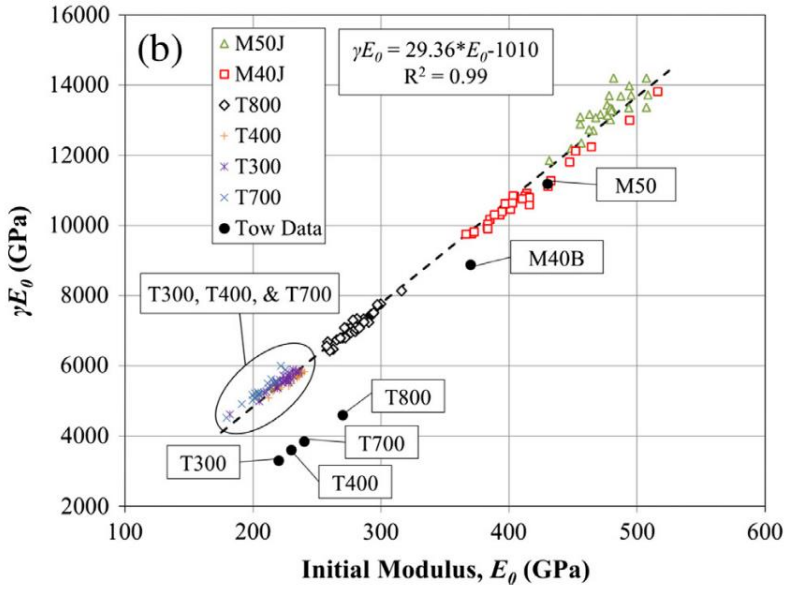

Figure 2-18: The relationship between the linear constant at which the modulus increases, γE_0 to the initial modulus E_0. Adopted from [49].

There is no information on whether the above relationship holds in compression. An investigation will be shown in section 7 and related to the literature.

This concludes the literature review section.

3 Shear Instability Modelling

Compressive failure in FRP materials is not a fibre-dominated property in contrast to tensile failure which is largely governed by the ultimate tensile strain of fibres. Dry fibre bundles can achieve similar tensile strains and stresses at failure as the equivalent composite but will easily buckle under compression.

3.1 Shear Instability in Composites Reinforced with Continuous Fibres

Wisnom [23], [24], [31], [50] presented an equilibrium-based iterative model for predicting shear instability in composites. The model assumed a rigid fibre layer embedded within deformable resin. Shear deformation of the composite is therefore achieved by shearing of the resin and rotation of the fibre. The model presented here assumes the composite to be a uniform, homogenous material undergoing shear deformation. The shear properties of the pure resin are thus not required and composite shear response is used instead.

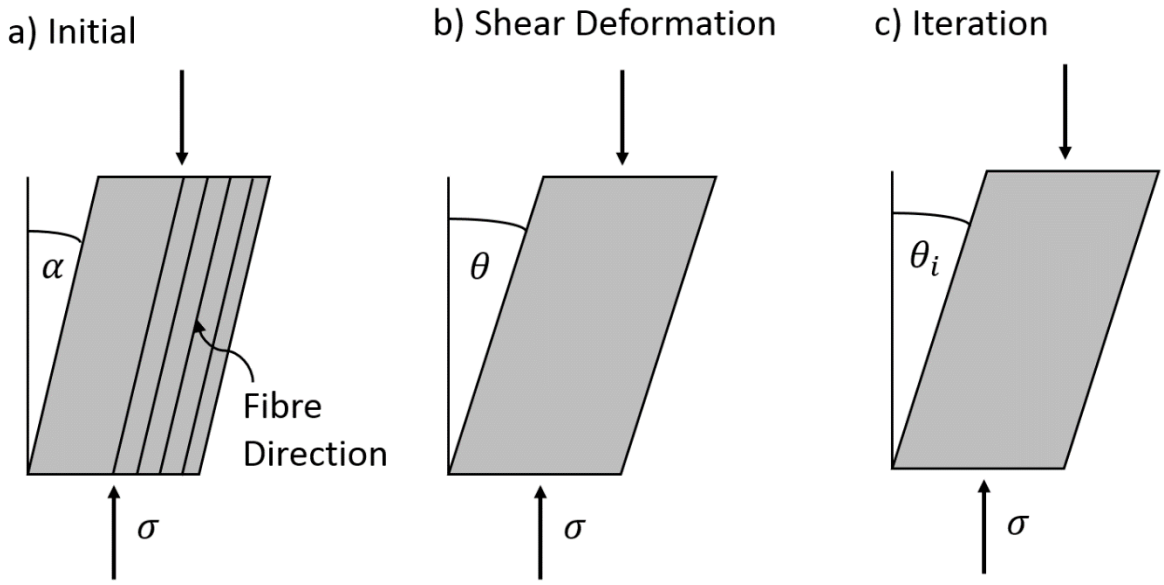

Figure 3-1: Element of unidirectional material with a) initial fibre misalignment alpha, b) after shear deformation and c) as iterated. The fibres run parallel to each elements side in all cases.

Consider an element of unidirectional composite with initial fibre misalignment α as shown in Figure 3-1 a). The applied compressive stress σ generates the shear stress τ due to the misalignment. Assuming the angles are small, the stress equilibrium at this state can be described as following:

$$\alpha\sigma = \tau \tag{3.1}$$

However, the presence of a shear stress induces shear deformation γ, which can be calculated using the material's shear modulus G:

$$\gamma = \frac{\tau}{G} \tag{3.2}$$

As the shear deformation occurs in the same direction as the initial misalignment as seen in Figure 3-1 b), the stress equilibrium equation becomes:

$$\theta\sigma = \tau \tag{3.3}$$

Where:

$$\theta = \alpha + \gamma \tag{3.4}$$

The now increased angle θ generates a higher shear stress τ which in return produces a greater deformation angle γ. The process can therefore be iterated as following:

$$\gamma_{i+1} = \frac{\tau_i}{G_i} \tag{3.5}$$

$$\theta_{i+1} = \alpha + \gamma_{i+1} \tag{3.6}$$

$$\tau_{1+1} = \theta_{i+1}\sigma \tag{3.7}$$

The shear stress in the element shown in Figure 3-1 can be evaluated by using Mohr's circle presented in Figure 3-2. Axial stress in the vertical direction is σ and there is no stress in the horizontal direction. The shear stress τ acting in the element at an angle α is accordingly drawn on the circle at an angle 2α.

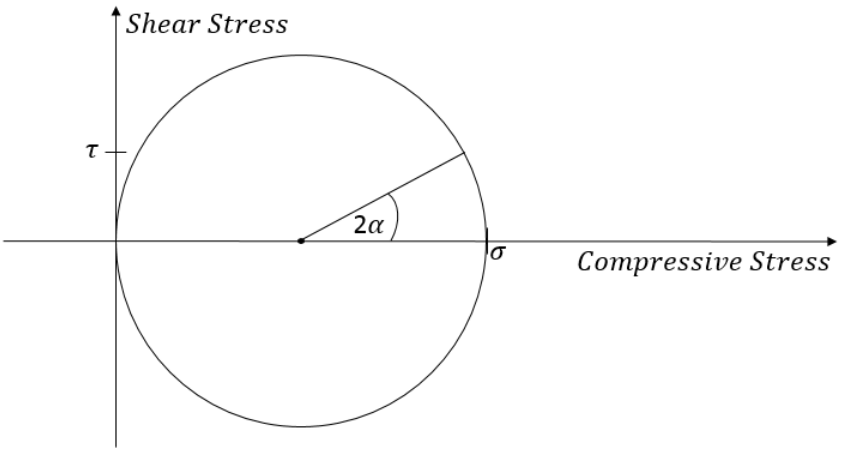

Figure 3-2: Mohr's circle for the infinitesimal element being considered.

Shear stress τ is calculated as:

$$\tau = \frac{\sigma}{2} sin2\alpha = \frac{\sigma}{2} * 2 * sin\alpha * cos\alpha \tag{3.8}$$

At low angles of α, $sin\alpha = \alpha$ and $cos\alpha = 1$, therefore the equation becomes:

$$\tau = \alpha\sigma \tag{3.9}$$

Accordingly, for the presented iteration:

$$\tau_0 = \alpha\sigma \tag{3.10}$$

As all composites investigated within the scope of this work have a non-linear response to shear loading the shear modulus G becomes G_i to account for the actual secant shear modulus at a given shear strain.

A typical γ convergence curve can be seen in Figure 3-3 a). As long as stable convergence is achieved the composite is in equilibrium for a given value of axial stress σ. This stress can incrementally be increased until γ becomes unstable as shown in Figure 3-3 b). Stable equilibrium can not be achieved in this case as eventually the shear deformation increment drives the shear stress τ and resulting deformation γ ad infinitum. This phenomenon will further be called shear instability and is assumed to correspond to the onset of kink band formation which leads to failure of the composite. The stress at which it occurs is therefore the predicted failure stress of the composite.

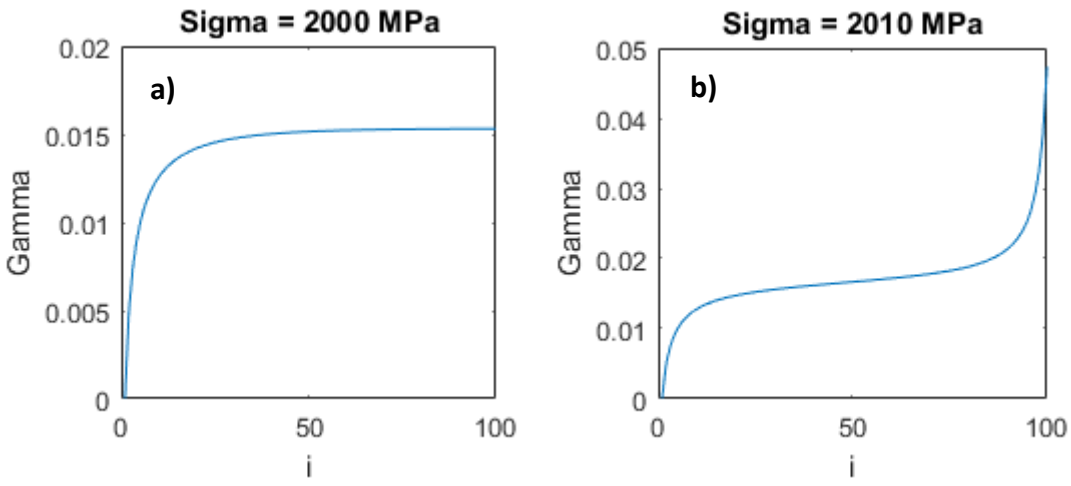

Figure 3-3: Convergence of shear strain showing a) stable convergence of γ and b) instability where γ increases at a rapid rate. The values were obtained based on 8552/33%/IM7 properties at $\alpha = 1°$. Note the value of shear strain $\gamma = 1.53\%$ which is typical for stable equilibrium. Shear instability does not occur at $\sigma = 2000\ MPa$ regardless of the number of γ iterations. The instability occurs at $\sigma = 2010\ MPa$ but it is not the lowest stress at which it is observed. The lowest instability stress is $\sigma = 2007.3\ MPa$.

The process can be repeated for a range of initial misalignment values α in order to predict the compressive failure stress of the composite versus the fibre misalignment as shown in Figure 3-4 a). Alternatively, this can be presented in terms of axial strain in the fibre ε seen in Figure 3-4 b) which is calculated as following:

$$\varepsilon = \frac{\sigma}{E} \tag{3.11}$$

Where E is the axial modulus of the composite. The failure envelope can be presented in terms of stress or strain. For a single material with a constant modulus in the fibre direction the values of stress and strain are directly proportional. Presenting the data in terms of compressive strain becomes more useful when considering hybrid composites containing fibres of different moduli that will be introduced in the next section.

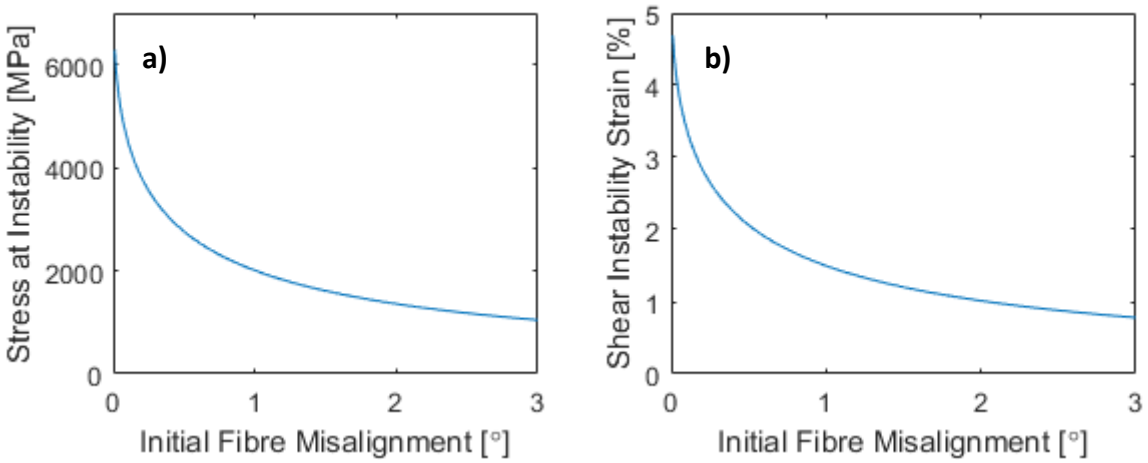

Figure 3-4: Shear instability curves a) in terms of axial stress and b) in terms of axial strain. Note that for a composite with a linear axial response the value of strain is proportional to the value of stress. Predictions based on 8552/33%/IM7 properties. Note that both stress and strain are compressive here.

Figure 3-4 shows the results of the modelling using real material properties of 8552/33%/IM7 which are discussed in detail in Chapter 6. The 33% in the material name denotes the fibre weight content. It can be seen that the predicted strain at which the shear instability occurs and the corresponding stress decrease as the initial misalignment angle increases. At low misalignment of $\alpha = 0.01°$ the instability strain is $\varepsilon = 4.39\%$ which is significantly higher than typically observed in testing. The strain quickly deteriorates as the initial misalignment increases, dropping to $\varepsilon = 1.99\%$ at $\alpha = 0.25°$, $\varepsilon = 1.42\%$ at $\alpha = 0.50°$, $\varepsilon = 0.93\%$ at $\alpha = 1.00°$ and $\varepsilon = 0.56\%$ at $\alpha = 2.00°$. For small initial misalignment angles the instability strain is high and other types of failure can be critical. For example, high modulus fibres exhibit fibre

fragmentation in compression [51] and at low misalignment angles this failure mechanism is likely to occur before the onset of instability, as depicted in Figure 3-5. This is analogous to steel columns where the effective strength decreases with increasing slenderness ratio due to buckling [52]. If the member is stocky enough the failure will occur not due to the buckling but material failure. Similarly, with a stiff enough matrix (or low enough failure strain in the fibre), the fibrous composite will shift its mode of failure from instability to carbon fibre crushing under compression.

As discussed before [2], [6], [53], some high-strength fibres have potential to be loaded to high strains and in those the shear instability failure mode will be critical. This work is focused on such fibres, where improving the shear instability failure envelope can lead to higher compressive strains. High and ultra-high modulus fibres with low tensile strains that tend to fragment in compression will not be investigated as suppressing shear instability in composites consisting of those fibres would not impact the failure strain.

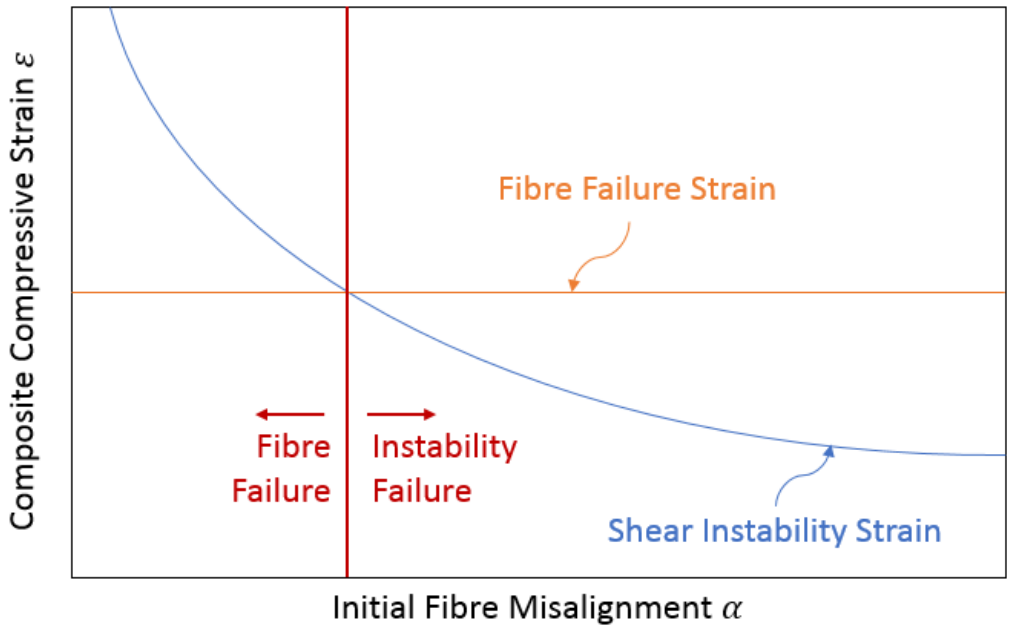

Figure 3-5: Idealised compressive failure model for a generic fibre-reinforced composite. The fibre failure strain is a fibre property and likely to dominate the failure in composites consisting of high modulus fibres with good alignment. Shear instability is likely to dominate the behaviour of composites with fibres which can achieve high compressive strains or are highly misaligned. Note that the shape of the shear instability curve depends largely on shear properties of the resin.

The following properties are required to predict the onset of shear instability of the material:

1. Composite modulus in the fibre direction
2. Fibre misalignment angle
3. Shear response of the composite

Also, in order to predict the compressive failure mode:

4. Compressive fibre fragmentation strain

These properties will be discussed in detail in subsequent sections. However, the model outlined earlier is limited to unidirectional composites with homogenous properties and can not account for composites consisting of more than one fibre type or with varying resin properties.

In addition, the fibre is assumed to have a linear response to axial compression. However, carbon fibres tend to have a softening response under this type of loading [2], [7]. This is not accounted for in the model, but some qualitative predictions can be made. If the modulus decreases as strain increases, the assumption of constant modulus will overestimate the compressive stress in the composite. The shear stress required to satisfy equilibrium will therefore also be overestimated. As the shear instability is related to a high shear deformation related to shear stress, the instability will occur earlier if fibre softening is not taken into account. The linear model will thus underestimate the strength.

3.1.1 Shear Properties Determination

The model introduced in this chapter works using the shear properties of the modelled material. However, the shear response of most composite materials is not trivial and representing it with a single value (shear modulus G) is a vast simplification. Data from real specimens tested using ASTM D3518 test [54] is shown in Figure 3-6. The specimens in question both contain IM7 fibre and 8552 resin system, however their fibre volume fraction is different, resulting in different shear response. A study performed using those materials is presented in section 6.2.

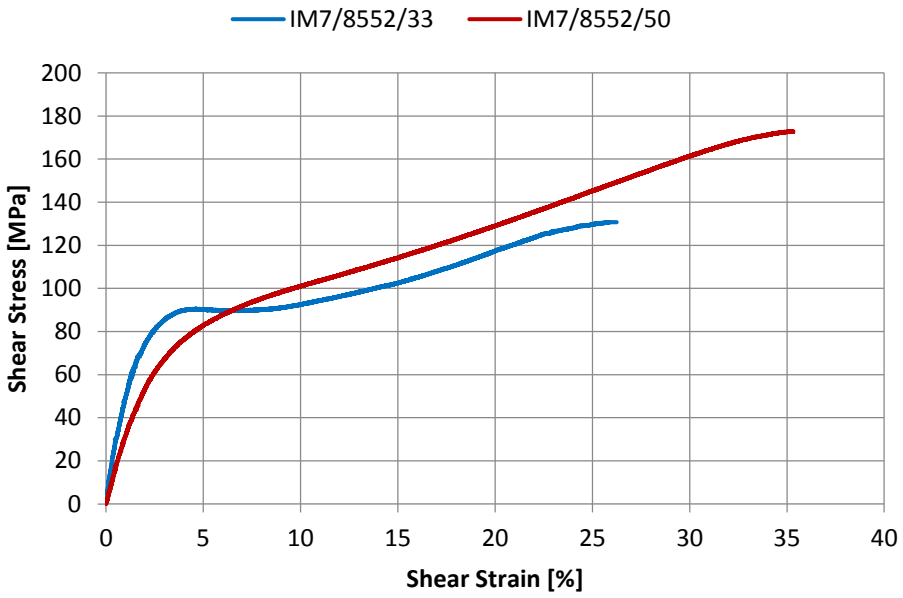

Figure 3-6: Shear test data for two specimens. Highly non-linear response is present.

It can be seen that the full shear response is far from linear. Both curves start with a high initial slope (or tangent modulus) which could be approximated using a linear function until about 2% shear strain. The gradient than gradually falls, decreasing the tangent modulus to zero (or even slightly negative) in the case of IM7/8552/33 sample around the 4% shear strain mark. For IM7/8552/50, the curve becomes close to linear around 8% shear strain, with a positive slope. The shapes of the curves can be explained by the presence of fibre rotation [55], where the sample cracks under sufficient axial deformation and the fibres start scissoring, thus further increasing the calculated shear strain [56], [57]. As the constraint from surrounding resin is present until failure, this causes the increase in load as the fibres can not rotate freely, but rather deform the matrix whilst carrying increasing amounts of stress in fibre tension.

Both sample behaviours could be approximated using bi-linear curves [55]. However, this approach is highly inaccurate around the kneepoint, as shown in Figure 3-7. Two bi-linear curves were fitted – one conforming to the horizontal plateau past the kneepoint and the other approximating the linear portion where fibre rotation is occurring. There is a significant divergence between the fitted curves and measured behaviour:

- The initial shear modulus at $\gamma < 1.5\%$ is underestimated to provide a better overall fit to the initial portion of the measured data. This is significant, as the

underestimation of shear modulus at low shear strain values will result in higher calculated misalignment in the shear instability model, which in turn will lower the calculated instability stress. As will be shown later, the shear strain at instability is often low ($\gamma \leq 2\%$), therefore it is crucial to obtain a good representation of the initial part of the curve.

- Where the plateau is taken as reference for secondary line, there is an overestimation of shear stiffness in the $1.8\% < \gamma < 4.2\%$ range due to overshoot of the kneepoint.
- Where the fibre rotation portion is taken as reference for secondary line, there is an underestimation of shear stiffness in the $1.8\% < \gamma < 8.6\%$ range due to undershoot of the kneepoint.

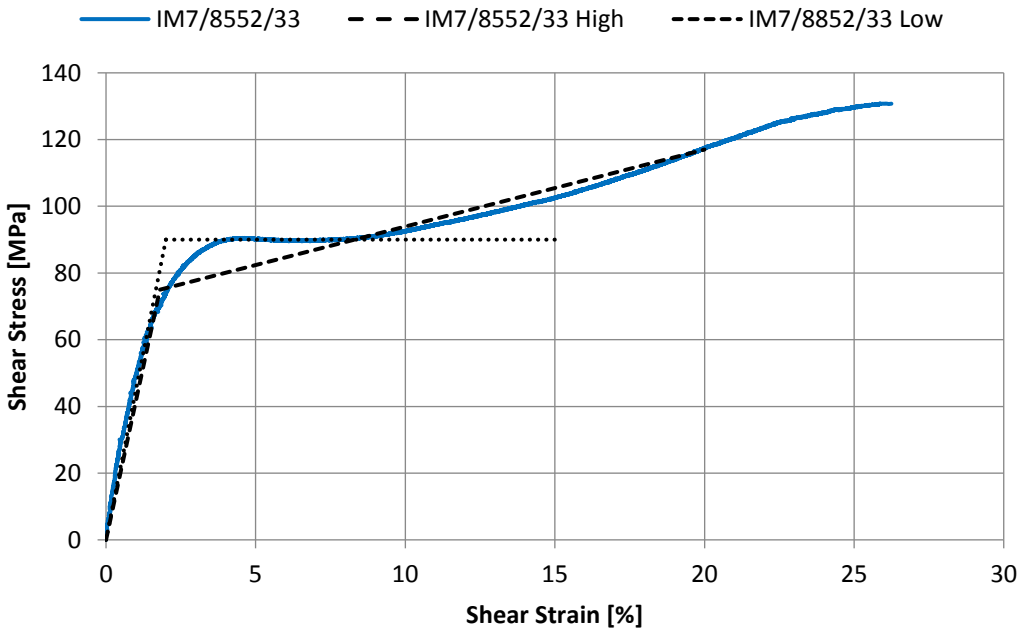

Figure 3-7: Bi-linear approximations of the IM7/8552/33 sample behaviour. It can be seen that the values at kneepoint are either overestimated or underestimated depending on which part of the curve is followed at higher shear strain.

More realistically, the shear response shown in Figure 3-7 can be approximated by using an exponential function in the form:

$$\tau = A(1 - e^{-B\gamma}) \tag{3.12}$$

Where τ and γ are shear stress and shear strain respectively, and A and B are fit parameters. In order to explain the physical significance of A and B, consider the cases shown in Figure 3-8.

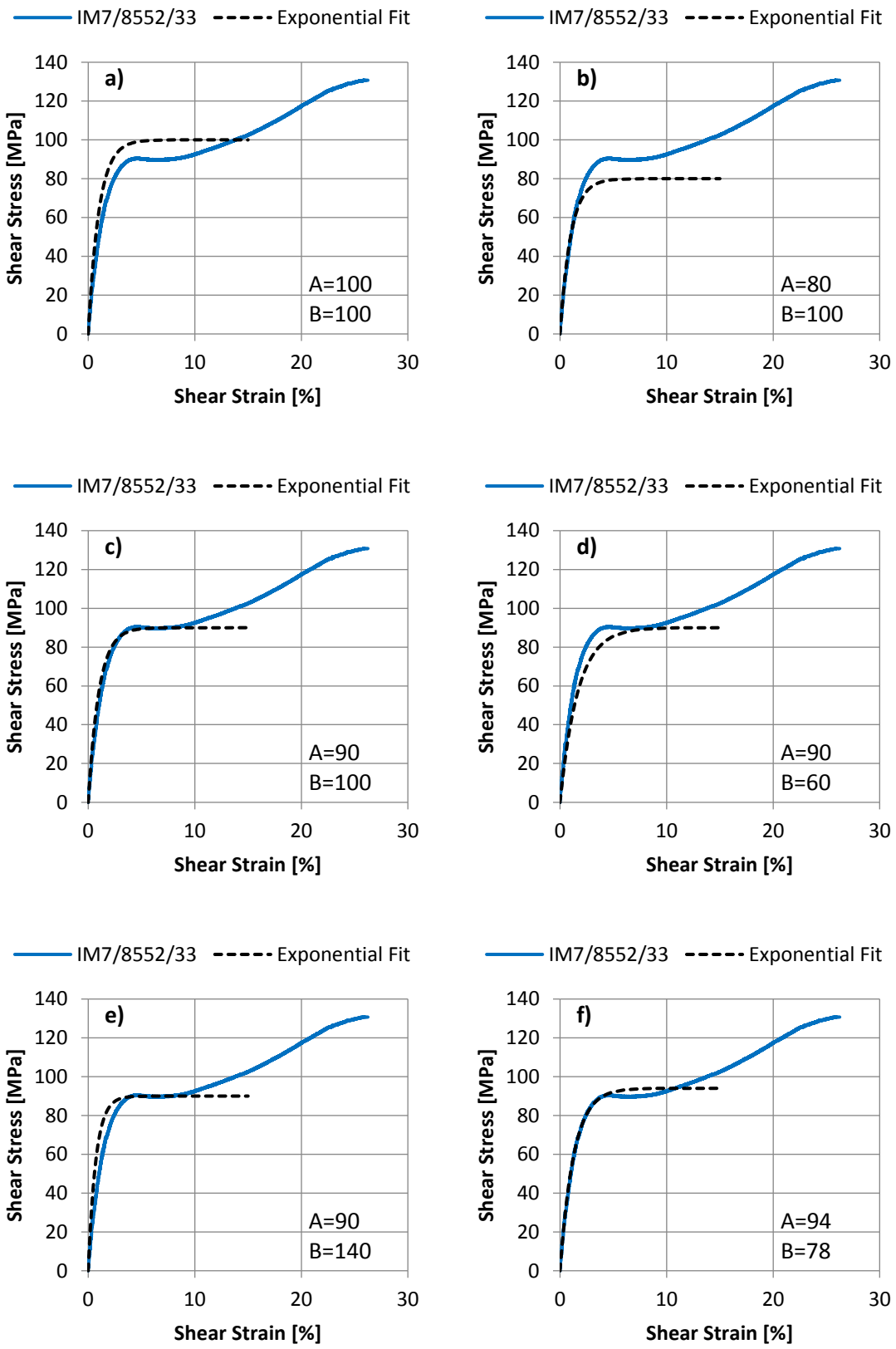

Figure 3-8: Change of the shape of exponential fitting curve depending on parameters A and B. Cases a) through e) demonstrate the behaviour of the curve when changing the parameters and f) depicts the best fit in the $\gamma < 4\%$ range with corresponding optimum parameters.

It can be seen from Figure 3-8 a) through c) that the parameter A determines the limit of the shear stress, with values of the two being equal at the maximum value (when the curve flattens at higher shear strain). Therefore:

$$A = \tau_{MAX} \tag{3.13}$$

Looking at Figure 3-8 c) through e), it can be seen that parameter B determines the slope of the curve, with a lower value resulting in a lower gradient and a higher value yielding a high gradient. The relationship is not linear, as B is the decay constant of the exponential function (with a negative value). As the slope of the curve at any given point is equal to the tangent shear modulus of the sample, it can be stated that:

$$B \propto G_{exp} \tag{3.14}$$

The two parameters are sufficient to describe the behaviour of sample IM7/8552/33 in the low strain range $\gamma < 4\%$. However, to accurately describe the behaviour of the other sample, IM7/8552/50, the function can be enhanced with a linear component C to yield a parametric curve in the form of:

$$\tau = A(1 - e^{-B\gamma}) + C\gamma \tag{3.15}$$

Where τ is the shear stress, A is the maximum shear stress of the exponential function, B is the decay constant, C is the linear constant and γ is the shear strain. The linear constant C is simply:

$$C = G \tag{3.16}$$

Or the linear shear modulus. The shear modulus is therefore a combination of the linear and exponential components. A comparison of exponential only and exponential-linear fit curves for the IM7/8552/50 sample can be seen in Figure 3-9. The curve with a linear component provides a better fit in a larger range of shear strain.

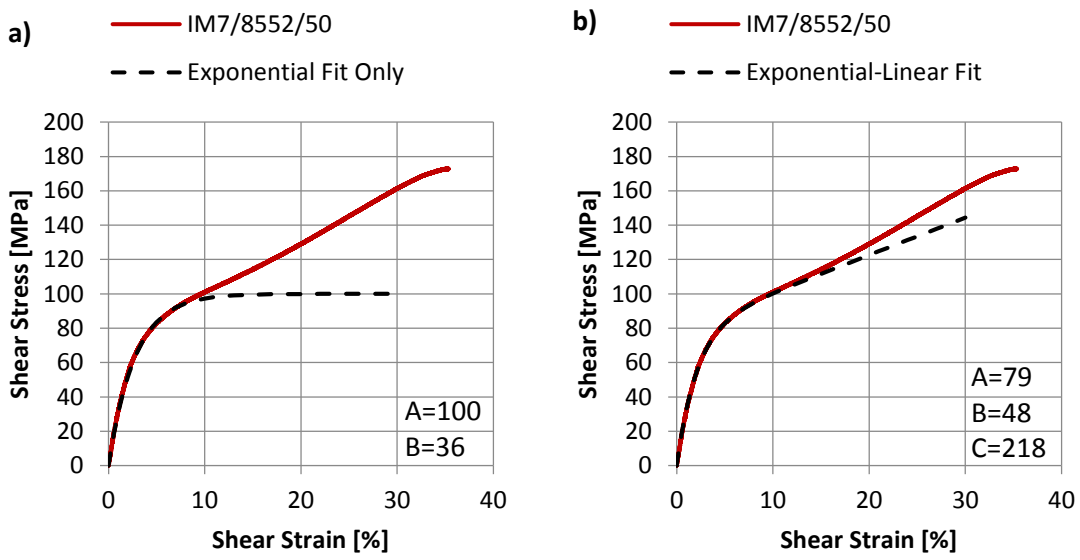

Figure 3-9: The comparison between a) exponential only and b) exponential-linear fit. It can be seen that the exponential-linear fit provides a better fit in a large range of shear strain values.

The equation in this exponential-linear form provides a good fit for most measured shear response curves due to the addition of the linear component. For the case shown in Figure 3-10, the 8552/S2GL material has a largely exponential response, but continues to rise linearly beyond the kneepoint. A simple exponential equation would not be sufficient to capture that.

The shear curves obtained from testing are fitted with the parametric curves visually, with an emphasis on good compliance in the low shear strain ($< 5\%$) range. As shown in Figure 3-31, the shear strain at instability for the model did not exceed $\gamma = 3\%$ and thus the focus on the initial part of the curve.

3.1.2 Example and Trends in Real Materials

Consider two cases to illustrate the dependencies found in typical materials:

a. 8552/33%/IM7 carbon composite ($E = 134\ GPa$)
b. 8552/36%/S2GL S-glass composite ($E = 45.7\ GPa$)

The shear response of the two materials is presented in Figure 3-10. The data comes from material testing outlined in section 5.3. Fitting of the shear response with parametric curves is performed according to the method outlined in the previous subsection.

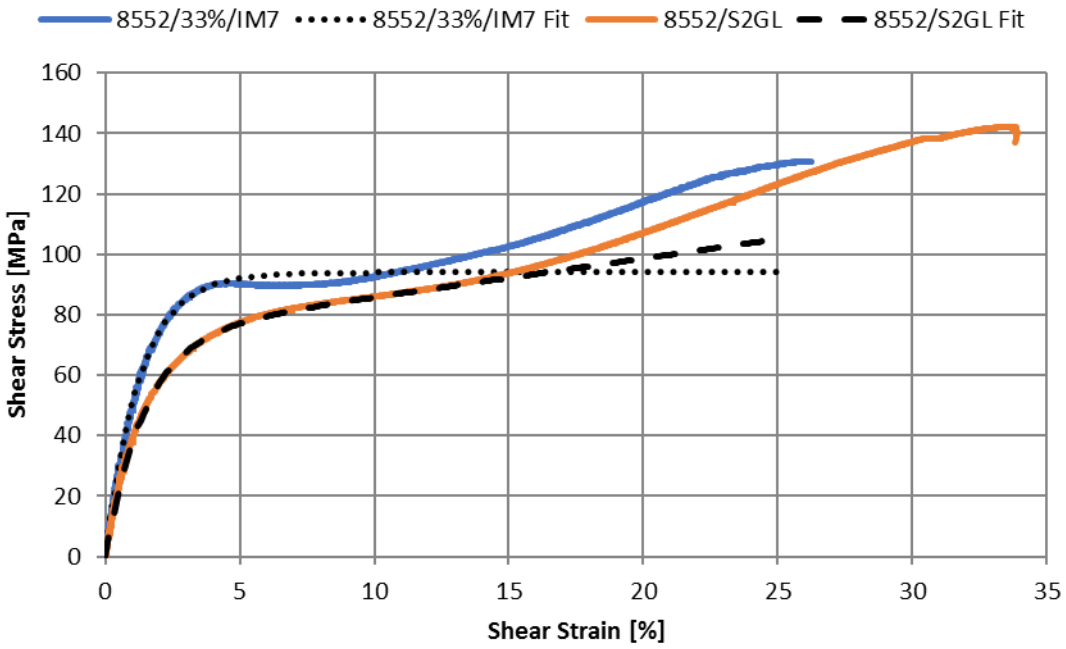

Figure 3-10: Composite shear response for 8552/33%/IM7 and 8552/36%/S2GL. Note the shear stiffness of the S-glass composite is lower compared to the carbon and does not exhibit a plateau.

As explained in the previous chapter, the shear response is fitted using an exponential-linear function. The fitting is aimed at ensuring good correlation with the modulus at low strains, while higher values of shear strain are of less interest as the shear instability would normally occur at $\gamma < 5\%$. The fit parameters are shown in Table 3-1.

Table 3-1: Fit parameters used for materials shown in Figure 3-10

Material	Maximum	Decay	Linear
8552/33%/IM7	94	78	0
8552/36%/S2GL	73	69	128

Using the modelling approach outlined above with each individual material yields the results presented in Figure 3-11.

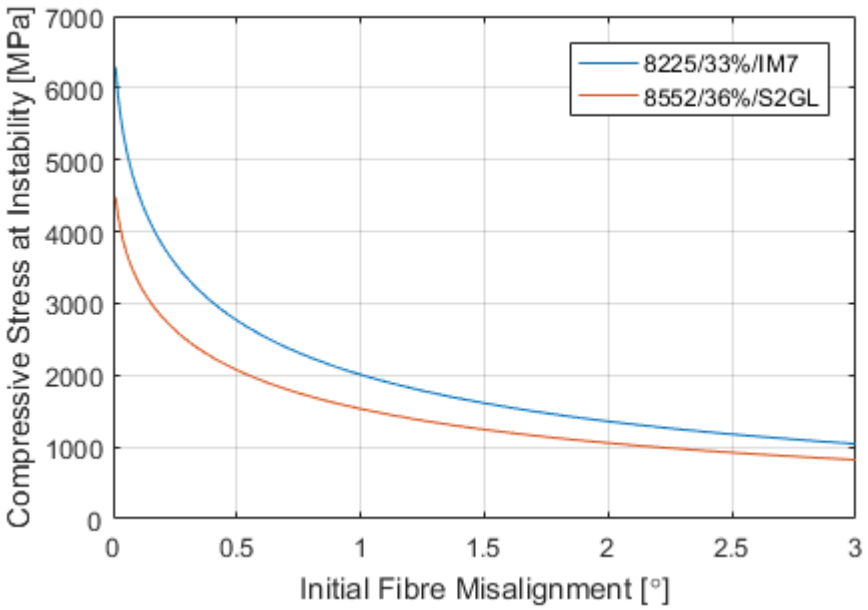

Figure 3-11: Shear instability modelling results for the two materials. Note the S-glass becomes unstable at a lower stress compared to the carbon. This is due to lower shear stiffness and higher shear deformation produced by shear stress required for equilibrium.

It can be seen that shear instability occurs at a lower stress in the S-glass. This is due to the lower shear stiffness of the S-glass composite. At the same compressive stress level and misalignment angle, the equilibrium shear stress is the same, however the resulting shear deformation is larger in the S-glass composite where shear modulus is lower than in case of carbon. The stiffer the material is in shear, the higher the compressive stress at which instability will occur. Conversely, the more compliant the matrix, the lower the compressive stress for instability onset. An extreme case to illustrate this point – although governed by a different mechanism – would be where there is no matrix at all ($G = 0$) and the fibres simply fold when subject to compressive loading.

Nevertheless, for glass to reach a stress similar to that of carbon, the required strain is much higher, as seen in Figure 3-12 depicting the results of the same model run with respect to compressive strain. Here the picture changes – the glass composite becomes unstable at a significantly higher strain compared to the carbon composite. Although the compressive stress at instability is lower due to inferior shear response, the corresponding strain is indeed higher due to lower compressive modulus of the S-glass composite.

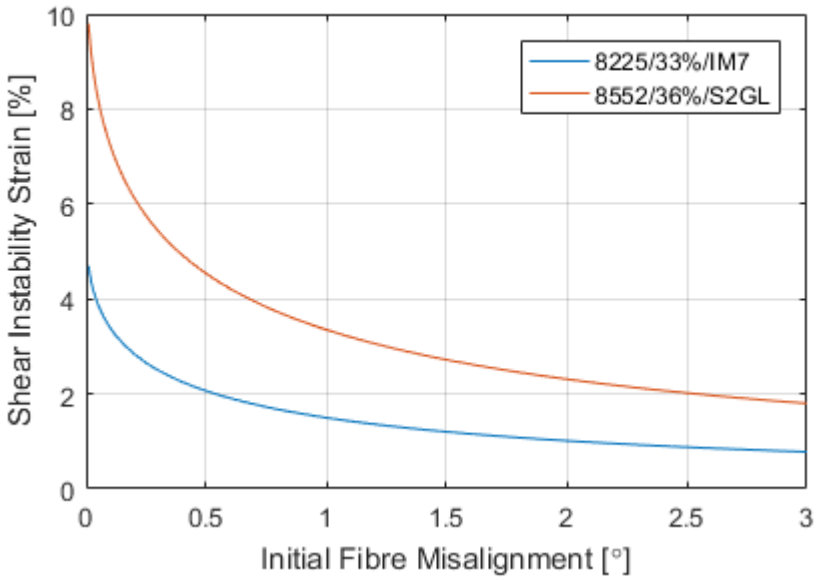

Figure 3-12:Results in terms of compressive strain. As the S-glass composite has a lower compressive modulus the stress at a given compressive strain is significantly lower than in the carbon.

Running the model with the shear response of S-glass assumed to be the same as that of the carbon yields two identical curves with regards to compressive stress at instability. The following statements can hence be derived from the investigated case:

1. Compressive stress at instability is dependent solely on initial misalignment angle and shear response of the material
2. Compressive strain at instability is a function of instability stress and compressive modulus of the material

It is still possible for a compliant material to have a lower strain at instability compared to a stiff material, provided the shear response of the former is significantly worse.

A useful implication of our considerations so far is that by lowering the compressive stiffness of the composite we can achieve higher strain at instability. It would be expected that by adding S-glass to the carbon in the above case the compressive modulus would drop and the strain at instability would increase due to lower average compressive and shear stresses in the composite. This will be investigated in-depth in the next section.

3.2 Shear Instability in Hybrid Composites

In order to address the limitation of a single homogenous material the model can be expanded to two materials. Figure 3-13 depicts two elements with individual properties

constrained to have the same deformation (joined by a rigid link). Elements have separate initial misalignment angles α and β, material stiffnesses E_1 and E_2, shear stiffnesses G_1 and G_2 and thicknesses t_1 and t_2. The thicknesses relate to total ply thickness of each constituent material.

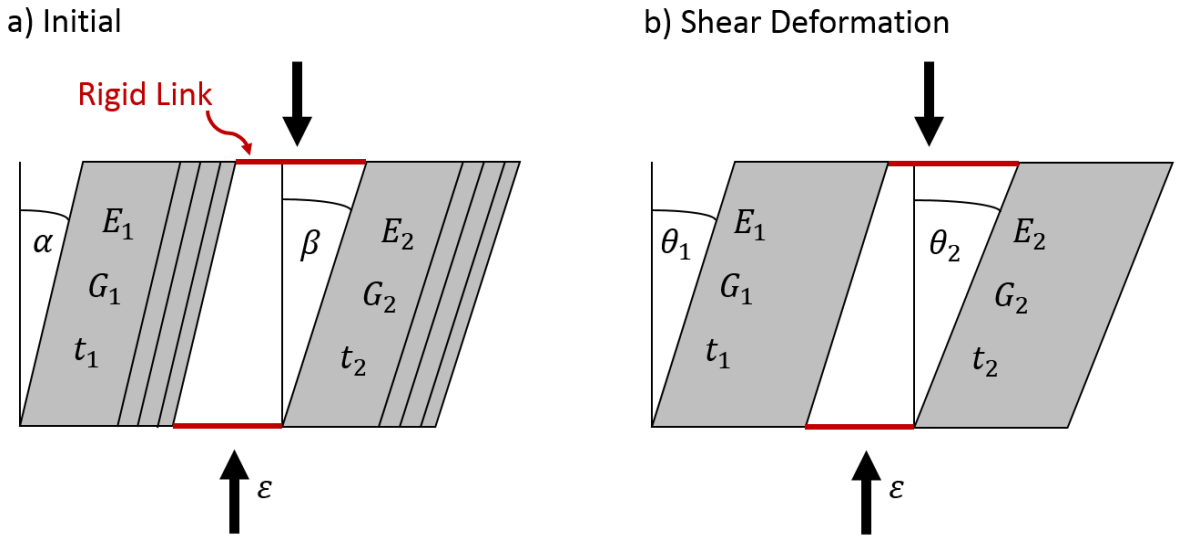

Figure 3-13: Schematic representation of two-material shear instability model at a) initial state and b) after shear deformation. The rigid link between two elements forces the shear deformation γ to be the same for both.

In a realistic loading scenario of a unidirectional hybrid composite the strain in the loading direction can be assumed uniform throughout a section normal to the loading. As the two materials have different moduli the stresses generated will be different. It is therefore convenient to discuss the results in terms of axial strain in the sample instead of stress. The applied strain ε is the same for both materials.

The stresses in two elements are as following:

$$\sigma_1 = \varepsilon E_1 \tag{3.17}$$

$$\sigma_2 = \varepsilon E_2 \tag{3.18}$$

As the two elements are rigidly tied together, the forces acting on the system when unit thickness is assumed can be added to calculate equilibrium. The equilibrium equation thus becomes:

$$\tau_1 t_1 + \tau_2 t_2 = \alpha \sigma_1 t_1 + \beta \sigma_2 t_2 \tag{3.19}$$

Where τ_1 and τ_2 are the shear stress components in the two elements. As the shear deformation is assumed to be the same for the two materials it can be obtained by homogenising the shear stiffness:

$$\gamma = \frac{\tau_1 t_1 + \tau_2 t_2}{G_1 t_1 + G_2 t_2} \tag{3.20}$$

The deformed state is therefore described by two angles:

$$\theta_1 = \alpha + \gamma \tag{3.21}$$

$$\theta_2 = \beta + \gamma \tag{3.22}$$

Which can then be iterated in the same fashion as in the model presented previously for a single material. If convergence of γ is achieved for a given longitudinal strain ε the material remains in equilibrium. If γ becomes unstable the corresponding strain ε is assumed to be the shear instability onset strain and therefore the failure strain of the composite.

In order to illustrate typical results obtained using the model and build on previous investigations, let us consider a hybrid composite consisting of 8552/33%/IM7 and 8552/36%/S2GL with thicknesses $t_1 = t_2 = 1\,mm$. As there are two materials being considered with two initial misalignment angles α and β the iterative process of calculating shear instability strains has to account for a variation of these two parameters. The results are therefore presented in Figure 3-14 as a 3D surface rather than a 2D curve.

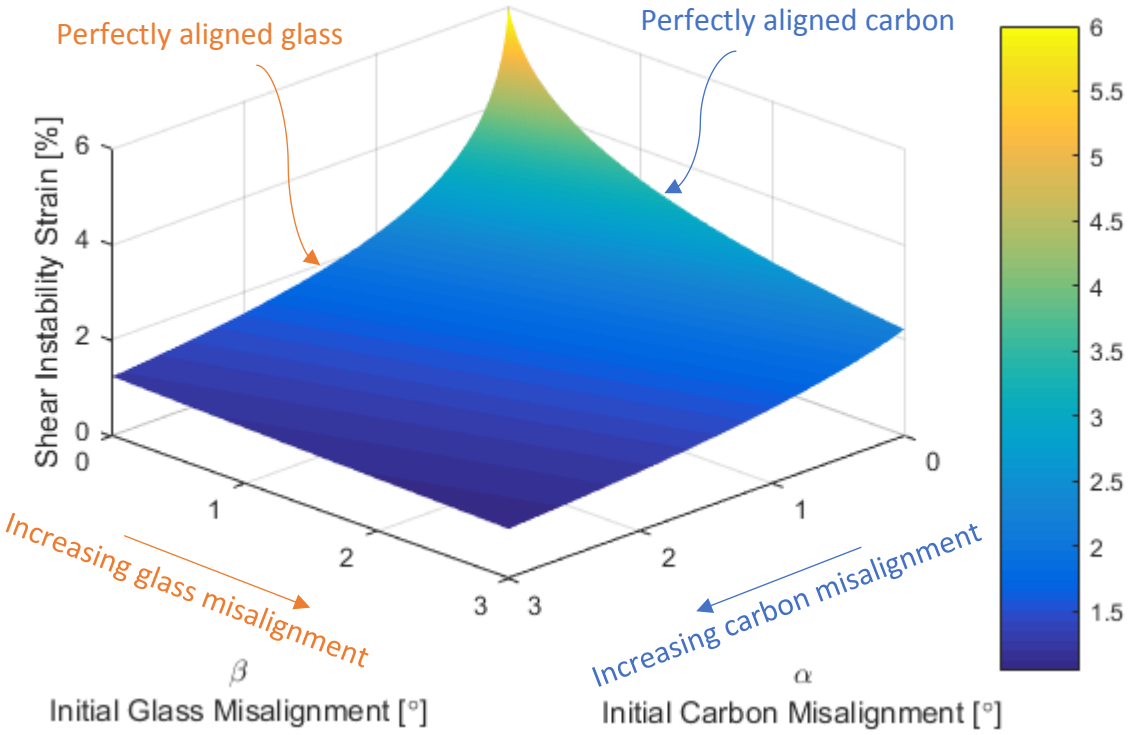

Figure 3-14: Shear instability strain surface for two materials. Note each possible pair of angles between 0° and 3° is investigated. Carbon misalignment increases from top right to bottom left and glass misalignment from top left to bottom right along their respective axes. The far corner corresponds to the lowest misalignment for the two materials where the instability strain is the highest. The near corner corresponds to the highest misalignment for the two materials where the instability strain is the lowest.

Two points can readily be recognized within the surface – the point of maximum instability strain $\varepsilon = 6.00\%$ occurring at $\alpha = \beta = 0.01°$ and the lowest calculated instability strain $\varepsilon = 1.04\%$ at $\alpha = \beta = 3.00°$. As expected, the highest instability strain corresponds to the best fibre alignment and the lowest calculated instability strain occurs at highest assumed misalignment angles.

3.2.1 Stress and Strain at Instability in Hybrid Materials

While the surface shown in Figure 3-14 provides a complete shear instability envelope for a hybrid consisting of the two assumed materials it is not easily compared to previously obtained results. In order to more directly compare the behaviour, the surface can be sliced, producing two-dimensional curves similar to those generated by the model for a single material. Numerically, this means retrieving a shear instability strain value for each pair of misalignment values where $\alpha = \beta$. As the model calculates shear instability strain ε for specified values of α and β, there is granularity in the obtained shear instability surfaces that was specified (300 by 300 grid for the ones shown here, in increments of $0.01°$). Should the

cutting surface not intersect any of the calculated nodes, the value can be interpolated from the neighbouring values. One such slice is shown in Figure 3-15 where the carbon and glass misalignment angles are identical.

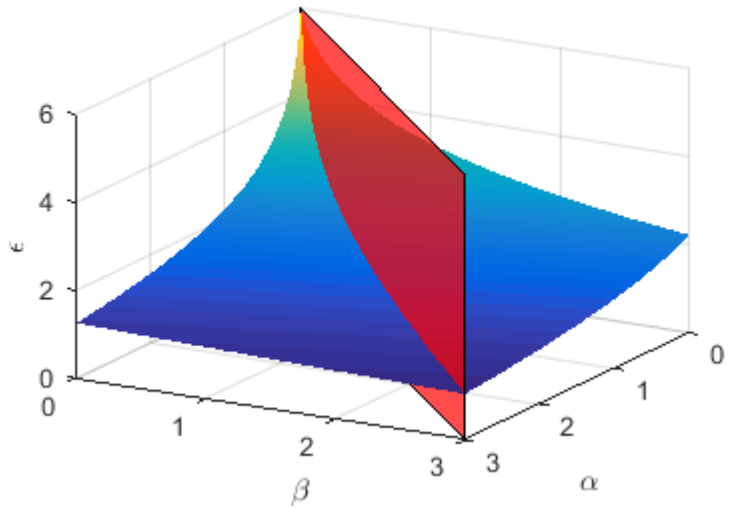

Figure 3-15: Slicing the shear instability envelope shown in Figure 3-14 with the red surface to produce a curve where carbon and glass misalignment angles are the same. Note this is only a schematic representation as these results have already been obtained and must simply be addressed from the storage matrix (in this case the values of interest lie on the diagonal).

The resulting curve is shown in Figure 3-16 along with previously obtained results for pure 8552/33%/IM7 and 8552/36%/S2GL.

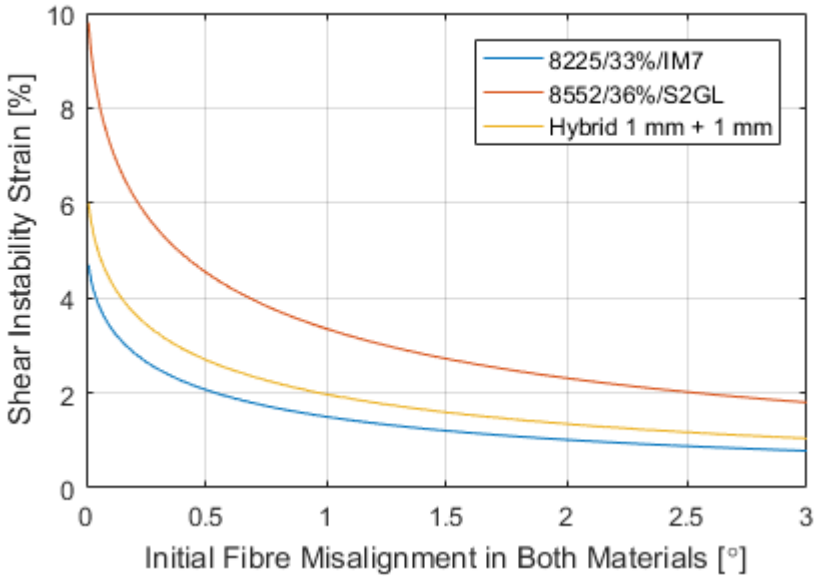

Figure 3-16: Shear instability in the hybrid as compared to the pure constituent materials. Note the initial misalignment angles are the same for carbon and glass in the hybrid. The hybrid response is closer to the response of carbon as the stiffer material generates a higher stress at a given strain.

As expected, the response of the hybrid material falls between the individual responses of each of its two constituents, however it is closer to the pure carbon results. This is likely due to the higher stiffness of carbon and the load being carried predominantly by the stiffer material. While in reality the stresses in glass and carbon will differ, we can calculate the average stress in the composite as:

$$\sigma_{AVG} = \frac{\varepsilon(E_1 t_1 + E_2 t_2)}{t_1 + t_2} \tag{3.23}$$

This average stress along the same slice is shown in Figure 3-17 with constituent material response from previous modelling for comparison.

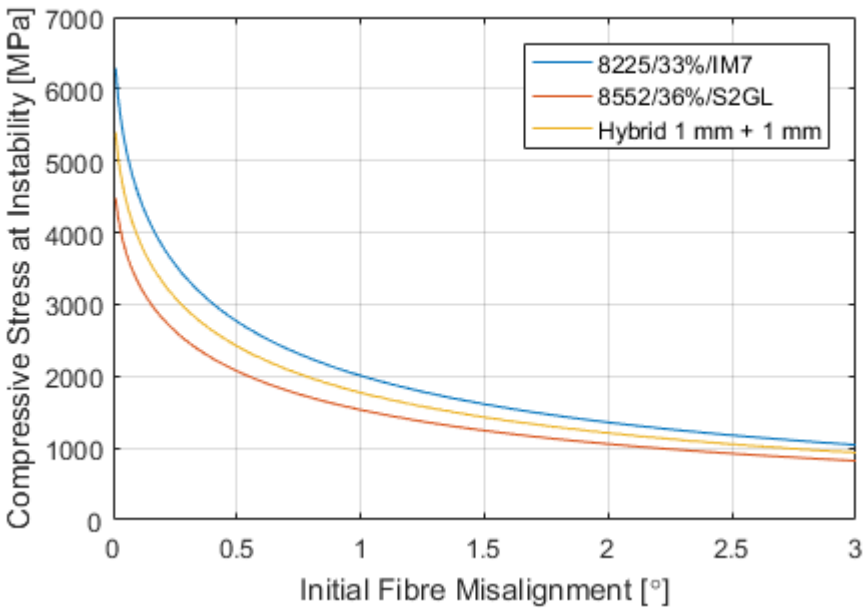

Figure 3-17: Average stress in the hybrid as compared to pure constituent materials. The stress response of the hybrid is the average of the two constituents as the thicknesses of glass and carbon are the same. Note the initial fibre misalignment in carbon and glass is the same in the hybrid.

It can be seen from Figure 3-17 that the average stress falls precisely in the middle of the stresses at instability for each constituent material. As the shear instability is a stress driven phenomenon and the hybrid contains the same amount of each material, this is expected. In order to check the trends of the stress response, consider the following cases:

1. Pure carbon
2. 1.5 mm of carbon + 0.5 mm of glass
3. 1 mm of carbon + 1 mm of glass
4. 0.5 mm of carbon + 1.5 mm of glass

5. Pure glass

Figure 3-18 shows that the average stress response scales linearly with the thickness of constituent materials and can therefore be interpolated between the pure material response curves to provide the results for any ratio of the two materials in a hybrid.

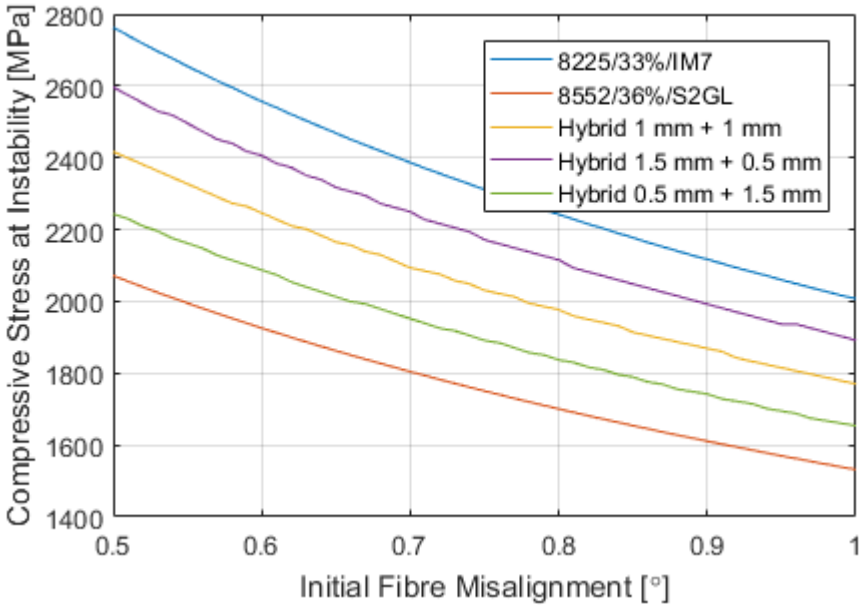

Figure 3-18: Results for the five cases of shear instability onset. Note the curves are only shown between 0.5° and 1° initial misalignment values for clarity. It can be seen that average stress at instability can be interpolated for a hybrid from the behaviour of each of the constituents.

As the shear instability is a stress-based phenomenon, the introduction of a low-stiffness material can be used to lower the average stress in a hybrid and effectively increase the instability strain of a high-stiffness material. This is different to the hybrid effect in tension [37], [40], [58] where high-stiffness fibres undergo fragmentation but remain partially loaded due to matrix shear transfer from intact low-stiffness fibres. In the case of compression, the critical mechanism is not a fibre break but a local instability in the matrix leading to a kink-band formation. As shown in Figure 3-5, composites where the critical mechanism is not fibre fragmentation in compression but shear instability will exhibit higher failure strains when hybridized with low-stiffness fibres, even at low volume of low-stiffness material added. The composites limited by the compressive fibre fracture do not experience shear instability before failure and therefore do not benefit from the increased instability stress.

3.2.2 Effects of Alignment on Instability in Hybrid Composites

The assumption of fibre misalignment being the same for both constituent materials in a hybrid composite is useful when examining the fundamental behaviour of those composites, but not realistic due to practical aspects of manufacturing such composites. The intrinsic fibre waviness is unlikely to be the same for two constituent materials as received, and further defects will be created during handling, cutting and curing. In order to examine the shear instability envelope in more detail and to account for these disparities, slices can be taken at constant initial misalignment angles for one of the constituents.

Considering the shear instability envelope previously produced for 8552/33%/IM7 and 8552/36%/S2GL with thicknesses $t_1 = t_2 = 1\,mm$, slices can be made at constant glass misalignment angles $\beta = 0.5°$ and $\beta = 1.0°$ as shown in Figure 3-19.

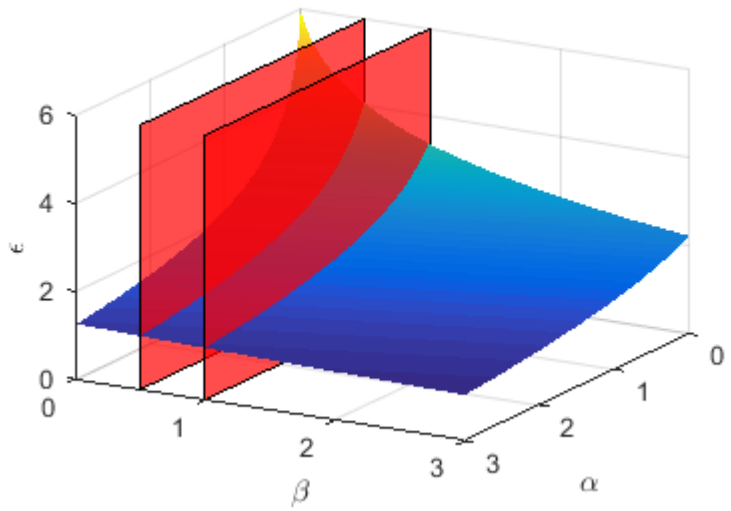

Figure 3-19: Slicing the shear instability envelope seen in Figure 3-14 with two red surfaces at constant glass misalignment values of $\beta = 0.5°$ and $\beta = 1.0°$. Note this is a graphical representation only.

Figure 3-20 shows the resulting shear instability curves. It can be seen that at the higher glass misalignment of $\beta = 1.0°$ the shear instability strain of the composite is lower compared to the constant glass misalignment of $\beta = 0.5°$ at the same carbon misalignment angles. This is expected as the shear stress generated by the more misaligned glass fibre is higher at the same longitudinal strain, leading to an earlier onset of shear instability.

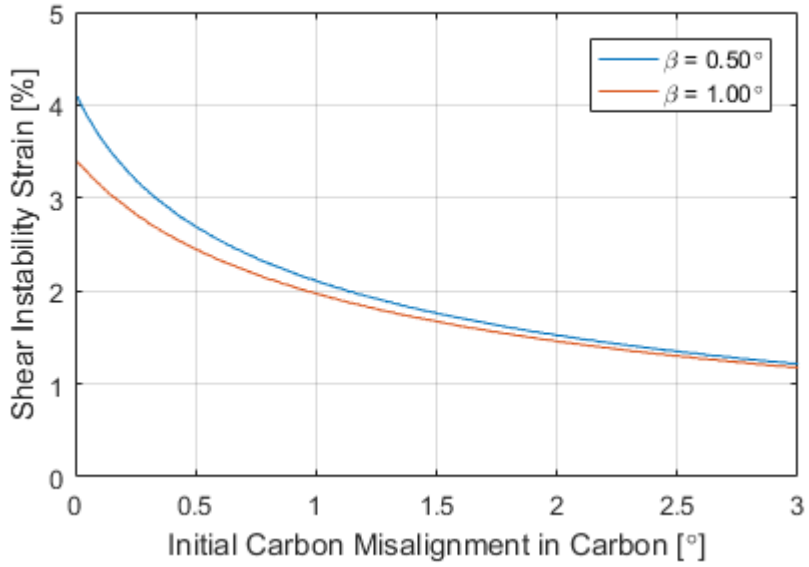

Figure 3-20: Shear instability curves at fixed glass misalignment $\beta = 0.5°$ and $\beta = 1.0°$. Note that the strain at low values of carbon misalignment does not reach values as high as seen in Figure 3-16, suggesting that the shear instability in the investigated hybrid composite may be more sensitive to the alignment of the glass fibre.

In order to investigate the sensitivity of the hybrid composite to the misalignment in each constituent material, a series of slices can be made for constant carbon and glass misalignment angles α and β at $0.25°$ intervals. The corresponding set of slices can is depicted in Figure 3-21.

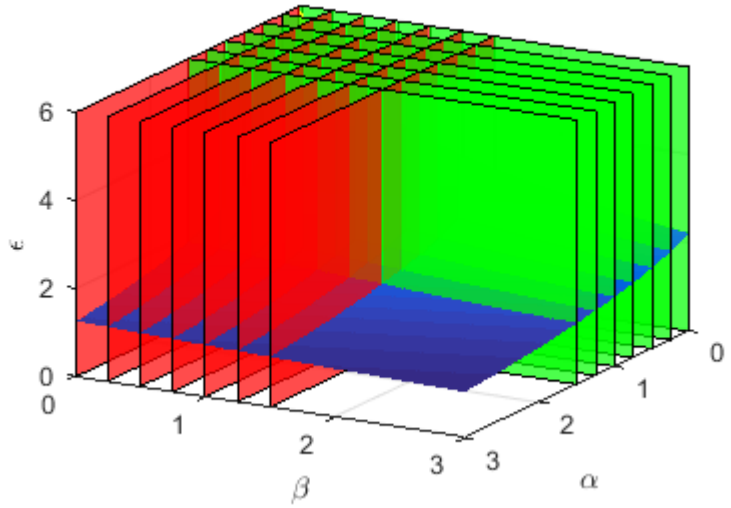

Figure 3-21: Shear instability envelope sliced at constant glass misalignment angles (in red) and at constant carbon misalignment angles (in green). Note that the slices are performed up to misalignment values of $\alpha = \beta = 1.5°$ as the surface flattens out at higher angles.

Slices are limited to a maximum angle of $\alpha = \beta = 1.50°$ as the shear instability strain variation is not as significant at higher angles and the results become difficult to read for an

increasing number of slices. Figure 3-22 shows a series of shear instability curves at constant glass misalignment angles represented by red slicing surfaces.

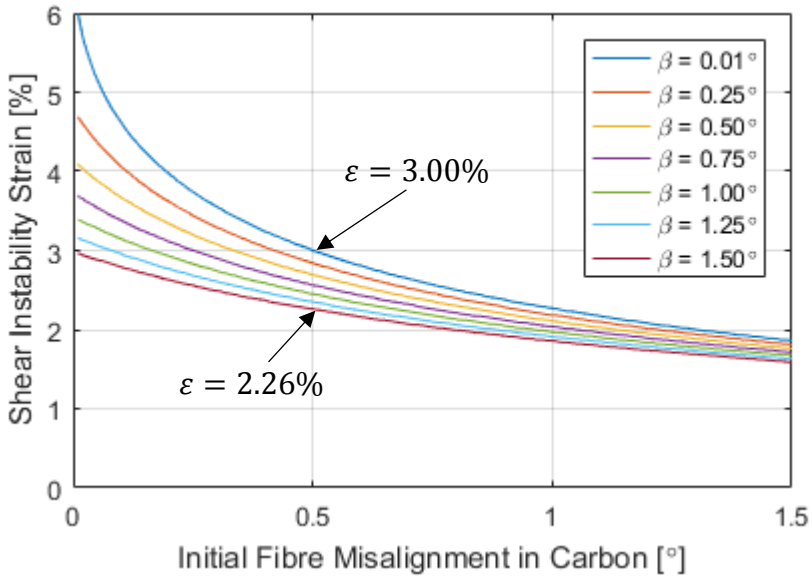

Figure 3-22: Shear instability at constant glass misalignment values β. Note the change in achieved composite strain between the lowest ($\beta = 0.01°$) and the highest ($\beta = 1.50°$) glass misalignment.

The series of curves correspond to the red slices in Figure 3-21. The topmost curve corresponds to the leftmost slicing surface at $\beta = 0.01°$. The curve underneath corresponds to the next slice to the right at $\beta = 0.25°$ and so on. A total of 7 curves corresponding to 7 slices are shown in Figure 3-22 up to a constant glass misalignment value of $\beta = 1.50°$ The curves follow similar paths with highest composite shear instability strain values on the left hand side where carbon fibres are most aligned. The values drop as the carbon misalignment increases. The curves do not intersect, as for every two composites where carbon misalignment is the same, the composite with higher misalignment of glass will be weaker to instability.

The absolute difference between the values of the top and the bottom curve decreases with increasing carbon misalignment. At low carbon misalignment the curves are spread apart and at high carbon misalignment they are close together.

Consider the shear instability strain at a carbon misalignment of $\alpha = 0.50°$. Depending on the misalignment of the glass in the hybrid composite the value of strain at instability can vary between $\varepsilon = 2.26\%$ for high glass misalignment of $\beta = 1.50°$ and $\varepsilon = 3.00\%$ for low glass misalignment value of $\beta = 0.01°$. Therefore improving the alignment of the glass fibres from

$\beta = 1.50°$ to $\beta = 0.01°$ while keeping the carbon fibres at a misalignment of $\alpha = 0.50°$ would improve the composite shear instability strain by a value of 0.74%, marking a 33% relative increase. This calculation can be repeated for all carbon misalignment values to indicate the increase in composite shear instability strain by aligning the glass fibres from a high value of $\beta = 1.50°$ to a very low value of $\beta = 0.01°$. Figure 3-23 depicts the relative increase in strain achieved by such improvement of alignment.

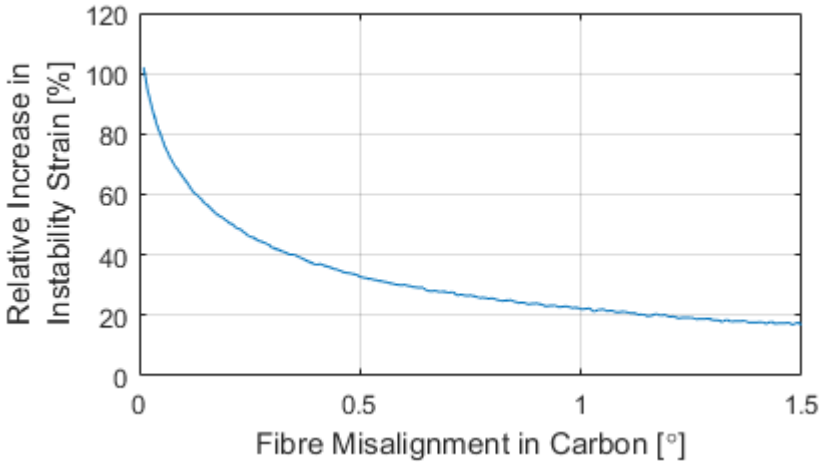

Figure 3-23: Relative increase in shear instability strain due to improving the alignment of glass fibre from $\beta = 1.50°$ to $\beta = 0.01°$. Note the high improvement at low misalignment of carbon.

Note that at low carbon misalignment the relative improvement is significant and decreases as the carbon becomes more misaligned. Therefore, the more aligned one of the constituents the greater the benefits of improving the alignment of the other. At poor alignment of one constituent aligning the other well yields little benefit.

The choice of glass misalignment angles for the relative improvement is somewhat arbitrary as it is difficult to establish a baseline alignment. Similar curves could be produced for improving the alignment from $\beta = 1.00°$ to $\beta = 0.50°$, as shown in Figure 3-24.

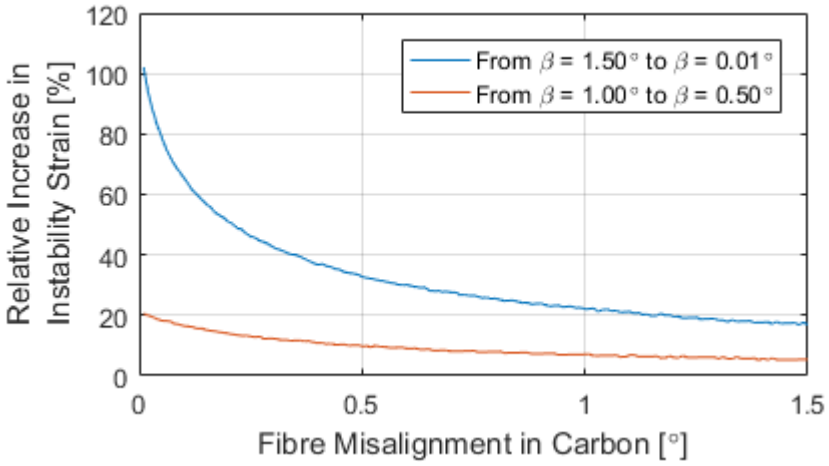

Figure 3-24: Relative increase in shear instability strain of the composite depending on the choice of glass angle improvement. Note the higher the difference in the angle the larger the improvement.

As expected, the resulting curve yields a smaller improvement, but follows similar trends with larger increase for small carbon misalignment. As the choice of angles to base the improvement calculation upon is arbitrary, the values of $1.00°$ and $0.50°$ will be used subsequently. This is due to the realistic alignment falling between $0.67°$ and $1.00°$ [59] and very low misalignment values being difficult to achieve.

Having investigated a series of slices taken at constant glass misalignment angles, now consider the set at constant carbon misalignment, depicted as green slices in Figure 3-21. The resulting curves can be seen in Figure 3-25.

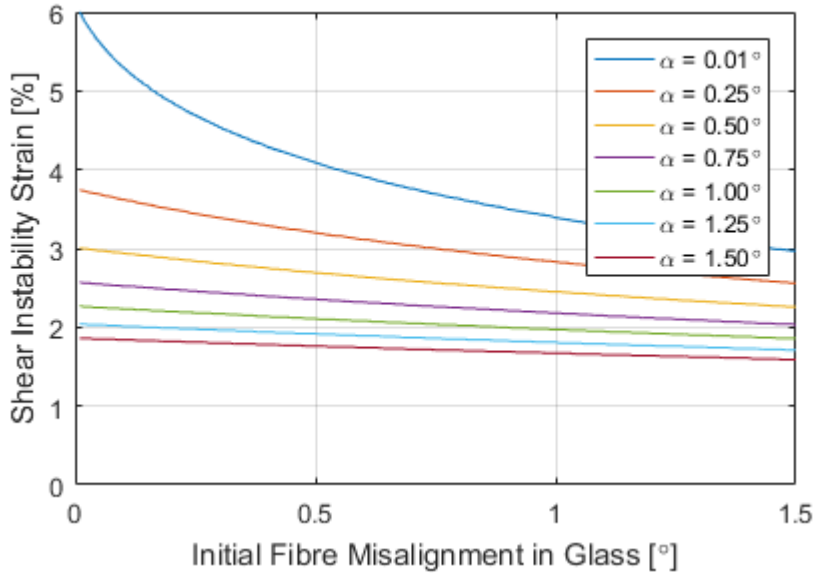

Figure 3-25: Shear instability at constant carbon misalignment values α. Note the large difference between the highest and lowest curve and the change in shape to almost linear for the bottom curves.

Analogous to Figure 3-22, the topmost curve corresponds to the rightmost slice at $\alpha = 0.01°$. Every curve below corresponds to the next slice to the left. As previously, the curves do not intersect and decrease in value along the horizontal axis. However, the absolute difference between the extreme curves is significantly higher than in Figure 3-22. Also, the curves change their shape to almost straight lines as the carbon misalignment angle increases. This, paired with the decrease in slope suggests the low sensitivity of results at high carbon misalignment to the misalignment of the glass. An extreme case would be where the curve is essentially a horizontal line, meaning the onset of instability of the hybrid composite is insensitive to change of glass misalignment and only dependent on the alignment of the other material.

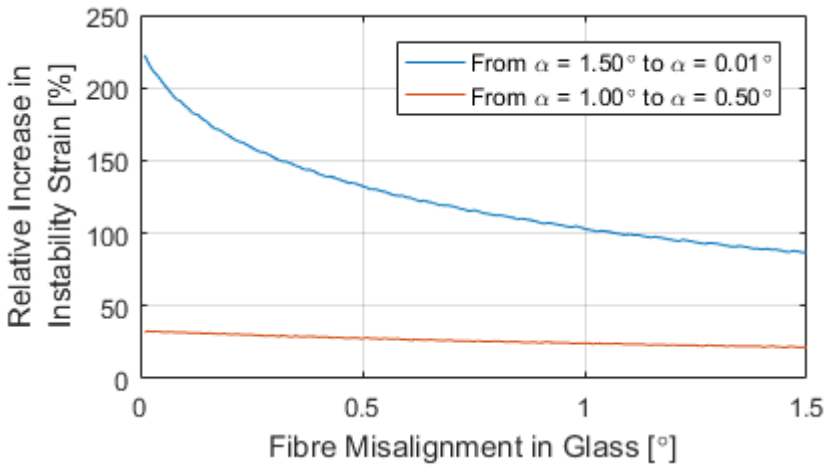

Figure 3-26: Relative increase in shear instability strain of the composite depending on the choice of carbon angle improvement. Compare with Figure 3-24 where corresponding values are smaller, suggesting the composite has higher sensitivity to carbon alignment.

Figure 3-26 shows the relative increase in shear instability strain when carbon alignment is changed from $\alpha = 1.50°$ to $\alpha = 0.01°$ and from $\alpha = 1.00°$ to $\alpha = 0.50°$. The former curve was introduced for completeness and easy comparison with Figure 3-24, but only improvement from $1.00°$ to $0.50°$ will be used as a benchmark from this point on. Compared to the corresponding curves for improving glass misalignment shown in Figure 3-24, the values are higher, suggesting that improving the alignment of carbon results in higher increase in strain to failure of the composite. The composite consisting of $1mm$ of carbon and $1mm$ of glass with the properties shown in Table 3-1 is therefore more sensitive to the carbon alignment. This is due to higher stiffness of carbon fibres which require a higher shear stress for equilibrium when misaligned.

To summarise, the following observations were made from the example investigating a hybrid composite consisting of $1mm$ of carbon fibre and $1mm$ of glass fibre:

1. The shear instability strain is a function of properties of both materials and can be represented in terms of fibre misalignment in either constituent, becoming a three-dimensional surface as seen in Figure 3-14.
2. Assuming the misalignment is the same in both constituents, the average stress at instability can be interpolated between the two constituents based on their thickness as seen in Figure 3-18. This is due to instability stress being a function of fibre misalignment and shear properties of the material.
3. Assuming the misalignment is the same in both constituents, the instability strain is increased compared to the constituent with lower shear instability strain shown in Figure 3-16. This effect is a function of axial stiffnesses of both materials, their misalignment and shear response.
4. Hybrid effect in compression is achieved by introducing fibres with lower stiffness which decrease the average stress in the composite at a given strain, leading to higher strain at instability.
5. The composite with equal thicknesses of carbon and glass is more susceptible to the alignment of the carbon layer, as indicated by Figure 3-25.

3.2.3 Effects of Volume on Instability in Hybrid Composites

Hybrid case with equal volumes of glass and carbon has been investigated in the previous section. However, it is rarely the case in reality that the hybrid composite contains the same amounts of constituent materials. Further cases must be investigated in order to account for varying volumes of carbon and glass in the hybrid. The following cases will be looked at:

1. $1.98mm$ of carbon + $0.02mm$ of glass (99% carbon volume)
2. $1.80mm$ of carbon + $0.20mm$ of glass (90% carbon volume)
3. $1.50mm$ of carbon + $0.50mm$ of glass (75% carbon volume)
4. $0.50mm$ of carbon + $1.50mm$ of glass (25% carbon volume)
5. $0.20mm$ of carbon + $1.80mm$ of glass (10% carbon volume)
6. $0.02mm$ of carbon + $1.98mm$ of glass (1% carbon volume)

The total thickness is kept the same at $2mm$. The results for each case will be analysed in the same fashion as for the equal volume case investigated in the previous section. However, for the sake of clarity some of the data can not be shown in a single figure for all the cases. Where possible, the data will be shown in a single figure.

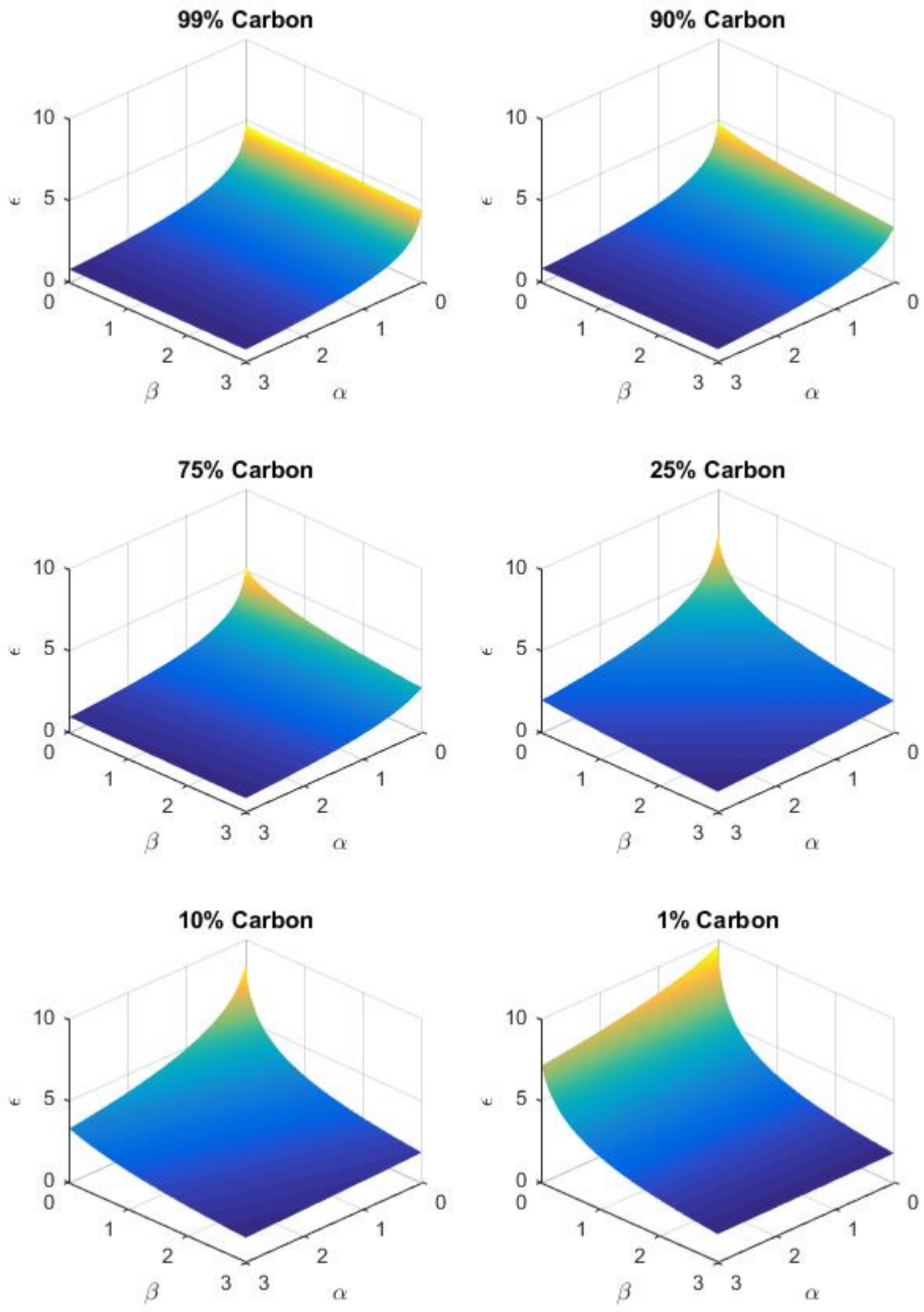

Figure 3-27: Shear instability surfaces for the six cases. Axis α is the carbon misalignment in °, β is the glass misalignment in ° and ϵ is the shear instability strain in %. Note the progressive change in strain at $\alpha = 0.01°$ and $\beta = 0.01°$ as the carbon volume decreases.

The complete shear instability envelopes for each case are shown in Figure 3-27. The maximum instability strain increases with increasing glass volume due to lower overall axial stiffness of the hybrid, similar to Figure 3-16. There is a progressive increase of the strain at $\beta = 0.01°$ as the carbon volume decreases. This is due to an increasing amount of well-aligned glass fibre in the hybrid which increases the maximum strain. An inverse effect is observed at $\alpha = 0.01°$ where the strain at high glass misalignment drops. Again, this is due to an increasing amount of poorly aligned glass fibre in the hybrid. The strain at $\alpha = 0.01°$ at low glass misalignment increases with increasing glass volume, again due to an increasing amount of well-aligned glass fibre.

Note the surface at 99% carbon volume changes very little with increasing value of glass misalignment β. This is due to the behaviour being dominated by the carbon and the influence of the glass fibre, even very misaligned, being negligible. Similarly, at 1% carbon volume the strain is relatively insensitive to the change in carbon alignment, although there is still a large drop at very small glass misalignment β. This again suggests that the instability strain of the hybrid is more susceptible to the alignment of the carbon fibre.

The surfaces can be sliced to produce shear instability curves that can readily be compared between the cases. Slicing at $\alpha = \beta$ as shown in Figure 3-15 yields the curves that can be compared to pure carbon and pure glass cases, as shown in Figure 3-28.

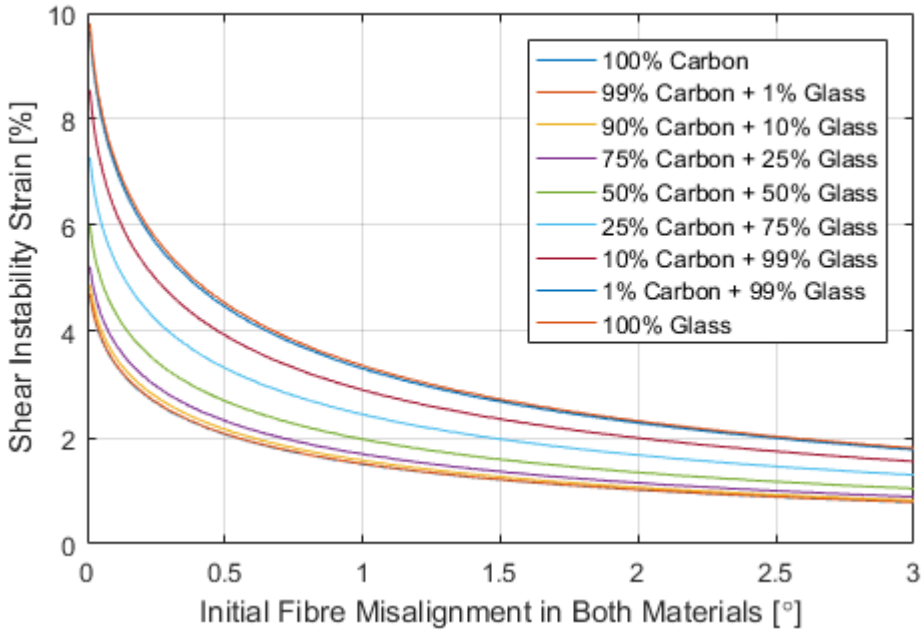

Figure 3-28: Comparison of shear instability curves for the six cases along with equal volume, pure glass and pure carbon data.

It can be seen that the strain does not scale linearly with the volume of carbon and glass, as already discussed with Figure 3-16. As the stress has previously been proven in Figure 3-18 to scale linearly with the material volume it will not be shown again for the new cases.

The surfaces can also be sliced in both directions as shown in Figure 3-21. The resulting sets of slices are then plotted for each individual surface. Figure 3-29 shows the effect of carbon volume on the glass fibre alignment susceptibility of the hybrid. As expected, at high carbon volume of 99% the effect of glass misalignment is negligible, with curves for all β values being almost identical. The lower the carbon volume, the further the curves diverge and the larger the difference between varying glass alignments. At 1% carbon the curves become almost horizontal, meaning there is no significant change in shear instability strain with respect to the carbon alignment α and the shear instability strain is governed mostly by the glass alignment β.

This effect is even more pronounced when looking at the 99% carbon volume curve in Figure 3-30. The instability strain is constant regardless of the glass alignment β and only changes with carbon alignment α. As the carbon volume decreases, the effects of glass alignment become more significant. However, compared to 99% carbon graph in Figure 3-29 the spread

is greater, yet again suggesting that the hybrid composite instability strain is more highly susceptible to carbon misalignment.

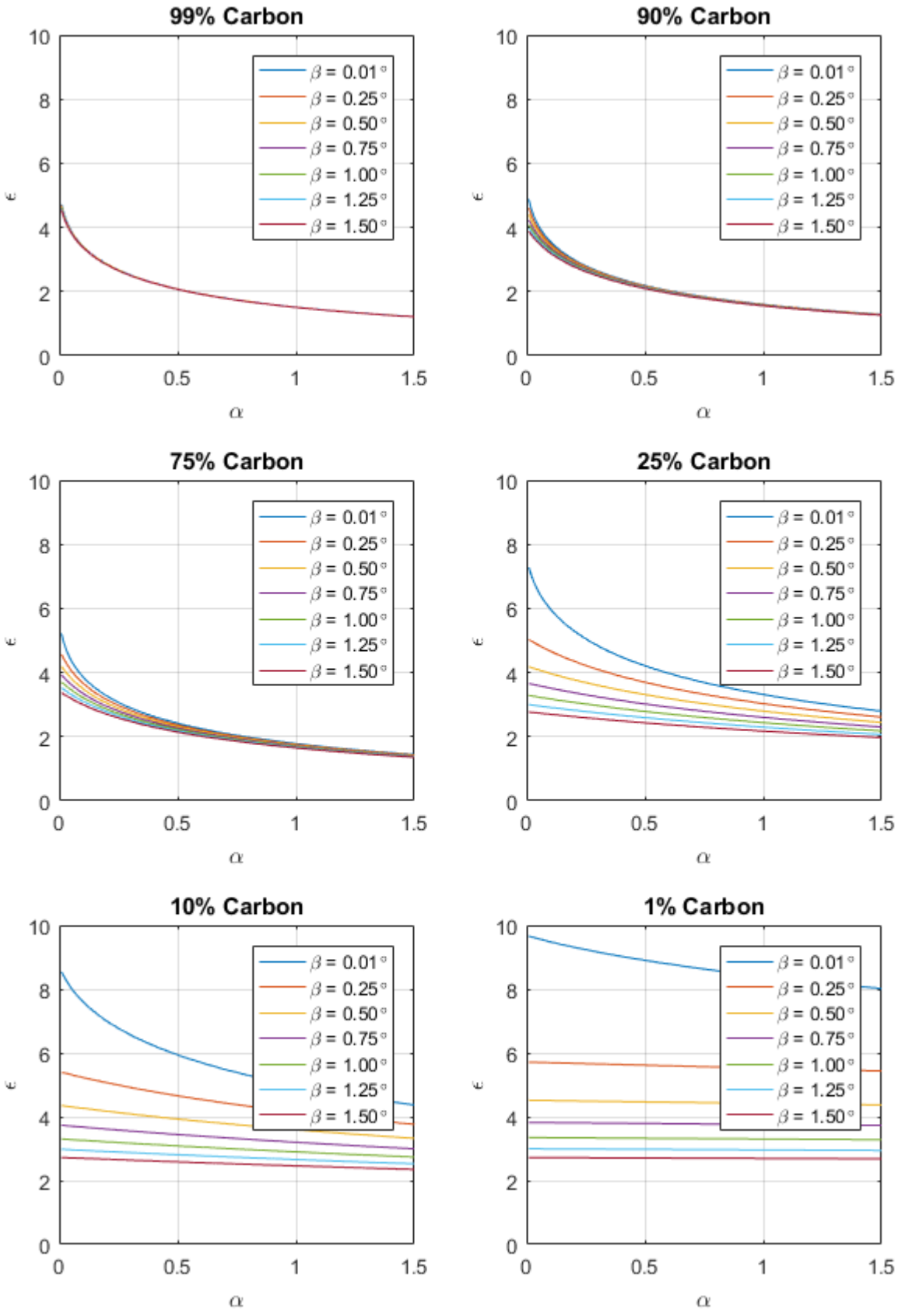

Figure 3-29: Shear instability at constant glass misalignment values β at different carbon volumes. Axis α is the carbon misalignment in ° and ϵ is the shear instability strain in %.

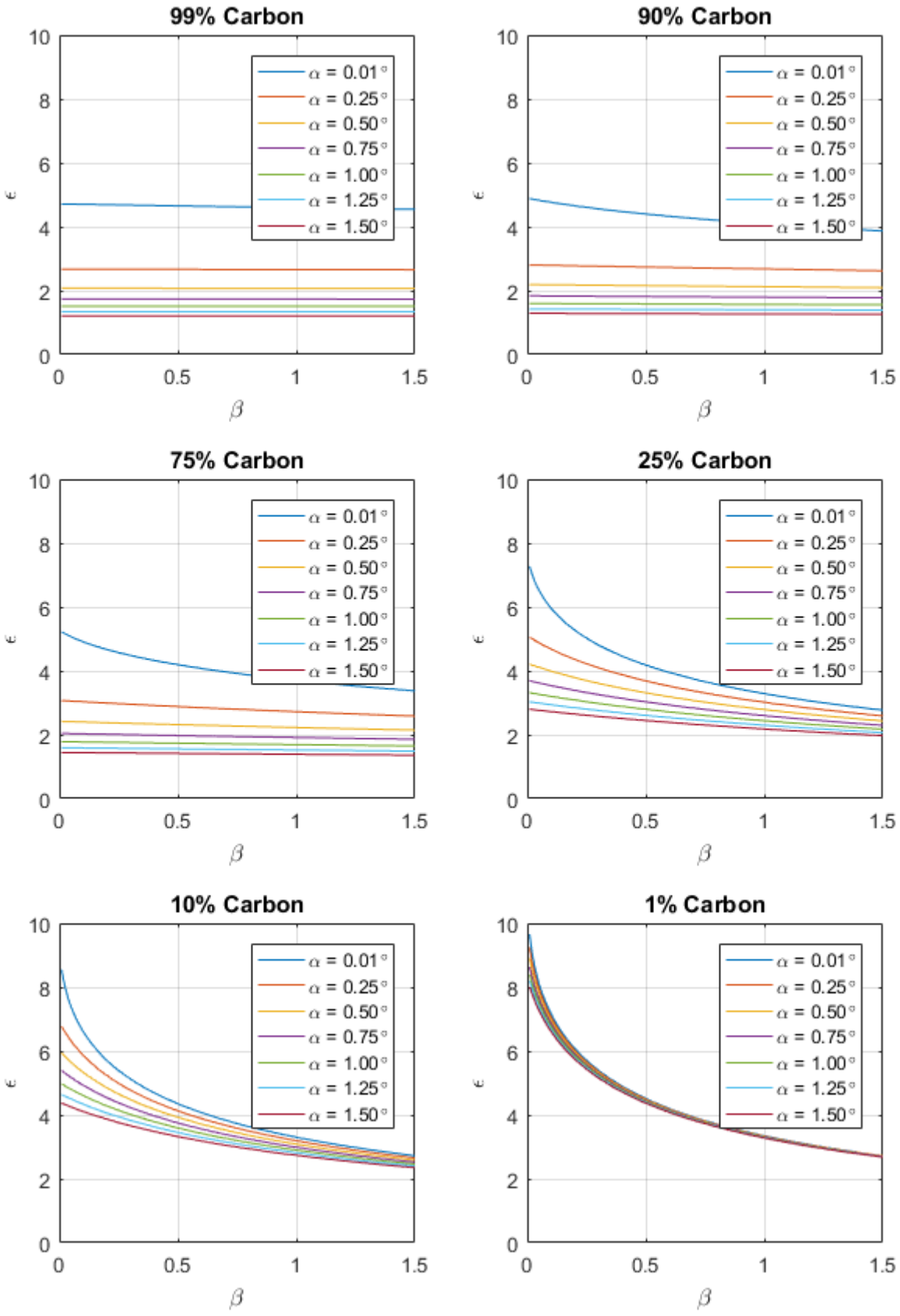

Figure 3-30: Shear instability at constant carbon misalignment values α at different carbon volumes. Axis β is the carbon misalignment in ° and ϵ is the shear instability strain in %.

In conclusion, the higher the volume of a constituent material the more its alignment affects the behaviour of the composite. This effect seems to be more significant for a constituent with higher axial stiffness (carbon fibre in this case). The effect will be more severe for higher axial stiffness mismatch n:

$$n = \frac{E_1}{E_2} \tag{3.24}$$

Where E_1 is the axial stiffness of the stiffer material and E_2 is the axial stiffness of the softer material.

In a real hybrid composite sample the misalignment of the fibres will vary throughout its volume [60]. The failure will most likely occur where the misalignment of both constituents produces the lowest shear instability strain.

3.2.4 Shear at Instability

As shown in Figure 3-3, the shear instability causes a very rapid increase in shear strain in the material. For a sample that does not experience the instability, the shear strain γ is relatively constant after several iterations of equilibrium calculation. The stable value can be recorded in the model to check what level of shear the sample is subjected to before the onset of instability. Figure 3-31 shows plots of the last stable γ for the cases investigated in the previous section. The plotted surfaces can be directly related to Figure 3-27.

It can be seen that the shear strain is relatively low at the last stable position, not exceeding a value of $\gamma = 3\%$ at any time for any of the samples and being limited to around $\gamma = 2\%$ in most cases. This means that the initial portion of the shear response curve is of primary importance as the high shear strain is unlikely to be present in the material, even at axial strains close to instability strain. Therefore, there is a temptation to simplify the rather complex shear response (for example the one shown in Figure 3-10) to the initial shear modulus G which would be a sufficient descriptor of material behaviour at low shear strains. Even more, since most shear response curves obtained in the course of this work have complex shapes.

However, the computational cost of introducing an exponential-linear equation to describe the shear curve is low, and the use of more accurate strain definition is presented next.

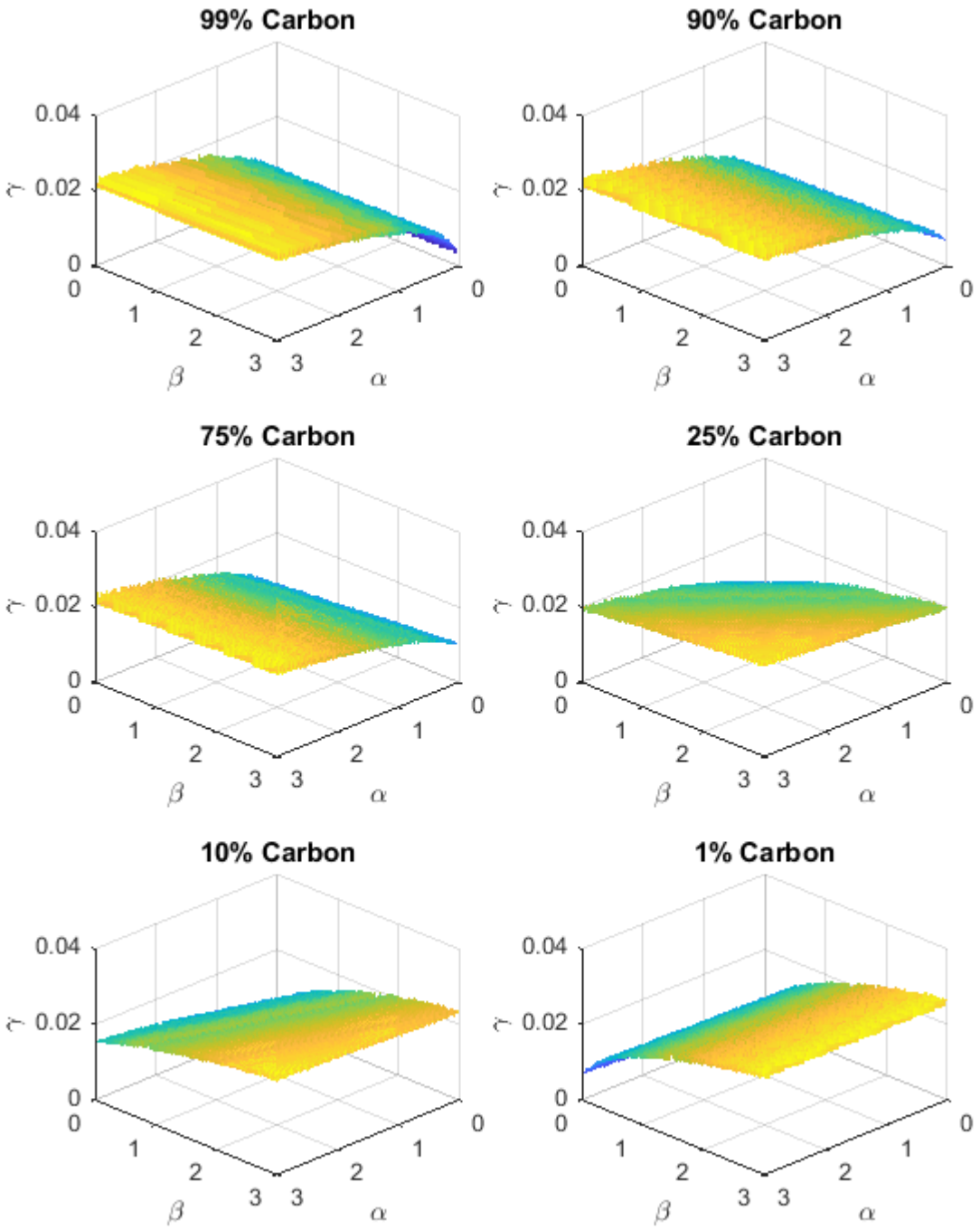

Figure 3-31: Last stable value of shear strain before the onset of shear instability. It can be seen that the values typically do not exceed $\gamma = 2\%$. This is low and typically within the initial, linear portion of the shear curve.

3.3 Fibre Waviness in Hybrid Composites

The hybrid composite investigated earlier consisted of S-glass and high-strength carbon fibres, but a range of fibres can be used, for example:

1. Carbon fibres of different strengths and moduli (high-modulus, ultra high-modulus, high-strength, intermediate modulus, etc.),
2. Glass fibres (E-glass and S-glass),
3. Polymeric fibres (polyethylene, polypropylene, nylon, etc.),
4. Cellulose and other natural fibres.

Various fibres exhibit different mechanical and chemical properties which can be chosen to achieve desired composite properties. One physical property of particular interest is the coefficient of thermal expansion (CTE). Most aerospace composites consist of thermosetting matrices that are cured at relatively high temperatures exceeding $100℃$. The cooling of a cured composite to a room temperature will therefore induce thermal deformation which may produce thermal stresses depending on the boundary conditions.

In the case of hybrid composites (especially glass and carbon) the CTE values may be significantly different as seen in Table 3-2.

Table 3-2: Coefficient of thermal expansion for the materials used

Material	Manufacturer	CTE [10^{-6}/°C]
IM7 [61]	Hexcel	-0.64
E-Glass	AGY	5.40
S2GL [62]	AGY	2.90

Materials with differential CTE values cured together will shrink differently as they cool down. The material with a higher CTE will shrink more and thus induce compressive stress on the material with lower CTE. Carbon fibres tend to have a negative CTE values meaning they shrink as the temperature increases. This further amplifies the mismatch with the glass.

Consider an extreme case of glass and carbon hybrid where a single carbon fibre is embedded within a large unidirectional block of glass fibre material. Upon curing the glass fibres will expand, but all fibres can be considered straight until the polymerisation is complete and the composite begins to cool down after the cure. As the glass fibres are contracting at the same rate, their straightness is assumed to be constant. However, the carbon fibre does not contract at the same rate as the glass (in fact it expands as it is cooling down) and can therefore be assumed to undergo deformation as it is embedded within the glass fibre block. Two different assumptions can be made at this point:

1. The carbon fibre stays straight and is compressed axially, or
2. The carbon fibre deforms out-of-axis and no axial compression is observed.

The first assumption will result in compressive stress being present within the carbon fibre and is typically used to calculate thermal stresses in hybrid composites. The latter assumption will render the fibre to change its shape without developing compressive stress. The resulting shape can be assumed as a sinusoidal wave for simplicity and ease of further manipulation. Figure 3-32 shows a schematic representation of the fibre in the initial straight state and the deformed sinusoidal shape.

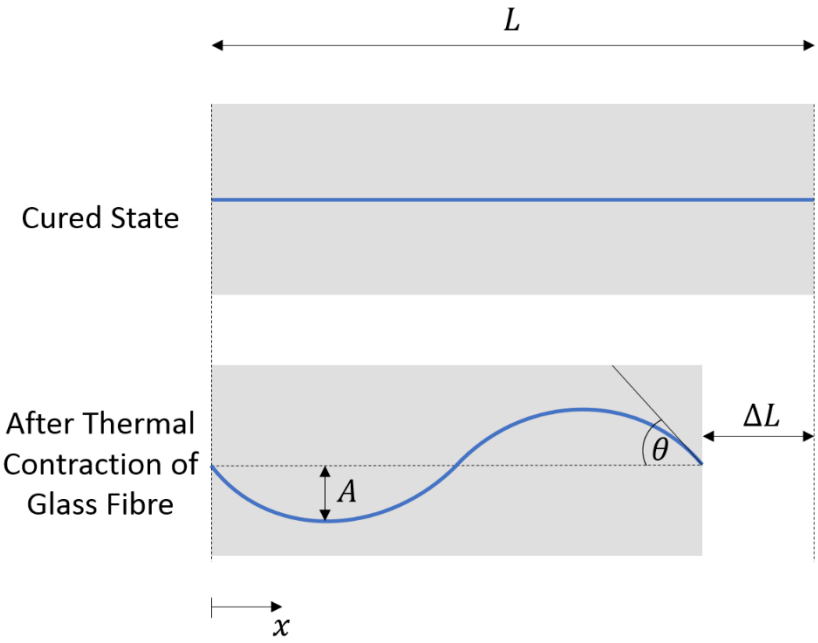

Figure 3-32: Initial and deformed geometry of a single carbon fibre embedded within a large sample of glass fibre with in-plane deformation only. The shortening of the glass fibre block is proportional to its thermal expansion coefficient and the temperature difference. The length of the carbon fibre remains constant as it assumes the shape of a sine wave.

The length of the fibre is assumed to stay constant in both states. In the initial state the length is L. ΔL is the change of length due to shrinkage in the glass fibre. The deformed state is the arc length of a single oscillation of sinusoid with amplitude A, which can be calculated as following:

$$L = \int_a^b \sqrt{1 + \left(\frac{dy}{dx}\right)^2}\, dx \tag{3.25}$$

Where a and b are integration limits and $\frac{dy}{dx}$ is the derivative of the function. As the function describing the sinusoid is $y = Asin(x)$, this becomes:

$$L = \int_a^b \sqrt{1 + \left(Acos(x)\right)^2}\, dx \tag{3.26}$$

The lower limit of integration $a = 0$, and the upper limit is:

$$b = L - \Delta L = L(1 - \Delta) \tag{3.27}$$

And the shrinkage due to cooling Δ can be calculated as:

$$\Delta = CTE * t \tag{3.28}$$

Where CTE is a coefficient of thermal expansion of the glass fibre in $°C^{-1}$ and t is the temperature difference in $°C$ between the cured and the cooled state. The equation thus becomes:

$$L = \int_0^{L(1-CTE*t)} \sqrt{1 + \left(Acos(x)\right)^2}\, dx \tag{3.29}$$

Which needs to be solved for A for given values of CTE and t. Solving for A analytically requires the use of elliptical integrals, however the solution can also be obtained by implementation of numerical integration, as was done in this instance.

Once the amplitude A is obtained, the maximum angle of the carbon fibre is simply obtained as the derivative of the original sinusoid at either end:

$$\alpha_{MAX} = Acos(0) = Acos(2\pi) \tag{3.30}$$

Solving numerically for both E-Glass and S2GL with respective values of $CTE = 5.40 * 10^{-6}$ and $CTE = 2.90 * 10^{-6}$ and a range of temperatures t between $1°$ and $120°$ yields the graph shown in Figure 3-33.

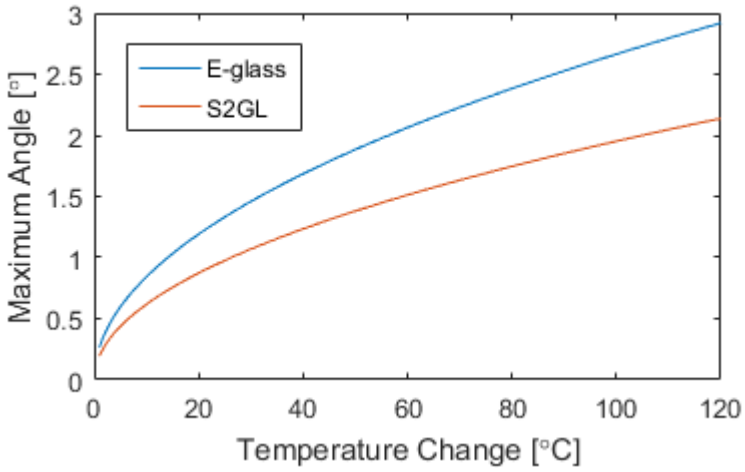

Figure 3-33: Maximum angle induced by the out-of-axis deformation of the single fibre due to shrinking of surrounding material at a given temperature change.

It can be seen from the curves produced that the angle created in the carbon fibre by the shrinking of the glass is not insignificant with values of $2.92°$ and $2.14°$ for E-glass and S2GL respectively at the temperature difference of $120°C$. As shown in the earlier sections of this chapter, misalignments of this extent would lower the compressive performance of the composite to a large extent.

The actual misalignment due to cooling the hybrid at mismatched CTE values of its constituents is unlikely to be as large as shown in the above example. The carbon fibre is likely to shrink axially resulting in development of compressive stress and the deformation will largely be inhibited by the cured matrix. Realistically, the effect will fall somewhere between the two extreme cases of sole axial compression and sole out-of-axis deformation.

The waviness resulting from the out-of-axis deformation can be investigated statistically. For any random variable, the probability density function would follow a normal distribution. This is the case for fibre misalignment values in a real composite sample. How does the waviness-induced misalignment influence the measured angle distribution?

Assuming there are multiple carbon fibres embedded within the glass and their deformations are independent, how likely is it that the maximum angle will occur along the length of multiple fibres at the same location? This can be investigated by constructing the probability density function (PDF) of a sine wave.

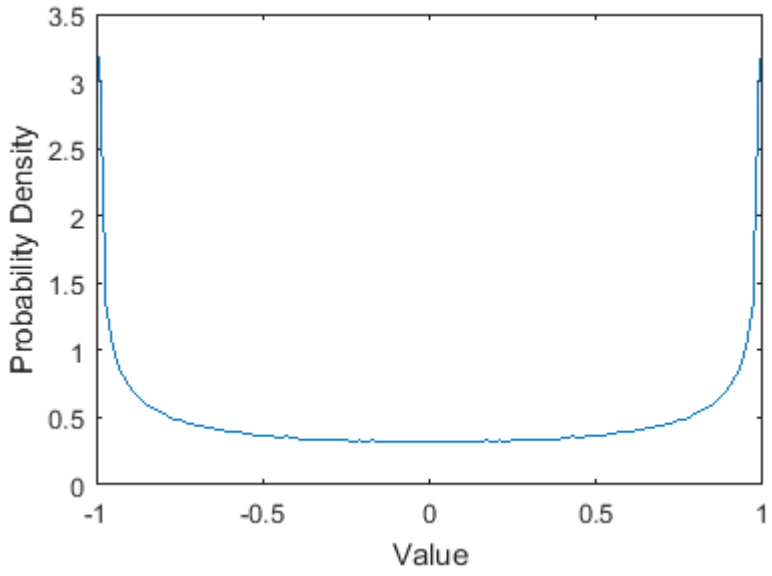

Figure 3-34: Probability density function (PDF) of a sine wave. Note the highest probability is that of extreme values occuring.

It can be seen from Figure 3-34 that probability of occurrence of high angles is relatively high. This means that when cutting a composite containing a wavy fibre at a random location, it is much more likely to cut where the fibre magnitude is high. However, this is true for a cut through a single wavy fibre. Standard distribution should still apply in a real case where thousands of fibres are cut.

3.4 Summary

A shear instability model was introduced that uses an iterative approach to solve equilibrium equations in order to predict the axial strain in the composite at which convergence of shear strain γ becomes unstable (value increases rapidly to infinity as seen in Figure 3-3).

The model uses the following parameters as input:

1. Shear response of the composite
2. Longitudinal stiffness of the composite
3. Initial fibre misalignment

It is therefore assumed that the above three parameters are the only ones affecting the compressive failure through shear instability. Fragmentation failure is possible for carbon fibre, but limited to high-stiffness materials, as shown in Figure 3-5.

It is found that the **shear instability is a stress-based phenomenon**. Once the critical stress is reached in the matrix, the instability will occur.

The model is extended to a secondary material with compatible shear deformation. Solving the equation for induced shear deformation yields:

$$\gamma = \frac{\tau_1 t_1 + \tau_2 t_2}{G_1 t_1 + G_2 t_2} \tag{3.31}$$

Which is equal to:

$$\gamma = \varepsilon \frac{\alpha E_1 t_1 + \beta E_2 t_2}{G_1 t_1 + G_2 t_2} \tag{3.32}$$

Therefore, assuming that the shear response of the two materials is the same ($G_1 = G_2$) and that they are identically misaligned ($\alpha = \beta$) yields:

$$\gamma = \frac{\varepsilon \alpha}{G_1} \frac{E_1 t_1 + E_2 t_2}{t_1 + t_2} \tag{3.33}$$

And in general it can be stated that:

$$\frac{E_1 t_1 + E_2 t_2}{t_1 + t_2} = E_{AVG} \tag{3.34}$$

Therefore:

$$\gamma \propto E_{AVG} \tag{3.35}$$

Meaning that the rate of shear deformation which leads to shear instability depends on the average stiffness of the composite. This explains why the addition of low stiffness material (glass fibre composite) to the carbon results in higher instability strain. **This effect is postulated to be the hybrid effect in compression.**

Also, the following observations can be made from the above equations:

1. The higher the misalignment, the lower the shear instability stress
2. The higher the shear stiffness of the matrix, the higher the shear instability stress

A number of test cases are investigated using real-life carbon and glass materials to determine the effects of different fibre alignment within the two constituent materials and the effects of changing the relative volume of the carbon and glass. The key finding is that the instability strain is more susceptible to the misalignment in high stiffness material due to its larger effect on stress.

This concludes the chapter. The two-material model presented here will be used in subsequently to provide explanation of testing results. Next chapter investigates the effects of varying the volume of carbon within a hybrid material under direct compression which relates to the model presented here.

4 Determining the Onset of Shear Instability in Direct Compression

To validate the model outlined in the previous section, a series of tests were conducted. These tests focused on hybrid specimens in direct compression with varying volumes of carbon fibre. Although the direct compression test is not the preferred test method as will be outlined in Chapter 5, the simple model introduced in Chapter 3 does not account for bending effects and therefore the data obtained from a bending test can not be directly correlated with the model.

4.1 General Considerations and Specimen Design

In tensile testing of hybrid specimens, carbon fragmentation is normally observed prior to critical failure [63]. This is due to glass fibres carrying the load beyond the failure strain of the carbon fibre. Once the carbon fibres reach their maximum strain (also called fragmentation strain) the load is redistributed to the surrounding glass fibres through the shear in the matrix and the load can further be increased. A stiffness drop is normally associated with this phenomenon and the critical strain in the specimen is about that of the glass fibre maximum strain.

Jalalvand et al. have demonstrated how this mechanism can be utilised to create pseudo-ductility in the hybrid specimen. The concept of pseudo-ductility has been explored at the University of Bristol [63]–[66] and similar work has been carried out at KU Leuven [67]. The hybrid specimen can be designed for a desired type of failure based on the properties of its constituents. With the correct choice of material thickness and volume, the low-elongation fibres (assume carbon for this case) will fragment without critical failure and the hybrid composite will continue taking load at a decreased stiffness until reaching high-elongation material (assume glass for this case) failure strain. Alternatively, the carbon may fail at its failure strain, leading to a significant increase in the loading of the glass fibres and causing immediate failure of the composite. The behaviour can be predicted based on the properties of the constituent materials of the hybrid composite. If delamination is taken into consideration, a graph showing possible failure mechanisms with regard to carbon volume and thickness of carbon layer can be produced. Such graph is called a damage mode map (DMM).

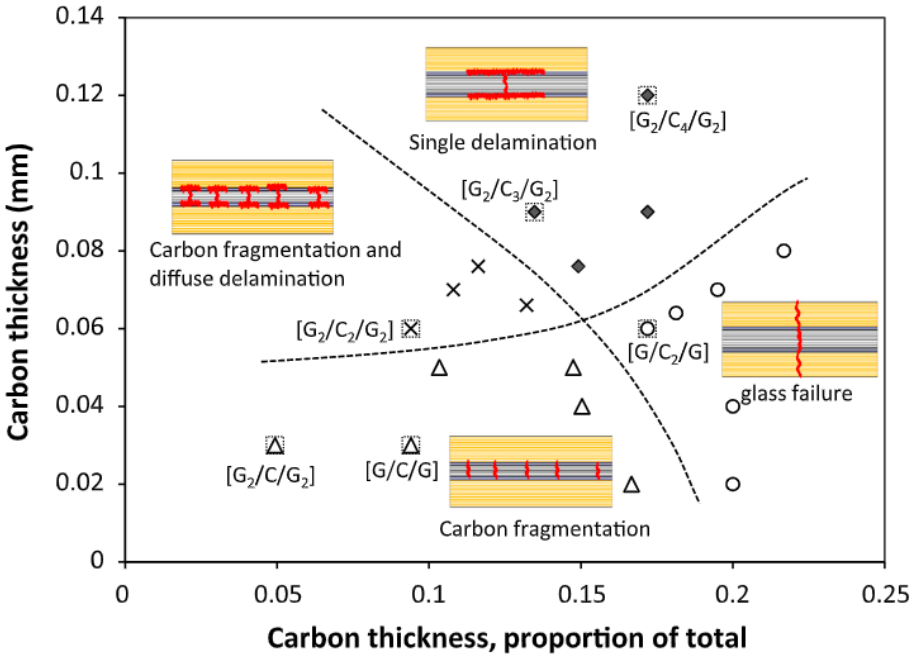

Figure 4-1: Damage mode map (DMM) representing the possible failure scenarios of a hybrid sample. Adapted from [68].

Figure 4-1 shows a DMM produced for a hybrid specimen. Four distinct failure modes can be achieved using the two constituent materials:

1. Fragmentation
2. Fragmentation and spread delamination
3. Single delamination
4. Failure of low stiffness material

While these mechanisms have been experimentally confirmed when testing in tension [63], their validity under compression has not been proven. Working under the assumption that the compressive failure in carbon occurs due to shear instability (in high-strength and high-elongation fibres), fragmentation of single fibres might not be achievable. Therefore the damage modes observed in tension would not be valid in compression. The work presented in this chapter will also aim to investigate that.

The direct compression specimen was designed with three objectives in mind:

1. Prevent premature delamination
2. Achieve maximum carbon non-linearity
3. Observe carbon failure

The most desirable behaviour would be a smooth load-displacement curve with decreasing stiffness up until a high compressive strain, at which carbon fragmentation or failure would be observed. Ideally, this would occur without delamination. Using the damage mode map, the samples would be positioned in the region of fragmentation without delamination, as shown in the shaded area in Figure 4-2 below.

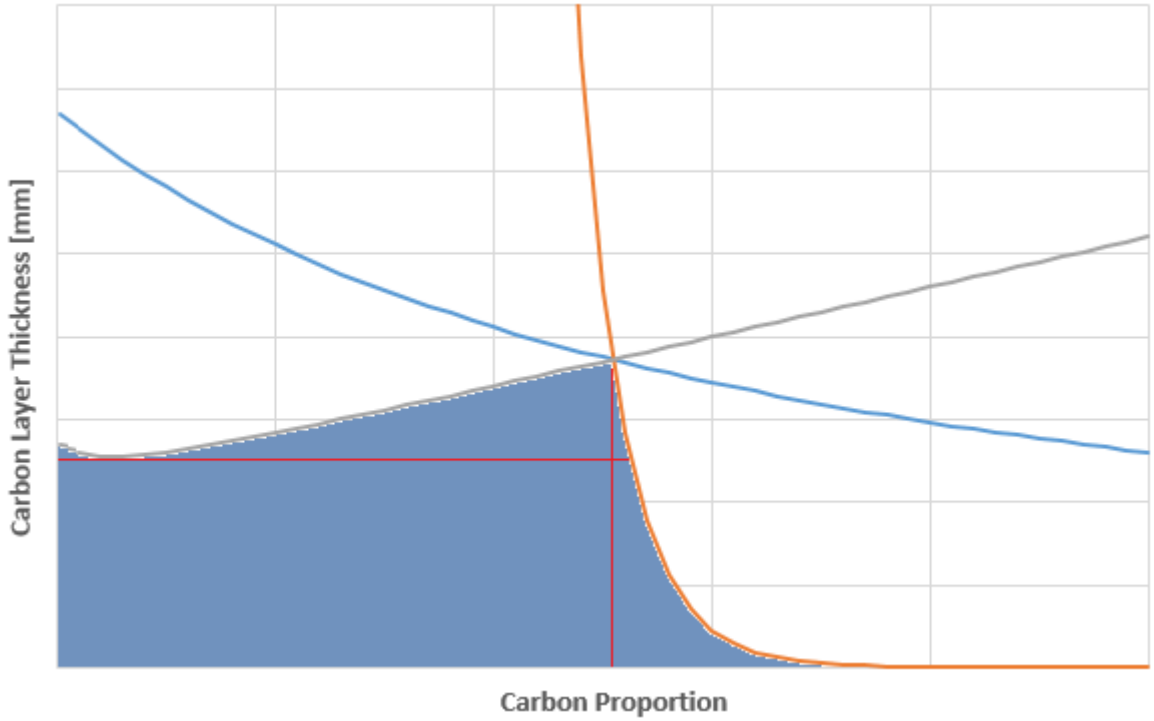

Figure 4-2: Generic shape of a damage mode map. The shaded region represents carbon fragmentation without delamination - a desirable response for the samples. The horizontal red line represents maximum carbon thickness that is acceptable for all carbon proportions within the region and the vertical line the maximum carbon proportion acceptable for all carbon thicknesses within the region.

As the glass is assumed to be linear elastic, in order to observe the maximum non-linearity in the sample, the carbon proportion needs to be as high as possible (closer to the orange line). For all practical purposes it is assumed that all samples must fall to the left of the orange line.

As the carbon is assumed to have a non-linear response in compression, as shown in Figure 4-4, the equations for energy release rate must be considered again. Consider a laminate consisting of three layers shown in Figure 4-3.

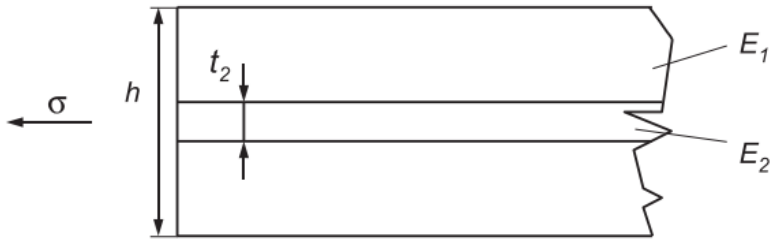

Figure 4-3: Three layer laminate considered in energy release calculations. Adopted from [41].

After [41], the undamaged sample can be assumed to have an equivalent modulus E_{eq0}:

$$E_{eq0} = \frac{E_1(h - t_2) + E_2 t_2}{h} \tag{4.1}$$

Where E_1 is the modulus of outer plies, E_2 is the modulus of inner ply, h is the total thickness of the lamine and t_2 is the thickness of the inner ply. The equivalent modulus can also be written for a case where the central ply is fully delaminated and not contributing to sample load carrying capacity. This will be equivalent modulus $E_{eq,f}$:

$$E_{eq,f} = \frac{E_1(h - t_2)}{h} \tag{4.2}$$

Where the central ply does not contribute. The elastic strain energy for unit length and depth of the laminate U can be calculated as:

$$U = \frac{1}{2}\sigma\varepsilon h = \frac{1}{2}\frac{\sigma^2 h}{E_{eq}} \tag{4.3}$$

Where σ is the average stress in the sample and ε is the axial strain in the sample. The strain energy equation can therefore be evaluated for two cases of equivalent modulus outlined above. Using E_{eq0} yields:

$$U_0 = \frac{1}{2}\frac{\sigma^2 h^2}{E_1(h - t_2) + E_2 t_2} \tag{4.4}$$

Which is the elastic strain energy for the intact sample. Substituting for $E_{eq,f}$:

$$U_f = \frac{1}{2}\frac{\sigma^2 h^2}{E_1(h - t_2)} \tag{4.5}$$

Which is the elastic strain energy for the delaminated sample. This derivation was originally performed for tension, where load transfer of the central ply after delamination is zero. In the case of compression, some fraction of the load may still be carried in bearing. The exact

value is unknown, but for the purposes of the calculations it will be assumed that there is no load transfer in compression. The pullout of the central ply is occurring in mode II only. As the total energy is split between two surfaces joining the middle ply to the outside plies, the energy release rate will become the difference of the two, further divided by two for a single interface:

$$G = G_{II} = \frac{1}{2}(U_0 - U_f) \tag{4.6}$$

$$\begin{aligned} G &= \frac{1}{2}\left(\frac{1}{2}\frac{\sigma^2 h^2}{E_1(h-t_2)+E_2 t_2} - \frac{1}{2}\frac{\sigma^2 h^2}{E_1(h-t_2)}\right) \\ &= \frac{1}{4}\left(\frac{\sigma^2 h^2 E_2 t_2}{E_1(h-t_2)(E_1(h-t_2)+E_2 t_2)}\right) \end{aligned} \tag{4.7}$$

And the stress in the central layer σ_2 can be written in terms of average stress:

$$\sigma_2 = \frac{\sigma h E_2}{E_1(h-t_2)+E_2 t_2} \tag{4.8}$$

Reordering for σ:

$$\sigma = \frac{\sigma_2(E_1(h-t_2)+E_2 t_2)}{hE_2} \tag{4.9}$$

Substituting back into the energy release rate G calculation:

$$G = \frac{h^2 E_2 t_2}{E_1(h-t_2)(E_1(h-t_2)+E_2 t_2)}\frac{\sigma_2^2(E_1(h-t_2)+E_2 t_2)^2}{h^2 E_2^2} \tag{4.10}$$

$$G = \frac{\sigma_2^2 t_2(E_1(h-t_2)+E_2 t_2)}{4E_1 E_2(h-t_2)} \tag{4.11}$$

This can be rewritten for strain:

$$G = \frac{\varepsilon^2 E_2 t_2(E_1(h-t_2)+E_2 t_2)}{4E_1(h-t_2)} \tag{4.12}$$

These equations are interchangeable when both the high and low strain materials are linear elastic. However, if non-linearity is assumed in the carbon, the modulus will vary depending on the strain, and therefore the secant modulus value should be used instead of initial modulus. As the material is softening, the energy release rates calculated for a linear elastic case will be smaller than actual values.

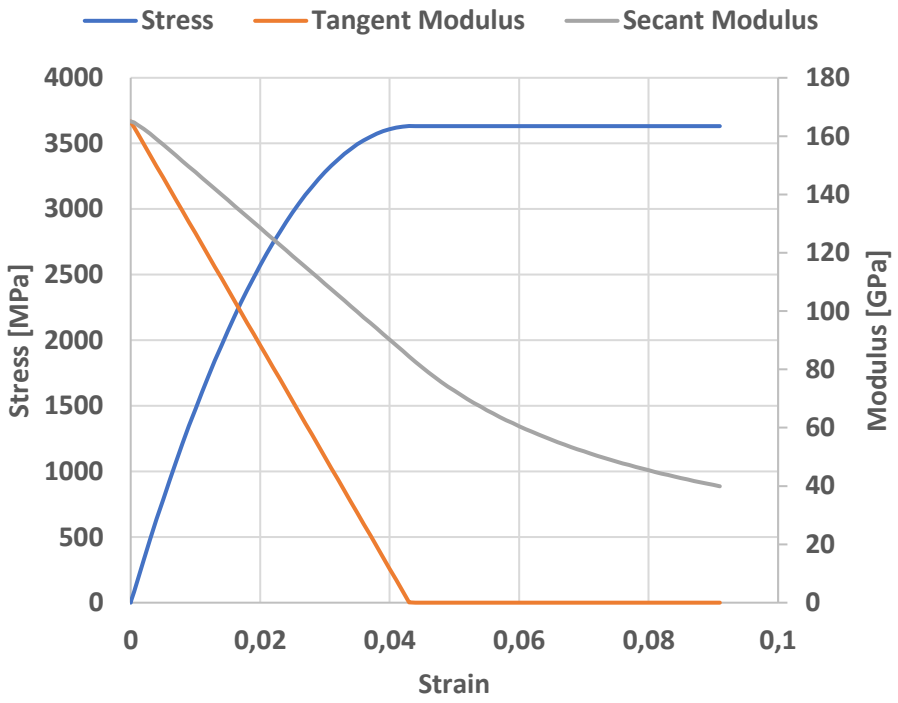

Figure 4-4: An example of the non-linear carbon response in compression. The blue line represents the stress and the orange line a linearly decreasing modulus of the sample as suggested by [2].

Properties of the materials are shown in Table 4-1. Note that the carbon properties are taken from manufacturer's datasheet rather than measured.

Table 4-1: Material properties

Material	t_{PLY} [mm]	$E_{TENSILE}$ [GPa]	$\varepsilon_{MAX,FIBRE}$ [%]	$\sigma_{MAX,TENSILE}$ [MPa]	$\sigma_{MAX,COMPRESSIVE}$ [MPa]
S-glass/Epoxy	0.155**	45.7**	5.5*	1763*	1172*
T1000/Epoxy	0.039*	165*	2.2*	3040*	1570*

*Datasheet

**Measured

It can be seen that the quoted compressive strength is significantly lower than the tensile strength for both materials. This is likely due to testing using ASTM D695 [28], which tends to underestimate strength compared to the modified ASTM method [1]. The failure stresses are therefore expected to be higher, especially in carbon which would further benefit from hybridisation with the glass. The calculation of the actual energy release rate is therefore not straightforward, as the failure stress is largely unknown, in addition to the secant modulus dropping with increasing failure strain due to carbon non-linearity. The previous equations can therefore be rewritten:

$$G = \frac{\sigma_C^2 t_C (E_G t_G + E_C t_C)}{4 E_G E_C t_G} \tag{4.13}$$

$$G = \frac{\varepsilon^2 E_C t_C (E_G t_G + E_C t_C)}{4 E_G t_G} \tag{4.14}$$

Where E_G and E_C are glass and carbon secant moduli respectively, t_G and t_C are glass and carbon total thicknesses respectively, σ_C is the stress in the carbon and ε is the strain in the sample. Checking the dimensions of the above equations:

$$G = \frac{\sigma_C^2 t_C (E_G t_G + E_C t_C)}{4 E_G E_C t_G} = \frac{\frac{N^2}{mm^4} * mm(\frac{N}{mm^2} * mm + \frac{N}{mm^2} * mm)}{\frac{N}{mm^2}\frac{N}{mm^2} mm} = \frac{N}{mm} \tag{4.15}$$

$$G = \frac{\varepsilon^2 E_C t_C (E_G t_G + E_C t_C)}{4 E_G t_G} = \frac{\frac{N}{mm^2} * mm(\frac{N}{mm^2} * mm + \frac{N}{mm^2} * mm)}{\frac{N}{mm^2} * mm} = \frac{N}{mm} \tag{4.16}$$

If carbon and glass are both assumed to be linear, these two equations are equivalent:

$$\sigma_C = \varepsilon E_C \tag{4.17}$$

An example calculation is shown for a configuration where a single carbon layer is sandwiched between two glass plies and the properties are taken directly from Table 4-1:

$$\begin{aligned} G &= \frac{\sigma_2^2 t_2 (E_1 (h - t_2) + E_2 t_2)}{4 E_1 E_2 (h - t_2)} \\ &= \frac{1570^2 * 0.039(45700 * 0.310 + 165000 * 0.039)}{4 * 45700 * 165000(0.310)} \\ &= 0.212 \frac{N}{mm} \end{aligned} \tag{4.18}$$

Which is very low. However, if the calculation is repeated using the strain-based equation with an assumed carbon failure strain value of 1.5%, (which is likely still an underestimation), the energy release rate becomes:

$$\begin{aligned} G &= \frac{\varepsilon^2 E_2 t_2 (E_1 (h - t_2) + E_2 t_2)}{4 E_1 (h - t_2)} \\ &= \frac{0.015^2 * 165000 * 0.039(45700 * 0.310 + 165000 * 0.039)}{4 * 45700(0.310)} \\ &= 0.526 \frac{N}{mm} \end{aligned} \tag{4.19}$$

This value seems more in line with previous findings [41]. It must be noted that the carbon modulus will in reality decrese with increasing strain value for these calculations, making the stress-based value higher and the strain-based result lower. In addition to that, the failure stress is likely to be significantly higher than quoted by the manufacturer. Table 4-2 shows the results of calculating the energy release rate for various assumptions. For all cases, the thicknesses are assumed as $t_G = 2 * 0.155 = 0.31\ mm$, $t_C = 0.039\ mm$ and glass modulus $E_G = 45.7\ GPa$.

The values of energy release rate obtained from the calculations were used for drawing damage mode maps of the four configurations with assumed properties. These are shown in Figure 4-5. It can be seen that cases 1 and 2 would imply samples failing either due to fragmentation and diffuse delamination or catastrophic delamination regardless of the total carbon content (as the single carbon layer thickness stays the same at $t_C = 0.039\ mm$). Case 3 suggests fragmentation without delamination and case 4 either fragmentation without or with defuse delamination. Please note that it is assumed that the samples must fall to the left of the orange line and that the carbon proportion can be adjusted.

Table 4-2: Assumed properties and the resulting input for DMM creation

Case	Carbon			Glass	G [N/mm]		Comments
	$E_{COMPRESSIVE}$ [GPa]	$\sigma_{MAX,COMPRESSIVE}$ [MPa]	$\varepsilon_{MAX,COMPRESSIVE}$ [%]	$\sigma_{MAX,COMPRESSIVE}$ [MPa]	Stress-based	Strain-based	
1	165	1570	0.95	1172	0.212	0.212	Modulus constant and equal to tensile from datasheet, stress from datasheet, strain calculated from stress and modulus
2	145	1570	1.06	1172	0.232	0.222	As previously, but with secant modulus and strain calculated using a non-linearity assumption
3	125	2743	2.20	1550	0.790	0.790	Strain and initial modulus equal to tensile, non-linearity, increased glass strength
4	165	1570	N/A	1172	0.500	0.500	Datasheet values with assumed energy release rate

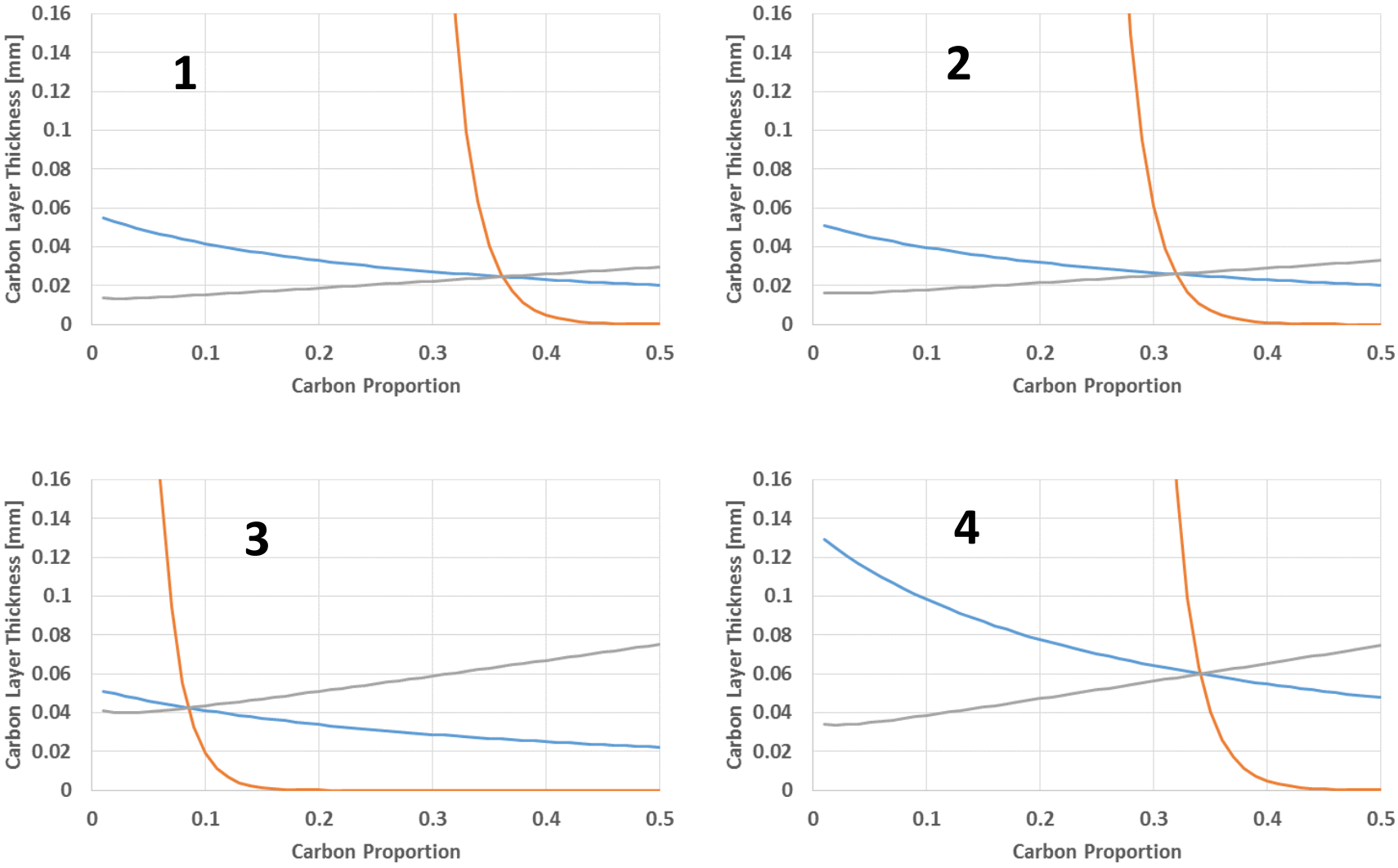

Figure 4-5: Damage mode maps corresponding to the assumed cases.

The four cases shown above are based on different assumptions and cannot all be true at the same time. The actual behaviour is likely to fall within the bounds defined by the assumed cases, but is impossible to determine without prior testing. Conclusions from a specimen design viewpoint:

- Cases 1 and 2 suggest it is impossible to obtain fragmentation without delamination with the available carbon thickness.
- Case 3 with the assumed high carbon strain would not delaminate using the available carbon fibre, but it does not allow for high carbon ratios.
- Case 4 using datasheet values, but with assumed higher energy release rate would suggest that high carbon ratios (20% to 30%) are not possible, but also desirable to achieve fragmentation without delamination.

The proposed test configurations cover a range of carbon ratios while keeping the minimum carbon layer thickness of $t_C = 0.039\ mm$. As the carbon layer thickness is the limiting factor in preventing delamination, no blocked carbon plies are allowed. In order to keep the lay-ups symmetric and as uniform in terms of material distribution, glass and carbon plies are alternating, with single, double or triple glass layer between the carbon plies. This yields a good spread of carbon volumes while minimising the complexity of the configurations, seen in Table 4-3. As these lay-ups would fail for cases 1 and 2, the corresponding DMM are only shown for cases 3 and 4 in Figure 4-6 and Figure 4-7 respectively.

Table 4-3: Proposed specimen configurations

№	Layup	Total Plies		Total Thickness [mm]	Carbon Proportion [%]
		Glass	Carbon		
1	[G/C/G/C/.../C/G]	18	17	3.453	19.2
2	[G_2/C/G_2/C/.../C/G_2]	18	8	3.102	10.1
3	[G_3/C/G_3/C/.../C/G_3]	18	5	2.985	6.5

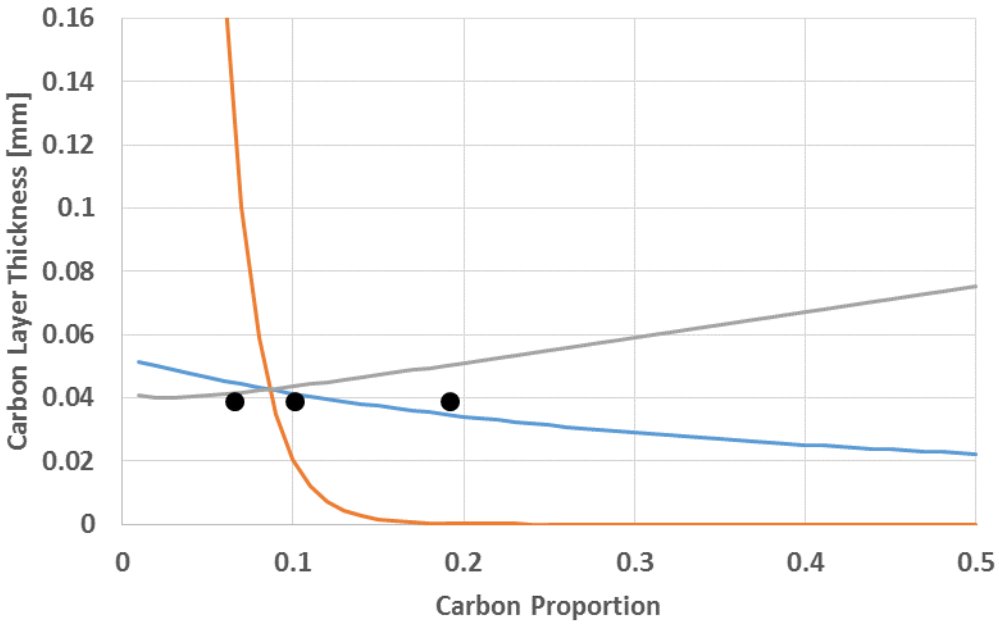

Figure 4-6: DMM for configuration assuming high compressive strain in carbon. Note that only one configuration falls within the desired range, with the other two failing critically due to glass failure.

The three proposed specimen configurations are marked as black dots on the DMM. It can be seen that the only configuration 1 would fail by carbon fragmentation and the other two would lead to catastrophic failure of the specimen once carbon failure strain is reached. There would therefore be a shift in the failure mode which should be observed in testing.

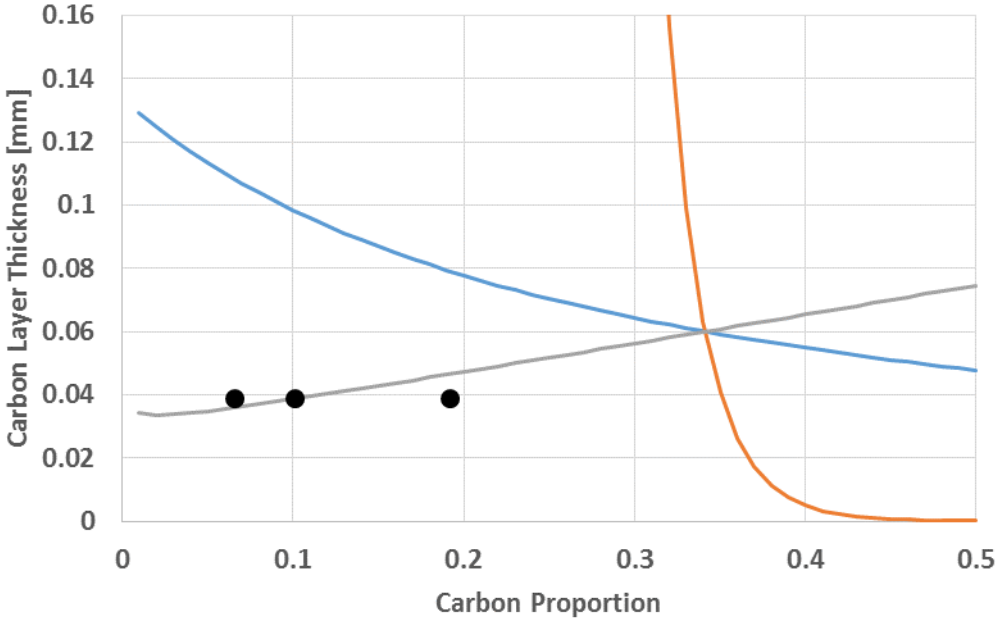

Figure 4-7: DMM for the datasheet values with assumed higher energy release rate. Note that one value falls within diffuse delamination zone, one on fragmentation without delamination and one on the border of the two.

If the DMM shown in Figure 4-7 is assumed, one configuration would fail by delamination, one by fragmentation and one would be borderline with likely failures in either of the aforementioned modes. This would again be observed in testing.

4.2 Specimen Manufacturing and Testing

Specimens were manufactured for the three configurations shown in Table 4-3. The manufactured configurations differed slightly from the proposed due to manufacturing error (one glass and one carbon ply added to configuration 1), but the specimen quality and overall usability were not affected. These are shown in Table 4-4.

Table 4-4: Manufactured specimen configurations

№	Layup	Total Plies		Total Thickness [mm]	Carbon Proportion [%]
		Glass	Carbon		
1	[G/C/G/C/.../C/G]	19	18	3.647	19.2
2	[G_2/C/G_2/C/.../C/G_2]	18	8	3.102	10.1
3	[G_3/C/G_3/C/.../C/G_3]	18	5	2.985	6.5

The samples were tested using the IC modified ASTM D695 method [1] on an Instron 600 kN hydraulic machine.

The instrumentation was as following:

1. Two strain gauges on top and bottom surfaces of the composite in the gauge length
2. Video gauge with a zoom lens on one side surface of the specimen with speckle pattern applied

The video gauge data was collected to check for the possibility of testing without using strain gauges. However, due to the granularity of VG data only the strain gauges were used for processing. The average strain in the sample is simply calculated as an average between the strain read by the two strain gauges.

4.3 Test Results and Failure Mode

The results for the three tested configurations are shown in Figure 4-8.

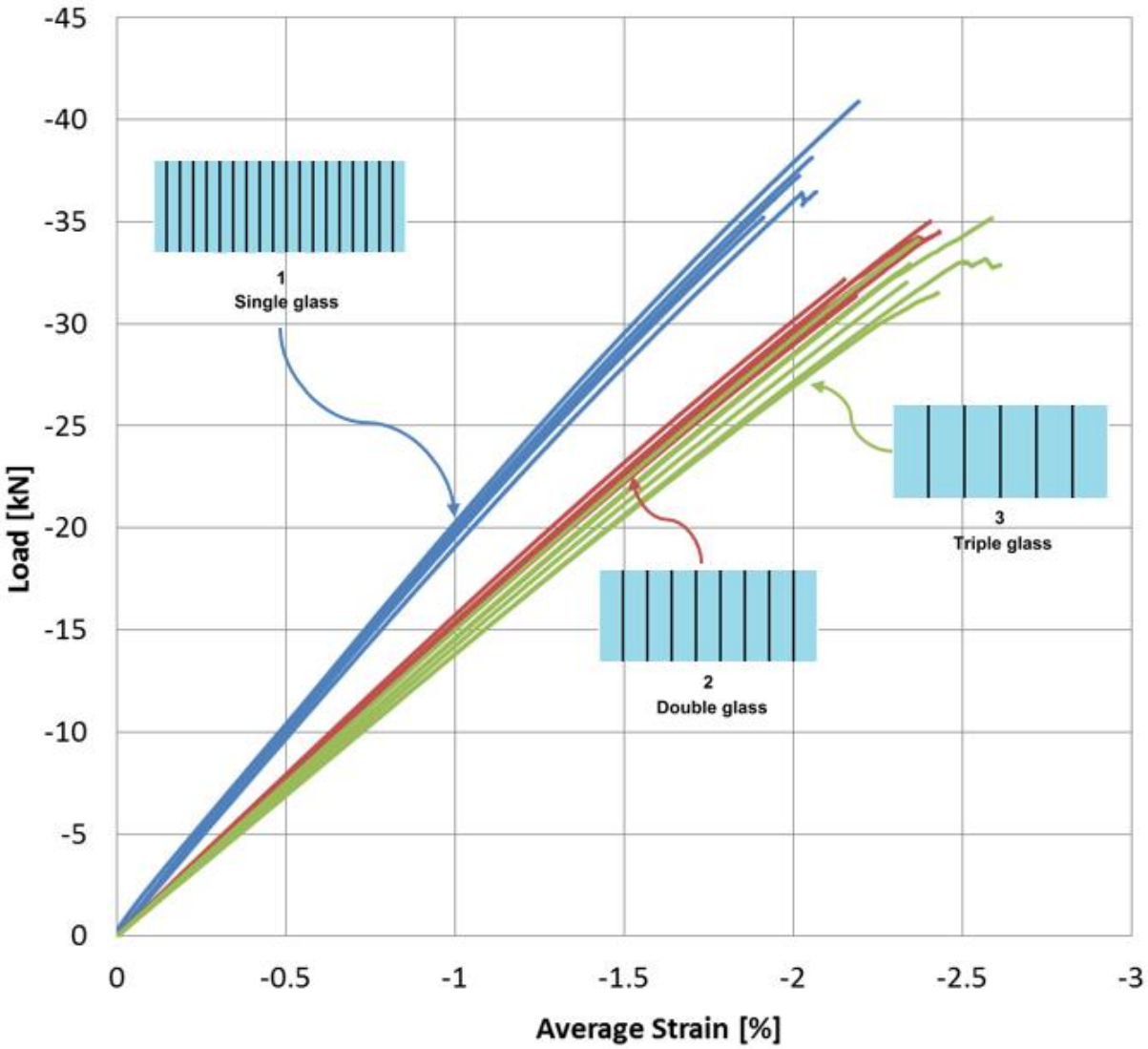

Figure 4-8: Results for three configurations tested in direct compression. The images corresponding to each configuration accurately reflect the relative thicknesses and number of plies with glass in teal and carbon in black. Notice the stiffness difference between the single glass (blue) and double or triple glass (red and green respectively) specimens.

The single glass case has a noticeably higher stiffness compared to double and triple glass due to increased thickness and higher carbon content. Also, there is an additional layer of glass compared to double and triple glass cases. There is a difference in average strain between the cases as shown in Table 4-5. The average compressive strain at failure in single glass case is $\varepsilon = -2.06\%$ which is higher than the manufacturer's value for tension at $\varepsilon = 1.90\%$. Similarly, the double and triple glass cases have average compressive strains of $\varepsilon = -2.31\%$ and $\varepsilon = -2.45\%$ respectively. The coefficient of variation is $< 5\%$ for all cases. On average, the stiffness of triple glass case is lower than that of double glass case. This is expected, as the double glass has 3 more carbon plies with the same number of glass plies. However, not all

double glass specimens have a higher stiffness than all triple glass specimens. This could simply be explained by material, manufacturing and testing uncertainties, but will be examined in more detail later. If double and triple glass cases were assumed to be a single dataset, the average strain would be $\varepsilon = -2.38\%$ with a coefficient of variation $CoV = 13.21\%$. Treating the test data as three distinct datasets is therefore more reasonable, as the variance is similar between the sets when done so.

Table 4-5: Strain at failure for the tested specimens

Sample №	Carbon Content [%]	Failure Strain		
		Sample [%]	Average [%]	CoV
1-01	19.2	-1.95	-2.03	4.52%
1-02		-1.91		
1-03		-2.07		
1-04		-2.19		
1-05		-2.06		
1-06		-2.02		
2-01	10.1	-2.41	-2.31	4.89%
2-02		-2.41		
2-03		-2.19		
2-04		-2.15		
2-05		-2.27		
2-06		-2.43		
3-01	6.5	-2.59	-2.45	4.61%
3-02		-2.61		
3-03		-2.34		
3-04		-2.37		
3-05		-2.34		
3-06		-2.43		

The failure modes can be described as:

1. Single glass specimens fail at the tab tip within the resin chamfer. There is a mix of brush type failure and clear break with a single failure surface. Three specimens are delaminated within the tab area after final failure with two showing total debonding of the tabs. There is no delamination observed prior to final failure.
2. Double glass specimens fail within the gauge section, close to the tip of the resin chamfer. Failure is brush type, keeping the two ends of a failed specimen together.

Slight delamination into the tab area is seen after the failure in two of the specimens but the tabs are kept in place. There is some delamination observed prior to final failure in the outermost plies.

3. Triple glass specimens fail in the same manner as double glass specimens with similar delamination observed in the outermost plies prior to final failure.

Figure 4-9 presents a side view of all specimens after testing.

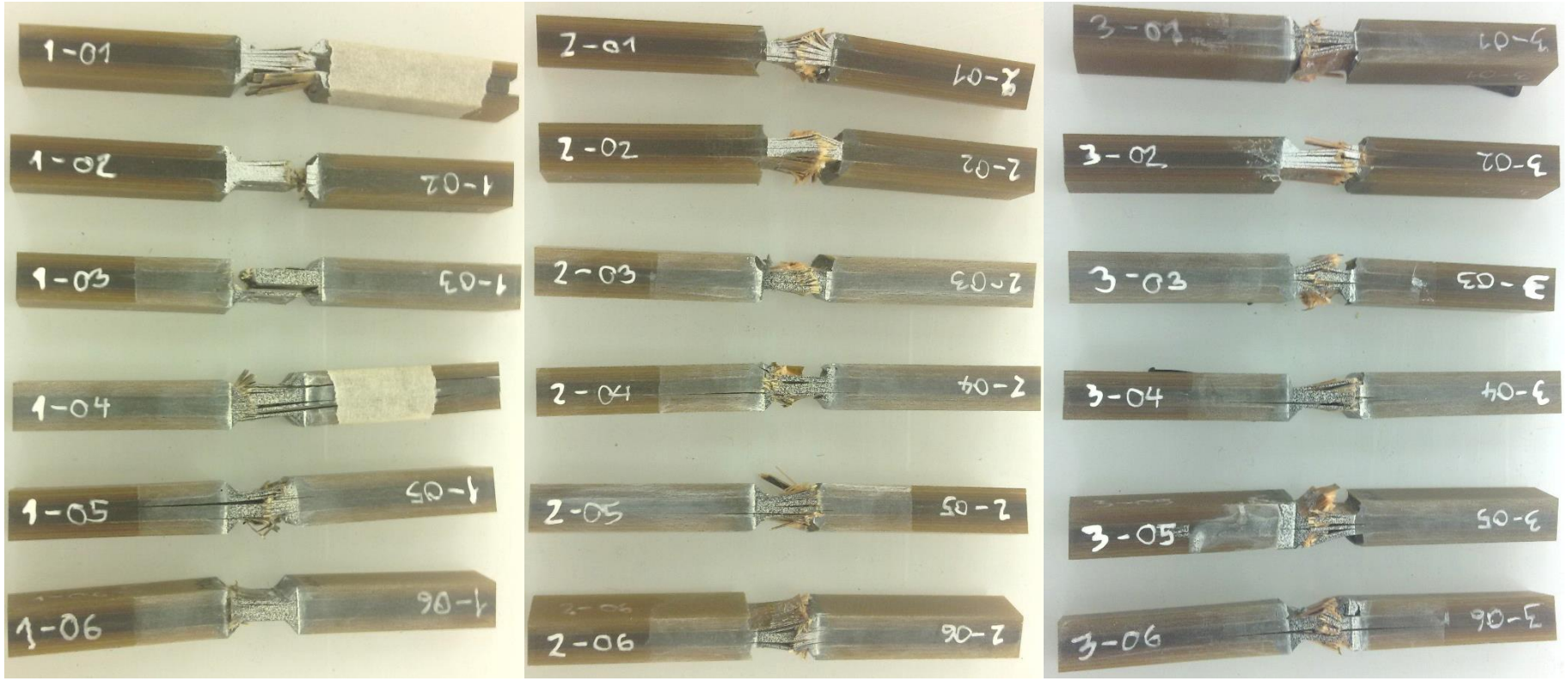

Figure 4-9: All direct compression specimens post-failure. Tape is used in 1-01 and 1-04 to keep delaminated tabs in place. The speckle pattern used for video gauge measurements is visible in the gauge area of the samples.

It can be seen that brush type damage is occurring in all double and triple glass specimens, but not in all single glass cases.

The failure modes expected from the DMM calculated earlier did not manifest. All samples failed in a brittle manner, with no fragmentation or delamination observed before failure. One explanation for this is that the energy release rate has a different value in compression. However, it could also be assumed that fragmentation does not occur in compression and that the failure is due to shear instability outlined in Chapter 3. This would confirm the assumption that the strain to failure in compression is determined by stiffness and misalignment rather than being a fibre property.

The single glass specimens all fail at or close to the tab region, suggesting a stress concentration being present in that area. In order to investigate the effects of the stress concentration, finite element modelling was employed.

4.4 Finite Element Analysis of Stress Concentration

The IC modified compression test requires tabs to be attached to the specimen. This is to prevent bearing failure at the end of the specimen by increasing the loaded area. Even though the specimens are machined to a high precision, it is difficult to achieve a uniform load at the end which leads to progressive crushing in the tabs are not present. Some load is transferred through shear by the sides of the specimen, but not enough to achieve gauge length failure without the tabs. The tabs have an inverse resin chamfer to help alleviate the stress concentrations. The thickness of the tabs should also be minimized to prevent shear lag effect [69], [70]. However, as can be seen from Figure 4-9 the tabs are of a thickness similar to that of the specimen and their thickness may contribute to a significant change in strain in tab termination area.

The direct compression specimen was modelled using standard analysis in ABAQUS FEA (version 2018) to investigate this effect. Figure 4-10 shows a typical test specimen.

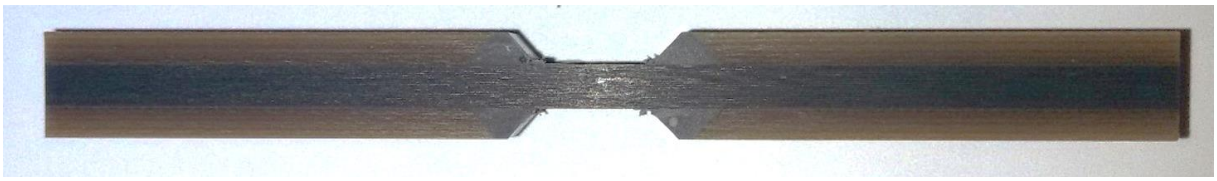

Figure 4-10: Side view of a typical direct compression specimen. Notice the glass fibre tab with an inverse chamfer and the resin block tapering to the gauge area.

It can be seen from Figure 4-10 that the specimen has two planes of symmetry – vertical and horizontal. These can be utilised to decrease the size of the FE model. A quarter model is used where the geometry of the top left quarter of the specimen is modelled, as shown in Figure 4-11. CPE4 elements were used, with the following considerations:

- The element is plane strain, meaning the strain out of plane is zero. As the specimen is relatively thick and well constrained, there is no expected deformation out of plane, making the element suitable.
- The elements are prone to shear locking, however the bending in the sample is assumed to be minimal due to constraints and loading and thus the elements are deemed well suited for measuring high axial and shear response of the material. High mesh density further alleviates the concern.

Orthotropic material properties were used for all materials except for the resin which was assumed to be isotropic. Properties of the constituent materials are approximated based on the manufacturer's datasheets except for the case of the tab material where the properties were approximated for the cross-ply layup based on the properties of the unidirectional E-glass material. The properties are shown in Table 4-6.

Table 4-6: Input values for FE (stiffness in MPa)

Material	E1	E2	E3	v12	v13	v23	G12	G13	G23
Carbon	145e3	8.8e3	8.8e3	0.3	0.35	0.45	4.5e3	4.5e3	2.37e3
Glass	47e3	13e3	13e3	0.31	0.35	0.42	4e3	4e3	2.6e3
Tab	20e3	20e3	11e3	0.12	0.12	0.4	4e3	4e3	2.6e3
Resin	3e3			0.4					

Units of N and mm were assumed for the modelling, thus the values of Young's modulus and shear modulus shown in Table 4-6 are in MPa, with Poisson's ratio being dimensionless.

4.4.1 Model Definition

As the tabbed area of the specimen is held within a steel block which prevents expansion due to Poisson's effects as the compressive force is applied, there will be a degree of friction present between the block and the tab surface in addition to the contact force at the ends. Therefore, two models were created:

1. Displacement is applied at the end of the specimen only and the tab is allowed to freely contract in the loading direction as shown in Case 1 in Figure 4-11. This assumes no friction between the tab and the steel block.
2. Displacement is applied at the end of the specimen and along tab surface as shown in Case 2 in Figure 4-11. This assumes high friction between the tab and the steel block where the tab does not contract at all as the compressive force is applied.

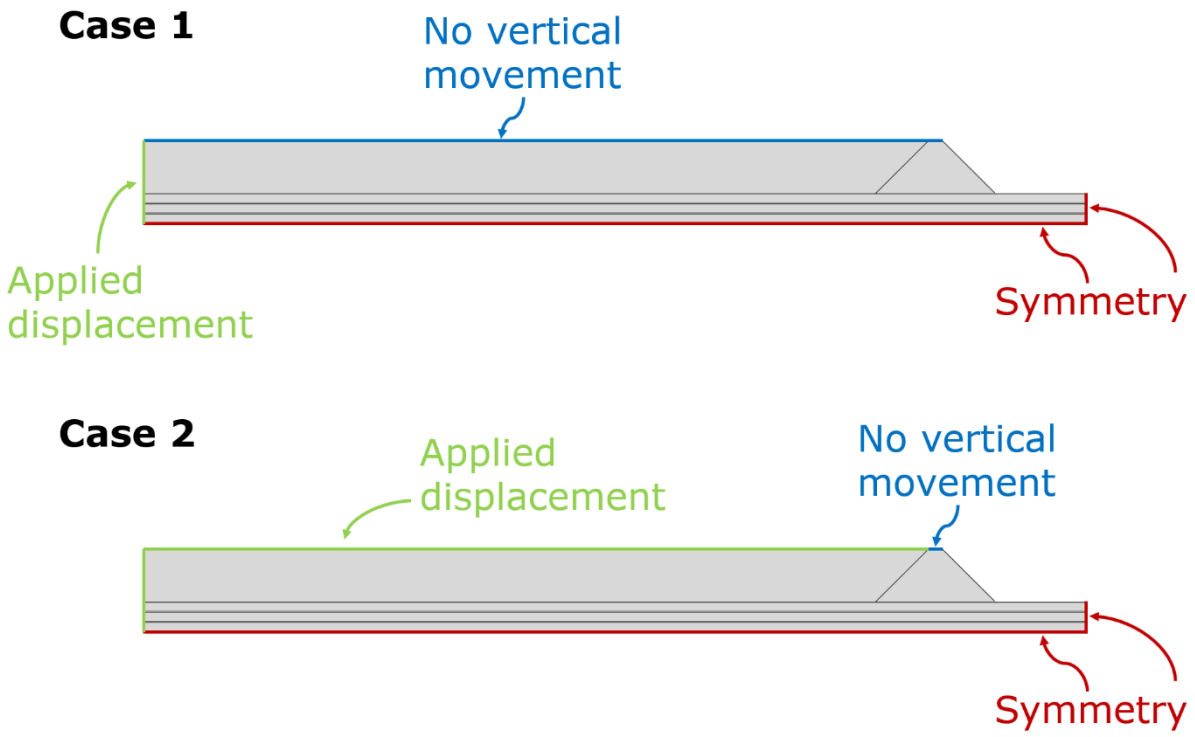

Figure 4-11: Two cases investigated using finite element analysis. The displacement is applied in the horizontal direction towards the vertical symmetry line.

Models were created using the measured geometry of the specimens except for ply thicknesses of carbon and glass which were taken as nominal values from manufacturer's datasheets. Mesh convergence study was conducted up to 10 elements through the thickness of the carbon and revealed that 3 elements were sufficient. No mesh optimisation was conducted beyond that as the models computed within several minutes. Results for Case 1 of

a single glass specimen are shown in Figure 4-12. Strain in the fibre direction is presented with a step size resulting in strain of $\varepsilon = 2.00\%$ in the rightmost surface element of the gauge section. The colour coding was adjusted to show a wide range of strains between 0% and 4%. Probing the strain in the outermost glass ply reveals a maximum strain of $\varepsilon_G = 2.80\%$ which is 40% higher than the strain on the surface in the middle of the specimen. The stress concentration at the tip of the resin chamfer is therefore significant and must be taken into account. The maximum strain in the outermost carbon ply is $\varepsilon_C = 2.21\%$, which is 10% higher than would be suggested from the strain gauge readings.

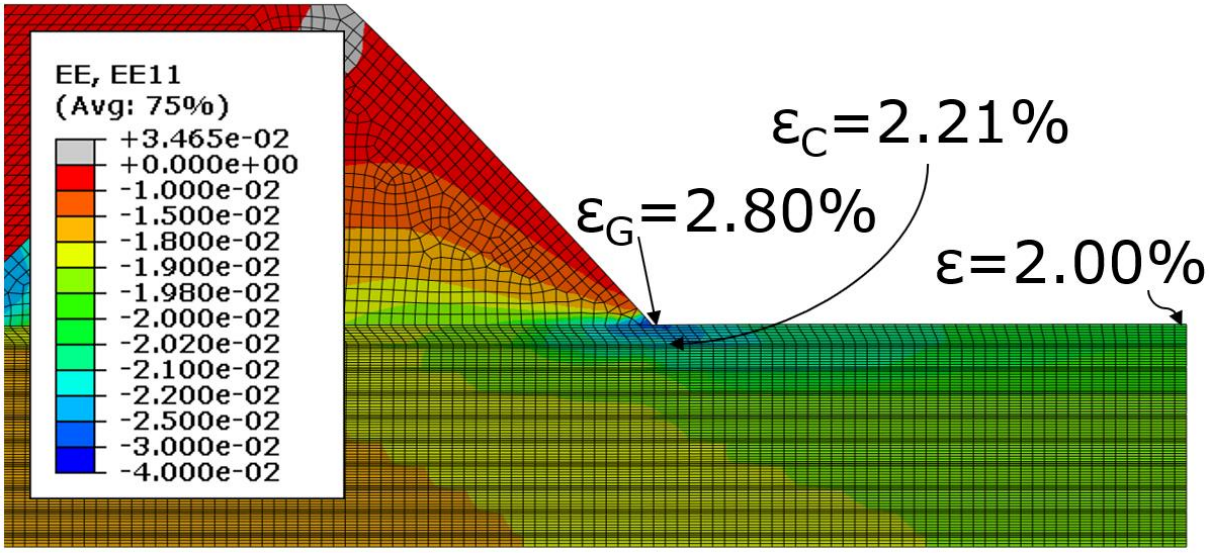

Figure 4-12: Results for Case 1 in single glass specimen at step size resulting in $\varepsilon = 2.00\%$ on the surface in the middle of the specimen. The significantly higher strains in both the carbon and the glass underneath the resin chamfer are a result of a stress concentration in that region.

It can be seen that the stress concentration caused by the resin chamfer causes a high strain in both the glass and the carbon. Figure 4-12 also suggests that the stress concentration effect decreases towards the middle of the specimen and would thus be critical in the outermost glass and carbon plies only. The stress concentration will have a less significant effect in the double and triple glass specimens due to increased glass thickness on the surface allowing for the concentration to dissipate to some extent, practically shielding the carbon ply from it.

Similar investigation can be performed for Case 2, revealing an even bigger increase in strain as compared to the probing point on the surface in the middle of the specimen. This is shown in Figure 4-13 and reveals a 53% higher strain in the glass at $\varepsilon_G = 3.11\%$ and 15% higher strain in the carbon at $\varepsilon_C = 2.33\%$ with the baseline of $\varepsilon = 2.03\%$.

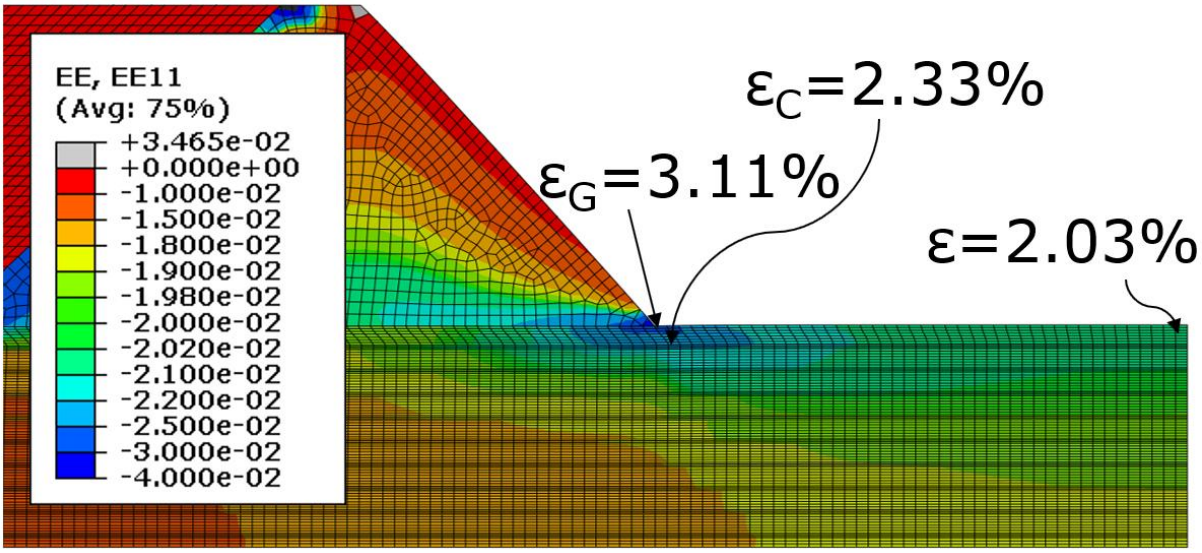

Figure 4-13: Results for Case 2 in single glass specimen at step size resulting in $\varepsilon = 2.03\%$ on the surface in the middle of the specimen. The effect with high friction between the tab surface and the steel block is more significant.

The case with high friction causes a more severe stress concentration as the shear lag effect of the tab stress being transferred into the gauge section is increased due to tab displacement being equal to end displacement. In the case with no friction the tab displacement is forced at the end only and some relaxation occurs closer to the gauge section.

Strain is averaged over the length of $3.15\ mm$ from the symmetry line. This is due to the strain gauge foil having a length of $6.30\ mm$. As the sample is compressed, the foil will deform at the same rate which will output into the strain reader.

4.4.2 Results

The displacement step can be adjusted in both models to produce strain in the middle of gauge section surface equal to that measured during the testing. This allows for finding the equivalent maximum carbon strain at failure for each of the specimens. Corresponding models can be run for double and triple glass geometries in a similar fashion for all samples as shown in Table 4-7.

Table 4-7: Strain at failure for the tested specimens

Sample №	Carbon Content [%]	Measured Strain		Case 1		Case 2	
		Sample [%]	Average (CoV)	Sample [%]	Average (CoV)	Sample [%]	Average (CoV)
1-01	19.2	-1.95	-2.03 (4.52%)	-2.12	-2.22 (4.54%)	-2.22	-2.31 (4.42%)
1-02		-1.91		-2.08		-2.17	
1-03		-2.07		-2.26		-2.35	
1-04		-2.19		-2.39		-2.49	
1-05		-2.06		-2.24		-2.34	
1-06		-2.02		-2.2		-2.3	
2-01	10.1	-2.41	-2.31 (4.89%)	-2.45	-2.35 (4.86%)	-2.48	-2.38 (5.34%)
2-02		-2.41		-2.45		-2.48	
2-03		-2.19		-2.23		-2.25	
2-04		-2.15		-2.19		-2.21	
2-05		-2.27		-2.31		-2.33	
2-06		-2.43		-2.48		-2.55	
3-01	6.5	-2.59	-2.45 (4.61%)	-2.63	-2.49 (4.53%)	-2.63	-2.49 (4.53%)
3-02		-2.61		-2.65		-2.65	
3-03		-2.34		-2.38		-2.38	
3-04		-2.37		-2.41		-2.41	
3-05		-2.34		-2.38		-2.38	
3-06		-2.43		-2.47		-2.47	

Case 1 strains are on average lower in single glass when compared to double glass which in turn has lower strains than triple glass. The effects of stress concentration cause an increase of the strain for all three specimen types. The most significant increase is observed for single glass and the least significant for triple glass. This is due to the stress concentration dissipating through the increasing glass thickness before affecting the outermost carbon layer.

Case 2 exhibits similar behaviour, but with a higher strain increase except for triple glass where the strain is the same as Case 1. Overall, the strains between the three specimen types are brought closer together for both modelling cases, but not to the same value. As there is a difference in the carbon volume for the single, double and triple glass, it is expected that the failure strain be different. This is explained by the model presented in Chapter 3, whereby decreasing the carbon content of a hybrid composite yields higher strains to failure at similar misalignment values.

Two effects are therefore present at the same time:

1. The stress concentration at the tab tip causing the failure strain in carbon to be higher than is measured with the strain gauge
2. Hybrid effect in compression where strain increases with a higher proportion of glass in the composite

The effect of stress concentrations can be explained by finite element modelling, but the exact values of strain in carbon at failure are difficult to obtain due to small changes of geometry and material properties being assumed in the model. The explanation outlined previously is therefore mostly qualitative.

4.5 Shear Instability Modelling

The samples can be modelled using the shear instability model presented in Chapter 3. The shear data is presented in Figure 6-20 in a subsequent chapter. The constituent materials were tested for longitudinal stiffness and tensile strain, the results for which are presented in Table 6-16.

Shear instability model can provide further insight into the test results. Using the available data produces three instability surfaces which are presented in Figure 4-14.

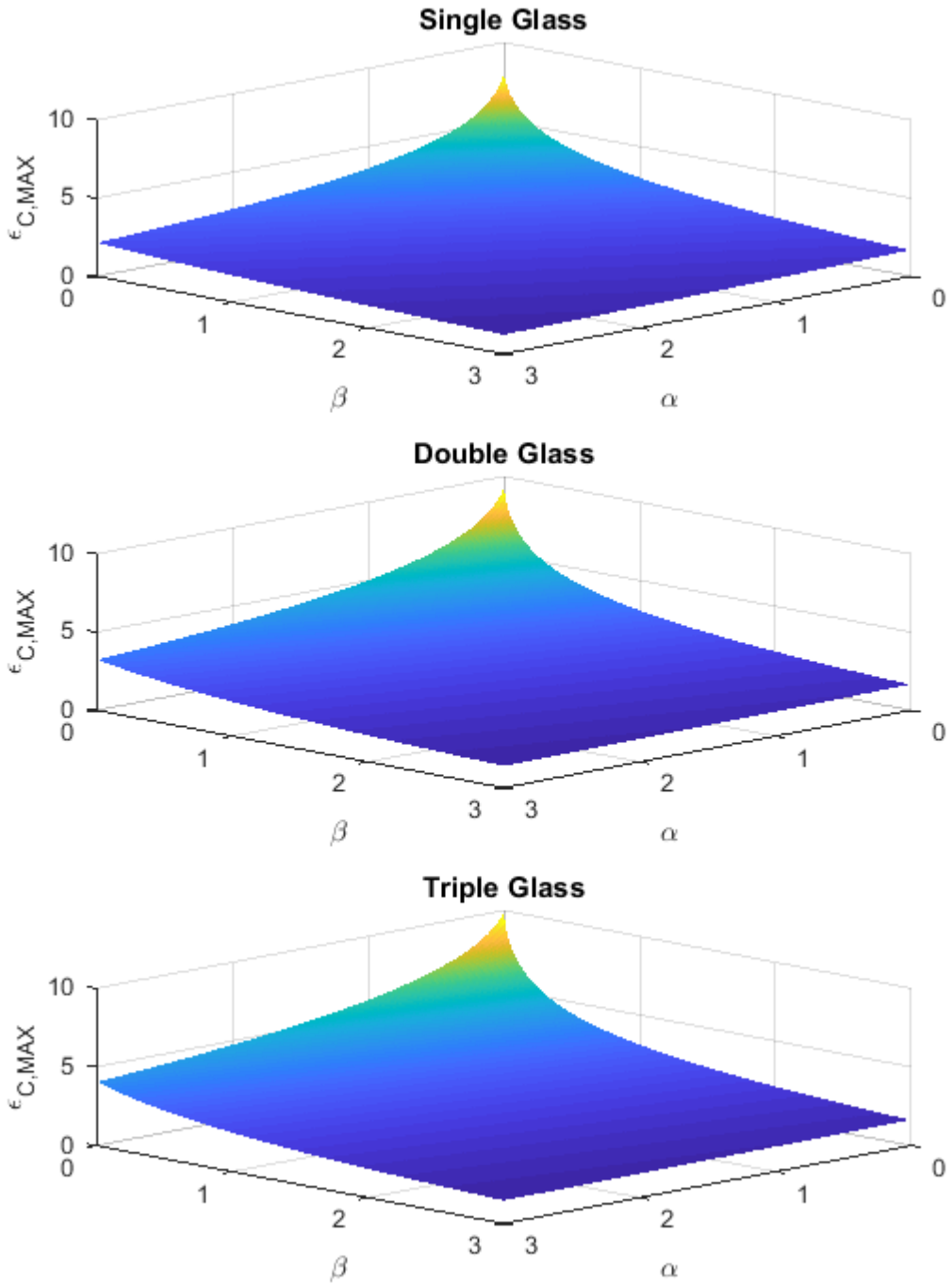

Figure 4-14: Three shear instability surfaces generated for the tested samples. Note that the single glass case has the lowest peak strain due to the highest carbon volume.

4.5.1 Fibre Misalignment Measurement

Obtaining the shear instability surfaces is useful but any point on the surface could correspond to the tested sample if the misalignment of the fibres is not known. The samples can be

investigated post-failure to measure the fibre misalignment [71]. The procedure for the samples used would be as follows:

1. Cut off approximately $30\ mm$ of the tabbed area of the sample where there is no damage
2. Embed the sample into a resin block
3. Grind the resin block at a desired angle to cut a surface through the tabbed area
4. Polish the sample
5. Obtain micrographs of exposed fibres cut at a desired angle
6. Inscribe the oval fibre shapes with ellipses
7. Calculate the length to width ratio of each ellipse
8. Determine fibre angle relative to the surface from equation $\alpha = \sin^{-1}\left(\frac{w}{L}\right)$
9. Assume the fibre angles follow a normal distribution and calculate the parameters of the curve
10. Plot the normal distribution of measured fibre angles

It can be seen that the process for obtaining the fibre misalignment has multiple steps that require time and precision. As such, it is not practical to be performed for every sample. However, one of the samples (namely 1-04) was tested for misalignment. The desired cutting and polishing angle was $5\ °$. A micrograph of the polished surface with inscribed ellipses is shown in Figure 4-15.

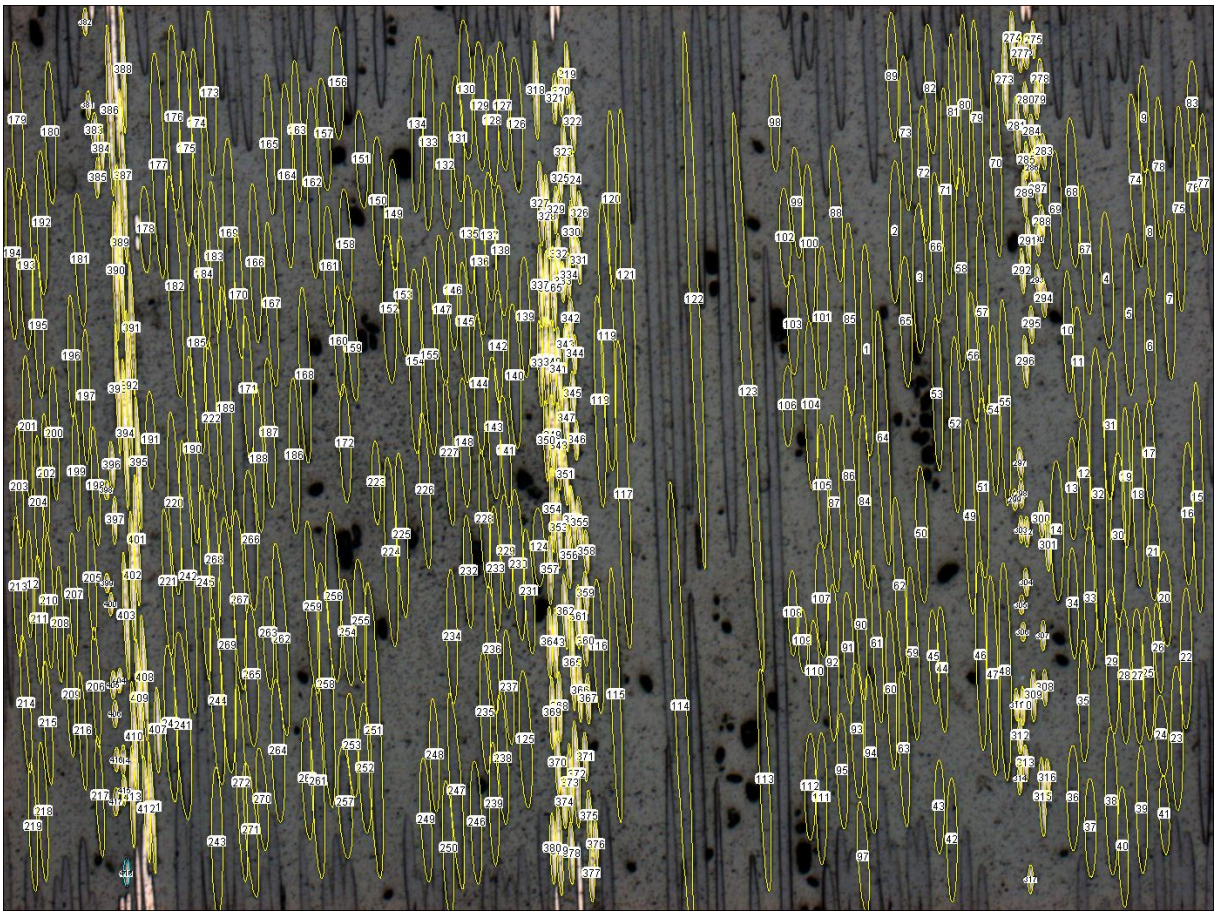

Figure 4-15: Ground and polished surface of sample 1-04 with ellipses manually inscribed onto the fibres.

The visible area is covered with ellipses. Their widths and lengths can then be imported into a database and processed. The fibres can be processed using the actual width of the drawn ellipse (which will attract some error as the drawn distance is relatively small on the screen) or the mean width for the fibre type (which is the same for all fibres in theory). Table 4-8 shows the results of statistical analysis of the fibre data.

Table 4-8: The calculated parameters of the misalignment distribution.

Fibre	Count	As Drawn		Constant Diameter	
		Mean [°]	SD	Mean [°]	SD
Glass	272	4.94	1.11	5.06	1.36
Carbon	146	7.22	3.43	7.36	3.66

Figure 4-16 shows the graphical representation of the measured misalignment.

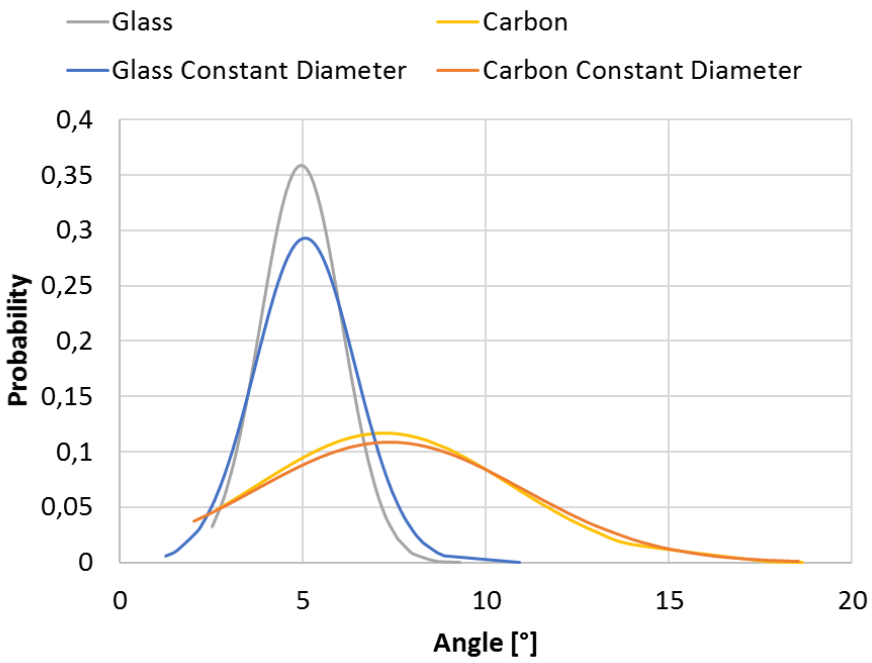

Figure 4-16: The normal distribution curves for the fibre misalignment in sample 1-04.

It should be noted that the curve to carbon misalignment is highly asymmetric. This suggests that there are fibres that have a misalignment higher than the assumed 5 °. In order to correct that, the sample would have to go trough the grinding, polishing and microscopy process again.

Instead, the obtained data was used to input into the SI model. As the surface is cut at 5 °, the peaks of the curves must be shifted accordingly, thus becoming -0.06 ° for glass and 2.22 ° for carbon. The mean value of the misalignment, however, does not ascertain that there are no misaligned fibres. It just means that the fibres are misaligned equally in all directions. The carbon fibre in this case has a definite direction – its peak is shifted.

4.5.2 Results

As it is difficult to relate the fibre distribution to the misalignment angle to be used in the model, the values of standard deviation are used. Ideally, every sample would be measured for fibre misalignment, but the same value of misalignment for carbon and glass shown in Figure 4-16 is used for all samples. SI surfaces can be sliced at a constant glass misalignment $\beta = 1.11$ ° and plotted on a 2D graph, as shown in Figure 4-17.

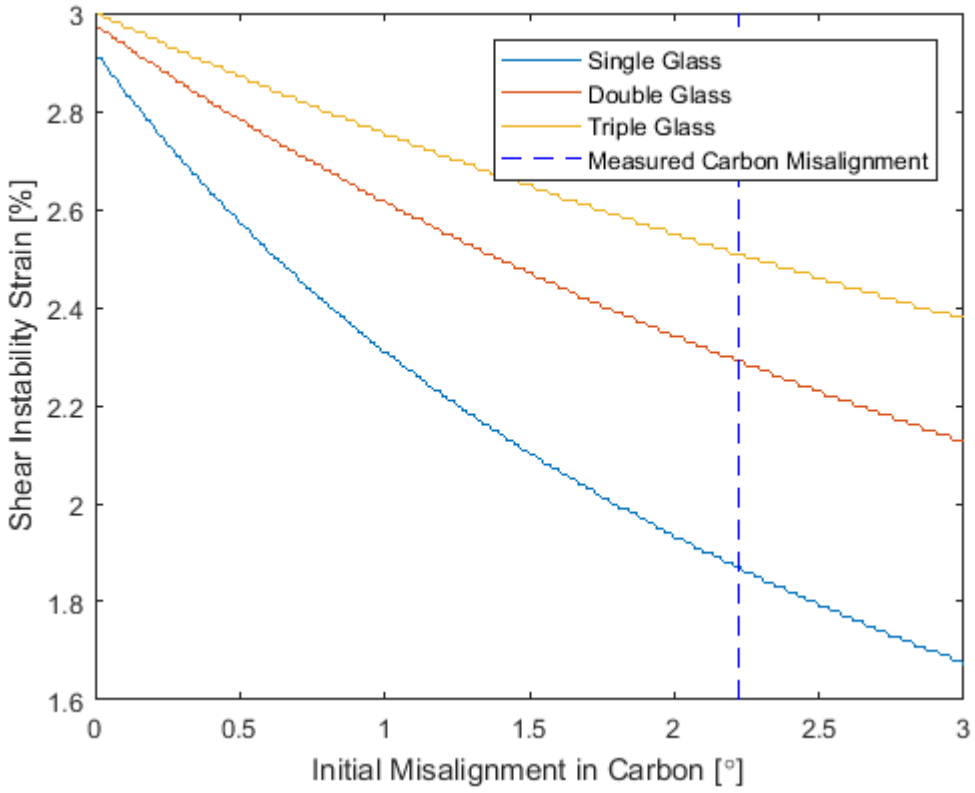

Figure 4-17: Results of SI modelling sliced at $\beta = 1.11$ °. Note the large drop in instability strain between double and single glass case.

The values obtained from the model at carbon misalignment of $\alpha = 2.22$ ° are as follows:

1. Single glass $\varepsilon_{C,MAX} = 1.87\%$
2. Double glass $\varepsilon_{C,MAX} = 2.29\%$
3. Triple glass $\varepsilon_{C,MAX} = 2.51\%$

Compared with average measured strain in Table 4-7, the values show a difference of 7.88%, 0.87% and 2.45% for single, double and triple glass respectively. This is fairly accurate, but does not explain the FE results indicating that the strains at failure are higher for single and double glass due to stress concentration.

4.6 Summary

Three hybrid lay-ups were designed using the DMM tool to investigate the effects of hybridization on compressive failure. The samples were tested using an ICSTM compression fixture with double-chamfered tabs.

The results suggested large changes in strain to failure with a moderate variation of carbon volume:

1. $\varepsilon_{C,MAX} = -2.03\%$ for carbon volume of 19.2%
2. $\varepsilon_{C,MAX} = -2.31\%$ for carbon volume of 10.1%
3. $\varepsilon_{C,MAX} = -2.45\%$ for carbon volume of 6.5%

Due to the significant thickness of the tab material, a finite element model was created to investigate the effects of shear lag. It was found that the strains in carbon plies are significantly larger than the strains in the gauge area. Corrected strains were extracted from the FE model to find that the hybrid effect was still present and carbon strain to failure increased with the glass/carbon volume ratio, although not as significantly as was indicated by the surface strain readings.

Shear instability model was utilised to predict the strains to failure of hybrid samples at a given misalignment. The normal distribution of fibre alignment was contructed from measured fibre angles for one specimen only and the standard deviation of the results was taken as the misalignment value for glass and carbon. The results were within several percent of the measured values.

5 Compression Testing of Composite Materials

Tensile strain to failure of a composite is largely a fibre property and will not change significantly for different material with the same fibre type. Therefore, knowing the fibre type provides the user with sufficient information to estimate the maximum strain of a unidirectional composite. For most practical cases, the strength can also be estimated based on the fibre volume fraction and fibre Young's modulus. As the stiffness of the fibre is normally significantly larger than the stiffness of the resin, the predicted failure stress can be estimated closely - even if the contribution of the matrix is assumed to be negligible.

As shown in Chapter 3, the strain to failure of a carbon fibre composite in compression is a function of its fibre misalignment, in-plane stiffness and shear stiffness. Therefore, predicting the compressive strain to failure of a carbon fibre composite requires the knowledge of those three parameters and the fibre type is not of primary importance. The prediction of stress becomes even more complex due to expected non-linearity (softening) as the composite is compressed.

5.1 Requirements of a Practical Test Method

The direct compression (DC) testing presented in section 4 yielded high strain results, but is not the preferred compression test method to be used [1]. The following characteristics of the test make it non-ideal [1], [70], [72], [73]:

1. The samples require precise machining (up to 0.2 mm) and can not be cut using a more standard equipment like a diamond saw.
2. Samples require bonding of tabs.
3. The gauge area of the samples is limited for instrumentation.
4. Weight of the rig exceeds 20 kg and it must be removed from the test setup after every test to load and unload samples.
5. The steel blocks can only accommodate a handful of sizes and have to be specially manufactured for non-standard specimens.
6. Ingress of dirt, sample pieces into the loading slots may result in stress concentration and premature failure.

More generally, a practical test method would fulfill the following practical criteria:

1. Allowables for specimen geometry – these will determine the required machining. The more strict the tolerances the more complex tools to be used which makes the specimen preparation both lengthy and costly.
2. Sensitivity of the test setup to misalignment – example of machine grips being twisted or translated relative to the assumed position. Would a small change have a significant influence on the failure strength of the sample?
3. Ease of setup and testing – modified ASTM test rig [1] weighs in excess of 20 kg. After each test it must be taken out of the machine, dismantled and cleaned of debris.
4. Scalability and volume of material that can be tested – ideally there should be no limitation as to the minimum and maximum width and thickness of the material.
5. Versatility – the test should not require a dedicated rig to be manufactured or should keep the manufactured bits as simple as possible to allow testing on a range of standard hydraulic and electromechanical machines.

Few available test methods fulfill these requirements. Any method that relies on direct compression is likely to involve either a guide system to keep the sample aligned [1], [74] or a plane of reduced cross-sectional area to be created.

Czél [75] has presented a method of indirect compression testing of glass/carbon hybrids by four-point bending. Glass fibre composite substrate is used to support the thin hybrid specimen which is being compressed indirectly by being located at the top of bent specimen. It is a variation of a standard four-point bending (4PB) test [34].

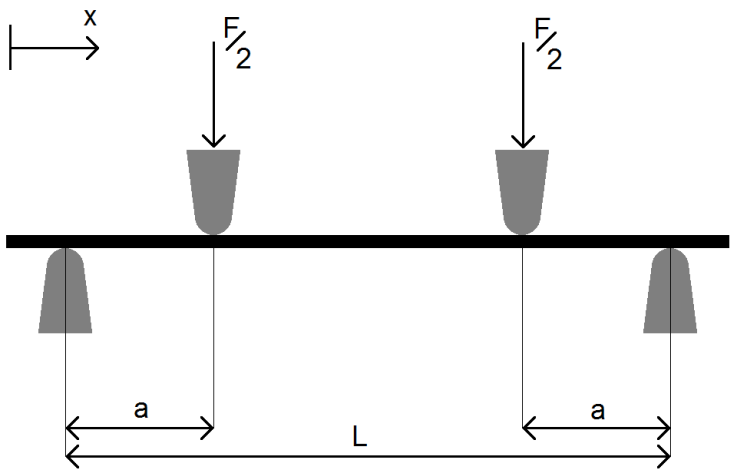

Figure 5-1: A four-point bending (4PB) setup with generic dimensions. Note that the symmetry ensures a constant bending moment and curvature inside of the middle spans.

Another important consideration is the ratio of thickness of the specimen to the distance between internal supports. In general:

$$\frac{t_{tot}}{L-2a} < \frac{1}{10} \tag{5.1}$$

However, fibre-reinforced composites tend to not dissipate edge effects as well as isotropic materials do [36], [76], therefore the length to thickness ratio would ideally be increased further.

5.2 Four-point Bending (4PB) Test

5.2.1 Predicting the Sample Response in 4PB Test

Consider a beam with a hybrid cross-section shown in Figure 5-2. There are three different materials that the section consists of:

1. Top layer with stiffness $E_{g,top}$ and thickness $t_{g,top}$
2. Middle layer with stiffness E_c and thickness t_c
3. Bottom layer with stiffness $E_{g,bot}$ and thickness $t_{g,bot}$

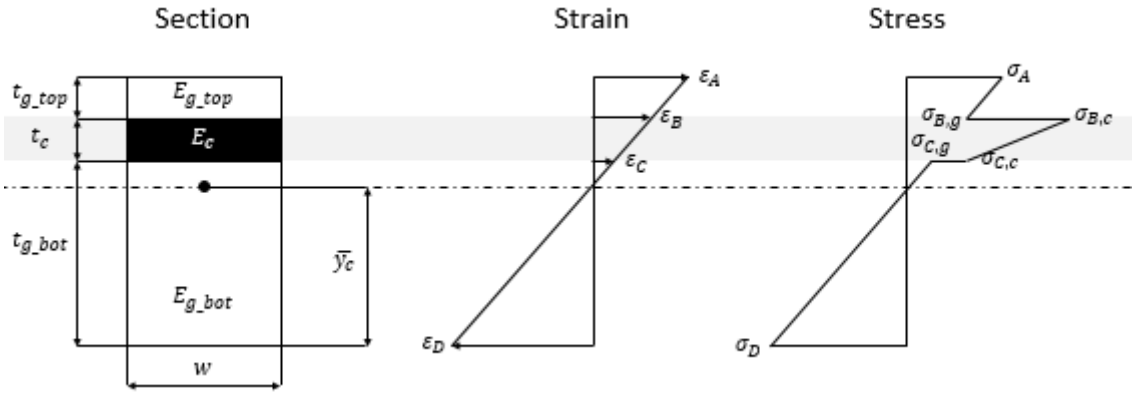

Figure 5-2: Cross-section of the beam used in the test development, the strain in the section and the corresponding stress. Note that there are two different stresses corresponding to each of the strains ε_B and ε_C.

The position of section centroid $\bar{y_c}$ is defined as:

$$\bar{y_c} = \frac{E_{g,bot} * t_{g,bot} * \frac{t_{g,bot}}{2} + E_c * t_c * \left(t_{g,bot} + \frac{t_c}{2}\right) + E_{g,top} * t_{g,top} * \left(t_{g,bot} + t_c + \frac{t_{g,top}}{2}\right)}{E_{g,bot} * t_{g,bot} + E_c * t_c + E_{g,top} * t_{g,top}} \tag{5.2}$$

Which can be calculated for any combination of thickness and stiffness of the three constituent materials. The strains ε_A, ε_C and ε_D can be defined as functions of the strain ε_B as:

$$\varepsilon_A = \varepsilon_B \frac{t_{g,bot} + t_c + t_{g,top} - \bar{y_c}}{t_{g,bot} + t_c - \bar{y_c}} \tag{5.3}$$

$$\varepsilon_C = \varepsilon_B \frac{t_{g,bot} - \bar{y_c}}{t_{g,bot} + t_c - \bar{y_c}} \tag{5.4}$$

$$\varepsilon_D = \varepsilon_B \frac{-\bar{y_c}}{t_{g,bot} + t_c - \bar{y_c}} \tag{5.5}$$

And the stresses corresponding to the strains are:

$$\sigma_A = \varepsilon_A E_{g,top} \tag{5.6}$$

$$\sigma_{B,g} = \varepsilon_B E_{g,top} \tag{5.7}$$

$$\sigma_{B,c} = \varepsilon_B E_c \tag{5.8}$$

$$\sigma_{C,g} = \varepsilon_C E_{g,bot} \tag{5.9}$$

$$\sigma_{C,c} = \varepsilon_C E_c \tag{5.10}$$

$$\sigma_D = \varepsilon_D E_{g,bot} \tag{5.11}$$

The moment carried by the section can then be calculated as a sum of forces around the centroid. Numerically, it requires finding the centroids of every block in the stress diagram and multiplying the area of the block by the distance from the centroid and width of the sample. In symbolic form this becomes:

$$M = w \int \sigma t (y - \bar{y_c}) dy \tag{5.12}$$

The tensile and compressive forces should be equal:

$$w \sum \sigma t = 0 \tag{5.13}$$

For a sample in four-point bending depicted in Figure 5-1 the bending moment in the middle section is calculated as:

$$M = \frac{Fa}{2} \tag{5.14}$$

Therefore, the force can be back calculated from the bending moment in the sample:

$$F = \frac{2M}{a} \tag{5.15}$$

Where a is the distance between the external and internal loading noses. The simulation of 4PB test of a hybrid sample using the above equations can be performed as follows:

1. Define thicknesses $t_{g,bot}$, t_c, $t_{g,top}$ using the ply thickness and number of plies in each block
2. Define the Young's modulus of each block and calculate the centroid position $\overline{y_C}$
3. Assume the maximum strain in carbon ε_B
4. Calculate the strains ε_A, ε_C, ε_D to define the strain profile of the section
5. Calculate the stresses σ_A, $\sigma_{B,g}$, $\sigma_{B,c}$, $\sigma_{C,g}$, $\sigma_{C,c}$, σ_D from the obtained strain
6. Integrate the moments around the centroid to obtain bending moment in the sample M
7. Calculate the force F required to induce the moment M in the specific 4PB setup
8. Change the assumed value of strain ε_B and repeat steps 3 to 8 until desired range of strain is achieved

The process presented above can be used to predict the behaviour of 4PB sample. However, the equations only allow for prediction of load-strain response for the assumed geometry. In order to use the equations in a design tool for 4PB samples, additional functionality must be added.

One of the common failure modes of hybrid specimens with thick glass and carbon blocks is delamination [77]. For maximum interlaminar shear strength of τ_{MAX}, the delamination load in a rectangular section can be calculated as:

$$F_{MAX,DEL} = \frac{2\tau_{MAX}}{3wt_{TOT}} = \frac{2\tau_{MAX}}{3w\left(t_{g,bot} + t_c + t_{g,top}\right)} \tag{5.16}$$

In reality, the shear flow will be impacted by the varying stiffness of the three materials that the section consists of, but the above equation is a good first approximation to predict delamination. The delamination force must only be calculated once for the sample and defines a cut-off load beyond which the sample is expected to fail in this mode.

Non-linearity can also be introduced into the model by relating the Young's modulus of the material to strain. It can be assumed that only the middle beam will behave in a non-linear manner, as it represents the carbon block within the sample (the other two being glass).

It becomes easier to define strain profile using the average strain in carbon rather than maximum strain that has been used up to this point. To do that, a new value of strain $\varepsilon_{c,AVG}$ must be introduced in the middle of the carbon block and other strains ε_A, ε_B, ε_C, ε_D redefined

in its terms in step 4. Steps 2 and 3 shown in the above process are inverted, as the strain in carbon must be defined first before its modulus can be known.

The modulus of the carbon in step 2 (now step 3) can be calculated as:

$$E_{c,NL} = E_c(1 + \gamma\varepsilon_{c,AVG}) \tag{5.17}$$

Where γ is a constant defining non-linear behaviour of the material [49]. It is positive for a material that softens in compression.

The non-linear prediction requires iteration through steps 2 to 8 as the modulus of carbon is calculated at every assumed strain. A calculation for parameters shown in Table 5-1 is performed. The properties come from a real material that was investigated in Chapter 6. The 4PB samples were designed for the investigation using the tool presented here.

Table 5-1: Parameters for the model predicting the behaviour of nSi material in 4PB

$t_{g,bot}$ [mm]	t_c [mm]	$t_{g,top}$ [mm]	w [mm]	$E_{g,bot}$ [GPa]	E_c [GPa]	$E_{g,top}$ [GPa]	τ_{MAX} [MPa]	γ [GPa]
2.170	0.148	0.155	10	45.7	168.9	45.7	70	3948.9

Steps 1 to 8 outlined above are performed for the properties listed. The calculation is automated within a spreadsheet that has been tested for all 4PB samples within this work. The assumed loading nose distance is $a = 20\,mm$. The calculated force required to induce the assumed deformation can be plotted against maximum carbon strain ε_B and maximum glass strain ε_D, as shown in Figure 5-3. The horizontal line depicting the expected delamination load is also shown. Both the linear and non-linear case are shown on the same graph, non-linear case simply assuming $\gamma = 0$.

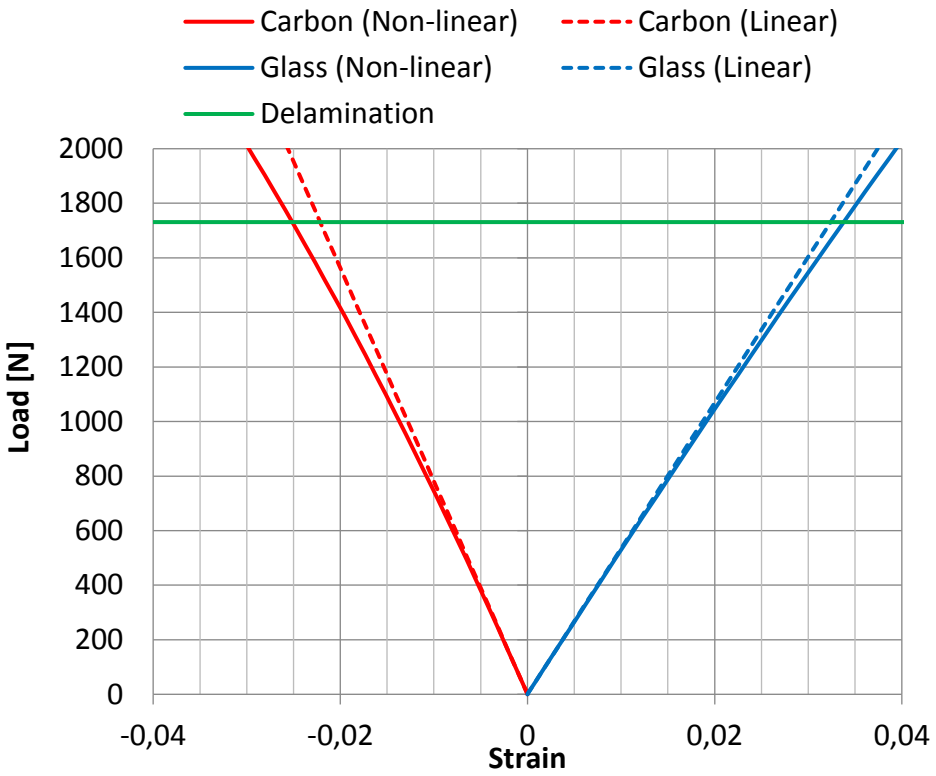

Figure 5-3: The predicted load-strain response for the 4PB sample defined in Table 5-1.

The strain in carbon is negative, indicating compression. The positive tensile strain in glass has a greater magnitude than the carbon strain due to the neutral axis being shifted up towards the carbon. The delamination load is a singular value for the sample, independent from strain in individual materials. Whether there is an interaction between material longitudinal strain and delamination or whether the 4PB loading impacts the delamination behaviour is not investigated in further detail.

Note that the non-linearity of carbon causes a drop in total apparent stiffness, as both the glass and carbon strain are higher at the same load for the non-linear case as compared to the linear. This softening behaviour will be present in all bending results presented here, however it is not only caused by the material non-linearity as will be discussed in the subsequent section.

5.2.2 Geometric Effects in 4PB Testing

4PB test can result in apparent softening of the tested samples if the deflections become high. This is due to non-linear geometry which does not keep the bending moment in the sample linear with the applied load. A correction will be derived to apply in high displacement cases and where accuracy of the load is of importance (in some cases the strains are enough).

Consider the beam depicted in Figure 5-1. A generic shape of a bending moment diagram for such beam is shown in Figure 5-4.

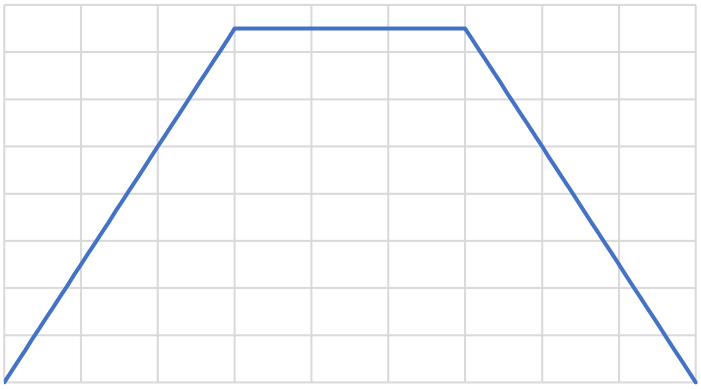

Figure 5-4: A generic bending moment diagram shape for the 4PB sample.

The moment can be defined with the following equations:

$$M(x) = \begin{cases} \frac{Fx}{2}, & 0 \le x \le a \\ \frac{Fa}{2}, & a \le x \le L-a \\ \frac{FL}{2} - \frac{Fx}{2}, & L-a \le x \le L \end{cases} \tag{5.18}$$

These can be divided by the beam stiffness to obtain the curvature:

$$\mathrm{K}(x) = \frac{F}{EI} \begin{cases} \frac{x}{2}, & 0 \le x \le a \\ \frac{a}{2}, & a \le x \le L-a \\ \frac{L}{2} - \frac{x}{2}, & L-a \le x \le L \end{cases} \tag{5.19}$$

Integrating and applying boundary conditions yields the slope:

$$v(x) = \frac{F}{EI} \begin{cases} \frac{x^2}{4} + \frac{a^2}{4} - \frac{aL}{4}, & 0 \le x \le a \\ \frac{ax}{2} - \frac{aL}{4}, & a \le x \le L-a \\ \frac{Lx}{2} - \frac{x^2}{4} + \frac{aL}{4} - \frac{a^2}{4} - \frac{L^2}{4}, & L-a \le x \le L \end{cases} \tag{5.20}$$

Integrating once again and applying boundary conditions results in general deflection equations:

$$\Delta(x) = \frac{F}{EI}\begin{cases} \frac{x^3}{12} + \frac{a^2x}{4} - \frac{aLx}{4}, & 0 \le x \le a \\ \frac{ax^2}{4} - \frac{aLx}{4} + \frac{a^3}{12}, & a \le x \le L-a \\ \frac{Lx^2}{4} - \frac{x^3}{12} + \frac{aLx}{4} - \frac{a^2x}{4} - \frac{L^2x}{4} + \frac{L^3}{12} - \frac{aL^2}{4} + \frac{a^2L}{4}, & L-a \le x \le L \end{cases} \quad (5.21)$$

Assume $EI = 1$, $F = 1\ N$, $L = 90\ mm$, $a = 30\ mm$. The curvature, slope and deflection will look like shown in Figure 5-5, Figure 5-6 and Figure 5-7 respectively.

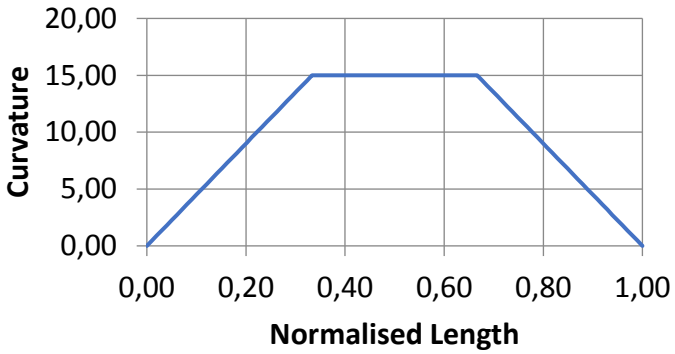

Figure 5-5: Curvature of the beam considered for non-linearity correction.

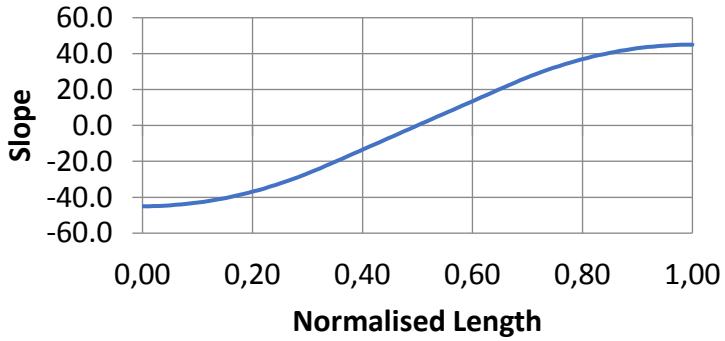

Figure 5-6: Slope of the beam in question.

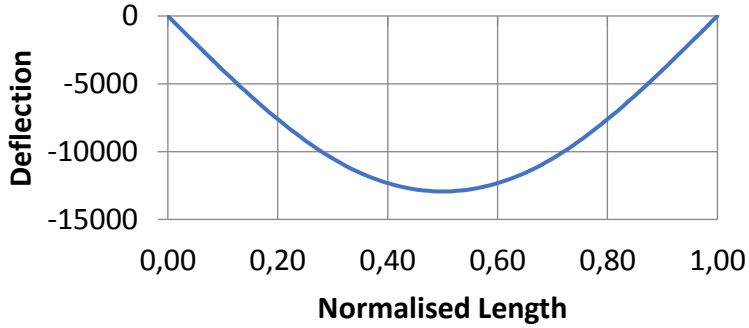

Figure 5-7: Deflection for the beam being considered.

Exact slope and deflection can thus be obtained for any value of L, a and EI. This will become useful momentarily. Now consider the rotation at supports shown in Figure 5-8:

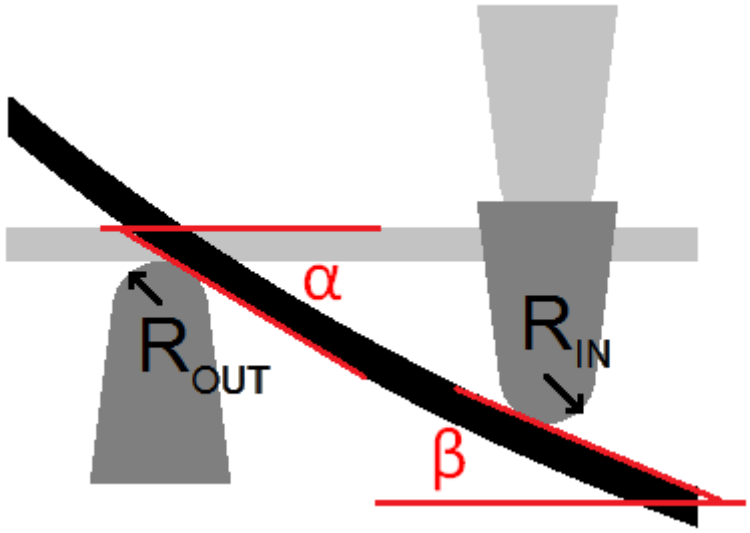

Figure 5-8: Rotation at support in 4PB test. The angles are different at the inner and outer supports.

Angles α and β correspond to the slope at outer and inner supports with radii R_{OUT} and R_{IN} respectively. The change in geometry will be as shown in Figure 5-9.

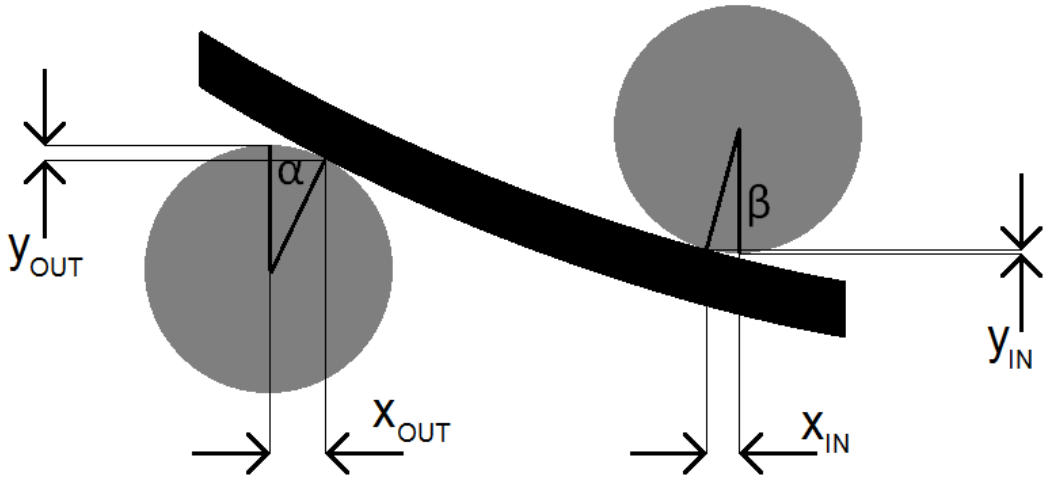

Figure 5-9: Change of sample geometry as a result of rotation at supports.

The change in geometry can be calculated as:

$$x_{OUT} = R_{OUT} * \sin(\alpha) \tag{5.22}$$

$$y_{OUT} = R_{OUT} * [1 - \cos(\alpha)] \tag{5.23}$$

$$x_{IN} = R_{IN} * \sin(\beta) \tag{5.24}$$

$$y_{IN} = R_{IN} * [1 - \cos(\beta)] \tag{5.25}$$

Now consider the deformed state of a beam with exaggerated supports:

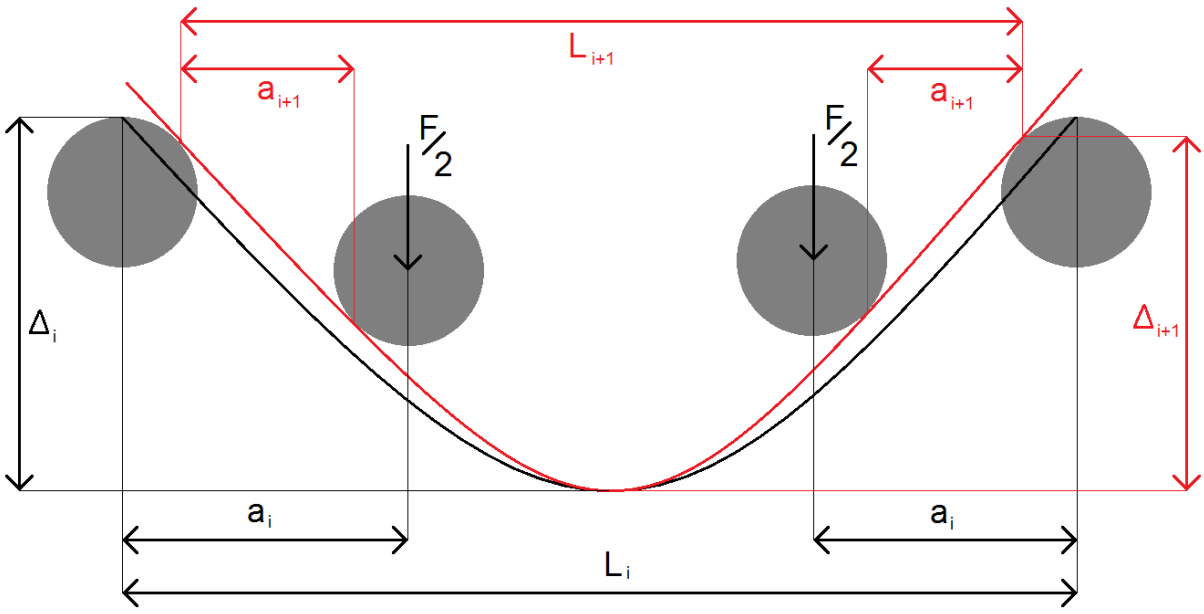

Figure 5-10: Beam in a deformed state contacting the supports in 4PB test.

It can be seen from Figure 5-10 that in the deformed state the horizontal distances between the supports L and a will reduce. They can be calculated as:

$$a_{i+1} = a_i - (x_{OUT} + x_{IN}) = a_i - [R_{OUT} * \sin(\alpha) + R_{IN} * \sin(\beta)] \quad (5.26)$$

$$L_{i+1} = L_i - 2 * x_{OUT} = L_i - 2[R_{OUT} * \sin(\alpha)\ ] \quad (5.27)$$

The recalculation of the a_{i+1} and L_{i+1} would be called a first correction.

The deflection of the shortened beam will reduce as well due to sliding down the supports:

$$\Delta_{i+1} = \Delta_i - y_{OUT} = \Delta_i - R_{OUT} * [1 - \cos(\alpha)] \quad (5.28)$$

However, due to the large curvature, the actual length of the beam spanning the supports is increased. This must be accounted for by obtaining the arc length of the curve. The general formula is:

$$length = \int_a^b \sqrt{1 + \left(\frac{dy}{dx}\right)^2}\, dx \quad (5.29)$$

As the function describing the deflection is piecewise, it must be integrated at least twice (from one end to the support and from the support to the middle). The length will therefore become:

$$L_{i+1} = 2\left[\int_0^{a_i} \sqrt{1 + \frac{F}{EI}\left(\frac{x^2}{4} + \frac{{a_i}^2}{4} - \frac{a_i L_i}{4}\right)^2}\, dx + \int_{a_i}^{\frac{L_i}{2}} \sqrt{1 + \frac{F}{EI}\left(\frac{a_i x}{2} - \frac{a_i L_i}{4}\right)^2}\, dx\right] \quad (5.30)$$

And the outer distance between supports:

$$a_{i+1} = \int_0^{a_i} \sqrt{1 + \frac{F}{EI}\left(\frac{x^2}{4} + \frac{{a_i}^2}{4} - \frac{a_i L_i}{4}\right)^2}\, dx \quad (5.31)$$

These can easily be integrated numerically as a realistic second correction. The deflection at any point x along the beam is calculated using the values of x, L, a, F and EI. In order to obtain the non-linear response of the beam, the following procedure is employed:

1. Assume the stiffness of beam EI and the initial geometry described by L_0, a_0, R_{OUT} and R_{IN}
2. Assume the initial applied deflection Δ_0
3. Solve for the force F_0 required to produce the deflection (goal seek or similar)
4. Calculate the slope at inner and outer support using the assumed geometry
5. Obtain angles α and β
6. Calculate the new geometry described by L_1 and a_1 by integrating the slope (do not solve for horizontal distances as these will create an inverse effect)
7. Calculate the reduced actual deflection Δ_1
8. Repeat steps 3 to 7 until the force converges
9. Assume a different initial applied deflection Δ_0 and repeat the steps 3 to 8 to obtain force values corresponding to a range of deflections

The above procedure was performed for a beam with the following parameters:

- $L_0 = 90\ mm$
- $a_0 = 30\ mm$
- $R_{OUT} = R_{IN} = 5\ mm$
- $E = 210\ GPa$
- $I = \frac{2.83^3 * 8}{12}\ mm^4$

The results are presented in Figure 5-11. It can be seen that the apparent stiffness is initially higher than for a simple linear beam. However, it reduces at higher displacement causing an apparent drop in stiffness.

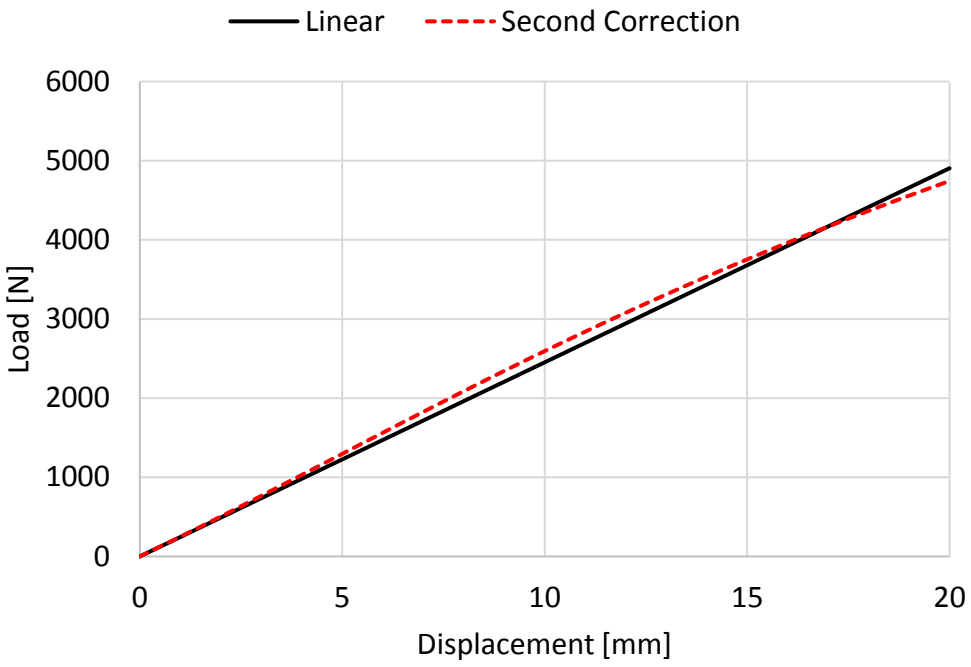

Figure 5-11: The corrected load-displacement curve for the assumed beam.

From this, the correction factor can be obtained dividing the corrected results by the linear.

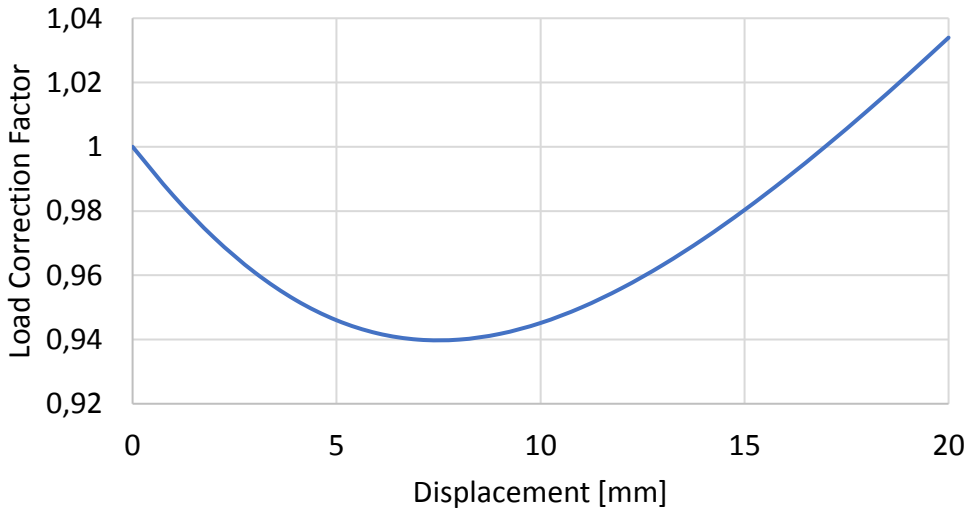

Figure 5-12: Correction factor derived for the non-linear 4PB bending.

It can be seen from Figure 5-12 that the correction has the expected shape and corrects the apparent stiffening followed by softening at high strains. The stiffness of the beam was adjusted for a set of samples tested early into the work, shown in Figure 5-13.

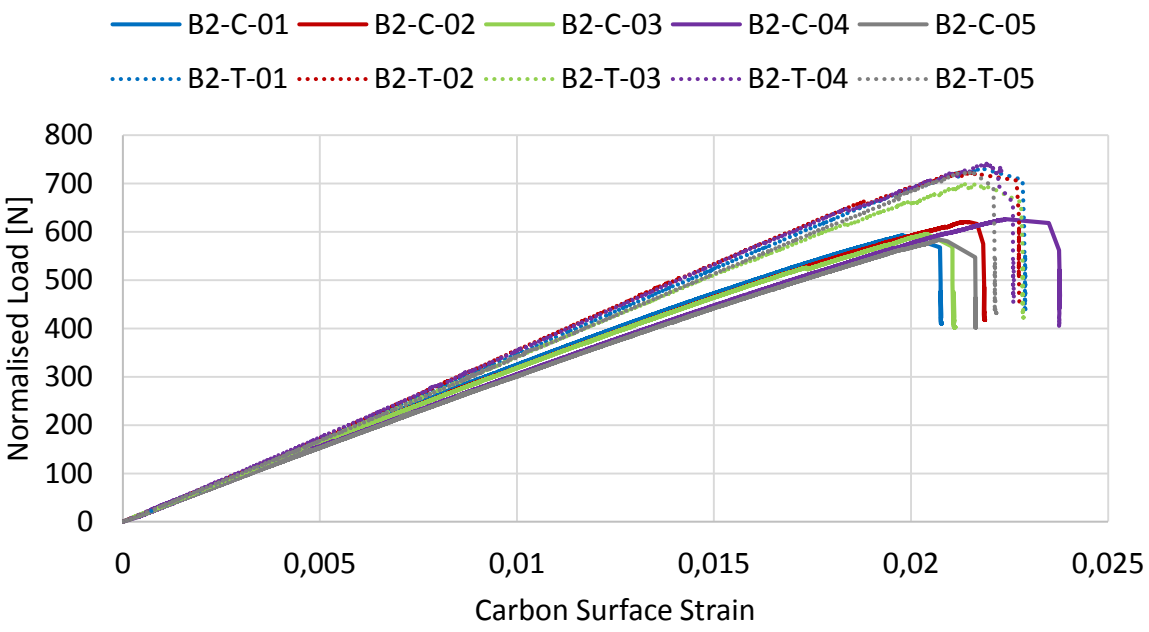

Figure 5-13: Results of early 4PB tests used for calibration. Note the visible geomeric non-linearity at high strains.

The results shown in Figure 5-13 are corrected using the load correction factor seen in Figure 5-12. Compare the corrected results in Figure 5-14.

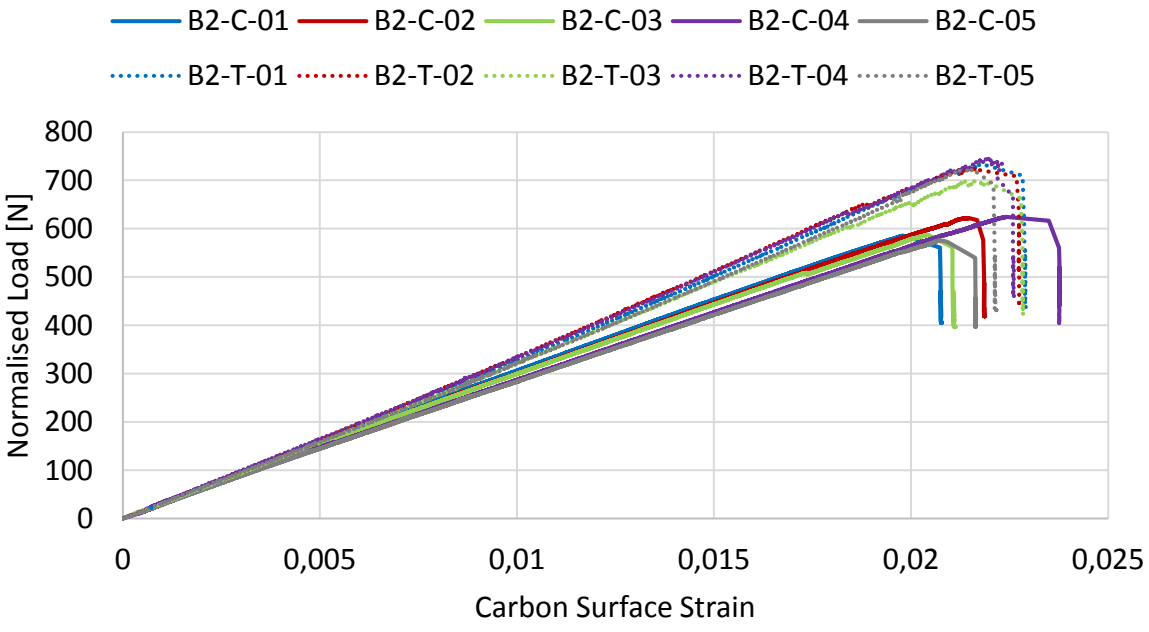

Figure 5-14: Corrected results from Figure 5-13. The response is visibly more straight.

The corrected results are visibly flatter. The procedure outlined in this section can be used to correct any sample at any geometry.

5.2.3 Instrumentation

The sample must be instrumented during the test to obtain relevant data. Two options are available:

1. Using the video gauge to capture the curvature of the internal span. This is a method proposed by Czél [75] which can be seen in Figure 5-15.
2. Using a pair of strain gauges to measure strains of the top and bottom surface between the inner supports. This has advantages that will be discussed shortly.

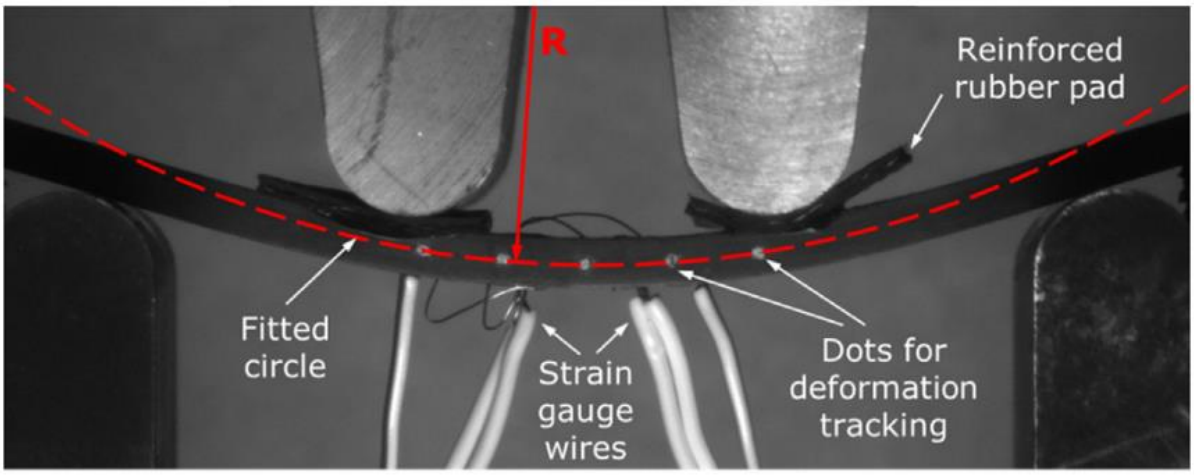

Figure 5-15: Instrumentation proposed by Czél. The locations of the five dots are tracked using a video gauge and can be described with a curve for post-processing. The ratio of thickness to length is $\frac{t}{L} = \frac{1}{7.2}, making\ the\ beam\ rather\ stocky$. Adapted from [75].

The method utilising the video gauge and describing the curvature is useful, as the strains can be simply obtained from the equation:

$$\varepsilon = \kappa y \tag{5.32}$$

Where ε is the strain, κ is the curvature and y is a distance from the neutral axis. This is a convenient solution that minimises the use of material and cost. However, it has one disadvantage compared to a more traditional strain gauge approach. The position of the neutral axis must be assumed for the sample in order to obtain the strains. Strain gauges provide top and bottom strain directly and therefore the neutral axis position can be obtained from the strain profile and sample thickness without any assumptions. This will prove especially useful when extracting the non-linear behaviour of carbon in 4PB testing.

5.2.4 Postprocessing

Testing with strain gauges will normally yield the load L along with the top and bottom strain values ε_{TOP} and ε_{BOT} at every sampling point. Looking at Figure 5-2, the strain at any given height of the section y can be obtained from the equation:

$$\varepsilon_y = \frac{y(\varepsilon_{TOP} - \varepsilon_{BOT})}{t_{g,bot} + t_c + t_{g,top}} + \varepsilon_{BOT} \tag{5.33}$$

For maximum carbon strain, the total thickness of the sample minus the top glass thickness should be used. For average strain in carbon, a height through the middle of the carbon block should be used.

5.3 Shear Testing

Shear properties of a fibrous composite depend largely on the properties of the constituent matrix, as the fibres have no significant rigidity when not embedded or embedded in a soft material [78]. A variety of tests exist for investigating the shear response of a composite [79]. A simple and effective such test is the ±45° tensile test detailed in ASTM D3518 [54].

5.4 Tensile Testing

The longitudinal modulus of the material can be obtained by using ASTM D3039 [80]. The sample does not need to be loaded to failure, as the strain of 0.6% is sufficient to comply with the standard.

As for testing of maximum tensile strain, a test developed by Czél can be used once again [75]. The test method uses continuous glass plies that are sandwiching the carbon ply to be investigated, eliminating the need for tabs. The obtained carbon fragmentation strains are consistent and high.

5.5 Summary and Recommendations

The four-point bending (4PB) test was introduced as an alternative do direct compression (DC) testing approach for carbon fibre. The main reasons for that are:

1. Ease of manufacturing the samples
2. Versatility in that it does not require a specialised fixture
3. Freedom to design a specimen for a desired thickness, span and material properties

4. Inherently higher strains achievable through bending due to strain gradient effect and hybridization with glass fibre
5. Minimum instrumentation required (2 strain gauges or a video gauge depending on desired properties)

As the 4PB test does not create a constant strain, careful post-processing of data is crucial to obtaining reasonable results. Some guidance is given on how to process the gathered data.

In some scenarios, the geometric effects of the 4PB loading may become significant. A correction for non-linearity caused by the high displacements is introduced.

Having established the 4PB test as a benchmark for comparative testing of compressive response in this work, the following testing regimen is proposed to compare the compressive behaviour of two carbon fibre composite materials:

1. Unidirectional tension test using a flat coupon (such as ASTM D3039 [80]) to determine the axial stiffness of the material at low strain
2. In-situ tabs tension (ISTT) test [81] to determine the strain to failure of the carbon fibre in tension
3. In-plane shear test (such as ASTM D3518 [54]) to determine the in-plane shear response of the composite
4. Indirect compression test through four-point bending (4PB) to determine the compressive response.

Performing the four tests should provide one with sufficient information and data to use the SI model in predicting strain to failure as long as reasonable estimates of fibre misalignment can be made. The proposed testing methodology will immediately be used in the following chapter.

6 Shear Instability in Bending

Direct compression response of hybrid specimens was investigated in the previous chapter, suggesting failure by shear instability and exploring the hybrid effect in compression. The model presented in Chapter 3 was used to explain the behaviour of the hybrid specimen and the increase of failure strain with increasing volume of glass fibre. Although the direct compression results can be readily correlated with the model, it is not the preferred test method for evaluating the compressive response of carbon fibre. The complexity of the setup and high machining precision that is required make the test relatively inefficient compared to four-point bending approach presented in section 5.2. For a relative comparison between the materials where maximizing the compressive strain and evaluating non-linearity are of primary concern the bending test represents a quicker, simpler method.

A range of materials will be explored in this chapter, focusing on relative compressive performance and relating it to shear and axial stiffness of the plies. Although the model outlined in Chapter 3 will not be directly applicable to the test results, it will provide a useful tool for qualitative understanding of the results.

As shown in Chapter 3, materials with higher shear stiffness are expected to exhibit higher compressive failure strains at the same fibre misalignment. There are a number of matrix materials available on the market, with a high range of elastic moduli. Novel matrices utilising nanomaterials are also commercially available. This section will investigate how the compressive strain to failure varies with different resin and fibre types. Modeling approach presented previously will be used to qualitatively assess the results.

6.1 Compressive Behaviour as a Function of Matrix Stiffness

Some resin systems available on the market contain additives intended to enhance the properties of the material. A prepreg that can be found in both a standard and a nano-enhanced version with the same fibre type and volume would make a good case for testing the effects of resin stiffness on compressive strain to failure.

Gurit's SE84LV is a low-viscosity, toughened epoxy prepreg system with cure temperatures up to 120 °C [82] that is also available in a nanosilica-enhanced version called SE84 Nano™ [83]. The manufacturer claims a 10% increase in compressive strength when using the modified version. Other nanosilica-based systems have shown significant improvements in compressive

behaviour [84], [85], but the literature detailing the performance of systems of this kind is still limited.

Nanosilica is a by-product of electronics manufacturing. It has historically been used in the construction industry [86], as an additive to concrete. In concrete, it markedly increases cured strength and improves flow, all at low addition by weight.

The novelty of the system is that the nano-sized (typically between 5 nm and 100 nm), round silica beads can be dispersed evenly in the epoxy. The stiffness of silica is high compared to the stiffness of epoxy, therefore resulting in a composite matrix, stiffness of which can be calculated from the rule of mixtures for dispersed reinforcement [17].

6.1.1 Testing

In order to investigate the effects of nanosilica-enchanced resin on compressive response of the composite and relate the findings to the model presented in Chapter 3, a series of tests were conducted in accordance with the recommendation given in section 5.5. The materials used in testing are shown in Table 6-1.

Table 6-1: Materials used in testing of the effects of nanosilica addition to the resin

Material Designation	Manufacturer	Fibre Type	Resin Type	Cure Temperature [°C]	Measured Ply Thickness [mm]
nSi	Gurit	HEC	SE84 Nano™	120	0.148
baseline	Gurit	HEC	SE84 LV	120	0.165
S-glass	Hexcel	S2GL	913	120	0.155

It can be seen that materials from two different manufacturers are used. The cure cycles of the materials are not identical, but have been adjusted to the slowest temperature ramp and the longest dwell time to ensure all plies were fully cured. No study was performed as to the compliance of the different resin systems, but delamination did not occur prematurely in any of the samples tested, therefore suggesting that interfacial strength between different materials was not significantly impacted. All samples tested have been cured in a single autoclave run, so no discrepancy from different curing conditions is present. Table 6-2 shows a summary of all tests performed.

Table 6-2: Tests performed to investigate the effects of adding nanosilica to the resin on compressive behaviour of composite

Test	Method	Material	Lay-up	Data Obtained
Shear	ASTM D3518 [54]	nSi baseline S-glass	$[+45/-45]_{4S}$	Full shear stress - shear strain curve
Tension	ASTM D3039 [80]	nSi baseline	$[0]_8$	Young's modulus
ISTT	Czél [81]	nSi baseline	[G/C/G]	Tensile strain to failure
4PB	Custom 20-20-20	nSi + S-glass	$[G_{14}/C/G]$	Indirect compression strain
	Custom 30-30-30		$[G_{14}/C_2/G]$	
			$[G_{14}/C_3/G]$	
	Custom 20-20-20	baseline + S-glass	$[G_{14}/C/G]$	
	Custom 30-30-30		$[G_{14}/C_2/G]$	
			$[G_{14}/C_3/G]$	

The custom method of 4PB testing has been discussed in Chapter 5. It should be noted that 4PB samples containing a single carbon ply were tested using a different span arrangement to the ones with double and triple carbon layers and therefore will be compared separately. It can also be seen that S-glass is not tested for strain to failure or modulus, as the modulus data has previously been obtained for this material at is $E_{11} = 45.7\ GPa$. The strain of failure of S-glass is of secondary interest, as the carbon is expected to fail well before there is damage in the glass.

Samples were tested using ±45 ° in-plane shear test to measure shear response. The results of the shear test are shown in Figure 6-1. Please note that 6 samples were tested for each configuration, but only a single typical curve is drawn for each material in the figure.

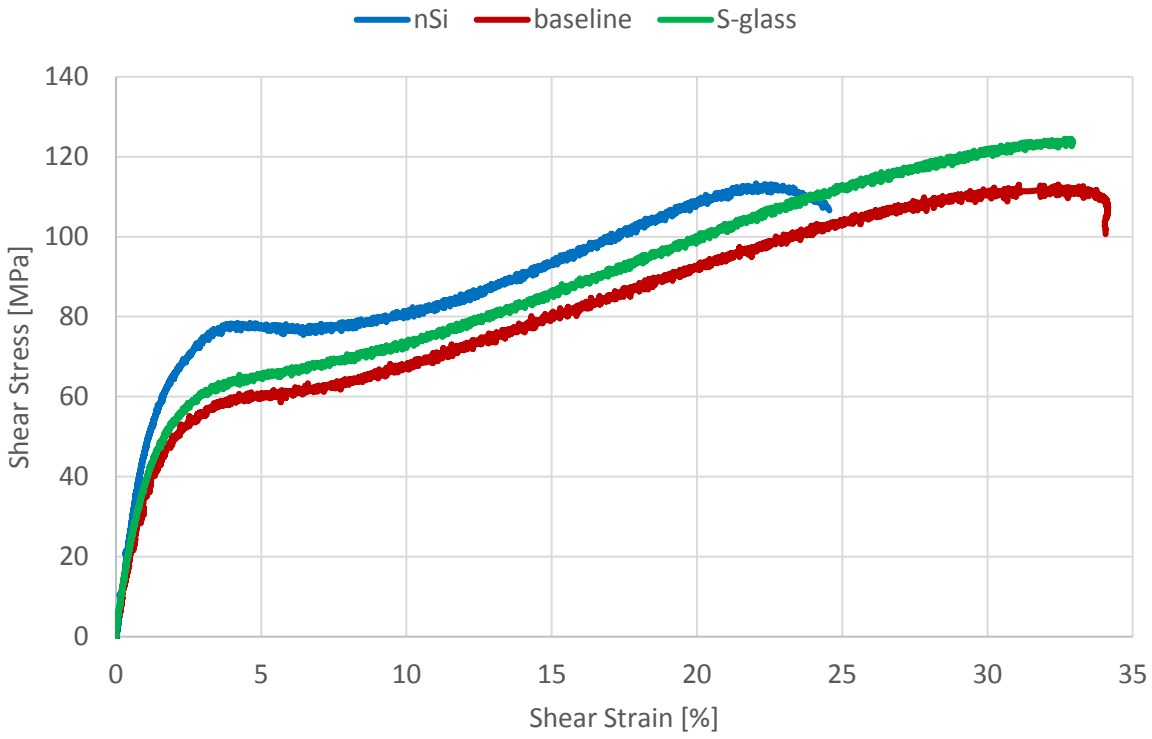

Figure 6-1: Results of shear testing of the three materials in the nanosilica study. Typical curves are shown for each material. Due to good consistency of the shear test results there is virtually no divergence between the curves for the same material up to about 15% strain. Some samples fail catastrophically at various strains over 20%, but the shear expected during compression testing does not exceed 5% and therefore only the initial portion of the curves is of interest.

It can be seen that the nanosilica material exhibits a plateau in the shear strain range between 4% and 8%. The baseline material and S-glass do not have the same behaviour and the shear stress increases linearly after about 5% shear strain. Interestingly, the nanosilica material has the highest stiffness of the three matrices, but not the highest strength, as the S-glass fails at the higher shear stress of approximately $\tau_{MAX} = 141\ MPa$.

It should also be noted that all three materials have a linear portion (nanosilica material at about 8% shear strain after the plateau) and that the gradients are similar between them. This is likely due to fibre rotation becoming significant and the stiffness of the surrounding matrix playing a smaller role at high shear strain [55].

The shear data was fitted with exponential-linear function as detailed in Chapter 5. The values of constants that have been used are shown in Table 6.3.

Table 6-3: Fit parameters for nanosilica shear modelling

Material	Maximum	Exponent	Linear
nSi	85	80	-120
baseline	60	85	20
S-glass	59	100	131

The resulting function shapes are superimposed over shear data in Figure 6-2.

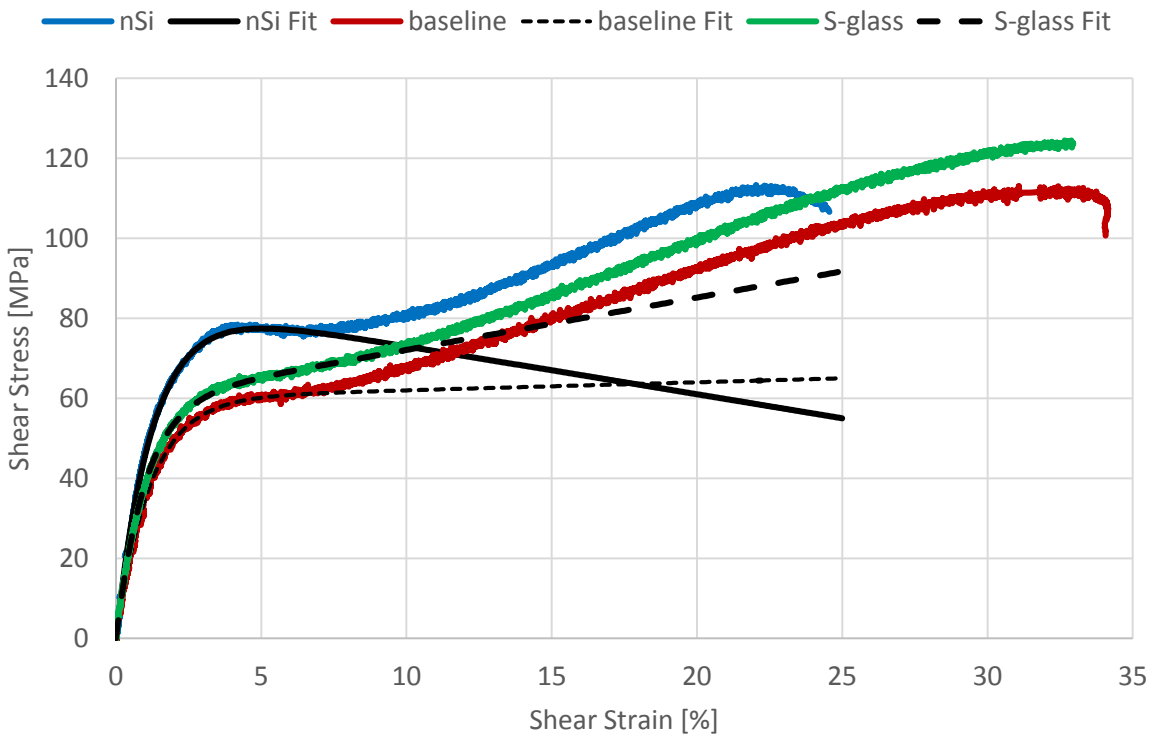

Figure 6-2: Shear data overlaid with simplified shear functions. Note that the emphasis is on approximating the initial part of the shear response curve. Behaviour at high strains does not need to be accurate, as the shear instability is normally reached in the model at strains $< 5\%$.

The parametric curves match the measured shear response well for strains $< 5\%$, with less emphasis on good fit at higher strains. This is because the shear instability model presented in Chapter 3 typically reaches instability at shear values lower than that. The use of negative linear constant to describe nSi captures the peak and the subsequent dip in stress well, with significant divergence beyond a shear strain of about 8%. Shear strain will be checked when modelling the samples to confirm that it does not exceed that value.

With the shear response measured and described for further modelling, fibre direction stiffness and fibre break strain were tested for. Table 6-4 shows the stiffness in fibre direction and tensile strain at failure for the tested materials.

Table 6-4: Tensile properties of carbon fibre materials used for the nanosilica study

Material	Young's Modulus		Strain to Failure	
	Value [GPa]	CoV	Value [%]	CoV
nSi	168.9	3.93%	1.76	2.58%
baseline	153.4	2.57%	1.69	5.86%
nSi + baseline	159.6	5.75%	1.73	4.89%

There is a discrepancy between the Young's modulus values of the nSi and the baseline material, suggested by the coefficient of variation for each individual set being lower than if samples for both materials are treated as a single population. This is likely due to a different fibre volume fraction in the two materials. Another possible cause could also be a higher stiffness of the nanosilica-loaded matrix, but not to the extent that is observed (difference in E_{11} of $15.5\ GPa$). As the inclusion of nanosilica particles is likely to change the viscosity of the resin, the prepreg production process is likely to require adjustments to achieve the same fibre to resin ratio in the end product. Some variation is therefore expected.

Both nSi and baseline use IMC fibre [87], which is expected to have a strength of $\sigma_{T,MAX} > 4400\ MPa$ and Young's modulus of $227\ GPa < E_{11} < 257\ GPa$. The lack of more accurate information from the manufacturer suggests a further degree of variability in the production process of the fibre itself. Calculating the expected strain to failure based on strength and modulus quoted above (along with the assumption that the fibre is linear) yields values of $1.71\% < \varepsilon_{T,MAX} < 1.94\%$. The strain value for nanosilica falls within this range, but baseline material is slightly lower at $\varepsilon_{T,MAX} = 1.69\%$. However, the coefficient of variation for the baseline material is relatively high at 5.86%, due to a single outlier with a strain of $\varepsilon_{T,MAX} = 1.59\%$. If the outlier is removed, the average strain for the baseline set becomes 1.74% with a coefficient of variation of 4.87%. However, the decrease of CoV for strain to failure relative to baseline - if both nSi and baseline are treated as a single population - is a good indicator that the fibre type is indeed the same for both.

Finally, the samples were tested in 4PB as described in Chapter 5. The load-strain curves for carbon are presented in Figure 6-3 and Figure 6-4 for 20-20-20 and 30-30-30 span

arrangement respectively. Direct comparison of two different span arrangements is not practical due to higher perceived stiffness of samples loaded in a shorter span.

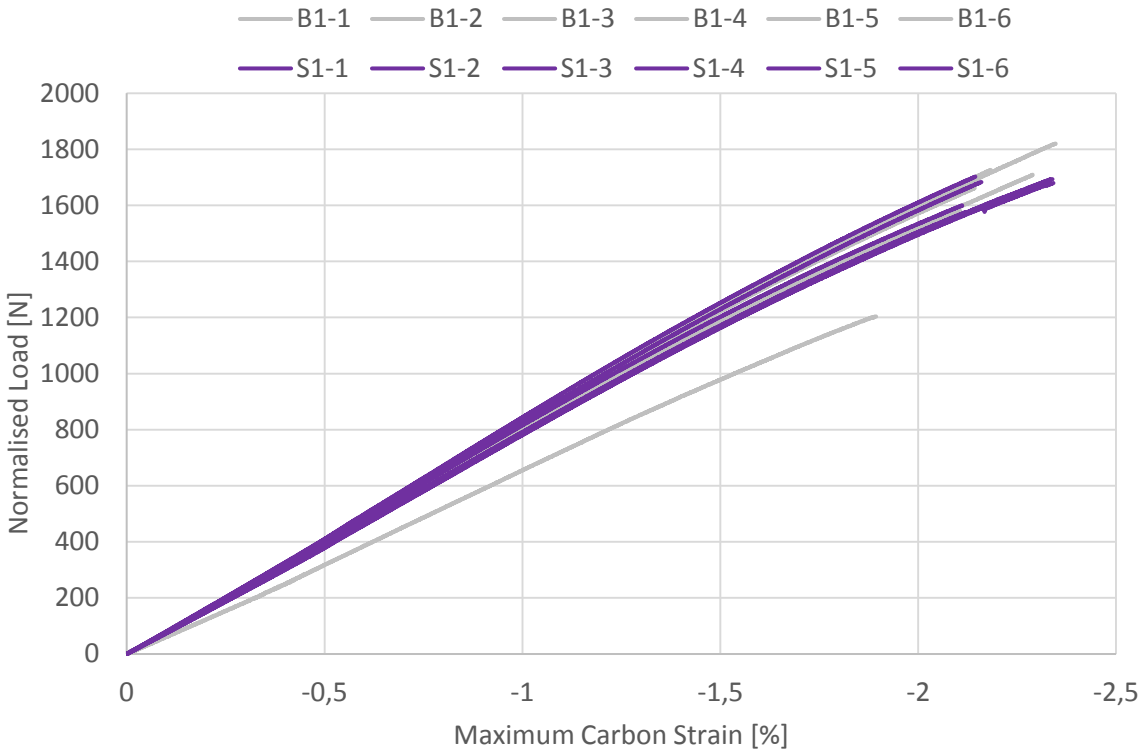

Figure 6-3: 4PB test results of single carbon ply nanosilica (denoted S1) and baseline material (denoted B1) in 20-20-20 span configuration. It can immediately be seen that one of the baseline samples (namely B1-1) exhibits unusually low stiffness and premature failure. The other samples show good consistency in terms of stiffness and strain at failure.

One of the baseline samples shows apparently lower stiffness and premature failure. This is due to the sample being cut from near the edge of the cured plate, where thickness is much lower ($t = 2.48\,mm$ compared to $t_{AVG} = 2.57\,mm$ for the rest of the samples). The metal Caul plate is pressed harder on the edges of the composite lay-up causing higher compaction. The resulting decreased thickness causes a drop in bending stiffness of the sample, as $I \propto t^3$. The low strain at failure could also be attributed to overcompaction and the possible fibre damage resulting from it. Due to the problems described above, the culprit sample B1-1 will be excluded when analysing the results.

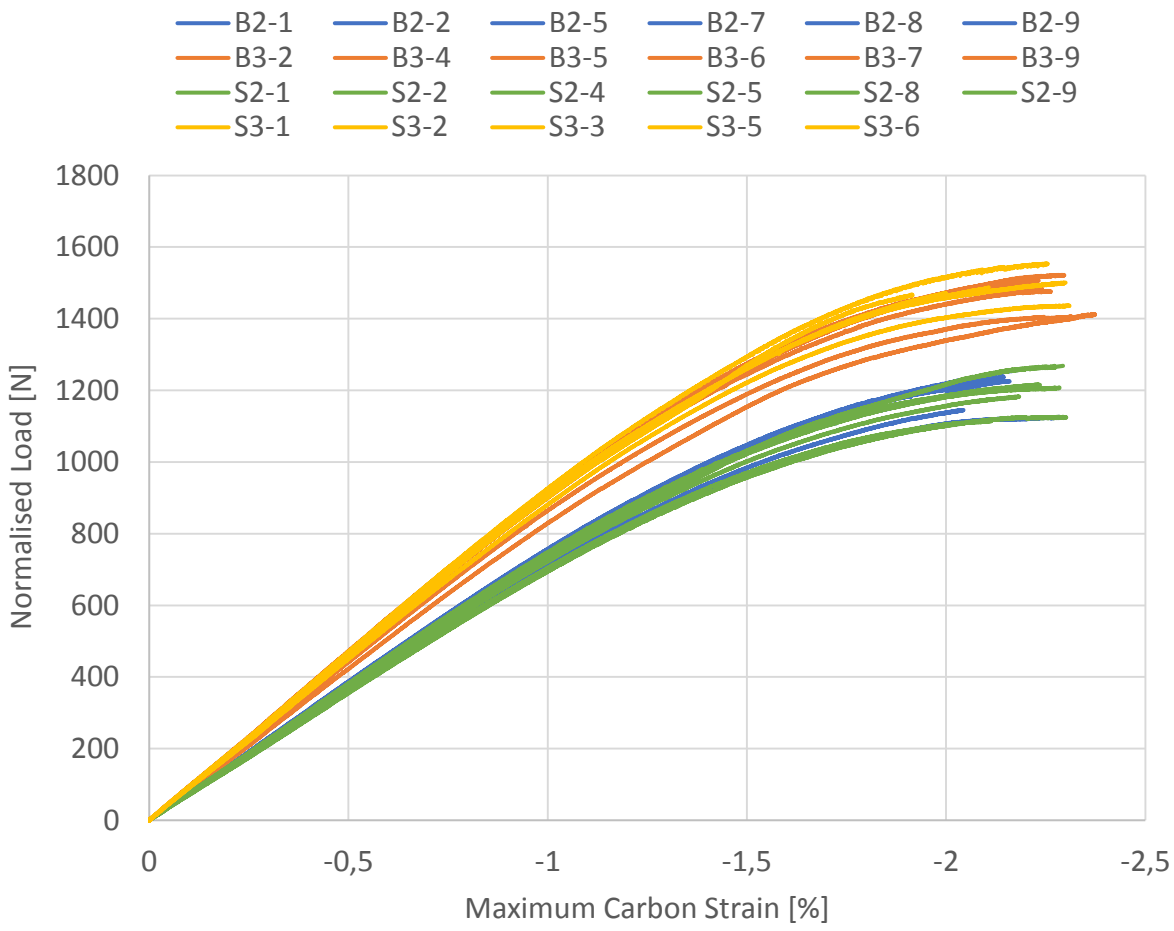

Figure 6-4: 4PB test results of double and triple ply nanosilica (denoted S2 and S3 respectively) and baseline material (denoted B2 and B3 respectively) in 30-30-30 span configuration. Only 5 samples are shown for S3 configuration due to loss of the strain gauge data for one of the samples, caused by software fault (crash at the end of the test).

The results for both span configurations follow the expected trend (initial apparent increase in stiffness followed by apparent softening behaviour due to geometric effects of 4PB loading). As expected, the samples containing 3 plies of carbon are stiffer than those containing 2 plies of carbon. There is no immediate difference in stiffness between the two materials with the same number of plies.

Table 6-5 summarises maximum strains in carbon for all samples tested. Please note the notation is as follows:

1. Material is designated with a letter (S for nanosilica and B for baseline)
2. Number of plies in the carbon block is denoted by a number that follows the letter (1, 2 or 3 depending on the lay-up)
3. Number following the hyphen denotes an individual sample number within the set

Table 6-5: Maximum strain in the carbon at failure for all samples tested in the nanosilica investigation

Set Name	Sample	Strain to Failure	Set Average		Material Average		All Samples Average	
		$\varepsilon_{C,MAX}$ [%]	Strain [%]	CoV	Strain [%]	CoV	Strain [%]	CoV
S1	S1-1	-2,11	-2,20	4,48 %	-2,21	4,97 %	-2,22	4,49%
	S1-2	-2,12						
	S1-3	-2,14						
	S1-4	-2,16						
	S1-5	-2,34						
	S1-6	-2,34						
S2	S2-1	-2,28	-2,23	2,95 %				
	S2-2	-2,24						
	S2-4	-2,18						
	S2-5	-2,30						
	S2-8	-2,11						
	S2-9	-2,27						
S3	S3-1	-1,92	-2,18	6,85 %				
	S3-2	-2,31						
	S3-3	-2,11						
	S3-5	-2,30						
	S3-6	-2,25						
B1	B1-2	-2,35	-2,21	4,10 %				
	B1-3	-2,18						
	B1-4	-2,14						
	B1-5	-2,29						
	B1-6	-2,11						
B2	B2-1	-2,18	-2,18	3,56 %	-2,23	3,91 %		
	B2-2	-2,04						
	B2-5	-2,24						
	B2-7	-2,16						
	B2-8	-2,29						
	B2-9	-2,14						
B3	B3-2	-2,37	-2,29	2,13 %				
	B3-4	-2,24						
	B3-5	-2,26						
	B3-6	-2,23						
	B3-7	-2,32						
	B3-9	-2,30						

The results are similar for all samples, with the lowest strain to failure of $\varepsilon_{C,MAX} = -1.92\%$ for sample S3-1 and the highest of $\varepsilon_{C,MAX} = -2{,}37\%$ for sample B3-2. The coefficient of variation is $< 5\%$ for all individual sets of samples except for S3, which contains the outlier is the form of the lowest overall strain.

The differences between individual sets are low, with the lowest average strain of $\varepsilon_{C,MAX} = -2.18\%$ for sets S3 and B2 and the highest average strain of $\varepsilon_{C,MAX} = -2.29\%$ for set B3.

The averages for the samples with the same number of blocked carbon plies could not be shown clearly without rearranging the table. They are as follows:

1. Average for single carbon (sets S1 and B1) $\varepsilon_{C,MAX} = -2.21\%$ with a CoV of 4.32%
2. Average for double carbon (sets S2 and B2) $\varepsilon_{C,MAX} = -2.20\%$ with a CoV of 3.49%
3. Average for triple carbon (sets S3 and B3) $\varepsilon_{C,MAX} = -2.24\%$ with a CoV of 5.37%

Again, the differences between those are statistically insignificant and within experimental variance.

The most significant outlier within the set of data presented in Table 6-5 is B3, which exhibits the highest average strain to failure. Even then, the difference between it and the set with the lowest strain is 5.06%. It can therefore be claimed that there is no significant variation in maximum carbon strain at failure between all samples tested.

However, the maximum strain only occurs at the top surface of the carbon. As the carbon block varies in thickness between each set of samples, the average strain within the block will vary as shown in Figure 6-5. It can be seen that the thicker carbon block has the same maximum strain on the top surface, but due to its increased thickness and the change of centroid position, the strain gradient through the carbon goes up. This causes the strain at the bottom of the block to be significantly lower than at the top. The thicker the carbon block, the more pronounced the effect. With a thick enough block, the centroid would shift to within the carbon, creating the situation where the bottom surface of the carbon would be in tension.

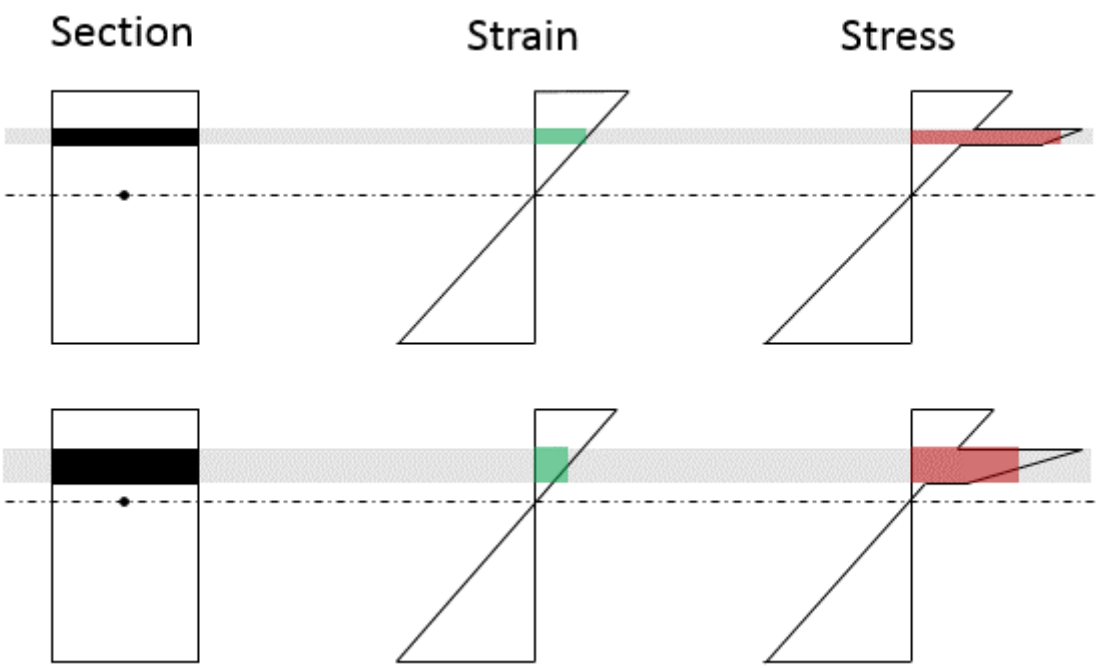

Figure 6-5: The variation of average strain and average stress with carbon block thickness. The green rectangle represents the averaged strain in the carbon. The red rectangle represents the averaged stress over the thickness of carbon in the 4PB sample.

As the maximum strain in carbon at failure appears to be similar for all samples, the average strain should also be investigated. This is done by assuming a linear strain profile through the sample and calculating the strain at a location in the middle of the carbon block in the same fashion that is was previously calculated from strain gauge data for top of the carbon.

The results for average strain in carbon at failure are shown in Table 6-6.

Table 6-6: Average strain in the carbon at failure for all samples tested in the nanosilica investigation

Set Name	Sample	Strain to Failure	Set Average		Material Average		All Samples Average	
		$\varepsilon_{C,AVG}$ [%]	Strain [%]	CoV	Strain [%]	CoV	Strain [%]	CoV
S1	S1-1	-1,96	-2,04	4,49%	-1,91	8,08%	-1,90	7,37%
	S1-2	-1,97						
	S1-3	-1,99						
	S1-4	-2,00						
	S1-5	-2,17						
	S1-6	-2,17						
S2	S2-1	-1,97	-1,92	3,08%				
	S2-2	-1,93						
	S2-4	-1,89						
	S2-5	-1,98						
	S2-8	-1,81						
	S2-9	-1,96						
S3	S3-1	-1,52	-1,74	7,09%				
	S3-2	-1,84						
	S3-3	-1,69						
	S3-5	-1,83						
	S3-6	-1,80						
B1	B1-2	-2,16	-2,04	4,15%				
	B1-3	-2,01						
	B1-4	-1,97						
	B1-5	-2,11						
	B1-6	-1,94						
B2	B2-1	-1,86	-1,85	3,33%	-1,88	6,47%		
	B2-2	-1,73						
	B2-5	-1,87						
	B2-7	-1,84						
	B2-8	-1,94						
	B2-9	-1,83						
B3	B3-2	-1,85	-1,79	2,08%				
	B3-4	-1,75						
	B3-5	-1,76						
	B3-6	-1,75						
	B3-7	-1,81						
	B3-9	-1,80						

The picture is much different to what can be seen in Table 6-5, with clear drop of average strain in carbon at failure as the thickness of the carbon block increases. The lowest value is $\varepsilon_{C,AVG} = -1.52\%$ for sample S3-1 and the maximum is $\varepsilon_{C,AVG} = -2.17\%$ for samples S1-5 and S1-6. The coefficient of variation is $< 5\%$ for all sample sets except for (again) S3 which contains an outlier in the form of lowest overall strain.

There is a significant difference between the sets, with the lowest average $\varepsilon_{C,AVG} = -1.74\%$ for set S3 and the highest average $\varepsilon_{C,AVG} = -2.04\%$ for sets S1 and B1.

The averages for the samples with the same number of plies are as follows:

1. Average for single carbon (sets S1 and B1) $\varepsilon_{C,AVG} = -2.02\%$ with a CoV of 5.94%
2. Average for double carbon (sets S2 and B2) $\varepsilon_{C,AVG} = -1.89\%$ with a CoV of 3.81%
3. Average for triple carbon (sets S3 and B3) $\varepsilon_{C,AVG} = -1.76\%$ with a CoV of 5.16%

There is a drop in average strain at failure as the thickness of carbon increases, as shown in Figure 6-6.

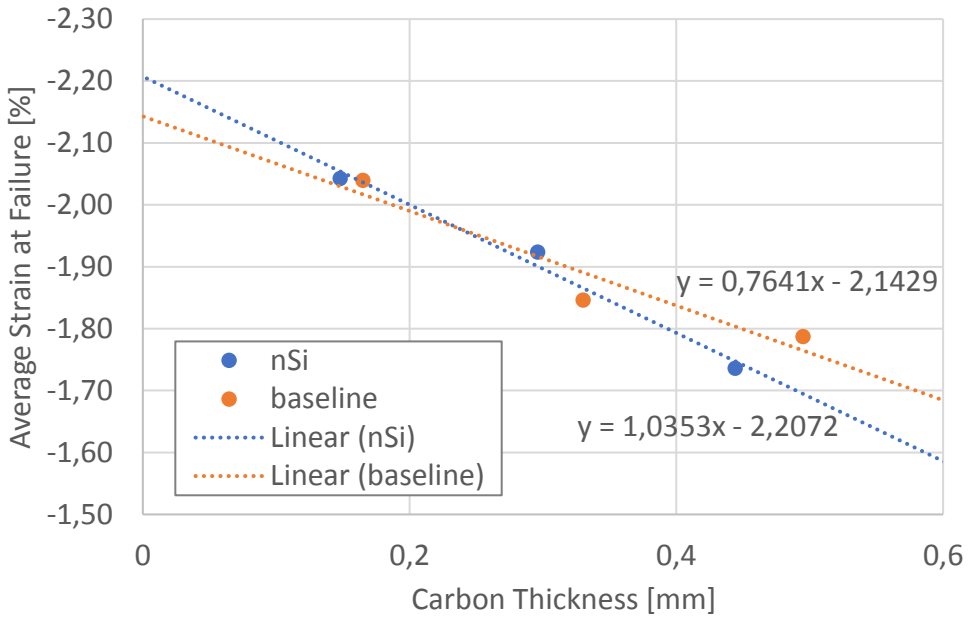

Figure 6-6: The variation of average strain at failure in carbon with the thickness of the carbon block within the 4PB sample in the nanosilica investigation.

The apparent drop in average strain for thicker carbon is the result of using the same thickness for the S-glass substrate (14 plies or $2.17\ mm$). The increased thickness of carbon will thus increase the strain gradient through the carbon block as there is no increase in the thickness of S-glass. To compare like with like, the thickness of the glass substrate would have to be

increased to achieve the same strain gradient, meaning the strains at the top of the carbon and the strains at the bottom of the carbon would have the same ratio for all sets of samples (single, double and triple carbon). This is suggested as future work.

In order to better understand the mechanism of failure in the tested samples and the effect that nanosilica-enhanced matrix may have on the compressive behaviour, let us resort to the modelling tool presented in Chapter 3. Although it is not designed for specimens in bending, it may provide a qualitative explanation of the resuls.

6.1.2 Modelling

The data obtained through testing can be used in shear instability model presented in Chapter 3. There are several assumptions that must be made in order to relate a 4PB test to the model:

1. A model based on uniform axial loading can approximate the behaviour of a 4PB specimen.
2. Asymmetric, hybrid 4PB sample can be considered in the two-material model as two materials only, ignoring the alternating layers of different materials and using total thickness for each constituent instead.
3. The presence of strain gradient effect does not impact the overall behaviour of the sample and has no impact on carbon strain at failure.

It becomes immediately apparent that all the above assumptions do not stand. The main reason for this is the strain not being constant through the sample cross-section. By definition, a bending test must result in a strain gradient, as bending results in tension on one side of the sample and compression on the other. However inadequate the assumptions, modelling the shear instability for the equivalent direct compression samples may provide useful insights into the behaviour or 4PB samples.

Using the axial and shear data presented in Table 6-4 and Table 6-3, a single-material model was used to create individual SI curves for each of the three materials used in the study. The results are shown in Figure 6-7.

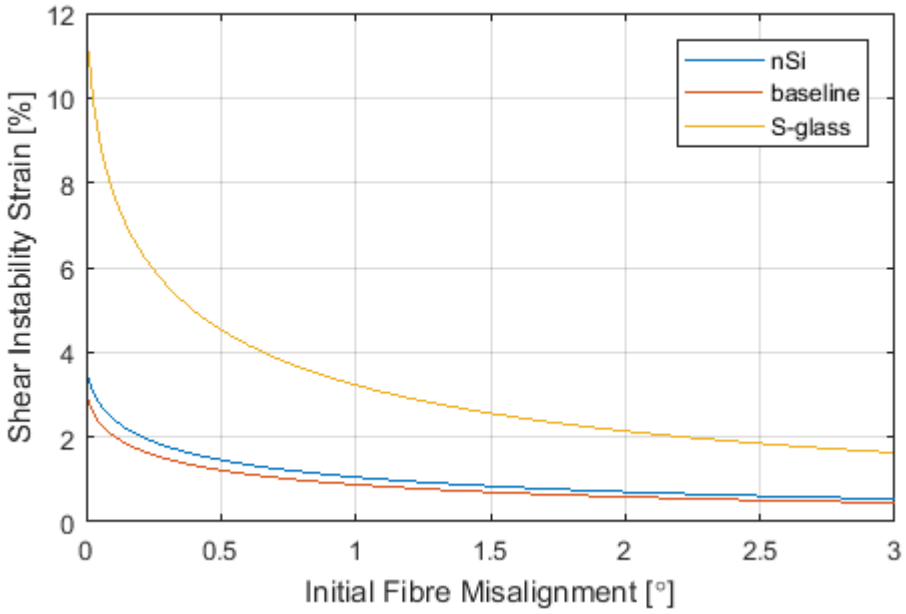

Figure 6-7: Results of shear instability modelling of individual materials used in the nanosilica study.

As seen previously in Chapter 3, the S-glass displays a much higher strain at instability than the two carbon materials. This is due to its lower axial stiffness and is expected. The nSi material has a stiffer shear response compared to the baseline at similar axial stiffness. This results in its SI envelope being higher. For comparison:

1. nSi sample with a fibre misalignment $\alpha = 0.5°$ becomes unstable at $\varepsilon_{SI} = 1.46\%$
2. baseline with the same misalignment $\alpha = 0.5°$ becomes unstable at $\varepsilon_{SI} = 1.26\%$

This is not an insignificant difference, but hybridising the carbon with S-glass will elicit a hybrid effect which will decrease the disparity between the nSi and baseline. The higher the S-glass to carbon ratio, the more unified the sample behaviour will become, as the softer material will dominate the hybrid response more and more.

An important question when modelling 4PB samples using the model designed for axial compression is whether to include the thickness of the entire sample. As the carbon is, in principle, attached to a glass fibre beam, only the top portion of the material is being compressed. However, the shear instability results from complimentary shear that is the product of compressive stress. It would be expected that introducing tensile stress into the sample would have a strong stabilising effect on the shear stress state within the composite, thus significantly delaying the SI failure. Such mechanism would also serve as a good

explanation of all-carbon samples undergoing bending failing in tension rather than compression [88].

Assumption that the entire thickness of the sample contributes to the hybrid effect seems reasonable. Should the same sample be used in a DC test after attaching the tabs, all of the material would be under compression (although there would be bending induced as the 4PB samples are not symmetric – therefore some strain gradient effects would still be present). The shear stress state in that case would be proportional to the compressive stress and fibre misalignment. However, in the case of bending the same sample the compressive stress would be high only at the top surface of the sample, decreasing towards the centroid and becoming tensile in the bottom portion of the specimen. It could therefore be assumed that the overall shear stress would be lower than in DC case. The use of the entire thickness of the sample may therefore not be sufficient to account for the positive effects of bending on shear instability onset.

On the other hand, only a portion of the material is being compressed in 4PB test, thus the axial model could only encompass the part above the neutral axis and disregard the material that is in tension. The actual problem is much more involved and requires a separate modelling approach, but the use of axial model may provide useful qualitative insight into sample behaviour, hence it is attempted here.

Two cases are investigated:

1. Where the 4PB sample is treated as being subjected to direct compression, meaning the total thickness of the glass and total thickness of the carbon are used
2. Where only the part of the sample that is in compression at the failure point is used as equivalent DC sample. The thickness of the S-glass is determined based on the total thickness minus the centroid position at the failure point

The total thickness approach is modelled using the model presented in Chapter 3. The shear response fitting parameters have been shown in Table 6-3 and the longitudinal modulus of the materials in Table 6-4. The resulting SI surfaces are shown in Figure 6-8.

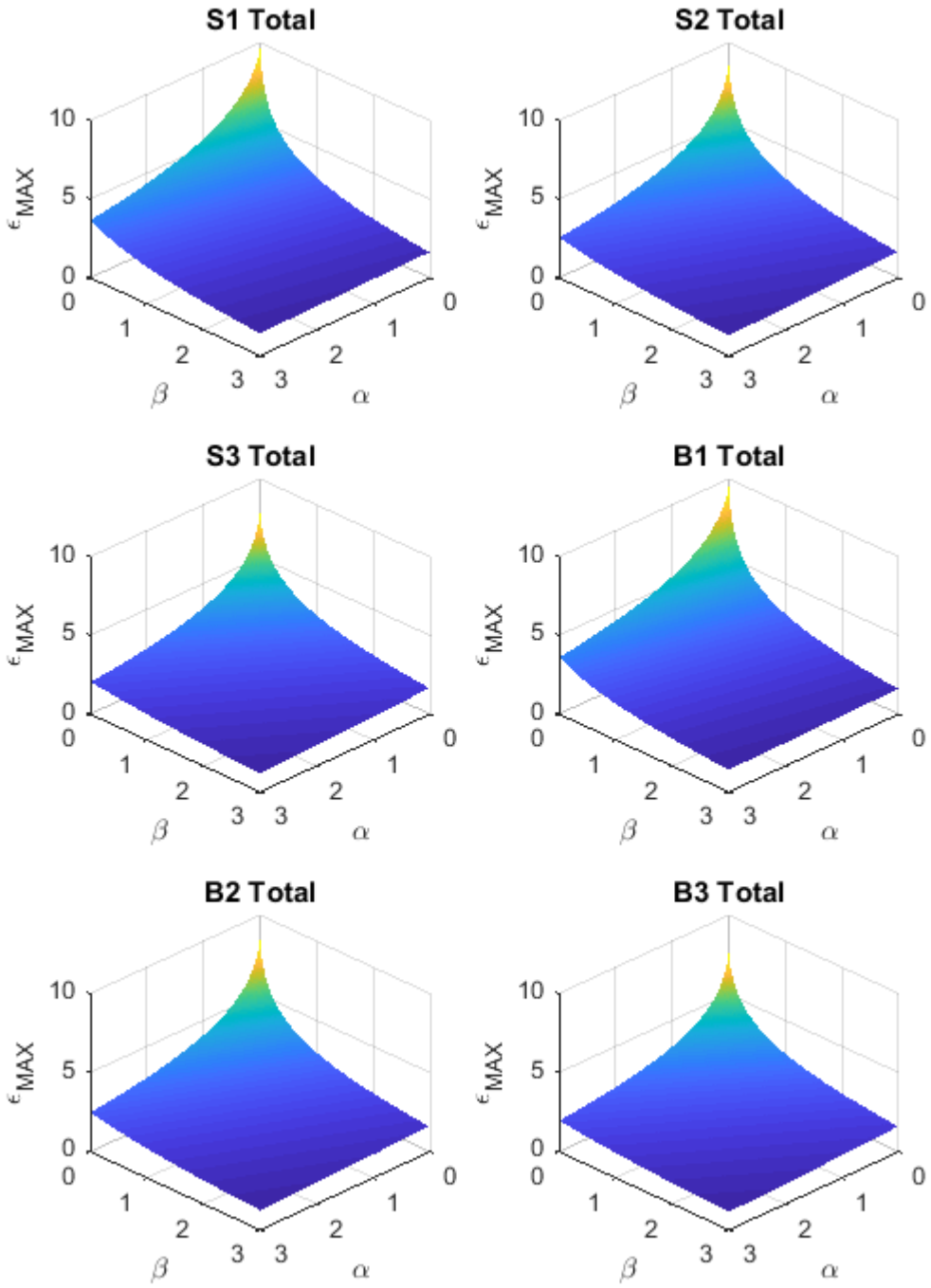

Figure 6-8: Results of the SI modelling for the nanosilica study assuming the 4PB samples are tested in DC with their full thickness.

In order to simplify the analysis of the results, a cut through diagonal of each surface is taken (as shown in Figure 3-15) and these are plotted in a single space in Figure 6-9.

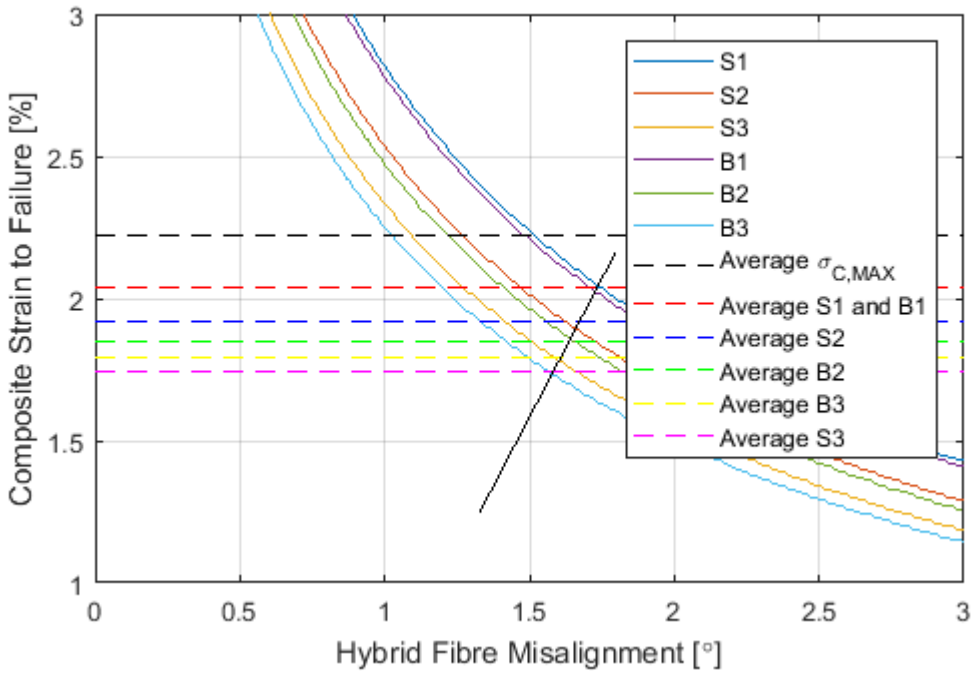

Figure 6-9: Diagonal cuts through all nanosilica SI surfaces using total thickness in equivalent DC test. Average strains at failure are shown for each set of samples. The black angled line is drawn that best matches the intersect of average strain with the SI curve for the set.

The strain range on the vertical axis has been chosen to provide the best view of the individual curves. It can be seen that the curves are spaced in pairs of S1 and B1, S2 and B2, S3 and B3 where the curve for B is below the S curve. This reflects the higher shear stiffness of the nSi as compared to baseline at similar longitudinal stiffness. The average maximum carbon strain at failure is plotted for comparison. Horizontal lines representing individual set average strains at failure are drawn. Where these lines intersect the SI curves is where the suggested misalignment of the sample would lie. However, the values of misalignment would be expected to be similar for all samples. It is highly unlikely that there is progressive decrease in sample misalignment that matches this prediction. However, the relative gradation of the curves (S1 has the highest strain at a given misalignment, followed by B1 and so on) matches the experimental results with the exception of S3 which has lower average strain that B3. However, S2 also contains the lowest overall strain which could be an outlier or premature failure. Qualitatively, the model predictions match the experimental results.

The modelling is repeated for the case where only the material above the neutral axis is simulated to be loaded under compression. Figure 6-10 shows the results.

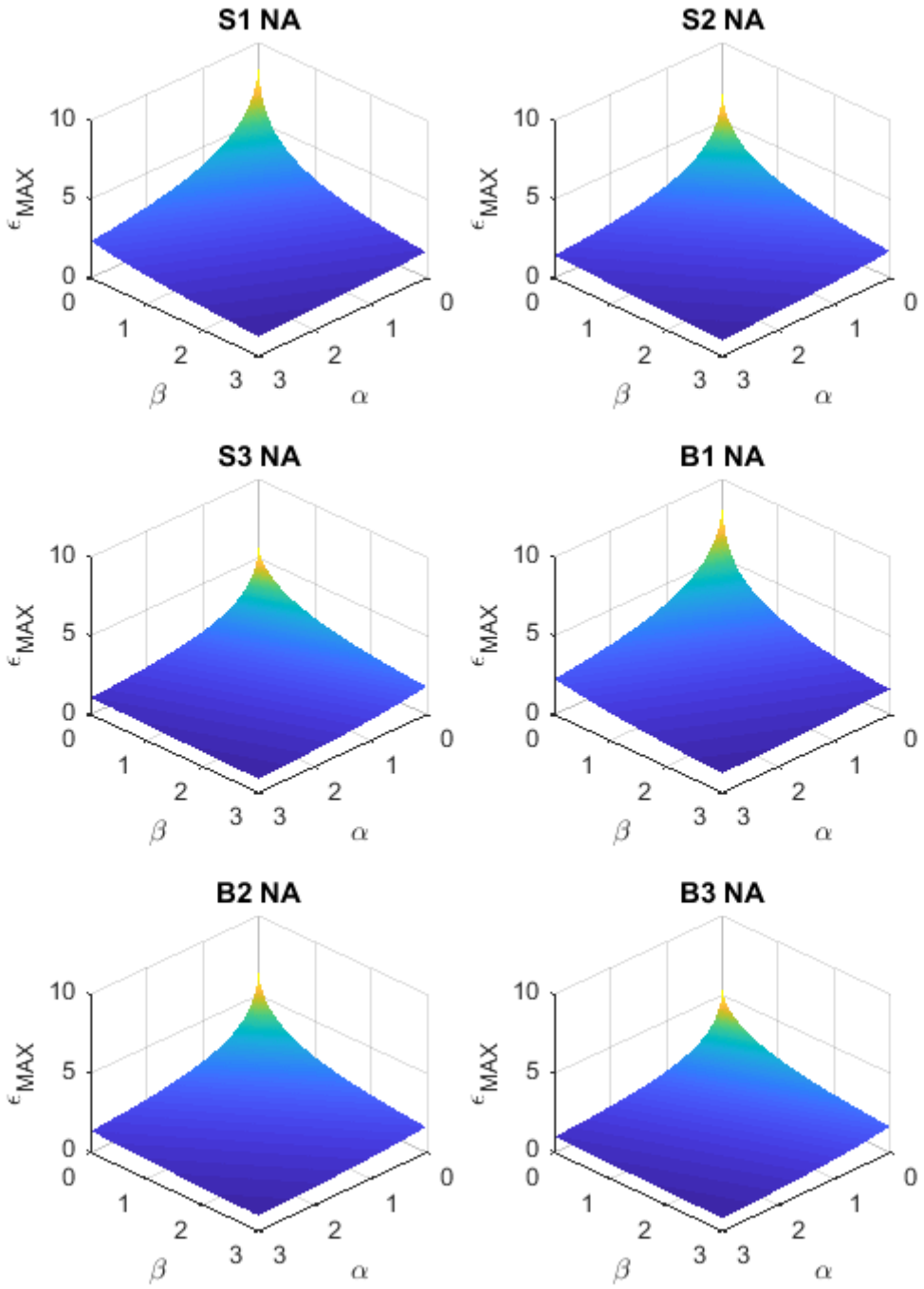

Figure 6-10: Results of SI modelling where only the portion above the neutral axis is simulated in an equivalent DC test.

Again, to simplify the results both materials are assumed to have the same initial misalignment, allowing cuts to be taken though the diagonal. This is shown in Figure 6-11.

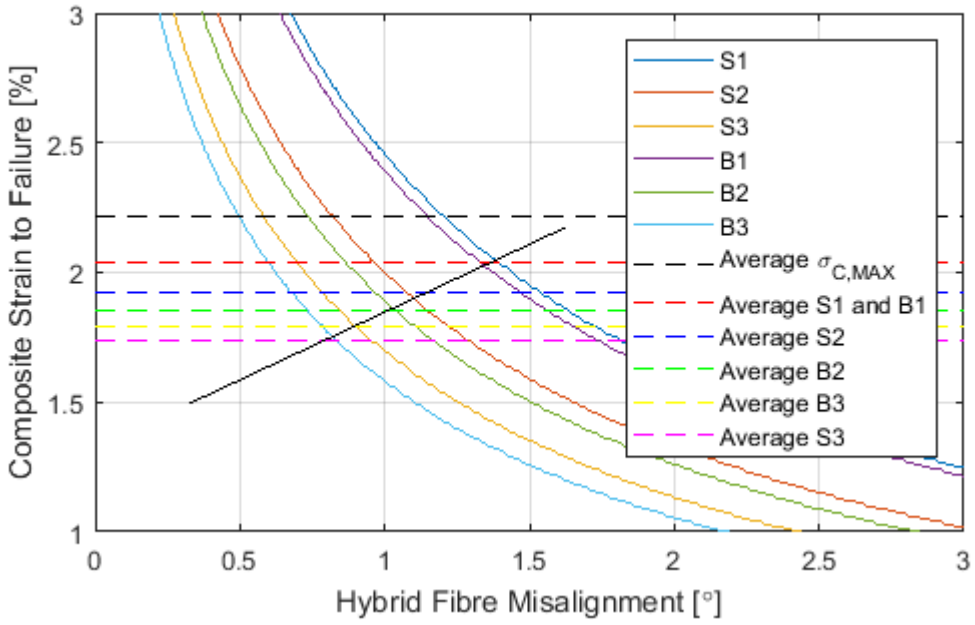

Figure 6-11: Diagonal cuts through all nanosilica SI surfaces using thickness above the neutral axis in equivalent DC test.

It can be seen that the curves are spaced further apart, but still occur in pairs (as for the total thickness case). The strains to failure are lower at a given strain due to a lower volume of S-glass that the carbon is hybridised with. Interestingly, the angled line that is drawn through the intersection points of SI curves with the predicted strains matches the results quite well. Again, with the exception of the set S3, the model accurately predicts the order in which the sets exhibit the highest average strain to failure.

6.1.3 Discussion

The maximum strain in carbon at failure was practically identical for all samples. The average strain at failure was different between the sets, with nSi material exhibiting higher strain than the baseline for the same number of plies (except for set S3 which contained the lowest overall strain – possibly a premature failure). The higher strain to failure observed for nSi samples can be attributed to the stiffer shear response of the matrix in that material. However, the thickness of the nSi plies is smaller than the thickness of the baseline ($t = 0.148\ mm$ and $t = 0.165\ mm$ respectively. The higher strain to failure could therefore be attributed to a decreased layer thickness and thus increased hybrid effect with the glass. However, the difference in stiffness is low. Moreover, the nSi material has higher stiffness which would cause its strain to be lower compared to the baseline. The two effects are therefore counteracting one another.

In addition to that, the SI modelling performed for the samples suggests a significant increase of instability strain for pure carbon ($\varepsilon_{MAX} = 1.26\%$ for baseline and $\varepsilon_{MAX} = 1.46\%$ for nSi at misalignment of $\alpha = 0.5\,°$.

The simulation of 4PB results using the model presented in Chapter 3 provides only qualitative results. It would be reasonable to assume the average fibre misalignment for all samples is similar, but this was not tested. However the SI model seems to match the experimental results when it is rotated as shown with lines drawn in Figure 6-9 and Figure 6-11. The replication of the 4PB test with limited material thickness (above neutral axis only) in the model showed similar results, but with a more severe rotation.

6.2 Compressive Behaviour as a Function of Fibre Volume Fraction

The ratio of resin to fibres in a unidirectional composite has a direct effect on the axial stiffness of the ply which can be calculated using the rule of mixtures [17]. The shear properties are also affected, as the resin is relatively soft compared to the fibres and decreasing its volume in the composite will increase the shear stiffness of the material.

Assuming that the compressive failure strain is a fibre property, it should not be affected by the fibre volume fraction of the material. However, it is postulated that compressive strain to failure is a function of shear response, axial stiffness and fibre alignment of the composite, as explained in Chapter 3. A series of tests have been performed to investigate the effects of fibre volume fraction and these will be presented here.

6.2.1 Testing

The compressive properties of the materials were obtained indirectly using a four-point bending (4PB) test. The materials used for the tests are presented in Table 6-7.

Table 6-7: Materials used in testing of the effects of fibre volume fraction

Material Designation	Manufacturer	Fibre Type	Resin Type	Cure Temperature [°C]	Measured Ply Thickness [mm]
33%	Hexcel	IM7	8552	180	0.129
50%	Hexcel	IM7	8552	180	0.130
Glass	Hexcel	S2GL	8552	180	0.159

The two carbon materials - $IM7/33\%/8552$ and $IM7/50\%/8552$ – use the same resin and fibres, but at a different volume fraction. The percentage value denominates the volume of

resin, suggesting that the 33% material has a higher fibre content within the same volume. Based on the rule of mixtures, it would therefore be expected to have a higher E_{11} modulus. The test schedule for the material is presented in Table 6-8.

Table 6-8: Tests performed to investigate the effects of fibre volume fraction on compressive behaviour of composite

Test	Method	Material	Lay-up	Data Obtained
Shear	ASTM D3518 [54]	33%	$[+45/-45]_{4S}$	Full shear stress - shear strain curve
		50%		
		Glass		
4PB	Custom 20-20-20	33% + Glass	$[G_{14}/C]$	Indirect compression strain
	Custom 30-30-30		$[G_{14}/C_2/G]$	
			$[G_{14}/C_3/G]$	
	Custom 20-20-20	50% + Glass	$[G_{14}/C]$	
	Custom 30-30-30		$[G_{14}/C_2/G]$	
			$[G_{14}/C_3/G]$	

It should be noted that the 4PB tests for single carbon ply do not have the additional glass ply on the surface. This may have an impact on the strain at failure, as the carbon is not shielded from the contact force introduced by the loading noses. This may result in complex stress state and lead to premature failure at the contact point.

Unlike the nanosilica samples, the volume fraction study did not involve testing of modulus and fibre tensile strain. Therefore, the 33% material properties were obtained from manufacturer's datasheet. The 50% material modulus was obtained by using the rule of mixtures [17].

Table 6-9: Properties of materials used in the volume fraction investigation

Material	Young's Modulus		Strain to Failure	
	Value [GPa]	Source	Value [%]	Source
33%	164	Datasheet	1.62	Datasheet
50%	123	Calculated	1.62	Assumed
Glass	45	Datasheet	3.87	Datasheet

The datasheet value for 33% material is consistent with the Young's modulus obtained from the rule of mixtures calculation based on basic fibre and resin properties. The shear test results can be seen in Figure 6-12.

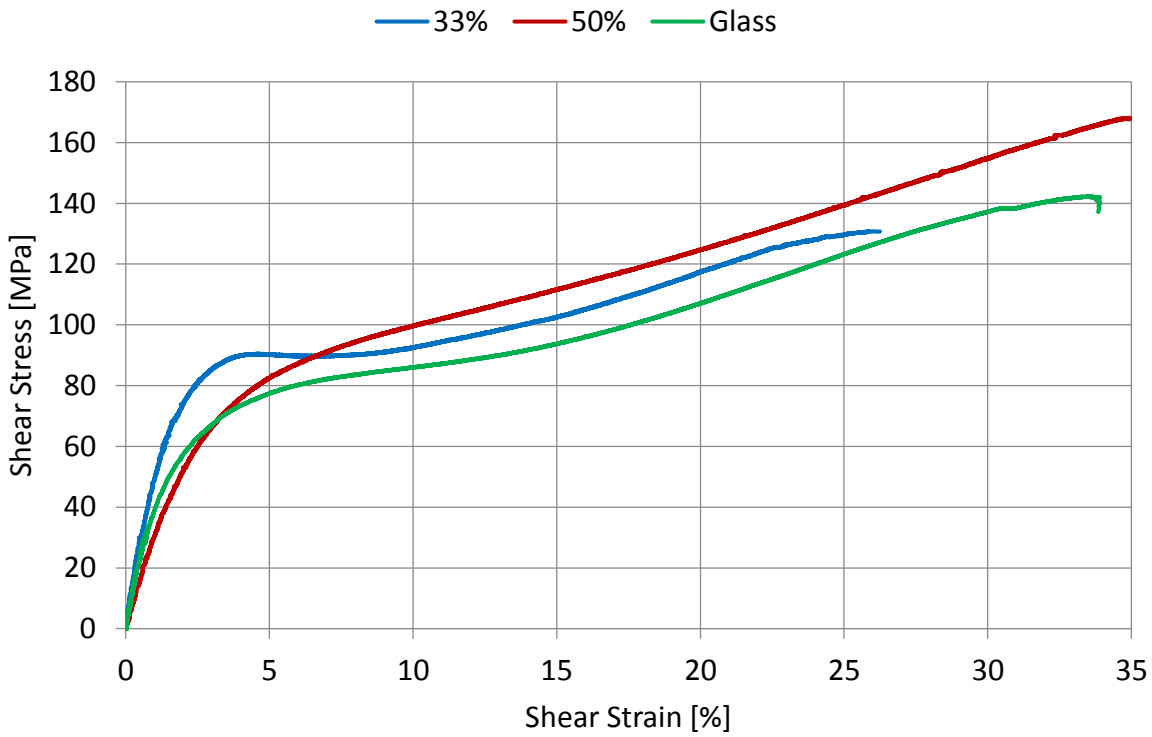

Figure 6-12: Shear testing results for the volume fraction study. Note that the 33% material exhibits a plateau between around 4% and 8% strain. Fibre rotation seems to occur at low strains in the 50% material, most likely due to high resin content. Glass has the lowest kneepoint stress of the three materials.

Visually matching the shear test curves with fitted functions yields the parameters shown in Table 6-10.

Table 6-10: Fit parameters for volume fraction shear instability modelling

Material	Maximum	Exponent	Linear
33%	94	78	0
50%	79	48	218
Glass	73	69	128

The fitted functions are shown in Figure 6-13. Again, it should be noted that good fit with the data is most important at low strains, as from previous experience the shear strain is unlikely to exceed a value of around $\tau = 60\ MPa$ when running the SI models.

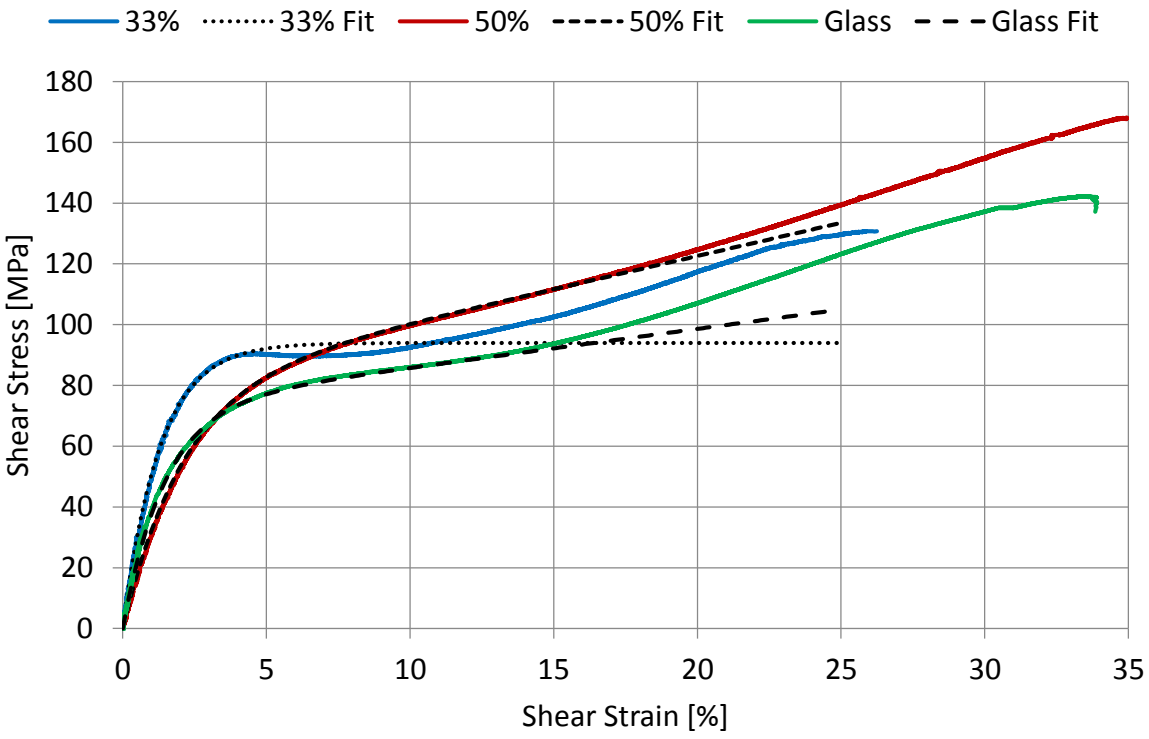

Figure 6-13: Shear response curves fitted with parametric curves. There is some overestimation of shear for the 33% material in the 5% to 10% range as the linear parameter is set to zero. This should not cause a problem as long as the shear strain at instability does not enter that range. The assumption must be checked for validity when running the model.

4PB tests were performed as outlined in Table 6-8. As the single carbon samples use a different span arrangement to the rest of the samples, they are shown independently in Figure 6-14.

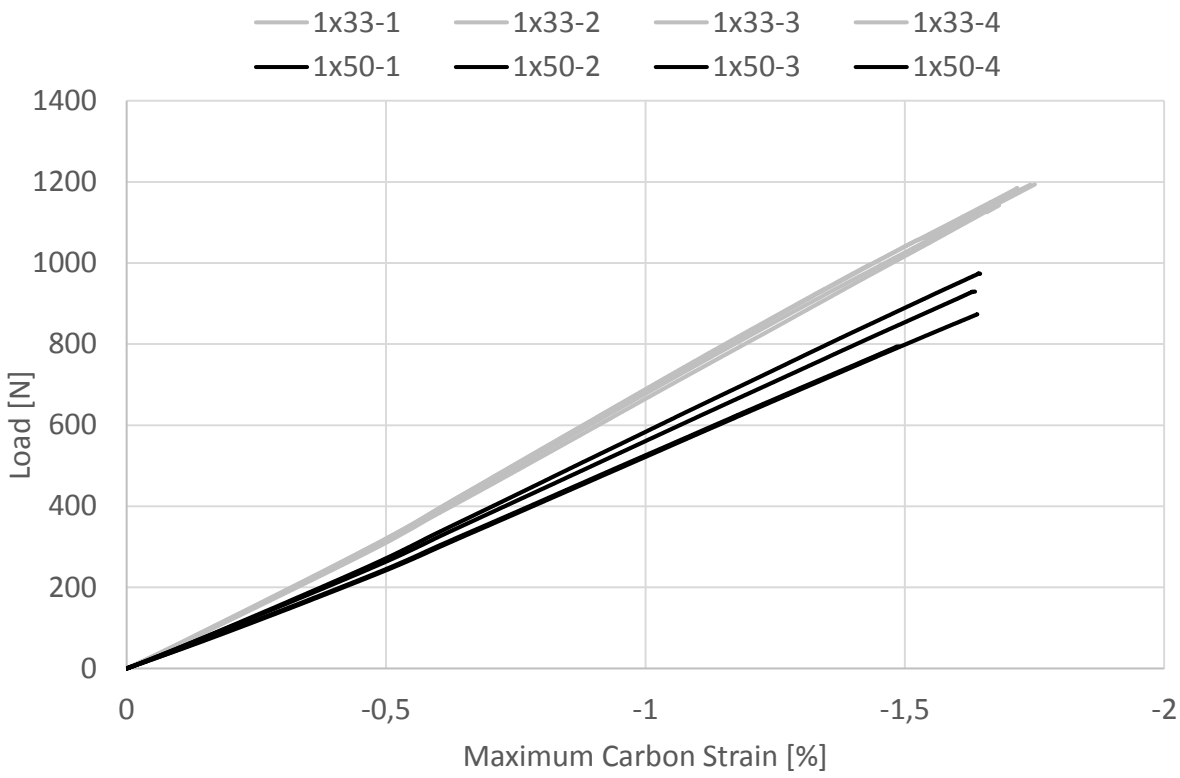

Figure 6-14: 4PB results of single carbon samples in the volume fraction investigation. Note the samples do not have a top glass ply to dissipate the loading nose contact stress and fail prematurely.

The 33% material samples are very consistent and follow the same load-strain path. There is some divergence in the 50% material, but the strains at failure are consistent for both sets. As expected, the 50% sample have a lower bending stiffness due to the lower stiffness of the carbon ply, all other factors being the same (with a slight change of carbon thickness). As the layup is lacking the top glass ply, it should not be compared to the double and triple carbon cases. The strains to failure are therefore regarded separately and can be seen in Table 6-11. The notation for the individual samples is similar to that for nanosilica:

1. The number in the front denotes the total carbon ply count
2. This is followed by the material designation
3. The number after the hyphen is the individual sample number within the set

Table 6-11: Maximum carbon strain at failure in single ply volume fraction samples

Sample	Failure Strain [%]	Set Average		All Samples Average	
	$\varepsilon_{C,MAX}$ [%]	Strain [%]	CoV	Strain [%]	CoV
1x33-1	-1.68	-1.72	1.56%	-1.66	4.75%
1x33-2	-1.74				
1x33-3	-1.75				
1x33-4	-1.72				
1x50-1	-1.64	-1.60	3.92%		
1x50-2	-1.64				
1x50-3	-1.63				
1x50-4	-1.49				

As it can be seen, the lowest maximum carbon strain at failure is $\varepsilon_{C,MAX} = -1.49\%$ for sample 1x50-4 and the highest is $\varepsilon_{C,MAX} = -1.75\%$ for sample 1x33-3. Visually, the samples can be regarded as two separate sets, and this is confirmed by the coefficient of variation being lower if they are treated as such as compared to treating them as a single set. However, the statistical significance is not strong.

As in the case of nanosilica samples, the maximum strain (at the top of the carbon layer) is different to the average strain. These are calculated and are shown in Table 6-12.

Table 6-12: Average carbon strain at failure in single ply volume fraction samples

Sample	Failure Strain [%]	Set Average		All Samples Average	
	$\varepsilon_{C,AVG}$ [%]	Strain [%]	CoV	Strain [%]	CoV
1x33-1	-1.58	-1.62	1.64%	-1.56	4.63%
1x33-2	-1.64				
1x33-3	-1.65				
1x33-4	-1.61				
1x50-1	-1.55	-1.51	4.05%		
1x50-2	-1.54				
1x50-3	-1.55				
1x50-4	-1.40				

The are very much alike to the maximum strain trends, with the same samples exhibiting maximum and minimum values and similar CoV values. Overall, the 50% material seems to

have lower strain to failure of the two materials. This is counterintuitive to what has been shown before. The expectation would be for the less stiff material to have a higher strain to failure, as the compressive stress would be lower at the same strain level, lowering the shear stress in the sample.

Before this is discussed further, let us have a look at the double and triple carbon sample results.

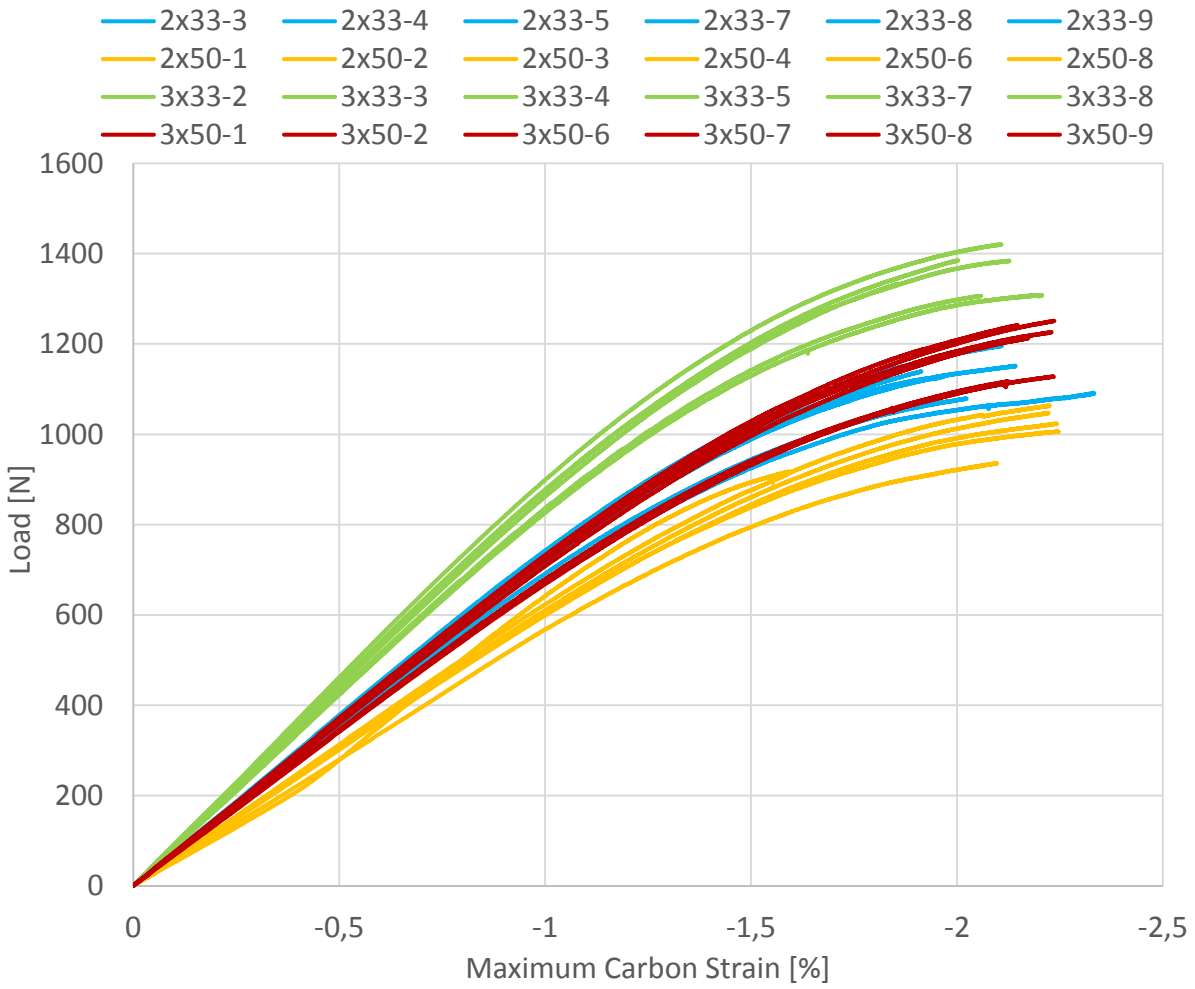

Figure 6-15: 4PB test results of double and triple carbon samples in the volume fraction investigation.

The overall shape of the loading curves is as expected with initial apparent stiffening followed by softening at higher strains. The triple 33% samples have the highest flexural stiffness due to their higher fibre content. Interestingly, the triple 50% samples have a similar modulus to double 33%. The summary of the results is presented in Table 6-13.

Table 6-13: Maximum carbon strain at failure in double and triple carbon samples for volume fraction investigation

Sample	Failure Strain [%]	Set Average		Material Average		All Samples Average	
	$\varepsilon_{C,MAX}$ [%]	Strain [%]	CoV	Strain [%]	CoV	Strain [%]	CoV
2x33-3	-2.11	-2.08	6.52%	-2.07	5.99%	-2.13	5.42%
2x33-4	-2.14						
2x33-5	-1.97						
2x33-7	-1.91						
2x33-8	-2.33						
2x33-9	-2.02						
3x33-2	-2.13	-2.06	5.35%				
3x33-3	-2.06						
3x33-4	-2.00						
3x33-5	-2.11						
3x33-7	-1.86						
3x33-8	-2.21						
2x50-1	-2.22	-2.21	2.53%				
2x50-2	-2.24						
2x50-3	-2.10						
2x50-6	-2.23						
2x50-8	-2.25						
3x50-1	-2.15	-2.19	2.05%	-2.20	2.31%		
3x50-2	-2.17						
3x50-6	-2.12						
3x50-7	-2.24						
3x50-8	-2.23						
3x50-9	-2.24						

Trends seem to be different for double and triple samples when compared to the single carbon set. 50% material has a higher maximum strain at failure than the 33% material, as would normally be expected. The opposite was true for the single carbon samples, most likely due to the lack of surface glass ply to dissipate the contact stress from the loading noses. Presence of a complex stress state in carbon under the loading nose is likely to lead to premature failure. 50% samples seem to be more susceptible to this, perhaps due to their lower out-of plane stiffness (caused by lower fibre content). In any case, the failure of single carbon samples can be deemed premature and not due to compressive failure of the carbon.

The lowest strain of $\varepsilon_{C,MAX} = -1.86\%$ occurs in sample 3x33-7 and the highest strain $\varepsilon_{C,MAX} = -2.33\%$ is observed in sample 2x33-8. The consistency of results is greater for 50% sets due to the lack of outliers, perhaps correlated with the lower stiffness of the material. Average strain for the sets is in line with expectations which can be summarised as follows:

1. The stiffer material would have a lower strain to failure due to increased compressive stress and resulting shear at the same strain
2. The same material would have a lower strain to failure at smaller carbon volume due to the hybrid effect with glass being more significant

The results are perfectly in line with these expectations, although the magnitude of the second effect is negligible (difference in strain of 0.02% between double and triple ply sets for both materials).

The maximum carbon strains shown in Table 6-13 are as expected, but a look on average strains should provide additional information. This can be seen in Table 6-14.

Table 6-14: Average carbon strain at failure in double and triple carbon samples for volume fraction investigation

Sample	Failure Strain [%]	Set Average		Material Average		All Samples Average	
	$\varepsilon_{C,AVG}$ [%]	Strain [%]	CoV	Strain [%]	CoV	Strain [%]	CoV
2x33-3	-1.86	-1.83	6.65%	-1.76	7.31%	-1.82	6.90%
2x33-4	-1.89						
2x33-5	-1.74						
2x33-7	-1.69						
2x33-8	-2.06						
2x33-9	-1.77						
3x33-2	-1.75	-1.69	5.27%				
3x33-3	-1.68						
3x33-4	-1.65						
3x33-5	-1.73						
3x33-7	-1.52						
3x33-8	-1.80						
2x50-1	-1.98	-1.96	2.77%				
2x50-2	-2.00						
2x50-3	-1.85						
2x50-6	-1.98						
2x50-8	-1.99						
3x50-1	-1.80	-1.83	2.19%				
3x50-2	-1.82						
3x50-6	-1.76						
3x50-7	-1.88						
3x50-8	-1.86						
3x50-9	-1.86						

The values for average carbon strain at failure in Table 6-14 match the above expectations of behaviour well. The same values of set average for set 2x33 and 2x50 are coincidental as the two materials seem to have an offset in their average strain at failure. Figure 6-16 shows how the average carbon strain varies with carbon thickness.

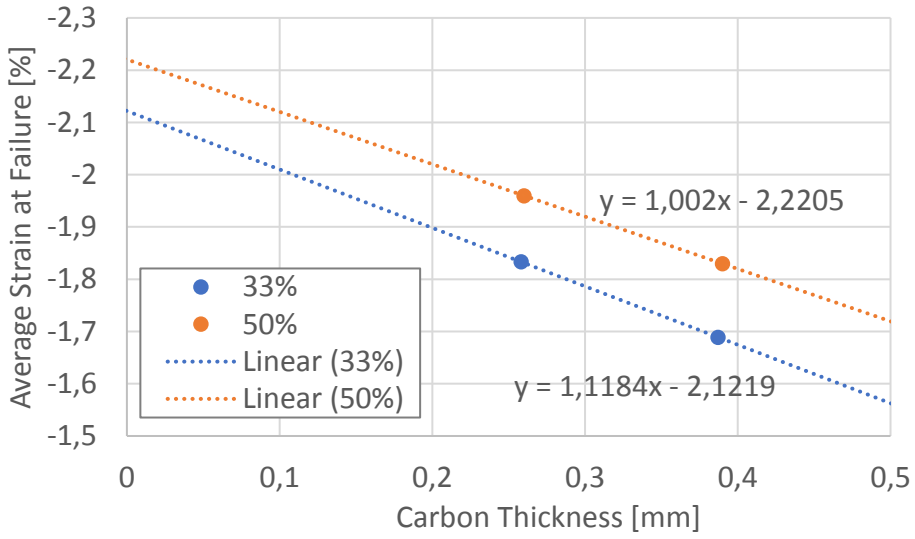

Figure 6-16: The variation of average strain at failure in carbon with the thickness of the carbon block within the 4PB sample in the volume fraction study

Results for single ply material are not included due to it failing prematurely. The drop in strain with increased carbon thickness is most likely due to a smaller hybrid effect with glass at increased carbon volume. Using the SI modelling tool may provide additional information.

6.2.2 Modelling

The shear and longitudinal stiffness data was used in the shear instability model to predict the SI curves for each individual material. These are shown in Figure 6-17.

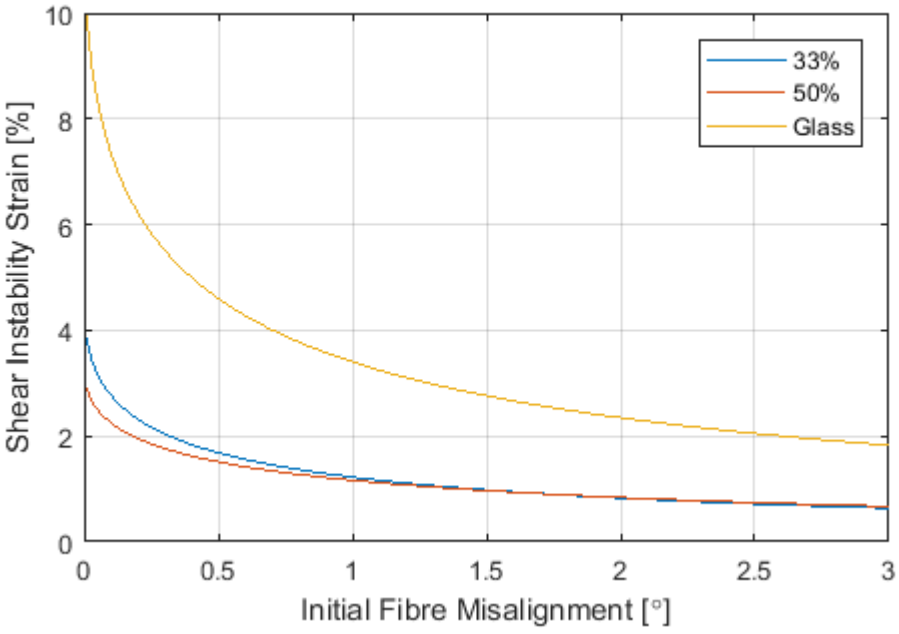

Figure 6-17: Individual shear instability curves modelled for the materials used in the volume fraction study.

As expected, the glass composite has a high instability strain and will likely fail due to fibre failure before the instability is reached. The carbon materials diverge at very low fibre misalignment with the 33% material having a higher instability strain, but they are essentially the same at misalignments of $> 1\,°$. This convergence is a mixture of two effects:

1. Lower longitudinal stiffness of 50% material increases its instability strain to a similar extent at all fibre misalignment values
2. Higher shear stiffness of 33% material increases its instability strain more significantly at low fibre misalignment values

For a benchmark value of $\alpha = 0.5\,°$, the instability strains in 33% and 50% materials are $\varepsilon_{MAX} = 1.69\%$ and $\varepsilon_{MAX} = 1.51\%$ respectively. The difference is small at 0.18% and the actual misalignment can be expected to be even larger, shrinking the difference. Because of this, the main difference in behaviour is likely to stem from the significant difference in stiffness between the two materials and the hybrid effect with the glass.

The trends between the two modelling approaches taken in section 6.1.2 were very similar and none predicted the strain accurately. Therefore, the more complex approach of modelling the material in compression (above the neutral axis) will not be repeated here.

Only four cases will be modelled – 2x33, 3x33, 2x50 and 3x50. The single carbon cases are assumed to have failed prematurely under the contact load from the loading noses due to lack of glass fibre ply on the surface. As the full SI surfaces are difficult to read in their full 3D form, they will be skipped and diagonal slices shown all on one graph, presented in Figure 6-18.

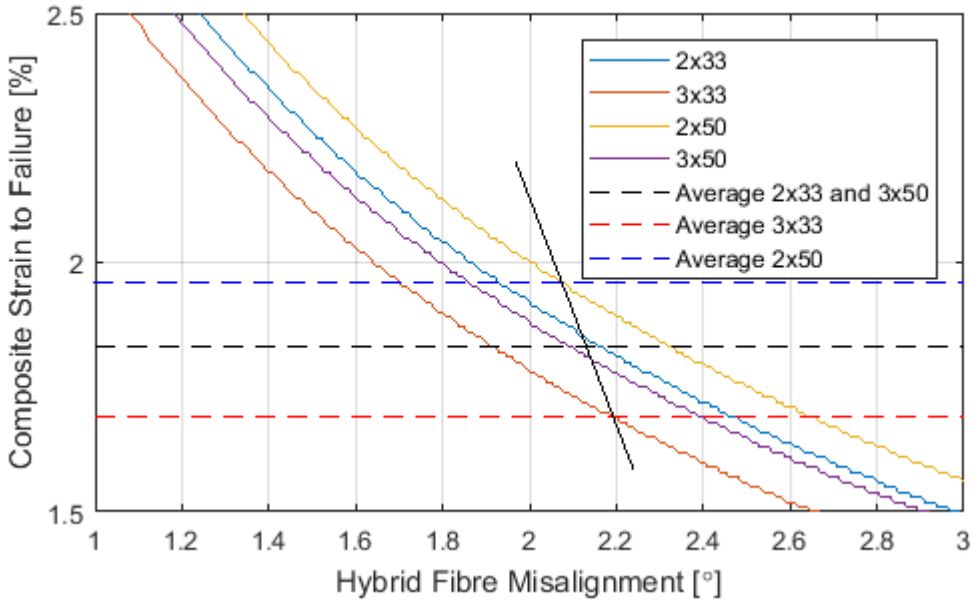

Figure 6-18: Shear instability modelling results for equivalent DC samples with the total thickness of 4PB samples.

The trends emerging from the modelling results are in line with the experimental results:

1. The tested sets with the highest (2x50) and the lowest (3x33) strain are correctly predicted by the model
2. The instability strain in 2x33 is predicted to be higher than 3x50, but test results show the same value of strain, however the difference between the two is only 0.03%

The angled black line joins the points at which the model matches the experimental results. The rotation of the SI envelope is in the opposite direction to the one shown in Figure 6-9. A further investigation is required to determine why that is.

6.2.3 Discussion

Two different carbon fibre prepregs made with the same fibre and resin, but to a different fibre volume fraction were tested using three sets of samples for each material with single, double and triple carbon ply. The single ply samples did not contain a top layer of glass to prevent contact failure under the loading noses and did not provide useful strain data. The remaining four sets of samples were tested in 4PB until failure and showed that the material with lower stiffness achieves a higher average strain at carbon failure. The SI model provides a qualitative explanation of the hybrid effect between the glass and the lower stiffness material resulting in lower overall stress in the sample, offsetting the shear instability. The

fibre misalignment values at which the failure is predicted in the model are high, but the model is not designed for 4PB and is mimicking a DC test.

One interesting observation was made in testing, namely the 2x50 material exhibiting a different failure angle to all other sets of samples. The failed specimens are shown in Figure 6-19. From it, the following can be seen:

1. There is a definite failure plane in carbon for each set of samples.
2. For samples 2x33 and 3x33 the plane is straight and at about $70\,°$ angle to the fibre direction
3. For samples 2x50 the plane is straight and at $90\,°$ angle to the fibre direction
4. For samples 3x50 the plane is not always straight and its angle may vary between $70\,°$ and $90\,°$ to the fibre direction. Damage is observed in two places rather than one for some specimens

The change in failure characteristics in 2x50 may be caused by the high volume fraction of the resin. However, it is not always observed within the 3x50 suggesting that the failure mode may be a result of the high failure strain. The angled failure plane is normally associated with a kink-band failure [89]. Samples 2x50 would require microscopic investigation to check whether a kink-band was formed. Unfortunately, the microscopy was not performed on this set of samples.

The damage in the carbon is seen in two distant locations in some of the 3x50 samples (first, fourth and fifth from the top), in the form of a failure plane located in the middle of the specimen, but not spanning both ends. There is delamination present around the crack plane, but the main failure plane is located elsewhere. This can be caused by abrasion of the top glass ply during surface preparation for strain gauge application. The abraded surface cracks under the high compressive loading. However, the set 2x50 is loaded to higher strains compared to 3x50 and does not see this behaviour despite undergoing the same surface preparation process.

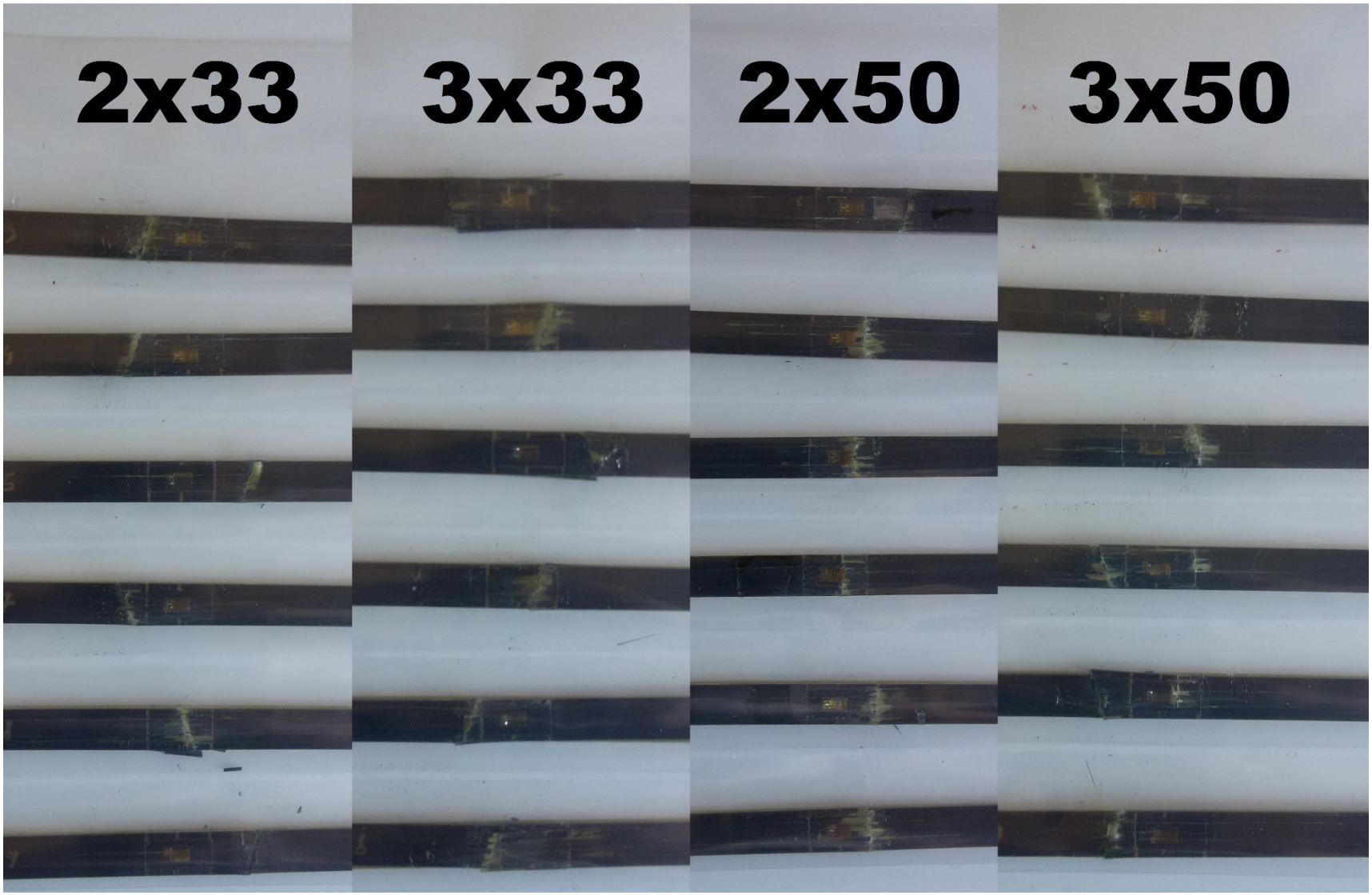

Figure 6-19: Failed specimens used in the volume fraction investigation. Note the different angle of failure in 2x50 and extensive damage in 3x50.

The cause of unusual failure modes in 50% material must be investigated further. This concludes the section on testing the variation in volume fraction using hybrid 4PB.

6.3 Comparison of 4PB and DC Testing for T1000 Hybrids

The testing methodology recommended in Chapter 5 can be followed for any material to define its basic tensile and shear properties, as well as gain insight into its compressive response. Paired with the SI model presented in Chapter 3, predictions of compressive failure can be made for hybrid samples. Two studies using the proposed methodology were presented so far:

1. The nanosilica-enhanced resin and its baseline with HEC from Gurit
2. The IM7 fibre with 8552 resin at 33% and 50% resin weight content

Both studies achieved high compressive strains in carbon and utilised SI model to successfully predict the relative strains between the sets of samples. However, how does the proposed 4PB test compare to a direct compression test for the same material?

This section will focus on 4PB investigation of T1000 fibre hybridised with 913/S2GL that were tested using the modified rig in Chapter 4 [1]. The same material tested previously was put through the recommended testing schedule. This was to compare the DC results with 4PB test in terms of the attainable strains. Due to lack of immediate correlation between DC and 4PB testing results and difficulty relating the SI model to 4PB data, the strain comparison can serve as a predictor on what compressive strain levels can be expected from the given test type.

6.3.1 Testing

Known material properties have previously been shown in Table 4-1. The summary of tests performed on T1000 can be seen in Table 6-15.

Table 6-15: Tests performed to compare DC results of T1000 hybrid testing to 4PB

Test	Method	Material	Lay-up	Data Obtained
Shear	ASTM D3518 [54]	T1000	$[+45/-45]_{4S}$	Full shear stress - shear strain curve
Tension	ASTM D3039 [80]	T1000	$[0]_{16}$	Young's modulus
ISTT	Czél [81]	T1000 + 913/S2GL	[G/C/G]	Tensile strain to failure
4PB	Custom 20-20-20	T1000 + 913/S2GL	$[G_{14}/C/G]$	Indirect compression strain

The results for the tension and ISTT tests are presented in Table 6-16.

Table 6-16: Measured properties of T1000

Property	Average	CoV
Young's Modulus [GPa]	125.7	2.59%
Strain to Failure [%]	2.04	2.22%

Fitted shear results for both materials used are shown in Figure 6-20.

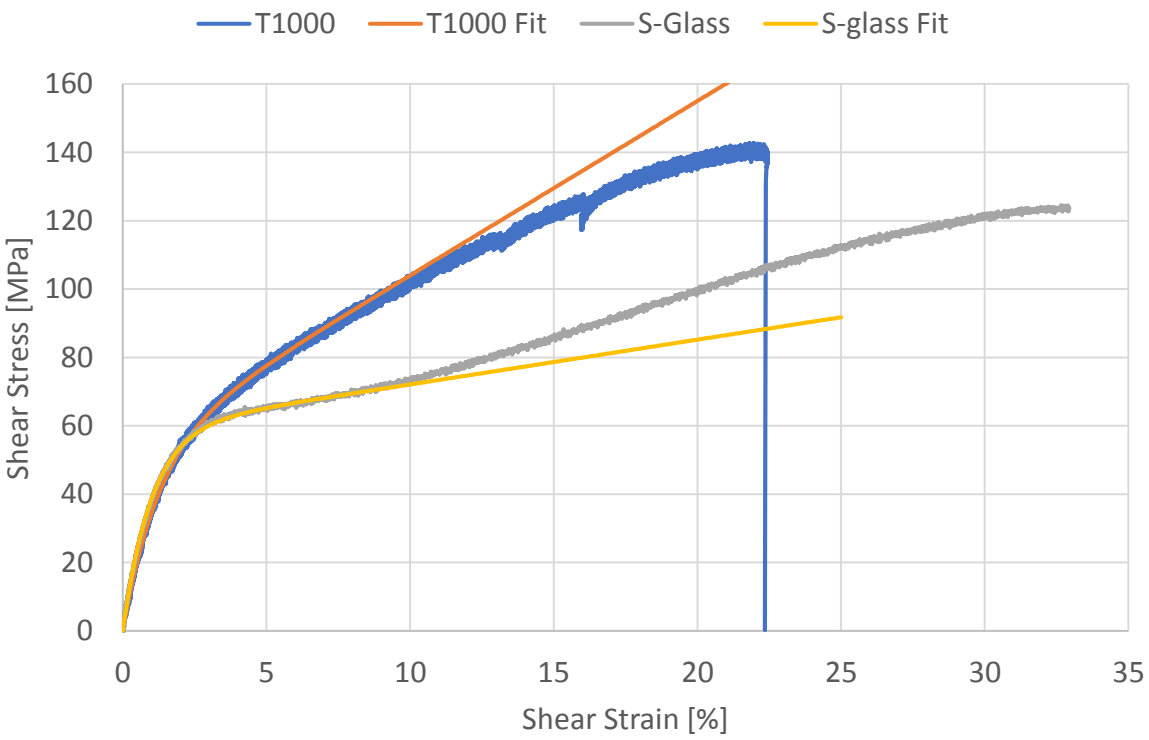

Figure 6-20: Shear results for T1000 and the fitted exponential-linear curves.

The constants used to fit the data are shown in Table 6-17:

Table 6-17: Fit parameters for T1000 shear instability modelling

Material	Maximum	Exponent	Linear
T1000	53	81	510
S-glass	59	100	131

The 4PB test results are presented in Figure 6-21.

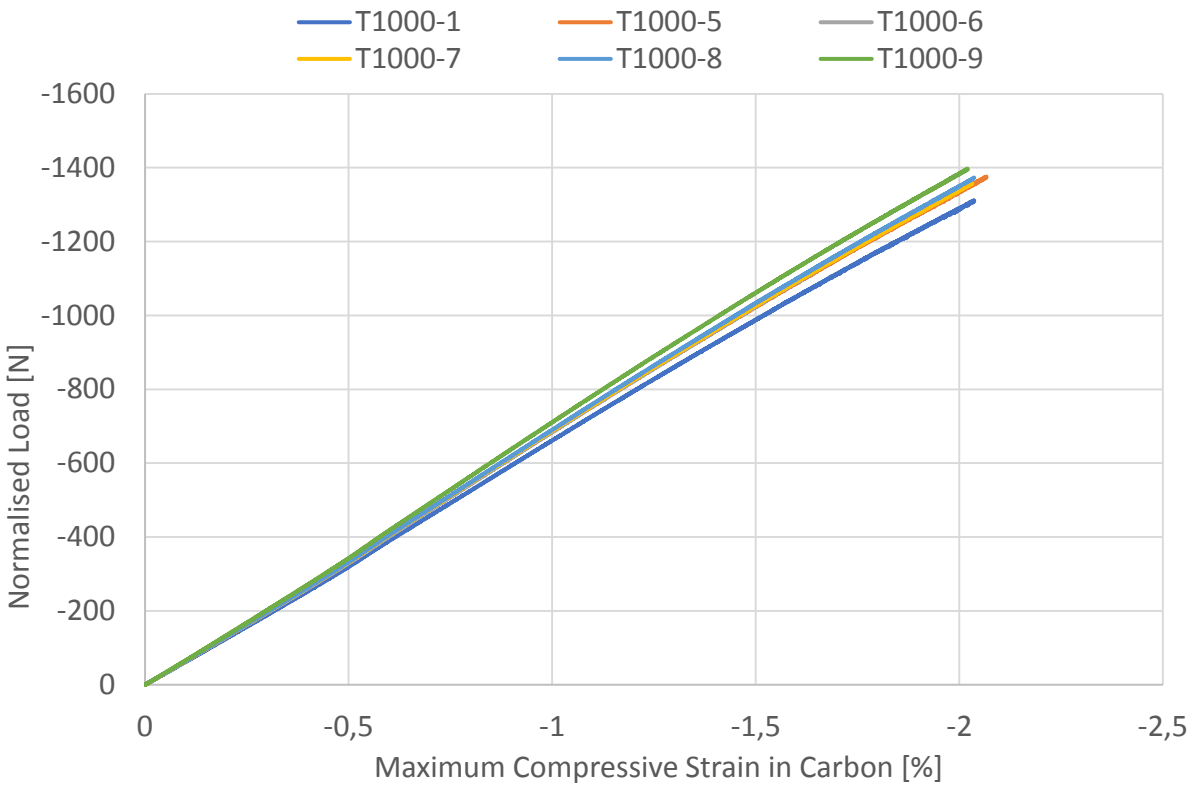

Figure 6-21: T1000 4PB testing results.

The maximum and average strains at failure are shown in Table 6-18.

Table 6-18: Carbon strain at failure in T1000 four-point bending samples

Sample	T1000-1	T1000-5	T1000-6	T1000-7	T1000-8	T1000-9	Average	CoV
$\varepsilon_{C,MAX}$	-2.04	-2.07	-1.89	-2.03	-2.04	-2.04	-2.02	2.86%
$\varepsilon_{C,AVG}$	-1.89	-1.91	-1.75	-1.88	-1.89	-1.87	-1.86	2.83%

The results are typical. Since only one material is being tested, there is no comparison to be made. SI modelling can be skipped as the material misalignment is not known and there is no other sample to compare the data to. The modelling was performed for the previous two studies presented in this chapter as they were all loaded in the same way, therefore. Comparison between samples that are actually loaded in DC and modelling of the *equivalent* sample that is tested in 4PB is not possible due to the completely different behaviour of the bending sample. In other words, the previous studies shown in this chapter *pretended* that the samples were loaded in DC for comparison purposes only. It is highly likely that if one of the two sets of samples fails at a lower strain in DC, it would also fail at a lower strain in 4PB.

6.3.2 Results and Discussion

Due to the inability of comparing SI modelling data between different loading arrangements, only the strains at failure can be compared. Table 6-19 shows the strains obtained from DC and 4PB testing

Table 6-19: Comparison of strains obtained for T100 through 4PB and DC testing

	Set Name	Carbon Content	Number of Blocked Plies	Strain [%]	CoV
DC	Single	19.2%	1	-2.03	4.52%
DC	Double	10.1%	1	-2.31	4.89%
DC	Triple	6.5%	1	-2.45	4.61%
4PB	T1000 Maximum	6.3%	4	-2.02	2.86%
4PB	T1000 Average	6.3%	4	-1.86	2.83%

It can be seen that the strains obtained from the DC test for a similar carbon content have a significantly higher strain compared to 4PB test. This may be due to the use of thin plies. In direct compression, thin plies are not blocked, thus having a glass fibre layer separating each T1000 ply. The hybrid effect in compression described in Chapter 3 is expected to be size-dependent. For very thick blocks of material and far away from the interface with the hybrid, the stress state is expected to be similar to the stress state in pure, single material under the same strain. If this is true, then the use of thin plies allows for maximum utilisation of the hybrid effect. In the case of 4PB testing shown here, the 4 blocked plies have a thickness of $t = 0.156\ mm$ which is of the order of a standard ply. The stress in the middle of the ply block may be higher due to the lack of hybrid effect at that distance from the interface with the glass, hence causing failure at a lower strain.

6.4 Summary

Three different studies were conducted using the four-point bending approach defined in Chapter 5. These were:

1. The impact of nanosilica addition to the resin using Gurit's SE84 LV and SE84 Nano™ resins with the same HEC fibre. The findings were as follows:
    a. The maximum carbon strain at failure was nearly identical for all samples with an average of $\varepsilon_{C,MAX} = -2.22\%$

b. The average strain in carbon at failure was more varied, as seen in Table 6-6: Average strain in the carbon at failure for all samples tested in the nanosilica investigation:
    i. The strain decreased with increased carbon volume for both nSi and baseline
    ii. The average strain in all nSi samples was slightly higher than the average strain in all baseline samples
c. The SI model correctly predicted the progression in strain at failure for the sets, with the exception of set S3 which had the lowest overall strain that could be considered an outlier

2. The impact of lower volume fraction for 8552/IM7 material. A standard 33% resin weight and a custom 50% resin weight materials were compared. The key findings:
    a. The maximum strains at failure were similar between the samples with double and triple ply carbon blocks
    b. The composite with lower fibre volume fraction exhibited a higher strain at failure due to its lower longitudinal stiffness
    c. The average strain was higher for the samples with lower carbon volume fraction
    d. SI model correctly predicted the general trends in terms of relative strains between the sets
    e. A different failure mode was observed for 2x55 set in which the failure plane was not angled to the cross-section of the specimen. This shift is attributed to the lower fibre volume fraction.
3. T1000 bending study to compare with the results presented previously in Chapter 4. It was found that:
    a. Strains obtained in DC are significantly higher for a similar volume fraction
    b. The difference in strain for 4PB may be due to blocking 4 carbon plies. This leads to suppression of hybrid effects which is postulated to be size (thickness) dependent

All studies achieved maximum strains in carbon in excess of 2%. Table 6-20 shows the comparison between the tensile strain to failure of individual materials and the maximum compressive strain achieved in testing.

Table 6-20: Comparison of tensile and compressive strains to failure in tested materials

Material	Tensile Failure Strain		Maximum Compressive Strain		Average Compressive Strain	
	Value [%]	CoV	Value [%]	CoV	Value [%]	CoV
nSi	1.76	2.58%	-2.23	2.95%	-2.04	4.49%
baseline	1.69	5.86%	-2.29	2.13%	-2.04	4.15%
33%	1.62	Datasheet	-2.08	6.52%	-1.83	6.65%
50%	1.62	Assumed	-2.21	2.53%	-1.96	2.77%
T1000	2.04	2.22%	-2.02	2.86%	-1.86	2.83%

It can be seen that the strains achieved in compression exceed in magnitude the tensile strains. This is a good indication that the assumptions of compressive failure being dependent on stiffness and misalignment are correct and that there is potential of compressing the carbon fibres far beyond their equivalent tensile strain.

This concludes the section. Extracting carbon fibre non-linearity from 4PB tests will be investigated next.

7 Non-linear Behaviour of Carbon in Compression

Chapter 6 presented results of testing using the 4PB test specified in Chapter 5. An additional advantage of using the test with the recommended instrumentation (strain gauges) is that the surface strains are measured directly. Assuming Timoshenko beam theory applies, the strain profile is linear across the specimen thickness. This allows the calculation of strain at any point in the section (which is used for calculating maximum and average strains in carbon in Chapter 6), but also the calculation of the neutral axis position. This can be used to extract additional information from a hybrid 4PB test in the form of carbon non-linearity.

7.1 Calculation of Carbon Modulus

The formula for calculating the centroid of the composite section was derived when creating the sample behaviour prediction spreadsheet explained in section 5.2.1. See Figure 5-2 and Equation 5.2:

$$\bar{y_c} = \frac{E_{g,bot} * t_{g,bot} * \frac{t_{g,bot}}{2} + E_c * t_c * \left(t_{g,bot} + \frac{t_c}{2}\right) + E_{g,top} * t_{g,top} * \left(t_{g,bot} + t_c + \frac{t_{g,top}}{2}\right)}{E_{g,bot} * t_{g,bot} + E_c * t_c + E_{g,top} * t_{g,top}} \tag{7.1}$$

It can be assumed that the glass at the top and bottom of the carbon has the same modulus:

$$E_{g,bot} = E_{g,top} = E_g \tag{7.2}$$

The formula then becomes:

$$\bar{y_c} = \frac{E_g t_{g,bot} \frac{t_{g,bot}}{2} + E_c t_c \left(t_{g,bot} + \frac{t_c}{2}\right) + E_g t_{g,top} \left(t_{g,bot} + t_c + \frac{t_{g,top}}{2}\right)}{E_g (t_{g,bot} + t_{g,top)} + E_c t_c} \tag{7.3}$$

$$\therefore \bar{y_c}(E_g(t_{g,bot} + t_{g,top}) + E_c t_c) = E_g \left(\frac{t_{g,bot}^2}{2} + t_{g,top}\left(t_{g,bot} + t_c + \frac{t_{g,top}}{2}\right)\right) + E_c \left(t_c t_{g,bot} + \frac{t_c^2}{2}\right) \tag{7.4}$$

$$\therefore \bar{y_c} E_c t_c - E_c \left(t_c t_{g,bot} + \frac{t_c^2}{2}\right) = E_g \frac{t_{g,bot}^2}{2} + E_g t_{g,top}\left(t_{g,bot} + t_c + \frac{t_{g,top}}{2}\right) - \bar{y_c} E_g (t_{g,bot} + t_{g,top}) \tag{7.5}$$

$$\therefore E_c\left(\bar{y_c}t_c - t_c t_{g,bot} - \frac{t_c^2}{2}\right)$$

$$= E_g\left(\frac{t_{g,bot}^2}{2} + t_{g,top}\left(t_{g,bot} + t_c + \frac{t_{g,top}}{2}\right) - \bar{y_c}\left(t_{g,bot} + t_{g,top}\right)\right) \tag{7.6}$$

$$\therefore E_c = E_g \frac{\frac{t_{g,bot}^2}{2} + t_{g,top}\left(t_{g,bot} + t_c + \frac{t_{g,top}}{2}\right) - \bar{y_c}\left(t_{g,bot} + t_{g,top}\right)}{\bar{y_c}t_c - t_c t_{g,bot} - \frac{t_c^2}{2}} \tag{7.7}$$

This can be rewritten in a simple form as:

$$E_c = E_g \frac{A - B\bar{y_c}}{\bar{y_c}t_c - C} \tag{7.8}$$

Where the constants A, B and C are simply geometric properties:

$$A = \frac{t_{g,bot}^2}{2} + t_{g,top}\left(t_{g,bot} + t_c + \frac{t_{g,top}}{2}\right) \tag{7.9}$$

$$B = t_{g,bot} + t_{g,top} \tag{7.10}$$

$$C = t_c t_{g,bot} + \frac{t_c^2}{2} \tag{7.11}$$

Assuming that the modulus of the glass E_g is constant, the carbon modulus can thus be calculated based on the sample geometry and the measured position of the centroid.

7.2 Carbon Modulus Change in T1000 Samples

The carbon modulus has been calculated for T1000 material investigated in section 6.3. The results can be seen in Figure 7-1. There is an initial dip in the modulus, most likely to the loading noses creating compression in the top surface before the force of friction is broken around 0.6% strain. There seems to be some disparity between the results, most likely due to thickness variation between the samples. However, the slope at which the calculated modulus decreases is very consistent.

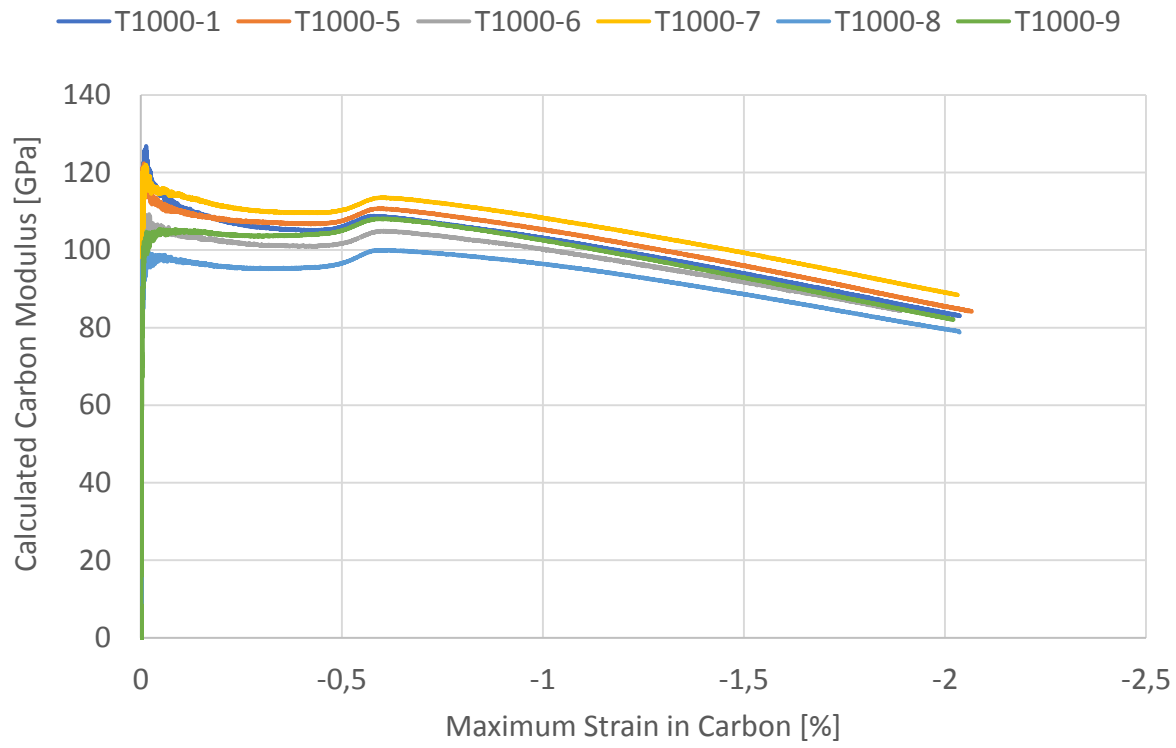

Figure 7-1: The calculated variation of modulus with strain of T1000 carbon material.

The initial, unstable portion of each curve was clipped. Trendlines have been drawn starting at a strain of $\varepsilon = 0.7\%$. The results are shown in Figure 7-2.

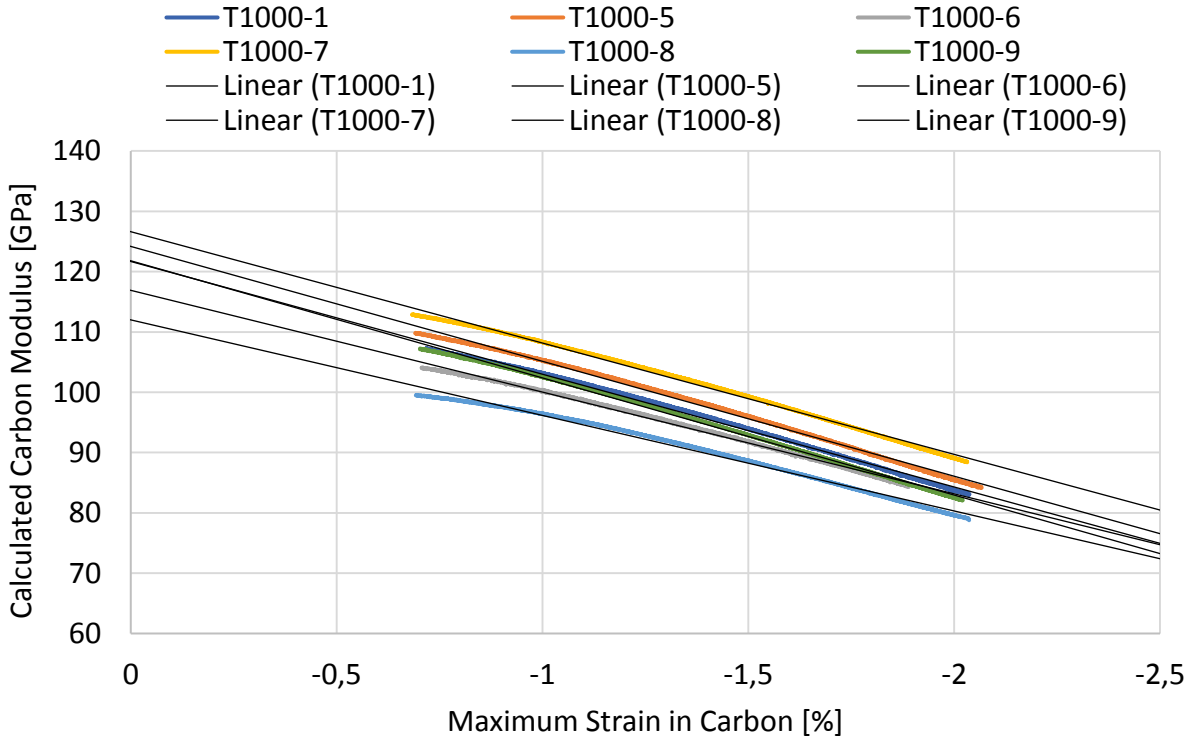

Figure 7-2: Best fit lines drawn through the linear potions of the graph in Figure 7-1.

The linear parameters of the best fit lines can be obtained. These are shown in Table 7-1.

Table 7-1: Line coefficients for trendlines shown in Figure 7-2.

Sample	A	B
B-1	18.70	121.7
B-5	19.05	124.2
B-6	16.87	116.9
B-7	18.46	126.6
B-8	15.84	112.0
B-9	19.42	121.8
Average	18.06	120.5
CoV	7.05%	4.00%

Parameter B is equal to the initial modulus at zero strain. Comparing with Table 6-16, the difference between the initial modulus calculated from the shift of the neutral axis and the tensile test results is 4.1% ($E_{11} = 125.7\ GPa$ versus $E_{11} = 120.5\ GPa$). This is consistent, especially when considering the small overall shift in the position of the neutral axis.

The linear parameter A is the slope of the curve or modulus degradation parameter $E_0\gamma$ [49]. It can be related back to the initial modulus:

$$E_0\gamma = 1806GPa \tag{7.12}$$

This is not very consistent with the value from Kant [49]:

$$E_0\gamma = 29.36E_0 - 1010 = 2527GPa \tag{7.13}$$

However, it is expected that the non-linearity coefficient is different in tension and compression.

7.3 Summary

The calculation of the carbon modulus from the centroid position yielded a value that is 4.1% smaller than the modulus measured using UD tensile test. This can potentially eliminate the need to test the modulus in tension if the 4PB test is conducted using strain gauges. The non-linear coefficient was derived for the carbon material, but did not match the relationship between the initial modulus and extent of non-linearity. However, the relationship seems to work for tension with no guarantee the same behaviour occurs in compression.

This concludes the work on non-linearity.

8 Conclusions

Over the course of this work, the author embarked on a quest to convince the reader that compressive failure of the more common (high strength) carbon fibres is not a fibre property. This fact is theoretically known, but no comprehensive and convincing reviews of the subject are known to the author.

8.1 Summary

Chapter 2 provided a brief overview of literature suggesting that carbon fibres are not inherently brittle in compression and that high strains are achievable.

Chapter 3 introduced a shear instability model that uses iterative solving of equilibrium equations in order to predict the axial strain in the composite at which convergence of shear strain γ becomes unstable. It is postulated that the following parameters impact the compressive failure:

1. Shear response of the composite
2. Longitudinal stiffness of the composite
3. Initial fibre misalignment

Fragmentation failure is possible for carbon fibre, but limited to high-stiffness materials, as shown in Figure 3-5.

It is found that the **shear instability is a stress-based phenomenon**. Once the critical stress is reached in the matrix, the instability will occur.

The model is extended to a secondary material with compatible shear deformation to allow for prediction of instability in hybrid samples. Hybrid effect is defined for compression as the relief of complimentary shear stress required for equilibrium by lowering the longitudinal stiffness of the composite:

$$\frac{E_1 t_1 + E_2 t_2}{t_1 + t_2} = E_{AVG} \tag{8.1}$$

Therefore:

$$\gamma \propto E_{AVG} \tag{8.2}$$

Also, the following observations can be made from the above equations:

1. The higher the misalignment, the lower the shear instability stress
2. The higher the shear stiffness of the matrix, the higher the shear instability stress

These findings suggest that hybridisation of carbon fibre with glass would lead to an improved compressive strain for the hybrid due to the described hybrid effect.

Hybrid samples are manufactured and tested using an existing ICMST test in Chapter 4. The obtained strains are higher than equivalent tensile strains for the material. It is shown that the strain to failure decreases with increasing volume of carbon in the hybrid, as expected from the modelling undertaken in Chapter 3.

Fibre misalignment measurement is performed for the DC samples to find very good consistency with the predictions of failure strain from the SI model.

Direct compression test suffers from stress concentrations due to shear lag from the tabs. FE modelling is introduced to calculate the strain in the affected area. It is found that despite the stress concentrations the hybrid effect holds true and samples with more carbon volume fail at lower strains.

Due to the stress concentration problems with the DC test, an indirect testing approach using four-point bending (4PB) is proposed in Chapter 5. Derivation of a sample design tool is performed, along with corrections for geometric non-linearity at high displacements. A test schedule utilising simple layups and methods is proposed in order to investigate compressive behaviour of materials.

Extensive testing using the proposed schedule is presented in Chapter 6. Two studies are performed on materials containing the same fibre to find the following:

1. Fibre type does not determine the compressive strain to failure
2. Lowering the longitudinal stiffness of the material improves strain to failure for the same fibre type
3. Improving the shear stiffness of the material improves strain to failure for the same fibre type

A comparison between the obtained tensile and compressive strains for the materials is shown in Table 6-20, with compressive strains being higher in magnitude than tensile strains for four out of the five materials testes. If results from Chapter 4 were also included, all of the tested materials would have higher strains in compression.

Chapter 7 investigates the possibility of capturing the softening behaviour of carbon fibre under compression and quantifies the non-linearity coefficient based on the T1000 results. The initial modulus obtained from centroid position is within 4.1% of the value obtained from tensile testing. 4PB test may therefore be used to obtain the longitudinal modulus of the carbon in a hybrid specimen, potentially eliminating the need for an additional test.

8.2 Conclusions

The test results seem to confirm the findings of Ueda [2], in that the compressive strain achievable with carbon fibre is higher than tensile strain. Non-linearity is measured and softening behaviour confirmed. The assumptions of the modelling framework presented in Chapter 3 are confirmed in Chapter 6 and very close predictions of failure strain are made for T1000 hybrids in Chapter 4. It has been shown that:

1. A fundamental, computationally inexpensive model is able to provide accurate predictions of compressive failure based only on shear stiffness, longitudinal stiffness and fibre misalignment
2. Hybridisation can be utilised within existing test methods to achieve significantly higher compressive strains in carbon composites
3. A versatile hybrid 4PB test can be used instead of direct methods to test carbon composites to high strains
4. The same test can be used to observe non-linear behaviour and potentially reliably measure longitudinal stiffness

However, the application of the results obtained herein may not be practical. The high strains in carbon are obtained only within a hybrid sample. The addition of glass fibre adds weight and degrades stiffness, effectively nullifying the two main advantages of carbon fibre composites.

8.3 Future Work

Several observations were made within this work that the author had no explanation for, and that seemed interesting areas of further research. These will be discussed here.

1. The SI model presented in Chapter 3 is limited to linear materials in axial compression. A derivation of a model specifically for bending loads could provide more insight into specimen design or improve predictions.
2. The axial model seems to correlate reasonably well with the samples tested in 4PB, but experiences rotation (see Figure 6-9). Can this be addressed and adjusted for?
3. The existing model can be improved to allow for the non-linear behaviour of the fibre.
4. Large validation strategy is required for the models. A method of quickly and reliably assessing the fibre misalignment in the composite samples would greatly assist this process [90].
5. Investigation of other bending test methods like pin-ended buckling may allow even higher strain to be obtained [35].
6. Repetitive loading of the material at high strains ($> 90\%$ compressive strain) could provide insight whether the plateau in single carbon fibres is associated with damage.
7. Testing with truly high-performance matrices (orders of magnitude higher stiffness than epoxy) could provide enough restraint to the fibres to achieve $> 10\%$ strains on a component level.

All avenues of exploration seem valid and interesting. These suggestions are intentionally kept general. Implementation of some seems plausible almost immediately, while others may have to wait for the evolution of available materials.

References

[1] J. Häberle and F. Matthews, “An improved technique for compression testing of unidirectional fibre-reinforced plastics; development and results,” *Composites*, vol. 25, no. 5, pp. 358–371, May 1994, doi: 10.1016/S0010-4361(94)80006-5.

[2] M. Ueda, W. Saito, R. Imahori, D. Kanazawa, and T.-K. Jeong, “Longitudinal direct compression test of a single carbon fiber in a scanning electron microscope,” *Compos. Part A Appl. Sci. Manuf.*, vol. 67, pp. 96–101, Dec. 2014, doi: 10.1016/j.compositesa.2014.08.021.

[3] K. S. Macturk, R. K. Eby, and W. W. Adams, “Characterization of compressive properties of high-performance polymer fibres with a new microcompression apparatus,” *Polymer (Guildf).*, vol. 32, no. 10, pp. 1782–1787, 1991, doi: 10.1016/0032-3861(91)90363-N.

[4] A. H. Shinohara, T. Sato, F. Saito, T. Tomioka, and Y. Arai, “A novel method for measuring direct compressive properties of carbon fibres using a micro-mechanical compression tester,” *J. Mater. Sci.*, vol. 28, no. 24, pp. 6611–6616, 1993, doi: 10.1007/BF00356404.

[5] M. Shioya and M. Nakatani, “Compressive strengths of single carbon fibres and composite strands,” *Compos. Sci. Technol.*, vol. 60, no. 2, pp. 219–229, Feb. 2000, doi: 10.1016/S0266-3538(99)00123-2.

[6] M. Ueda and M. Akiyama, “Compression test of a single carbon fiber in a scanning electron microscope and its evaluation via finite element analysis,” *Adv. Compos. Mater.*, vol. 28, no. 1, pp. 57–71, 2019, doi: 10.1080/09243046.2018.1433506.

[7] F. Tanaka, T. Okabe, H. Okuda, I. a. Kinloch, and R. J. Young, “The effect of nanostructure upon the compressive strength of carbon fibres,” *J. Mater. Sci.*, vol. 48, no. 5, pp. 2104–2110, Nov. 2012, doi: 10.1007/s10853-012-6984-z.

[8] J. D. Littell, C. R. Ruggeri, R. K. Goldberg, G. D. Roberts, W. A. Arnold, and W. K. Binienda, “Measurement of Epoxy Resin Tension, Compression, and Shear Stress–Strain Curves over a Wide Range of Strain Rates Using Small Test Specimens,” *J. Aerosp. Eng.*, vol. 21, no. 3, pp. 162–173, Jul. 2008, doi: 10.1061/(ASCE)0893-1321(2008)21:3(162).

[9] a. Jumahat, C. Soutis, F. R. Jones, and A. Hodzic, “Fracture mechanisms and failure

analysis of carbon fibre/toughened epoxy composites subjected to compressive loading," *Compos. Struct.*, vol. 92, no. 2, pp. 295–305, Jan. 2010, doi: 10.1016/j.compstruct.2009.08.010.

[10] P. Berbinau, C. Soutis, P. Goutas, and P. Curtis, "Effect of off-axis ply orientation on 0°-fibre microbuckling," *Compos. Part A Appl. Sci. Manuf.*, vol. 30, no. 10, pp. 1197–1207, Oct. 1999, doi: 10.1016/S1359-835X(99)00026-3.

[11] C. Soutis and P. T. Curtis, "A method for predicting the fracture toughness of CFRP laminates failing by fibre microbuckling," *Compos. Part A Appl. Sci. Manuf.*, vol. 31, no. 7, pp. 733–740, Jul. 2000, doi: 10.1016/S1359-835X(00)00003-8.

[12] E. Orowan, "A type of plastic deformation new in metals," *Nature*, no. 3788, pp. 643–644, 1942.

[13] J. Anderson, "Kink bands and related geological structures," *Nature*, no. 4960, pp. 801–802, 1964.

[14] A. G. Evans and W. F. Adler, "Kinking as a mode of structural degradation in carbon fiber composites," *Acta Metall.*, vol. 26, no. 5, pp. 725–738, May 1978, doi: 10.1016/0001-6160(78)90023-8.

[15] E. T. Camponeschi, J. W. Gillespie, and D. J. Wilkins, "Kink-Band Failure Analysis of Thick Composites in Compression," *J. Compos. Mater.*, vol. 27, no. 5, pp. 471–490, Jan. 1993, doi: 10.1177/002199839302700502.

[16] S. Pimenta, R. Gutkin, S. T. Pinho, and P. Robinson, "A micromechanical model for kink-band formation: Part I - Experimental study and numerical modelling," *Compos. Sci. Technol.*, vol. 69, no. 7–8, pp. 948–955, 2009, doi: 10.1016/j.compscitech.2009.02.010.

[17] G. R. Liu, "A step-by-step method of rule-of-mixture of fiber- and particle-reinforced composite materials," *Compos. Struct.*, vol. 40, no. 3–4, pp. 313–322, Dec. 1997, doi: 10.1016/S0263-8223(98)00033-6.

[18] B. W. Rosen, "Mechanics of composite strengthening," *Fiber Compos. Mater. Am. Soc. Met.*, vol. 726, pp. 95–109, 1965.

[19] M. Hetényi, *Beams on elastic foundation: theory with applications in the fields of civil*

and mechanical engineering. University of Michigan, 1971.

[20] A. S. ARGON, “Fracture of Composites,” 1972, pp. 79–114.

[21] B. Budiansky, “Micromechanics,” *Comput. Struct.*, vol. 16, no. 1–4, pp. 3–12, Jan. 1983, doi: 10.1016/0045-7949(83)90141-4.

[22] B. Budiansky and N. A. Fleck, “Compressive failure of fibre composites,” *J. Mech. Phys. Solids*, vol. 41, no. 1, pp. 183–211, Jan. 1993, doi: 10.1016/0022-5096(93)90068-Q.

[23] M. Wisnom, “The effect of fibre misalignment on the compressive strength of unidirectional carbon fibre/epoxy,” *Composites*, vol. 21, no. 5, pp. 403–407, Sep. 1990, doi: 10.1016/0010-4361(90)90438-3.

[24] M. Wisnom and J. Atkinson, “Compressive failure due to shear instability: experimental investigation of waviness and correlation with analysis,” *J. Reinf. Plast. …*, vol. 15, pp. 420–439, 1996, doi: 10.1177/073168449601500404.

[25] D. H. Woolstencroft, A. R. Curtis, and R. I. Haresceugh, “A comparison of test techniques used for the evaluation of the unidirectional compressive strength of carbon fibre-reinforced plastic,” *Composites*, vol. 12, no. 4, pp. 275–280, Oct. 1981, doi: 10.1016/0010-4361(81)90018-5.

[26] G. A. Schoeppner and R. L. Sierakowski, “Review of compression test methods for organic matrix composites,” *J. Compos. Technol. Res.*, vol. 12, no. 1, pp. 3–12, 1990.

[27] E. Camponeschi, “Compression of Composite Materials: A Review,” in *Composite Materials: Fatigue and Fracture (Third Volume)*, 100 Barr Harbor Drive, PO Box C700, West Conshohocken, PA 19428-2959: ASTM International, 2019, pp. 550-550–29.

[28] ASTM D695, “Standard Test Method for Compressive Properties of Rigid Plastics,” *ASTM Int.*, no. July, pp. 1–8, 2010, doi: 10.1520/D0695-15.

[29] ASTM, “Standard Test Method for Compressive Properties of Polymer Matrix Composite Materials Using a Combined Loading Compression (CLC) Test Fixture,” *D6641*, vol. 12, no. 1, p. 3, 2019, doi: 10.1520/D6641_D6641M.

[30] D3410, “Compressive Properties of Polymer Matrix Composite Materials with Unsupported Gage Section by Shear,” *ASTM Stand.*, vol. 03, no. Reapproved 2008, pp.

1–16, 2008, doi: 10.1520/D3410.

[31] M. R. Wisnom, “On the high compressive strains achieved in bending tests on unidirectional carbon-fibre/epoxy,” *Compos. Sci. Technol.*, vol. 43, no. 3, pp. 229–235, 1992, doi: 10.1016/0266-3538(92)90093-I.

[32] M. Wisnom, “Size effects in the testing of fibre-composite materials,” *Compos. Sci. Technol.*, vol. 59, no. 13, pp. 1937–1957, Oct. 1999, doi: 10.1016/S0266-3538(99)00053-6.

[33] ASTM D790-10, *Standard Test Methods for Flexural Properties of Unreinforced and Reinforced Plastics and Electrical Insulating Materials*. West Conshohocken, PA: ASTM International, 2010.

[34] A. D6272-10, “Standard Test Method for Flexural Properties of Unreinforced and Reinforced Plastics and Electrical Insulating Materials by Four-Point Bending,” *ASTM D6272-10*. pp. 1–9, 2014, doi: 10.1520/D6272.

[35] M. R. Wisnom, J. W. Atkinson, and M. I. Jones, “Reduction in compressive strain to failure with increasing specimen size in pin-ended buckling tests,” *Compos. Sci. Technol.*, vol. 57, no. 9–10, pp. 1303–1308, Jan. 1997, doi: 10.1016/S0266-3538(97)00057-2.

[36] G. C. Everstine and A. C. Pipkin, “Stress channelling in transversely isotropic elastic composites,” *Zeitschrift für Angew. Math. und Phys. ZAMP*, vol. 22, no. 5, pp. 825–834, 1971, doi: 10.1007/BF01591811.

[37] J. Summerscales and D. Short, “Carbon fibre and glass fibre hybrid reinforced plastics,” *Composites*, vol. 9, no. 3, pp. 157–166, 1978, doi: 10.1016/0010-4361(78)90341-5.

[38] G. Marom, S. Fischer, F. R. Tuler, and H. D. Wagner, “Hybrid effects in composites: conditions for positive or negative effects versus rule-of-mixtures behaviour,” *J. Mater. Sci.*, vol. 13, no. 7, pp. 1419–1426, 1978, doi: 10.1007/BF00553194.

[39] P. W. Manders and M. G. Bader, “The strength of hybrid glass/carbon fibre composites,” *J. Mater. Sci.*, vol. 16, no. 8, pp. 2246–2256, Aug. 1981, doi: 10.1007/BF00542387.

[40] Y. Swolfs, L. Gorbatikh, and I. Verpoest, “Fibre hybridisation in polymer composites: A

review," *Compos. Part A Appl. Sci. Manuf.*, vol. 67, pp. 181–200, 2014, doi: 10.1016/j.compositesa.2014.08.027.

[41] G. Czél and M. R. Wisnom, "Demonstration of pseudo-ductility in high performance glass/epoxy composites by hybridisation with thin-ply carbon prepreg," *Compos. Part A Appl. Sci. Manuf.*, vol. 52, pp. 23–30, Sep. 2013, doi: 10.1016/j.compositesa.2013.04.006.

[42] H. N. Yu, M. L. Longana, M. Jalalvand, M. R. Wisnom, and K. D. Potter, "Hierarchical pseudo-ductile hybrid composites combining continuous and highly aligned discontinuous fibres," *Compos. Part A Appl. Sci. Manuf.*, vol. 105, pp. 40–56, 2018, doi: 10.1016/j.compositesa.2017.11.005.

[43] G. Czél *et al.*, "Pseudo-ductility and reduced notch sensitivity in multi-directional all-carbon/epoxy thin-ply hybrid composites," *Compos. Part A Appl. Sci. Manuf.*, vol. 104, pp. 151–164, 2018, doi: 10.1016/j.compositesa.2017.10.028.

[44] G. Czél, M. Jalalvand, M. R. Wisnom, and T. Czigány, "Design and characterisation of high performance, pseudo-ductile all-carbon/epoxy unidirectional hybrid composites," *Compos. Part B Eng.*, vol. 111, pp. 348–356, 2017, doi: 10.1016/j.compositesb.2016.11.049.

[45] M. Wisnom *et al.*, "High Performance Ductile Composite Technologies (HiPerDuCT) EPSRC Programme Grant," no. November, pp. 1–64, 2018.

[46] R. W. Curtis GJ, Milne JM, "Non-Hookean Behaviour of Strong Carbon Fibres," *Nature*, 1968, doi: 10.1017/CBO9781107415324.004.

[47] W. H. m Van Dreumel and J. L. m Kamp, "Non Hookean Behaviour in the Fibre Direction of Carbon-Fibre Composites and the Influence of Fibre Waviness on the Tensile Properties," *J. Compos. Mater.*, vol. 11, no. 4, pp. 461–469, 1977, doi: 10.1177/002199837701100408.

[48] I. M. Djordjević, D. R. Sekulić, M. N. Mitrić, and M. M. Stevanović, "Non-hookean elastic behavior and crystallite orientation in carbon fibers," *J. Compos. Mater.*, vol. 44, no. 14, pp. 1717–1727, 2010, doi: 10.1177/0021998309357087.

[49] M. Kant and D. Penumadu, “Dynamic mechanical characterization for nonlinear behavior of single carbon fibers,” *Compos. Part A Appl. Sci. Manuf.*, vol. 66, pp. 201–208, Nov. 2014, doi: 10.1016/j.compositesa.2014.07.019.

[50] M. R. Wisnom, “The Effect of Fibre Waviness on the Relationship between Compressive and Flexural Strengths of Unidirectional Composites,” *J. Compos. Mater.*, vol. 28, no. 1, pp. 66–76, Jan. 1994, doi: 10.1177/002199839402800105.

[51] H. D. Wagner, M. S. Amer, and L. S. Schadler, “Residual compression stress profile in high-modulus carbon fiber embedded in isotactic polypropylene by micro-Raman spectroscopy,” *Appl. Compos. Mater.*, vol. 7, no. 4, pp. 209–217, 2000, doi: 10.1023/A:1008956929081.

[52] B. W. Schafer, “Local, distortional, and Euler buckling of thin-walled columns,” *J. Struct. Eng.*, vol. 128, no. 3, pp. 289–299, 2002, doi: 10.1061/(ASCE)0733-9445(2002)128:3(289).

[53] T. Takahashi, M. Ueda, K. Iizuka, A. Yoshimura, and T. Yokozeki, “Simulation on kink-band formation during axial compression of a unidirectional carbon fiber-reinforced plastic constructed by X-ray computed tomography images,” *Adv. Compos. Mater.*, vol. 28, no. 4, pp. 347–363, 2019, doi: 10.1080/09243046.2018.1555387.

[54] ASTM D3518, *Standard Test Method for In-Plane Shear Response of Polymer Matrix Composite Materials by Tensile Test of a ±45° Laminate*, vol. 94, no. Reapproved 2007. West Conshohocken, PA: ASTM International, 2001.

[55] M. R. Wisnom, “The effect of fibre rotation in ±45° tension tests on measured shear properties,” *Composites*, vol. 26, no. 1, pp. 25–32, 1995, doi: 10.1016/0010-4361(94)P3626-C.

[56] S. Kellas, J. Morton, and K. E. Jackson, “An evaluation of the±45 tensile test for the determination of the in-plane shear strength of composite materials.,” 1991.

[57] S. Kellas and J. Morton, “Scaling Effects in Angle-Ply Laminates,” 1992.

[58] G. Kretsis, “A review of the tensile, compressive, flexural and shear properties of hybrid fibre-reinforced plastics,” *Composites*, vol. 18, no. 1, pp. 13–23, Jan. 1987, doi:

10.1016/0010-4361(87)90003-6.

[59] J. G. Davis, “Compressive strength of fiber-reinforced composite materials,” *Composites*, vol. 7, no. 4, p. 261, Oct. 1976, doi: 10.1016/0010-4361(76)90243-3.

[60] M. P. F. Sutcliffe, S. L. Lemanski, and A. E. Scott, “Measurement of fibre waviness in industrial composite components,” *Compos. Sci. Technol.*, vol. 72, no. 16, pp. 2016–2023, 2012, doi: 10.1016/j.compscitech.2012.09.001.

[61] Hexcel, “HexTow ® IM7 Carbon Fiber Product Data Sheet,” vol. 000, pp. 1–2, 2020.

[62] AGY, “AGY Advanced Materials For Demanding Composite Applications,” *Catalogue*, vol. 0945, pp. 2–3, [Online]. Available: www.agy.com.

[63] G. Czél and M. R. Wisnom, “Demonstration of pseudo-ductility in high performance glass/epoxy composites by hybridisation with thin-ply carbon prepreg,” *Compos. Part A Appl. Sci. Manuf.*, vol. 52, pp. 23–30, 2013, doi: 10.1016/j.compositesa.2013.04.006.

[64] J. D. Fuller and M. R. Wisnom, “Pseudo-ductility and damage suppression in thin ply CFRP angle-ply laminates,” *Compos. Part A Appl. Sci. Manuf.*, vol. 69, pp. 64–71, 2015, doi: 10.1016/j.compositesa.2014.11.004.

[65] G. Czél, S. Pimenta, M. R. Wisnom, and P. Robinson, “Demonstration of pseudo-ductility in unidirectional discontinuous carbon fibre/epoxy prepreg composites,” *Compos. Sci. Technol.*, vol. 106, pp. 110–119, 2015, doi: 10.1016/j.compscitech.2014.10.022.

[66] H. Yu, M. L. Longana, M. Jalalvand, M. R. Wisnom, and K. D. Potter, “Pseudo-ductility in intermingled carbon/glass hybrid composites with highly aligned discontinuous fibres,” *Compos. Part A Appl. Sci. Manuf.*, vol. 73, pp. 35–44, 2015, doi: 10.1016/j.compositesa.2015.02.014.

[67] Y. Swolfs *et al.*, “Tensile behaviour of intralayer hybrid composites of carbon fibre and self-reinforced polypropylene,” *Compos. Part A Appl. Sci. Manuf.*, vol. 59, pp. 78–84, 2014, doi: 10.1016/j.compositesa.2014.01.001.

[68] M. Jalalvand, G. Czél, and M. R. Wisnom, “Numerical modelling of the damage modes in UD thin carbon/glass hybrid laminates,” *Compos. Sci. Technol.*, vol. 94, pp. 39–47, 2014, doi: 10.1016/j.compscitech.2014.01.013.

[69] J. Haberle, “Strength and Failure Mechanisms of Unidirectional Carbon Fibre-Reinforced Under Axial Compression,” no. December, pp. 79–115, 1991.

[70] D. Petersen, J. Häberle, and F. Matthews, “The Influence of Test Piece Preparation on the Compressive Strength of Unidirectional Fiber-Reinforced Plastic,” *J. Test. Eval.*, vol. 22, no. 4, p. 360, Nov. 1994, doi: 10.1520/JTE11845J.

[71] S. W. Yurgartis, “Measurement of small angle fiber misalignments in continuous fiber composites,” *Compos. Sci. Technol.*, vol. 30, no. 4, pp. 279–293, Jan. 1987, doi: 10.1016/0266-3538(87)90016-9.

[72] M. R. Wisnom and J. Häberle, “Prediction of buckling and failure of unidirectional carbon fibre/epoxy struts,” *Compos. Struct.*, vol. 28, no. 3, pp. 229–239, Jan. 1994, doi: 10.1016/0263-8223(94)90011-6.

[73] J. Häberle and F. Matthews, “Macro-instability of unidirectional CFRP compression test specimens,” *Compos. Sci. Technol.*, vol. 50, no. 2, pp. 229–236, Jan. 1994, doi: 10.1016/0266-3538(94)90144-9.

[74] S. TAN, “Stress analysis and the testing of Celanese and IITRI compression specimens☆,” *Compos. Sci. Technol.*, vol. 44, no. 1, pp. 57–70, 1992, doi: 10.1016/0266-3538(92)90025-X.

[75] G. Czél, M. Jalalvand, and M. R. Wisnom, “Hybrid specimens eliminating stress concentrations in tensile and compressive testing of unidirectional composites,” *Compos. Part A Appl. Sci. Manuf.*, vol. 91, pp. 436–447, Dec. 2016, doi: 10.1016/j.compositesa.2016.07.021.

[76] C. O. Horgan, “Saint-Venant End Effects In Composites,” *J. Compos. Mater.*, vol. 16, no. 5, pp. 411–422, 1982, doi: 10.1177/002199838201600506.

[77] M. Jalalvand, G. Czél, and M. R. Wisnom, “Parametric study of failure mechanisms and optimal configurations of pseudo-ductile thin-ply UD hybrid composites,” *Compos. Part A Appl. Sci. Manuf.*, vol. 74, pp. 123–131, 2015, doi: 10.1016/j.compositesa.2015.04.001.

[78] P. M. Jelf and N. A. Fleck, “Compression Failure Mechanisms in Unidirectional

Composites," *J. Compos. Mater.*, vol. 26, no. 18, pp. 2706–2726, Dec. 1992, doi: 10.1177/002199839202601804.

[79] S. R. Swanson, M. Messick, and G. R. Toombes, "Comparison of torsion tube and Iosipescu in-plane shear test results for a carbon fibre-reinforced epoxy composite," *Composites*, vol. 16, no. 3, pp. 220–224, 1985, doi: 10.1016/0010-4361(85)90605-6.

[80] A. Standard, "Standard test method for tensile properties of polymer matrix composite materials," *ASTM D3039/D 3039M*, pp. 1–13, 1995, doi: 10.1520/D3039.

[81] G. Czél, M. Jalalvand, and M. R. Wisnom, "Hybrid specimens eliminating stress concentrations in tensile and compressive testing of unidirectional composites," *Compos. Part A Appl. Sci. Manuf.*, vol. 91, pp. 436–447, 2016, doi: 10.1016/j.compositesa.2016.07.021.

[82] Gurit Ltd., "SE 84LV - Low Temperature Cure Epoxi Prepreg," pp. 1–6, 2019, [Online]. Available: https://www.gurit.com/-/media/Gurit/Datasheets/se-84lv.PDF.

[83] Gurit, "SE 84 Nano," *Tech. Datasheet*, pp. 1–7, 2000.

[84] C. Chen, R. S. Justice, D. W. Schaefer, and J. W. Baur, "Highly dispersed nanosilica–epoxy resins with enhanced mechanical properties," *Polymer (Guildf).*, vol. 49, no. 17, pp. 3805–3815, Aug. 2008, doi: 10.1016/j.polymer.2008.06.023.

[85] K. L. Thunhorst, A. M. Hine, P. Sedgwick, M. R. Huehn, and D. P. Goetz, "Nanosilica Concentration Effect on Epoxy Resins and Filament-Wound Composite Overwrapped Pressure Vessels," 2011, [Online]. Available: http://multimedia.3m.com/mws/media/791707O/nanosilica-concentration-effects-on-pressure-vessels.pdf.

[86] L. P. Singh, S. R. Karade, S. K. Bhattacharyya, M. M. Yousuf, and S. Ahalawat, "Beneficial role of nanosilica in cement based materials - A review," *Constr. Build. Mater.*, vol. 47, pp. 1069–1077, 2013, doi: 10.1016/j.conbuildmat.2013.05.052.

[87] Gurit Ltd., "Gurit Product Catalogue," *Manufactirer's Cat.*, 2020, doi: 10.1108/ijhcqa.2006.06219bab.002.

[88] M. R. Wisnom, "The effect of specimen size on the bending strength of unidirectional

carbon fibre-epoxy," *Compos. Struct.*, vol. 18, no. 1, pp. 47–63, Jan. 1991, doi: 10.1016/0263-8223(91)90013-O.

[89] C. V. Opelt, G. M. Cândido, and M. C. Rezende, "Fractographic study of damage mechanisms in fiber reinforced polymer composites submitted to uniaxial compression," *Eng. Fail. Anal.*, vol. 92, no. November 2017, pp. 520–527, 2018, doi: 10.1016/j.engfailanal.2018.06.009.

[90] K. K. Kratmann, M. P. F. Sutcliffe, L. T. Lilleheden, R. Pyrz, and O. T. Thomsen, "A novel image analysis procedure for measuring fibre misalignment in unidirectional fibre composites," *Compos. Sci. Technol.*, vol. 69, no. 2, pp. 228–238, 2009, doi: 10.1016/j.compscitech.2008.10.020.